Developing Low Shrinkage Stress Thiol–Ene Dental Resins & Two-color Photopolymerization Chemistries

by

Harry L. van der Laan

A dissertation submitted in partial fulfillment
of the requirements for the degree of
Doctor of Philosophy
(Macromolecular Science and Engineering)
at the University of Michigan
2019

Doctoral Committee:
Associate Professor Timothy F. Scott, Chair
Professor Emeritus Brian H. Clarkson
Associate Professor Kenichi Kuroda
Associate Professor Ariella Shikanov

Harry Luit van der Laan

hllaan@umich.edu

ORCID ID: 0000-0001-6765-1180

© Harry L. van der Laan 2019

Dedication

To Chione

The best companion I could wish for

Acknowledgements

I want to thank my PhD advisor Tim Scott for all of his guidance, support as well as encouragement throughout my doctoral studies. I would also like to thank the members of my dissertation committee for their advice and feedback.

I am very fortunate to have met some wonderful colleagues in the Scott Polymer Dojo. Scott Zavada, Tao Wei, Dowon Ahn, Megan Dunn, Max Ma, Sam Leguizamon, Abdulla Alqubati, Austin Bingham, Alex Commisso, Futianyi Wang, Junting Li, Jae Hwan Jung, Joe Furgal, Megan Cole, Giuseppe Tronci, Sameer Sathe, Dan Li, and Nathan Wood. I want to thank them all for their help, camaraderie, and insights throughout my PhD.

The Macro program and community have been a very important part of my PhD. It is thanks to the excellent leadership of Rick Laine, Mark Banaszak Holl, and Jinsang Kim, supported by Adam Mael and Julie Pollak that the Macro program feels like a family.

None of this would have happened if it hadn't been for Anne McNeil and Ed Palermo. Working with these wonderful people all these years ago has inspired me to pursue my doctoral studies in the US and it is thanks to them that I ended up in Macro.

Thanks to the immense love support of my mom, dad, and brother my family never felt to be far away, despite the great distance that separates us. It kept me going when times were tough

Table of Contents

Dedication ii

Acknowledgements iii

List of Figures viii

List of Tables xxii

Abstract xxiv

Chapter 1 Introduction 1

1.1 Photochemistry and photopolymerizations 1

1.1.1 Photoinitiator chemistries 1

1.2 Materials for dental restorative resins 3

1.2.1 Methacrylate-based dental composites 3

1.2.2 Polymerization-induced shrinkage 4

1.2.3 Chemical approaches to Shrinkage stress mitigation 6

1.2.4 Thiol–ene chemistry 8

1.2.5 Addition-fragmentation chain-transfer chemistries 9

1.2.6 Restoration adhesion to mineralized tissues 10

1.2.7 Self-etch adhesives 12

1.3 Hexaarylbiimidazoles 15

1.3.1 History of HABIs 15

1.3.2 HABIs as free radical photoinitiators 16

1.3.3 Hexaarylbiimidazoles in functional materials 19

1.4 Polymerization inhibition 19

1.4.1 Universal polymerization inhibition 19

1.4.2 Controlled Free Radical Polymerizations 20

1.5 Photocontrolled reactions in (stereo)lithography 23

1.6 Overview of subsequent chapters 26

1.7 References 27

Chapter 2 Development of Novel High T_g, Low Shrinkage Stress Thiol–ene Resins 43

2.1 Original Publication information 43

2.2 Abstract 43

2.3 Introduction 44

2.4 Experimental 47

2.4.1 Materials 47

2.4.2 Methods 49

2.4.3 Synthesis 54

2.5 Results and Discussion 59

2.6 Conclusion 71

2.7 Acknowledgements 72

2.8 References 72

Chapter 3 Further Development of Thiol–ene Dental Resins Through Addition-Fragmentation Chain-Transfer Chemistry and Adhesive Monomers 78

3.1 Abstract 78

3.2 Introduction 79

3.2.1 Addition-fragmentation chain-transfer chemistry in thiol–ene systems 79

3.2.2 Acidic monomers to improve adhesion to mineralized tissues 81

3.3 Experimental 84

3.3.1 Materials...............84

3.3.2 Methods 85

3.3.3 Synthesis 87

3.4 Results and discussion...............101

3.4.1 Effect of Addition-Fragmentation CT on thiol–ene resins 101

3.4.2 Acidic monomers for improved tissue adhesion...............115

3.5 Conclusion...............125

3.6 References...............126

Chapter 4 Hexaarylbiimidazoles as Efficient Photoinhibitors of Free-Radical Chain-Growth Photopolymerizations 133

4.1 Original Publication information...............133

4.2 Abstract...............133

4.3 Introduction 134

4.4 Experimental 136

4.4.1 Materials...............136

4.4.2 Methods 137

4.4.3 Synthesis 139

4.5 Results and Discussion 147

4.5.1 o-Cl-HABI as a photoinhibitor of free-radical chain-growth polymerizations 147

4.5.2 Covalently linked, diffusion-limited HABIs as photoinhibitors...............157

4.6 Conclusion...............166

4.7 Acknowledgements...............166

4.8 References ... 167

Chapter 5 Dual-Wavelength Volumetric Photopolymerization Confinement Through Butyl Nitrite Free-Radical Photoinhibition ... 173

5.1 Original Publication Information ... 173

5.2 Abstract ... 173

5.3 Introduction ... 174

5.4 Experimental ... 179

5.4.1 Materials ... 179

5.4.2 Methods ... 180

5.5 Results & discussion ... 182

5.5.1 Patterned free-radical and cationic photopolymerizations ... 198

5.6 Conclusion ... 204

5.7 References ... 205

Chapter 6 Summary and Future Work ... 211

6.1 Research Summary ... 211

6.2 Future directions ... 215

6.3 References ... 220

List of Figures

Figure 1.1 Examples of photoinitiating systems, initiating species generation from (a) the cationic photoinitiator diphenyliodonium hexafluoroantimonate (b) type I radical photoinitiator TPO (c) type II radical photoinitiator CQ/EDAB 3

Figure 1.2 Monomer contraction following polymerization.................................. 5

Figure 1.3 Ring-opening monomers 7

Figure 1.4 Cationic ring-opening polymerization mechanism of cyclohexene oxide.. 7

Figure 1.5 The thiol–ene reaction mechanism is described by repeating cycles of thiyl addition to vinyl groups and chain transfer of the carbon-centered radical to thiols. 9

Figure 1.6 AFCT monomers studied for stress relaxation in dental restorative resins[38, 40, 42].. 10

Figure 1.7 Schematic illustration of bond structure of a self-etching system and etch-and-rinse system (total-etching system). The structure of the hybrid layer of total-etch adhesives consists of resin and collagen fibrils. The combination of resin, collagen fibrils and inorganic matter (the smear layer) is a typical hybrid layer of self-etching adhesives. The hybrid layer of self-etching systems is thinner than that of total-etching adhesives, due to the mild acidic effect of their acidic monomers on dentin.[50] 12

Figure 1.8 Structures of self-etch methacrylate monomers (a) methacryloyloxydecyl dihydrogen phosphate (b) methacryloyloxyethyl phosphonic acid (c) 10-methacryloyloxydecyl malonic acid(d) 4-methacryloyloxyethyl trimellitate anhydride. Etching acidic moieties denoted in red 14

Figure 1.9 HABI cleavage and chain transfer to thiol coinitiator[66] 17

Figure 1.10 Illustration of sensitization pathways in a dye/HABI photoinitiating system[74] 18

Figure 1.11 Structures of common radical inhibitors 20

Figure 1.12 Equilibrium in the ATRP of a methacrylate 21

Figure 1.13 NMP equilibrium of Styrene 22

Figure 1.14 RAFT equilibrium between 2 polymers 22

Figure 1.15 Comparison between SLA and DLP irradiation (Formlabs, https://formlabs.com/blog/3d-printing-technology-comparison-sla-dlp/) 23

Figure 1.16 Photochromic ring-opening of STP to MC and subsequent thiol–Michael reaction with a maleimide[101] 25

Figure 2.1 Materials used in this study (a) TMES (b) PETMP (c) TPO (d) TATATO (e) TNTATO (f) DNBPA 49

Figure 2.2 ^{1}H-NMR Spectrum of Tetra(S-ethylethanethioate)silane 54

Figure 2.3 ^{1}H-NMR Spectrum of Tetra(2-mercaptoethyl)silane (TMES) 55

Figure 2.4 ^{1}H-NMR Spectrum of Trinorbornyl triazine trione (TNTATO) 56

Figure 2.5 ^{1}H-NMR Spectrum of Dinorbornyl bisphenol A (DNBPA) 57

Figure 2.6 ^{1}H-NMR Spectrum of TMES-TNTATO oligomer 58

Figure 2.7 ^{1}H-NMR Spectrum of TMES-DNBPA oligomer................................ 58

Figure 2.8 Photopolymerization kinetics Conversion versus time for the photopolymerizations of (a) PETMP/TATATO, (b) TMES/TATATO, (c) TMES-TNTATO/TATATO, and (d) TMES-DNBPA/TATATO. Continuous irradiation with 405 nm at intensities of 1 (blue triangles), 3 (red circles), and 10 (black squares) mW/cm^{2}. TATATO ene conversions are displayed as solid lines and symbols, whereas thiol conversions are dashed lines and open symbols 60

Figure 2.9 ^{1}H-NMR spectra of (a) TMES, (b) TNTATO, and (c) TMES-TNTATO oligomer Complete incorporation of TNTATO in the oligomer is confirmed by the disappearance of the norbornyl signal centered at 6 ppm highlighted in the dashed box 61

Figure 2.10 Dynamic Mechanical Analysis traces of storage modulus (E', solid lines) and tan δ (dashed lines) as a function of temperature (a) PETMP/TATATO, (b) TMES/TATATO, (c) TMES-TNTATO/TATATO, and (d) TMES-DNBPA/TATATO, irradiated with 405 nm at 10 mW·cm^{-2}. First heating ramp is in black, and second heating ramp is in red. Storage modulus is displayed as solid lines and symbols, whereas tan δ is displayed as dashed lines and open symbols 63

Figure 2.11 Dynamic Mechanical Analysis comparison of cured thiol–ene monomeric and oligomeric resins as indicated and irradiated with 405 nm at 10 mW·cm^{-1} in the first (maize) and second (blue) heating cycles (a) glass transition temperature as indicated by tan δ, and (b) storage modulus at 37 °C. 64

Figure 2.12 Tensometry Polymerization Shrinkage stress versus time for the photocuring of (a) PETMP/TATATO, (b) TMES/TATATO, (c) TMES-TNTATO/TATATO, and (d) TMES-DNBPA/TATATO. Continuous irradiation with 405 nm at intensities of 1 (blue triangles), 3 (red circles), and 10 (black squares) $mW\cdot cm^{-2}$. 66

Figure 2.13 Shrinkage stress comparison of thiol–ene monomeric and oligomeric resins as indicated and irradiated with 405 nm at 10 $mW\cdot cm^{-1}$ for 10 minutes. 68

Figure 2.14 Correlation of TATATO double bond conversion with the observed polymerization shrinkage stress of (a) PETMP/TATATO, (b) TMES/TATATO, (c) TMES-TNTATO/TATATO, and (d) TMES-DNBPA/TATATO. Continuous irradiation with 405 nm at intensities of 1 (blue), 3 (red), and 10 (black) $mW\cdot cm^{-2}$. Data from Figure 2.8 and Figure 2.12. 69

Figure 2.15 Cell viability testing 70

Figure 3.1 ^{1}H-NMR Spectrum of endo-Norbornyl bromide (major isomer)........ 87

Figure 3.2 ^{1}H-NMR of 2-methylenepropane-1,3-di(ethylxanthogenate) 88

Figure 3.3 ^{1}H-NMR Spectrum of 2-methylenepropane-1,3-dithiol...................... 89

Figure 3.4 ^{1}H-NMR Spectrum of NAS.. 90

Figure 3.5 ^{1}H-NMR Spectrum of 1,3-dibromo-2-methylpropane 91

Figure 3.6 ^{1}H-NMR Spectrum of 2-methylpropane-1,3-di(ethylxanthogenate)... 92

Figure 3.7 ^{1}H-NMR Spectrum of 2-methylpropane-1,3-dithiol 93

Figure 3.8 ^{1}H-NMR Spectrum of NPS 94

Figure 3.9 ^{1}H-NMR Spectrum of DAC 96

Figure 3.10 ^{1}H-NMR Spectrum of TAC... 97

Figure 3.11 ^{1}H-NMR Spectrum of DAP... 98

Figure 3.12 ^{31}P-NMR Spectrum of DAP 99

Figure 3.13 ^{1}H-NMR Spectrum of TAP 100

Figure 3.14 ^{31}P-NMR Spectrum of TAP... 101

Figure 3.15 Possible mechanism for thiol consumption in AFCT..................... 103

Figure 3.16 Photopolymerization kinetics Conversion versus time for the photopolymerizations of TMES/TATATO formulated with (a) 5% NAS, (b) 10% NAS, (c) 15% NAS, and (d) 10% NPS Continuous irradiation with 405 nm at intensities of 10 (black squares), 3 (red circles), and 1 (blue triangles) $mW \cdot cm^{-2}$. TATATO ene conversions are displayed as solid lines and symbols, whereas thiol conversions are dashed lines and open symbols 104

Figure 3.17 NAS and NPS norbornene photopolymerization kinetics versus time in formulations of (a) TMES/TATATO, and (d) TMES-TNTATO/TATATO. Continuous irradiation with 405 nm at 10 $mW \cdot cm^{-2}$ of formulation containing 5% NAS (black squares), 10% NAS (red circles), 15% NAS (blue triangles), and 10% NPS (green diamonds).. 105

Figure 3.18 Photopolymerization kinetics Conversion versus time for the photopolymerizations of TMES-TNTATO/TATATO formulated with (a) 5% NAS, (b) 10% NAS, (c) 15% NAS, and (d) 10% NPS. Continuous irradiation with 405 nm at

intensities of 10 (black squares), 3 (red circles), and 1 (blue triangles) mW·cm^{-2}. TATATO ene conversions are displayed as solid lines and symbols, whereas thiol conversions are dashed lines and open symbols 106

Figure 3.19 Polymerization-induced shrinkage stress versus time for the photopolymerizations of TMES/TATATO formulated with (a) 5% NAS, (b) 10% NAS, (c) 15% NAS, and (d) 10% NPS. Continuous irradiation with 405 nm at intensities of 10 (black squares), 3 (red circles), and 1 (blue triangles) mW·cm^{-2}.................................. 107

Figure 3.20 Polymerization-induced shrinkage stress versus time for the photopolymerizations of TMES-TNTATO/TATATO formulated with (a) 5% NAS, (b) 10% NAS, (c) 15% NAS, and (d) 10% NPS. Continuous irradiation with 405 nm at intensities of 10 (black squares), 3 (red circles), and 1 (blue triangles) mW·cm^{-2}. 108

Figure 3.21 Polymerization shrinkage stress versus allyl sulfide (NAS) content for TMES/TATATO (maize) and TMES-TNTATO/TATATO (blue) based formulations containing 1% TPO as the photoinitiator and irradiated for 10 minutes with 405nm light @ 10 mW/cm^2.. 109

Figure 3.22 Correlation between monomer conversion and polymerization-induced shrinkage stress of TMES/TATATO formulated with (a) 5% NAS, (b) 10% NAS, (c) 15% NAS, and (d) 10% NPS Continuous irradiation with 405 nm at intensities of 10 (black squares), 3 (red circles), and 1 (blue triangles) mW·cm^{-2}. TATATO ene conversions are displayed as solid lines and symbols, whereas thiol conversions are dashed lines and open symbols 111

Figure 3.23 Correlation between monomer conversion and polymerization-induced shrinkage stress of TMES-TNTATO/TATATO formulated with (a) 5% NAS, (b) 10% NAS, (c) 15% NAS, and (d) 10% NPS Continuous irradiation with 405 nm at intensities of 10 (black squares), 3 (red circles), and 1 (blue triangles) mW·cm^{-2}. TATATO ene conversions are displayed as solid lines and symbols, whereas thiol conversions are dashed lines and open symbols 112

Figure 3.24 Dynamic Mechanical Analysis traces of storage modulus (E', solid lines) and tan δ (dashed lines) as a function of temperature (a) TMES/TATATO, (b) TMES/TATATO/NAS (10%), (c) TMES/TATATO/NPS (10, irradiated with 405 nm at 10 mW·cm^{-2}. First heating ramp is in black, and second heating ramp is in red. Storage modulus is displayed as solid lines and symbols, whereas tan δ is displayed as dashed lines and open symbols 113

Figure 3.25 Dynamic Mechanical Analysis traces of storage modulus (E', solid lines) and tan δ (dashed lines) as a function of temperature (a) TMES-TNTATO/TATATO, (b) TMES-TNTATO/TATATO/NAS (10%), (c) TMES-TNTATO/TATATO/NPS (10%), irradiated with 405 nm at 10 mW·cm^{-2}. First heating ramp is in black, and second heating ramp is in red. Storage modulus is displayed as solid lines and symbols, whereas tan δ is displayed as dashed lines and open symbols 114

Figure 3.26 Dynamic Mechanical Analysis comparison of cured TMES/TATATO and TMES-TNTATO/TATATO resins formulated with AFCT monomer NAS and negative control NPS at 10 wt% as indicated and irradiated with 405 nm at 10 mW·cm^{-1} in the first (maize) and second (blue) heating cycles (a) glass transition temperature as indicated by tan δ, and (b) storage modulus at 37 °C 114

Figure 3.27 Structures of proposed self-etching monomers 116

Figure 3.28 Photopolymerization kinetics conversion versus time for the photopolymerizations of TMES/TATATO formulated with (a) 10% DAC, (b) 20% DAC, (c) 10% TAC, and (d) 20% TAC. Continuous irradiation with 405 nm at intensities of 10 (black squares), 3 (red circles), and 1 (blue triangles) mW·cm^{-2}. TATATO ene conversions are displayed as solid lines and symbols, whereas thiol conversions are dashed lines and open symbols 118

Figure 3.29 Photopolymerization kinetics conversion versus time for the photopolymerizations of TMES/TATATO formulated with (a) 10% DAP, (b) 20% DAP, (c) 10% TAP, and (d) 20% TAP. Continuous irradiation with 405 nm at intensities of 10 (black squares), 3 (red circles), and 1 (blue triangles) mW·cm^{-2}. TATATO ene conversions are displayed as solid lines and symbols, whereas thiol conversions are dashed lines and open symbols 120

Figure 3.30 Dynamic Mechanical Analysis traces of storage modulus (E', solid lines) and tan δ (dashed lines) as a function of temperature OF TMES/TATATO formulated with (a) 10% DAC, (b) 20% DAC, (c) 10% TAC, and (d) 20% TAC), irradiated with 405 nm at 10 mW·cm^{-2}. First heating ramp is in black, and second heating ramp is in red. Storage modulus is displayed as solid lines and symbols, whereas tan δ is displayed as dashed lines and open symbols 121

Figure 3.31 Dynamic Mechanical Analysis comparison of cured TMES/TATATO resins formulated with carboxylic acid monomer as indicated and irradiated with 405 nm

at 10 mW·cm^{-1} in the first (maize) and second (blue) heating cycles (a) glass transition temperature as indicated by tan δ, and (b) storage modulus at 37 °C............................ 122

Figure 3.32 Dynamic Mechanical Analysis comparison of cured TMES/TATATO resins formulated with phosphoric acid monomer as indicated and irradiated with 405 nm at 10 mW·cm^{-1} in the first (maize) and second (blue) heating cycles (a) glass transition temperature as indicated by tan δ, and (b) storage modulus at 37 °C............................ 122

Figure 3.33 Dynamic Mechanical Analysis traces of storage modulus (E', solid lines) and tan δ (dashed lines) as a function of temperature OF TMES/TATATO formulated with (a) 10% DAP, (b) 20% DAP, (c) 10% TAP, and (d) 20% TAP), irradiated with 405 nm at 10 mW·cm^{-2}. First heating ramp is in black, and second heating ramp is in red. Storage modulus is displayed as solid lines and symbols, whereas tan δ is displayed as dashed lines and open symbols 124

Figure 4.1 ^{1}H-NMR of 4,5-diphenyl-2-(4'-phenylboronic acid)imidazole 140

Figure 4.2 Structures of (a) photoinitiator CQ, (b) co-initiator EDAB, (c) photoinhibitor o-Cl-HABI. (d) UV-Vis absorbance spectrum of CQ (blue solid line) and o-Cl-HABI (violet dashed line) in THF. The UV and blue wavelengths used in the two-color irradiation system are highlighted by the violet and blue vertical bars, respectively. 148

Figure 4.3 (a) Photodissociation and thermal recombination reaction of o-Cl-HABI (b) absorbance at 554 nm of o-Cl-HABI, o-Cl-HABI and EDAB, and o-Cl-HABI and 2-MBT under irradiation with 365 nm @ 30 mW/cm^{2} as indicated by the vertical violet bars, and (b) methacrylate conversion vs time under continuous irradiation with

365 nm @ 30 mW/cm^2 for formulations containing o-Cl-, o-Cl-HABI and EDAB, and o-Cl-HABI and 2-MBT 149

Figure 4.4 Structures of monomers examined (a) Bisphenol A ethoxylate diacrylate (BPAEDA; n=4), (b) triethylene glycol dimethacrylate (TEGDMA), (c) bisphenol A glycidyl dimethacrylate (bisGMA), (d) triethylene glycol divinyl ether (TEGDVE), (e) N-(n-propyl)maleimide (NPM), Alkene conversion versus time for resin formulations of (f) BPAEDA (g), bisGMA/TEGDMA, and (h) TEGDVE/NPM (vinyl ether and maleimide conversions denoted by solid and dashed lines, respectively). Continuous irradiation with exclusively 470 nm @ 100 mW/cm^2, 470 nm @ 100 mW/cm^2 & 365 nm @ 30 mW/cm^2, and 365 nm @ 30 mW/cm^2 as indicated. 152

Figure 4.5 Alkene conversion versus time for commercial resin formulations received from, and (a) Dentsply, and (b) 3D systems. Continuous irradiation with exclusively 470 nm, and concurrent 470 nm & 365 nm 153

Figure 4.6 Schematic diagram of the photoinitiation-photoinhibition system using mask-based photolithography. The photomask used to pattern the photoinhibiting wavelength and a sample produced by using the photoinitiation-photoinhibition system. 154

Figure 4.7 (a) Optical setup for two-color, stereolithographic AM by concurrent photopolymerization and photoinhibition. Near UV (365 nm) is superimposed onto patterned blue (458 nm) with a dichroic mirror and projected through a transparent window into a photopolymerizable resin vat. (b) A solid block M (left) and a 3DBenchy

(right) printed using the two-color, stereolithographic AM. Images courtesy of Martin de Beer. 155

Figure 4.8 Wavelength selective photoinitiation and transient photoinhibition of methacrylate polymerization. Methacrylate conversion versus time for bisGMA/TEGDMA formulated with CQ/EDAB and o-Cl-HABI under continuous irradiation, starting at 0.5 minutes, with 470 nm @ 100 mW/cm^2 and intermittent irradiation with 365 nm @ 30 mW/cm^2 during the shaded periods as indicated........... 157

Figure 4.9 Covalently bound HABIs with different transient radical lifetimes[28-32] 158

Figure 4.10 ESI mass spectrum of oxidated pincer showing 1,8-TPID-naphthalene at 714.28 and the oxidized species at 746.30 m/z... 159

Figure 4.11 Proposed reaction of the naphthalene linked HABIs with molecular oxygen[34] 160

Figure 4.12 UV-Vis Spectra of (a) cyclophane HABI and (b) cyclophane HABI during irradiation and (c) post irradiation (both low and high intensity) 164

Figure 4.13 Kinetics experiments of cyclophane HABI as a photoinhibitor...... 165

Figure 5.1 (a) SLA setup for two-color SLA support-free printing and (b) scheme for solvent removal of supports in complex, sparse structures..................................... 179

Figure 5.2 Structures of (A) photoinitiator CQ, (B) co-initiator EDAB, (C) near-UV photoinhibitor BN, (C) UV-Visible absorbance spectrum of CQ (solid blue line) and BN (dashed purple line) in THF. The near-UV and visible wavelengths used in this study

are highlighted. Monomer structures of (E) TEGDMA, (F) bisGMA, (G) TMPTMA, (H) TMPTA, (I) BPAEDA. 184

Figure 5.3 Methacrylate conversion versus time for the photopolymerization of bisGMA/TEGDMA resins formulated with 0.2 wt% CQ/0.5 wt% EDAB and (A) 0 wt% BN, (B) 0.5 wt% BN, (C) 1.0 wt% BN, and (D) 3.0 wt% BN. Formulations were irradiated with 470 nm light at an intensity of 100 mW/cm^2 (black, squares), 365 nm light at an intensity of 30 mW/cm^2 (red, circles), or concurrent 470 nm and 365 nm light at intensities of 100 and 30 mW/cm^2 (blue, triangles). 186

Figure 5.4 Acrylate conversion versus time for the photopolymerization of TMPTA resins formulated with 0.2 wt% CQ/0.5 wt% EDAB and (A) 0 wt% BN, (B) 0.5 wt% BN, (C) 1.0 wt% BN, and (D) 3.0 wt% BN. Formulations were irradiated with 470 nm light at an intensity of 100 mW/cm^2 (black, squares), 365 nm light at an intensity of 30 mW/cm^2 (red, circles), or concurrent 470 nm and 365 nm light at intensities of 100 and 30 mW/cm^2 (blue, triangles). 187

Figure 5.5 Methacrylate conversion versus time for the photopolymerization of TMPTMA resins formulated with 0.2 wt% CQ/0.5 wt% EDAB and (A) 0 wt% BN, (B) 0.5 wt% BN, (C) 1.0 wt% BN, and (D) 3.0 wt% BN. Formulations were irradiated with 470 nm light at an intensity of 100 mW/cm^2 (black, squares), 365 nm light at an intensity of 30 mW/cm^2 (red, circles), or concurrent 470 nm and 365 nm light at intensities of 100 and 30 mW/cm^2 (blue, triangles). 190

Figure 5.6 Acrylate conversion versus time for the photopolymerization of BPAEDA resins formulated with 0.2 wt% CQ/0.5 wt% EDAB and (A) 0 wt% BN, (B)

0.5 wt% BN, (C) 1.0 wt% BN, and (D) 3.0 wt% BN. Formulations were irradiated with 470 nm light at an intensity of 100 mW/cm^2 (black, squares), 365 nm light at an intensity of 30 mW/cm^2 (red, circles), or concurrent 470 nm and 365 nm light at intensities of 100 and 30 mW/cm^2 (blue, triangles). 191

Figure 5.7 Methacrylate conversion versus time for the photopolymerization of a bisGMA/TEGDMA resin formulated with 0.2 wt% CQ/0.5 wt% EDAB/0.5 wt% BN and subject to continuous blue light irradiation (470 nm, 100 mW/cm^2) starting at t = 0 and intermittent near UV light irradiation (365 nm, 30 mW/cm^2) for 0.5 minute periods as indicated by the violet vertical bars. 194

Figure 5.8 Polymerization confinement through dual-wavelength photopatterning in 2D. (A) Schematic diagram of formulated resin subject to flood blue light irradiation and concurrent, antiparallel irradiation with near UV light through a photomask. (B) A patterned sample of CQ/EDAB/BN-formulated TMPTA produced by using concurrent, antiparallel blue and near UV irradiation. The photomask used to pattern the near UV light is also shown..................... 196

Figure 5.9 Polymerization confinement through dual-wavelength photopatterning in 3D (A) Schematic diagram of perpendicular blue and near UV irradiation to photopattern in depth the polymerization of a formulated resin. (B) and (C) Patterned sample of CQ/EDAB/BN-formulated TMPTA produced by using concurrent, perpendicular blue and near UV irradiation..................... 197

Figure 5.10 Structures of (a) free radical blue photoinitiator CQ, (b) free radical co-initiator EDAB, (c) near-UV cationic photoinitiator Sylanto 7-MS, free radical

photoinhibitor BN. (e) UV-Vis spectra of CQ (solid blue line), Sylanto 7-MS (dash-dotted black line), and BN (dashed violet line) in THF 198

Figure 5.11 Structures of (a) COMA and (b) COA ((meth)acrylate solid and cyclohexene oxide dashed, conversion versus time for (c) cyclohexene oxide methacrylate and (d) cyclohexene oxide acrylate ((meth)acrylate and epoxide denoted by solid and dashed lines, respectively). Continuous irradiation with exclusively 470 nm @ 100 mW/cm^2 (black line, squares), and 365 nm @ 30 mW/cm^2 (red line, circles), and 470 nm @ 100 mW/cm^2 & 365 nm @ 30 mW/cm^2, (blue line, triangles). And (e) polymerization routes of monomer upon exposure to 365 nm and 470 nm light 199

Figure 5.12 Structures of (a) CO, d (b) MMA, and (c) . conversion versus time for (d) 50:50 CO/MMA formulations and (d) 50:50 CO/TMPTMA (methacrylate and epoxide denoted by solid and dashed lines, respectively). Continuous irradiation with exclusively 470 nm @ 100 mW/cm^2 (black line, squares), and 365 nm @ 30 mW/cm^2 (red line, circles), and 470 nm @ 100 mW/cm^2 & 365 nm @ 30 mW/cm^2, (blue line, triangles). And (e) polymerization routes of monomer upon exposure to 365 nm and 470 nm light 202

Figure 6.1 Structures of HEMA and potential adhesive thiol–ene monomers capable of penetration into demineralized dentin 216

Figure 6.2 Structures of 2,3-dichloro, 2,4-dichloro, and 2,6-dichloro disubstituted hexaarylbiimidazoles 217

List of Tables

Table 2.1 DMA Summary thiol–ene formulations as indicated and irradiated with 405 nm at 10 mW·cm^{-1} for 10 minutes 65

Table 2.2 Shrinkage stress comparison of thiol–ene monomeric and oligomeric resins as indicated and irradiated with 405 at the noted intensity for 10 minutes 67

Table 2.3 Mechanical testing results of composite formulations 71

Table 3.1 Summary of polymerization-induced shrinkage stress of thiol–ene formulations based on TMES/TATATO and TMES-TNTATO/TATATO after constant irradiation for 10 minutes with 405nm light at the indicated light intensity. 110

Table 3.2 Compilation glass transition temperatures and storage moduli at 37°C in both heating ramps of TMES/TATATO and TMES-TNTATO/TATATO-based formulations irradiated with 405 nm at 10 mW·cm^{-2} 115

Table 3.3 Compilation glass transition temperatures and storage moduli at 37°C in both heating ramps of TMES/TATATO formulated with acidic and irradiated with 405 nm at 10 mW·cm^{-2} 125

Table 5.1 Maximum C=C conversion rates for the photopolymerization of bisGMA/TEGDMA resins formulated with 0.2 wt% CQ/0.5 wt% EDAB and varying concentrations of BN as shown........ 188

Table 5.2 Maximum C=C conversion rates for the photopolymerization of TMPTA resins formulated with 0.2 wt% CQ/0.5 wt% EDAB and varying concentrations of BN as shown. 188

Table 5.3 Maximum C=C conversion rates for the photopolymerization of TMPTMA resins formulated with 0.2 wt% CQ/0.5 wt% EDAB and varying concentrations of BN as shown 192

Table 5.4 Maximum C=C conversion rates for the photopolymerization of BPAEDA resins formulated with 0.2 wt% CQ/0.5 wt% EDAB and varying concentrations of BN as shown 192

Table 5.5 C=C conversion rates for the photopolymerization of bisGMA/TEGDMA resins formulated with 0.2 wt% CQ/0.5 wt% EDAB/0.5 wt% BN under constant blue irradiation and intermittent near UV light irradiation for 0.5 minute periods at a time 194

Table 5.6 Maximum C=C and epoxide conversion rates for the photopolymerizations of COMA formulated with 1 wt% CQ/0.5 wt% EDAB/1 wt% Sylanto 7-MS/2 wt% BN 201

Table 5.7 Dissolution of polymer films containing cationic and radically curable moieties formulated with CQ/EDAB/Sylanto 7-MS/BN cured for 30-60 seconds in organic solvents 203

Abstract

Photopolymerizations are an important class of chemical reactions that find ubiquitous use in our daily lives. The intimate interaction of light and matter in these systems allows unprecedented spatial and temporal control of polymerization lending these systems to innumerable applications in manufacturing of electronics, medical devices, and consumer products. This dissertation focuses on two of the most well-known applications of photopolymerizations: dental restorative composites and additive manufacturing.

To address the deleterious effects associated with polymerization-induced shrinkage stress in methacrylate dental resins, silane-based norbornyl-bearing thiol–ene oligomers were investigated for dental restorative resins. The glassy polymeric materials prepared here demonstrated glass transition temperatures (T_g) exceeding 100 °C, being on par with those of widely-used methacrylate polymers. Simultaneously, this approach yielded over 60% reduction in polymerization shrinkage stress relative to a thiol–ene standard. Subsequently, allyl sulfide addition-fragmentation chain-transfer chemistry was demonstrated to further lower polymerization-induced shrinkage stress of these high T_g polymers to over 80% reduction. The impact of this chemistry on polymerization shrinkage stress exceeded and eclipsed that of the pre-oligomerization, polymers without significant T_g reduction. To examine the potential for thiol–ene compatible adhesive monomers for adhesion of thiol–ene restorative materials to dental tissue and eliminate the need for methacrylate-based adhesives, acid-containing allyl-bearing monomers were

prepared and evaluated for their impact on photopolymerization kinetics and thermomechanical properties.

Following the improvements to dental restorative composites, the development of two-color irradiation chemistries for application in additive manufacturing is discussed. Hexaarylbiimidazoles (HABIs) were discovered to act as efficient photoinhibitors in acrylate, methacrylate, and vinyl ether/maleimide chain-growth photopolymerizations. Photoinhibition was then demonstrated as an effective adhesion-prevention strategy in continuous stereolithographic additive manufacturing – which allowed for vertical print rates up to 2 m/hr, the highest reported print rates to date. Additionally, to counteract the deleterious effects of the long-lived transient inhibitor species, diffusion-limited HABIs were synthesized and tested. Sharper contrast in polymerization inhibition was achieved at the expense of inhibition efficacy. To broaden the scope of two-color irradiation chemistries in volumetric additive manufacturing, butyl nitrite was found to be a suitable photoinhibitor of free radical chain-growth photopolymerizations. Through this means, the efficacy of butyl nitrite to inhibit photopolymerizations under near-UV irradiation enabled volumetric confinement of photopolymerization through perpendicular irradiation. This unique chemistry was demonstrated to selectively photoinhibit free radical polymerizations in a dual-cure cationic and radical monomer system, paving the way for support-free stereolithographic additive manufacturing.

Chapter 1

Introduction

1.1 Photochemistry and photopolymerizations

Photochemical reactions might be the single most important chemical reactions to happen in our daily lives. Photosynthesis generates the oxygen dearly needed for us to breathe. At the same time UV light in the stratosphere leads to ozone formation, in turn protecting us from harmful UV irradiation, while the light that does make it through is essential in the synthesis of vitamin D. In turn it should come as a surprise that light-mediated chemical reactions represent a significant type of reactions employed in chemistry. Examples of this can be found in pericyclic rearrangements useful in organic synthesis to light-generated reactive species (photoinitiators) to produce polymeric materials.

1.1.1 Photoinitiator chemistries

Photopolymers prepared with these photoinitiators describe another important use of photochemical reactions. Photopolymers are polymeric materials, which are prepared through curing with light, typically UV or visible light. This type of polymerization has found widespread use in our daily lives. These applications range from photolithography in the manufacturing of microscale semiconductors for electronics, to stereolithographic 3D printing, and to composite hardening in dental restorations. Typically, the resins are formulated with a combination of curable material, photoinitiator, and other additives

(dyes, composite filler, etc.), and react through either a cationic or a free radical mechanism. Cationic photopolymer resins typically contain electron-rich vinyl ethers or cyclic ethers (epoxides, oxetanes) as the monomer, and an onium or iodonium salt as the photoinitiator. As demonstrated in Figure 1.1a the (iod)onium cleaves upon excitation with light, which through a further reaction with monomer or solvent generates the initiating acid species. The counter ion used in these photoinitiators plays an important role in the monomer scope and polymerization rates. Free radical photoinitiators can broadly be divided into 2 classes. Type I photoinitiators represent single molecule photoinitiators that upon exposure to light cleave into initiating free radical species. Type II photoinitiators describe 2-component systems utilizing a sensitizer, which in the excited state undergoes either a hydrogen abstraction or electron transfer reaction with a co-initiating species, as shown through the camphorquinone/tertiary amine system in Figure 1.1c. The resultant radicals then proceed to initiate the polymerization. The camphorquinone/tertiary amine system has found a particular use in curing dental restorative composite materials.

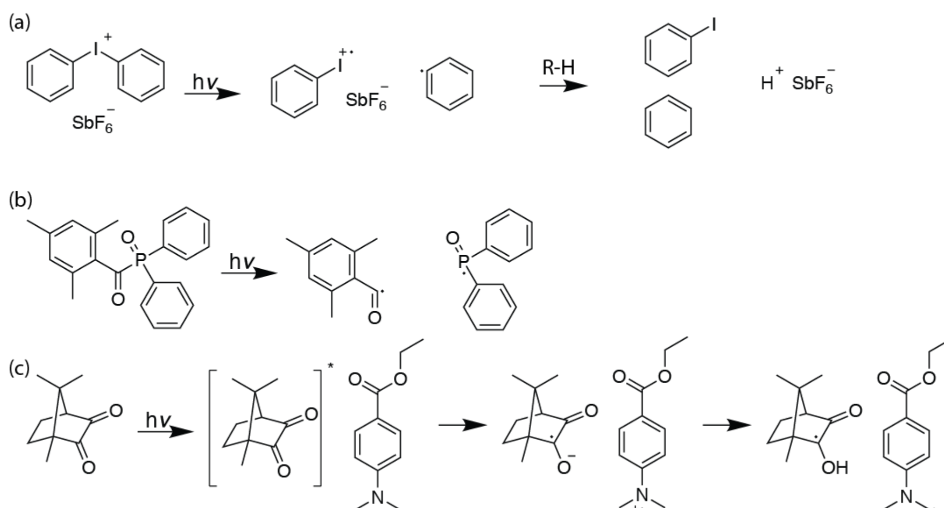

Figure 1.1 Examples of photoinitiating systems, initiating species generation from (a) the cationic photoinitiator diphenyliodonium hexafluoroantimonate (b) type I radical photoinitiator TPO (c) type II radical photoinitiator CQ/EDAB

1.2 Materials for dental restorative resins

1.2.1 Methacrylate-based dental composites

Dental caries poses a significant health concern in the US. It is estimated that over 90% of all adults in the US have experience a form of dental caries in their permanent teeth. Unsurprisingly, tens of millions of dental restorative fillings are placed each year in the US. Historically silver amalgam fillings were used for dental restorative fillings, however growing concerns over toxicity related to the use of mercury, as well as aesthetic concerns have caused the dental amalgams to be phased out in favor of dental composite fillings for dental restorations.

Dental composite fillings are comprised of an inorganic filler material dispersed throughout a continuous cross-linked polymeric matrix. Processing of the dental composite occurs *in situ* via a photopolymerization. The formulation is placed in the patient's mouth, and it irradiated with visible or UV light. This initiates the

photopolymerization, and as the photopolymerization proceeds, the resin cures and hardens, preparing the dental composite filling.

Methacrylate-based composites have been a cornerstone of dental restorative materials for decades. Initially introduced as filled monofunctional methacrylates, improved properties lead towards a shift of dimethacrylate-based resins.[1, 2] BisGMA-based dimethacrylate restorations demonstrated many favorable qualities for their use in this application. The methacrylate formulations cure rapidly with a variety of initiators and result in highly crosslinked materials with excellent mechanical and thermal properties while showing very low water sorption. The polymerization is insensitive to moisture, the resin has a long shelf-life in the dark and mixes well with many different filler materials.[3-6]

1.2.2 Polymerization-induced shrinkage

Methacrylates polymerize through a chain-growth polymerization mechanism, in which high molecular weight species are formed early on in the process, leading to rapid vitrification. Commonly observed in free radical polymerizations is volumetric shrinkage of the resin upon curing. This shrinkage occurs as a result of a decrease in free volume and monomer distance as illustrated through the change in Van der Waals diameter of ethylene to the carbon-carbon bond length in polyethylene in Figure 1.2.[7]

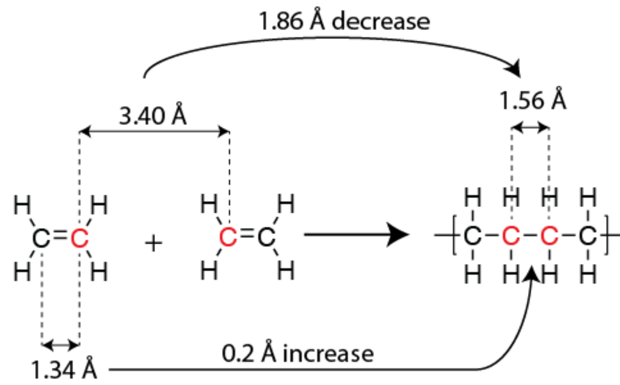

Figure 1.2 Monomer contraction following polymerization

If this process occurs in a confined, bound environment preventing shrinkage, a shrinkage stress develops. This polymerization-induced shrinkage stress can lead to various deleterious effects including microleakage through marginal gap formation,[8] secondary caries development, postoperative sensitivity, and potential tooth cracking and tooth deflection.[9] While correlation between shrinkage stress and clinical performance is subject to strong debate, clinical evidence does suggest shrinkage stress to negatively impact the restoration.[10] As such significant research efforts have been made to reduce and mitigate the effects of polymerization-induced shrinkage.[11]

One rationale follows that material placement and treatment can reduce the effects of polymerization-induced shrinkage stress. By layering the resin composite material and sequentially curing it, the confinement is changed and as a result the overall shrinkage stress is reduced. In the line of altering resin placement, by lining the cavity wall with a more elastomeric composite material, this could serve to absorb the stress generated from the curing of the bulk of the material.[12] Pre-treating the composite material by warming it would lead to increased radical mobility and thus could reduce shrinkage stress.[13] Finally, by adjusting the photopolymerization protocol through dual stage curing, initial slower

curing followed by more intense curing was hypothesized to decrease the impact of shrinkage stress.[14, 15] The common factor of these approaches is that their success strongly depends on the skill and care of the dentist applying the material, and as such results are very mixed.

To mitigate the impact of practitioner technique in reducing shrinkage stress, chemical changes to the polymeric resin could be applicable. While resin composition and chemistry makes an impact on polymerization shrinkage stress development and composite properties, the impact of filler material, ratio, and composition further affects the dental restoration as a whole. In this context, resin chemistry will exclusively be discussed.

1.2.3 Chemical approaches to Shrinkage stress mitigation

A well-explored approach to achieve reduced polymerization shrinkage in dimethacrylate-based formulations involves the use of ring-opening monomers. As the name implies, the reaction mechanism of these monomers results in opening of the cyclic structure, thereby increasing the free volume rather than the conventional free volume reduction. Spiroorthocarbonates (SOCs) and spiroorthoesters (SOEs) (see Figure 1.3a and b respectively) were among the first monomers described for this purpose.[16-18] Combining these materials with methacrylate formulations resulted in reduced polymerization shrinkage. However, these materials generally suffered from significantly decreased polymerization rates, were sensitive to water, and displayed incomplete ring-opening at clinically relevant temperatures. While some materials in this class of monomers displayed favorable properties, their crystalline nature limited their solubility in methacrylate resins.[19]

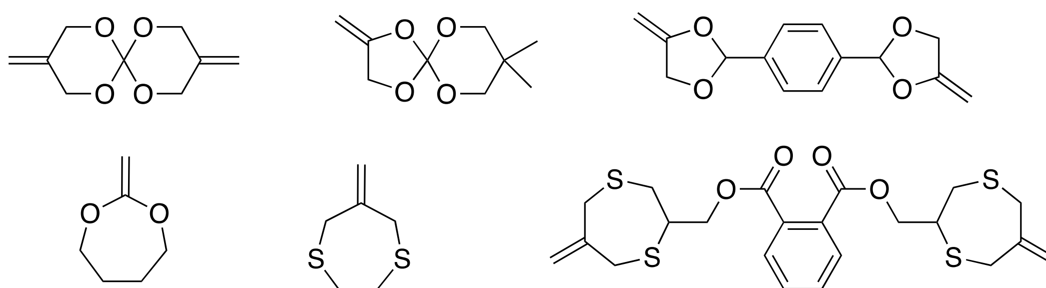

Figure 1.3 Ring-opening monomers

In contrast to SOC and SOE, vinyl-1,3-dioxolanes and vinyl-1,3-dioxepanes have been demonstrated to undergo near-complete ring-opening at ambient conditions.[20] While this improvement is significant, these materials also suffered from several severe drawbacks. As with SOE and SOC, polymerization rates were significantly reduced,[21] and likewise these compounds also showed sensitivity to resin additives. Importantly, the polymeric materials derived from these exhibited glass transition temperatures well below room temperature, rendering these materials ill-suited for dental restorative composites. Further exploration of these types of materials leads to the development of cyclic allyl sulfides, which demonstrated stability to water and could easily be adapted into crosslinked structures.[22, 23] Unfortunately, these allyl sulfides similarly resulted in significantly decreased reactivity and highly flexible polymers.

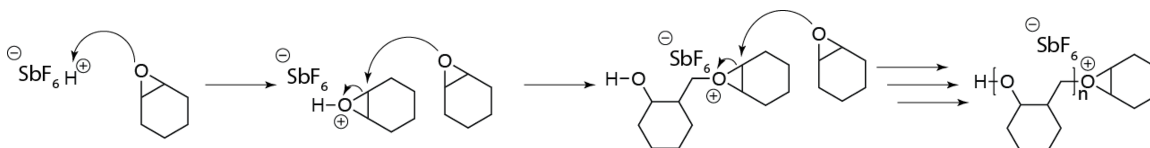

Figure 1.4 Cationic ring-opening polymerization mechanism of cyclohexene oxide

An alternative chemical pathway towards low shrinkage stress polymers is through the cationic ring-opening polymerization of epoxides and oxetanes.[24, 25] The

polymerization is typically initiated by a strongly electrophilic, often acidic, cation accompanied by a loosely bound anion (typically PF_6^- or SbF_6^-), resulting in an oxonium intermediate cation. The intermediate cation is then attacked nucleophillicaly by another monomer, and reiteration of this reaction ultimately lads to polymer formation (Figure 1.4).

As this reaction is inherently ring-opening the resultant polymerization shrinkage is significantly reduced. Cationic polymers generally show excellent adhesion, mechanical properties and chemical resistance. While the cationic polymerization is sensitive to basic moieties and water, cationic polymers have seen some success in the silorane line of dental composites.[26] The previously mentioned SOC, SOE and dioxolanes also show compatibility with cationic dental resins. Despite some advantages of this chemistry, concerns over water sensitivity, limited functional group compatibility, and induction times have prevented widespread replacement of methacrylate-based materials by cationically curing cyclic ethers.

1.2.4 Thiol–ene chemistry

In order to counteract the issues with methacrylate-based systems, thiol–ene polymerization has been proposed as an alternative. [27, 28] Thiol–ene polymerizations follow a radical-mediated step-growth polymerization mechanism between a multifunctional thiol and a multifunctional vinyl monomer. Upon initiation, a thiyl radical is formed, this thiyl radical adds to a vinyl group, resulting in a carbon-centered radical.[29] This radical proceeds to abstract a proton from a nearby thiol monomer, resulting in the formation of a thioether and a new thiyl radical. The step-growth polymerization mechanism followed by the thiol–ene polymerization leads a delayed

gelation relative to the chain-growth mechanism of methacrylates.[30] When compared to the methacrylate systems, volumetric shrinkage per mole of double bond decreases from 22.5 cm^3/mol for methacrylates[31] to 12-15 cm^3/mol for thiol–ene systems.[27] As a result of these factors materials cured from thiol–ene resins show a significant decrease in polymerization-induced shrinkage stress.

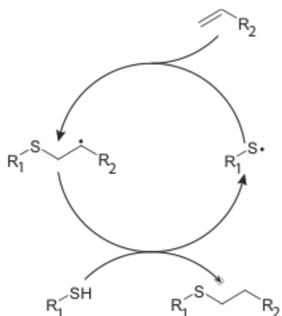

Figure 1.5 The thiol–ene reaction mechanism is described by repeating cycles of thiyl addition to vinyl groups and chain transfer of the carbon-centered radical to thiols.

Thiol–ene polymerization systems show nearly all advantages of the conventional free-radical polymerization. They show high polymerization rates, polymerization can be performed in bulk, give optically clear materials, and allow for a wide variety of mechanical properties. Furthermore, the system allows for a variety of thiol and vinyl groups to be used, and has also been shown compatible with methacrylate monomers to incorporate advantages from both chemistries. Thiol–ene materials however remain underexplored as alternative dental restorative materials, as they often exhibit subpar glass transition temperatures, vastly inferior to dimethacrylate-based resins.

1.2.5 Addition-fragmentation chain-transfer chemistries

One approach that has been demonstrated to be compatible with various free-radical based resins, is through the use of chain-transfer agents. Most well-known for their role in controlled radical polymerizations (RAFT), the addition-fragmentation chain

transfer agents control the polymerization of linear polymers, and in the case of bulk polymerizations of highly crosslinked materials, can lead to a rearrangement of the crosslinked network, relieving internal shrinkage stress. RAFT agent-inspired allyl sulfides and trithiocarbonates have led to success in decreasing methacrylate,[32, 33] thiol–(meth)acrylate,[34-36] and thiol–ene[37-39] shrinkage stresses without the necessary drawback of low T_g and flexible materials obtained from the aforementioned ring-opening allyl sulfides. Other approaches involve the use of an internal double bond with a β-quaternary carbon center[40] and β-allyl sulfones[41] both of which fragment internally upon incorporation into polymer networks and the subsequent chain transfer allows for stress relieve. The latter approach has been successfully demonstrated for methacrylate formulations[42, 43] as well as for vinylcyclopropanes.[44]

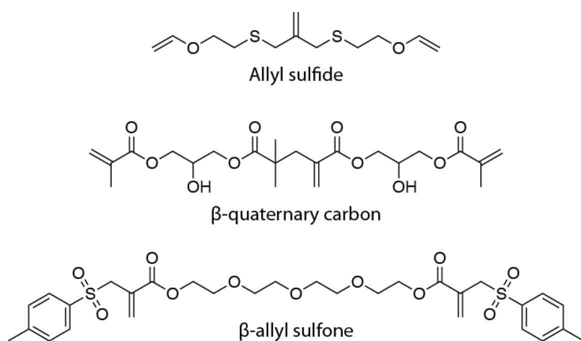

Figure 1.6 AFCT monomers studied for stress relaxation in dental restorative resins[38, 40, 42]

1.2.6 Restoration adhesion to mineralized tissues

One essential facet of dental restorations is adhesion of the restoration to the tooth tissue, a combination of enamel on the outside, and dentin on the inside. Both dentin and enamel primarily consist of hydroxyapatite and organic matter. As the outer protective layer of the tooth, enamel consists of 96% inorganic material, whereas dentin contains 70% inorganic material, 10% water, and 20% organic material, primarily collagen

fibers.[45] In addition to this, consideration should also be given to the smear layer of organic and inorganic debris, which remains following abrasive treatment of the tooth (e.g. drilling, cutting).[46]

The conventional approach for improving dental restoration adhesion is the "etch & rinse" approach. In this approach, following treatment of the cavity the newly exposed surface is treated for 10-30 seconds with a strongly acidic solution-gel of (typically) 30-40% phosphoric acid. The phosphoric acid serves to remove the smear layer, and dissolve the hydroxyapatite in enamel and dentin. The etching increases the surface area of enamel, and leaves a microporous network of collagen in in the demineralized dentin. The surface is subsequently primed and adhesive monomer impregnates the microporous networks and dental tubules, resulting in mechanical interlocking of the cured adhesive material with the dental tissue as a hybrid adhesive/tissue layer is formed.[47]

A key aspect of the "etch & rinse" technique is the effective diffusion of adhesive monomer into the exposed tissue. Essential in this is a highly effective priming step, in which the etched tooth surface is primed for adhesive monomer infiltration. The success and techniques used strongly depend on the solvent of the adhesive, as well as skill and experience of the dentist. Poor infiltration of the tissue by the adhesive can result in significant post-operative sensitivity, and micro/nanoleakage.[48, 49] While historically primer and adhesive were separate steps, recently one component primer & adhesive formulations have grown in popularity.

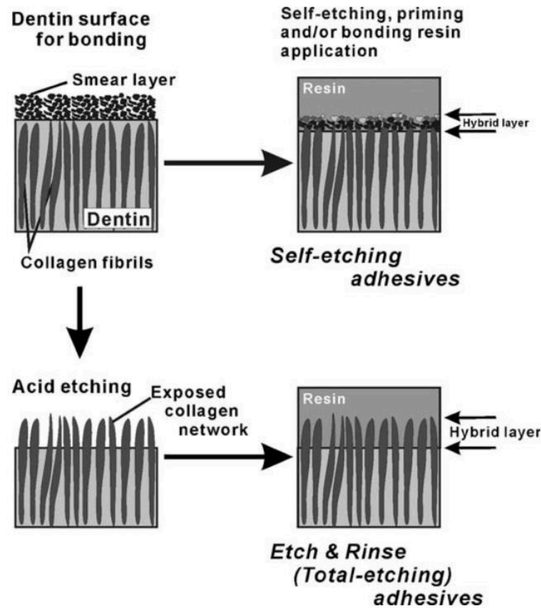

Figure 1.7 Schematic illustration of bond structure of a self-etching system and etch-and-rinse system (total-etching system). The structure of the hybrid layer of total-etch adhesives consists of resin and collagen fibrils. The combination of resin, collagen fibrils and inorganic matter (the smear layer) is a typical hybrid layer of self-etching adhesives. The hybrid layer of self-etching systems is thinner than that of total-etching adhesives, due to the mild acidic effect of their acidic monomers on dentin.[50]

1.2.7 Self-etch adhesives

An alternative approach to promoting dental restorative adhesion can be found in self-etching adhesives. These systems, rather than the total removal of the smear layer and significant demineralization of dentin by phosphoric acid, contain acid-bearing moieties (carboxylate, phosphate, phosphonate…) on the priming and adhesive monomers. The decreased acidity of these self-etching resins, generally leads to only partial removal of the smear layer and reduced demineralization of dentin. The smear layer is integrated into the adhesive surface, and retention of hydroxyapatite in the mineralized tissue allows chemical bonding between the acidic monomer and the hydroxyapatite. The degree of smear layer dissolution, hydroxyapatite removal and

chemical bonding to hydroxyapatite is strongly dependent on the acidic moiety and concentration in the formulation. The milder nature of the self-etch is more user-friendly, and less technique sensitive than the total etch approach, and is often reported to lead to reduced post-operative sensitivity of the patient.

Phosphate-ester bearing methacrylates were among the first type of self-etching monomers to be explored for improved dentin/enamel adhesion. Conveniently synthesized through esterification of hydroxyl groups, a wide range of phosphate-bearing monomers is synthetically accessible, both in the form of monoesters and diesters. The mono- and dialkyl phosphates exhibit strong acidity on par or exceeding that of neat phosphoric acid.[51] As “strong” self-etch monomers, these are capable of etching and bonding to enamel well, but lack sufficient interaction with the demineralized dentin. Subsequently, performance of these “strong” self-etch adhesives tend to display decreased adhesion and performance relative to other self-etch types.[52-54] The presence of the strongly acidic phosphates also limits the shelf life of these self-etch monomers. The ester moieties, both methacrylate and phosphate are inherently hydrolytically unstable and in the presence of moisture the monomers degrade to both hydroxyl- and methacrylic acid fragments.[55]

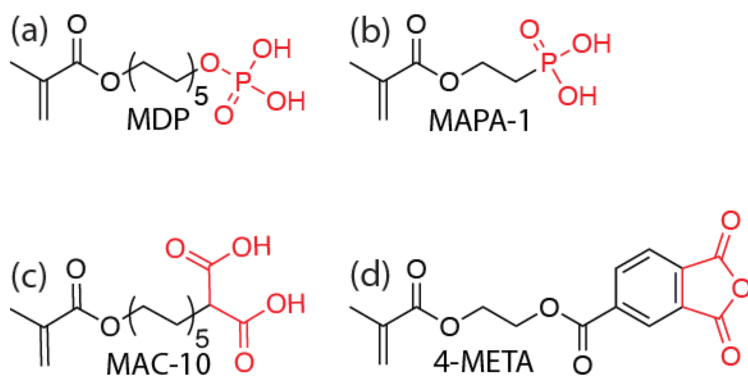

Figure 1.8 Structures of self-etch methacrylate monomers (a) methacryloyloxydecyl dihydrogen phosphate (b) methacryloyloxyethyl phosphonic acid (c) 10-methacryloyloxydecyl malonic acid(d) 4-methacryloyloxyethyl trimellitate anhydride. Etching acidic moieties denoted in red

Phosphonates have garnered interest as components for self-etch adhesives as a results of their increased hydrolytic stability relative to phosphates. Whilst phosphates are connected to the polymerizable methacrylate through a phosphate ester, phosphonates are connected directly to the carbon spacer, which is unable to undergo hydrolysis. Notably, these methacrylates do contain the hydrolysable methacrylate ester, still rendering them susceptible to hydrolysis. As with phosphoric acids, the phosphonates are strongly acidic and etch dentin and enamel is a manner similar to the "strong" self-etch phosphate monomers and phosphoric acid. As with the phosphoric acid monomers, phosphonates bind well to calcium and thus further serve to improve adhesion mineralized tooth tissue.

Carboxylic acids are stable to hydrolysis in the same manner as phosphonates are. While used extensively in adhesives for total etch treatment, contemporary use of carboxylic acids as self-etch monomers is limited. Owing to the reduced affinity for calcium relative to the phosphorous-containing acids, carboxylic acid formulations typically contain acidic anhydride monomers able to covalently bind to the exposed collagen for improved adhesion. Mention should be given to the polycarboxylic acids in

glass ionomer restorations. While the glass-ionomers cure fundamentally different from methacrylates, the polycarboxylic acids in these restoratives serve to both etch the tooth surface and improve adhesion through ionic bonding.

A combination of factors is needed for a successful self-etch adhesive. While the acid etch is key, acidic groups such as sulfones are only sparingly encountered in literature in self-etch adhesives. Besides acidity, the monomers should exhibit rapid free-radical polymerization, and be stable in both monomer and polymer form. Crucial to the success of a self-etch monomer is its miscibility with other monomers and solvents in the adhesive, in addition to low water uptake, and exhibiting good wettability of and adhesion to both types of mineralized tissue. Lastly, oral toxicity, cytotoxicity, and biofilm formation are other important factors in the design of self-etch adhesives. With various aspects such as number of acidic moieties, hydrolytic stability, spacer length, and type of polymerizable double bond, various designs for self-etch adhesive monomers are constantly being explored.

1.3 Hexaarylbiimidazoles

1.3.1 History of HABIs

Hexaarylbiimidazoles (HABIs) are a particularly interesting class of materials. Most well-known as commercialized by DuPont in their Dylux color proofing systems and Cromalin photoinitiators,[56] HABIs as a class of materials have been subject to intensive study since their discovery in 1960 by Hayashi and Maeda.[57] These materials are readily prepared through oxidation of 2,4,5-triarylimidazoles and allows for many different functional group substitutions on the phenyl rings.[58] The resultant dimer is bound through a weak C-N bond, which can readily and reversibly be cleaved

homolytically through photolysis, thermolysis, and piezolysis.[59] The resultant lophyl radicals are often brightly colored[60] as a result of the electron delocalization and aromatization of the formed species. In addition, owing to the electron delocalization and steric bulk from the pendant phenyl groups, the lophyl radicals are generally unreactive towards molecular oxygen and have a half-life in the order of seconds to minutes, whereas organic free radicals, save for notable exceptions (i.e. DPPH or nitroxides) recombine or react in the order of milliseconds.

The synthetic accessibility of these HABIs allows for facile modification in order to achieve desired properties. Significant effort has been put into expanding the light absorbance range from the typical near-UV absorbance well into the visible range through functional group substitution[58, 61, 62] and π-conjugation extension.[63] Additionally such modifications can also result in significantly extending the radical half-life,[63] or shortening it by design.[64,65] While light absorbance and lophyl radical lifetime are often the driving force behind HABI modification, functionalization with alkane[66] or ethylene glycol[67] pendant groups has been shown to significantly improve solubility of HABIs in monomeric resins.

1.3.2 HABIs as free radical photoinitiators

Although best known as photoinitiators, as a consequence of the aforementioned electron delocalization and steric hindrance HABIs show little to no photoinitiation activity in (meth)acrylate formulations lacking the presence of a suitable hydrogen-donating coiniator.[66, 68] In the presence of a hydrogen-donating coinitiator such as a thiol, HABIs do effectively and efficiently initiate free-radical chain-growth polymerization.

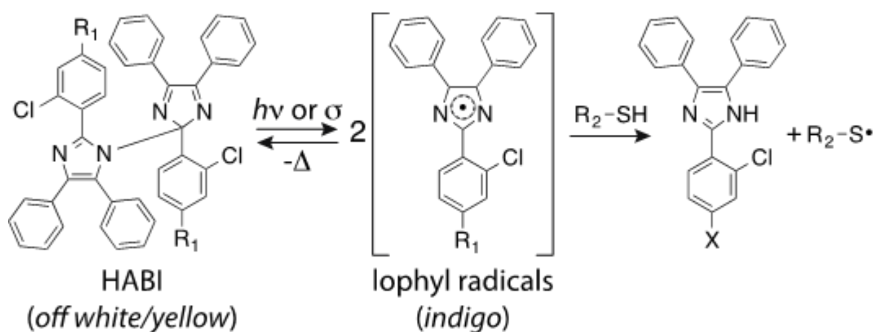

Figure 1.9 HABI cleavage and chain transfer to thiol coinitiator[66]

The intuitive mechanism of this photoinitiation process in the presence of thiols would be hydrogen transfer from the thiol to the lophyl radical as shown in figure X, generating an initiating thyil radical, akin to the chain transfer step in the previously discussed thiol–ene reaction. A study of co-initiating *o*-Cl-HABI with a series of known hydrogen abstracting and electron transfer co-initiators demonstrated that the thiols 2-mercaptobenzthiazole, 2-mercaptobenzoxazole and 2-mercaptobenzimidazole initiated through an electron transfer/proton loss mechanism, rather than a direct abstraction, with the reactivity of the co-initiators following the trend of their oxidation potential.[69] Another study examining the mechanistic aspects of photoinitiation of *o*-Cl-HABI with triazole- and tetrazole- substituted thiols suggested that an addition-elimination cycle through a tautomeric thione with the release of chlorine radicals potentially plays a significant role in the photoinitiation of these thiols with *o*-Cl-HABI.[68] Aliphatic thiols on the other hand are incapable of reacting with the lophyl radicals through an electron transfer/proton loss mechanism, but have also been demonstrated to react with these radical in order to yield lophine and thiyl radicals.[70] In thiol–ene formulations, various types of HABI have been demonstrated as efficient thiol–ene polymerization photoinitiators.[66] Other initiation systems, such as *o*-Cl-HABI combined with N-phenylglycine[71, 72] or dyes[73], were demonstrated to initiate though an electron

transfer/proton loss mechanism, which with coinitiators followed the same trend as the previously studied thiols in terms of oxidation potential.

An alternative approach towards expanding the photoactive regime of HABI initiators lies in dye sensitization of multicomponent photoinitiating systems. In a dye-sensitized system, the dye upon visible light exposure enters an excited state. Then through either an electron transfer/proton loss or a chemical reaction the excited state dye reacts with HABI to yield a photo-oxidized dye and the desired lophyl radical. This approach has been demonstrated to be successful for HABIs a variety of dyes such as A, B, and C.

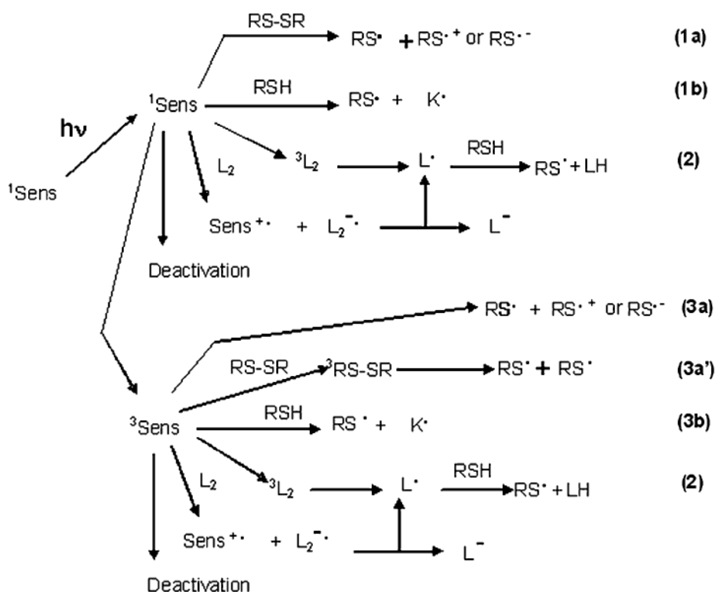

Figure 1.10 Illustration of sensitization pathways in a dye/HABI photoinitiating system[74]

As demonstrated by Figure 1.10 the mechanism and possible mechanistic pathways of dye-activated HABI photoinitiation is highly complex, and depends strongly on the specific components used in the photoinitiating system. This complexity of HABI photoinitiating systems should be kept in mind in formulating HABIs. Regardless of the

initiation mechanism, it is well agreed upon that for HABIs to act as efficient photoinitiators a suitable hydrogen donating co-initiator is essential.[75]

1.3.3 Hexaarylbiimidazoles in functional materials

The transient and stable nature of the generated lophyl radicals have generated interest in employing HABIs in stimuli responsive materials. As a result of the synthetic accessibility HABIs have been incorporated in polymeric materials, in which they served to crosslink and de-crosslink the polymer,[76] could be used as photoresponsive self-healing organogels,[70] were employed to induce solvent-free metamorphosis,[77] and used in stress-induced coloration and crosslinking.[78]

The chemical diversity of HABI functionalization further extends into small molecule applications. Covalently coupled HABIs to fluorescent probes employed the fluorescence-quenching behavior of free radicals to repeatedly achieve super-resolution fluorescence imaging in both the visible and NIR regimes.[79-83] Interestingly, covalent coupling through the aryl groups of HABIs strongly alters the lophyl radical recombination kinetics. As a consequence the now diffusion-limited HABIs exhibit lifetimes which are strongly dependent on the nature of the linkage and resultant lophyl radical orientation with half-lives which are orders of magnitude shorter than conventional HABIs.[64, 84-88]

1.4 Polymerization inhibition

1.4.1 Universal polymerization inhibition

Polymerization inhibition plays a critical aspect in the process of polymer synthesis. Often described as stabilizer, the inhibitors serve to prevent monomer

polymerization, increasing stability of the monomer during transport and storage, and improving shelf-life of the monomers. Inhibitors commonly used for this application include butylated hydroxytoluene (BHT), 4-*tert*-butylcathecol (TBC), and hydroquinone (HQ). These materials inhibit free radical polymerization stemming from the antioxidative properties associated with the phenolic alcohol, which in turn get oxidized to ketones and quinones.

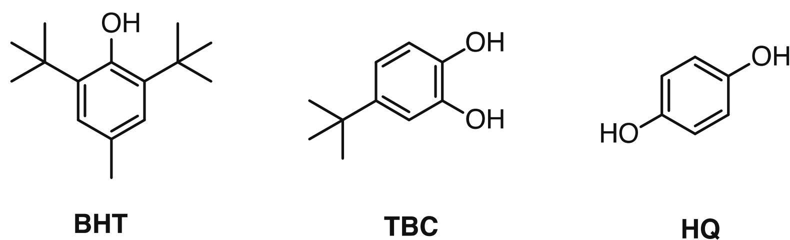

Figure 1.11 Structures of common radical inhibitors

Universal inhibition of free radical polymerizations is an effective means of polymerization inhibition, but controlled, reversible inhibition and chain-transfer is an essential part in the process of controlled free-radical polymerization (CRP). CRP has been of great interest across academia and industry, as it allows for precise control over vinyl monomer molecular weights, and leads to narrow molecular weight distributions of linear polymers. The three main schools of CRP are atom transfer radical polymerization (ATRP), nitroxide-mediated polymerization (NMP), and reversible addition-fragmentation chain-transfer (RAFT).

1.4.2 Controlled Free Radical Polymerizations

ATRP is based on a reversible activation-deactivation cycle of free radical polymerizations. ATRP employs a complexed transition metal catalyst and halogen-activated esters to generate active radicals.[89-92] Following propagation of these radicals,

the now oxidized transition metal reacts with the polymer radical, deactivating (terminating) it. The newly formed halogen-terminated polymer is able to activate by reoxidizing the metal catalyst. The reversible nature of this process, coupled with statistical processes and the equilibrium of the activation-deactivation cycle lead to well-defined polymeric materials with narrow distributions for a wide selection of monomers.

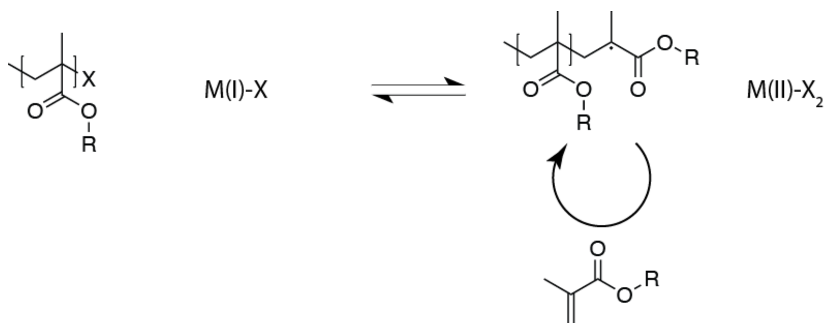

Figure 1.12 Equilibrium in the ATRP of a methacrylate

NMP relies on the presence of a stable, sterically hindered organic nitroxide additive. The nitroxide radical is able to reversibly react with a propagating polymer radical to yield a nitroxide-capped polymer. [93, 94] As this carbon-oxygen bond is relatively weak as a result of the steric hindrance and stabilized nitroxide radical, this bond can be thermally reversed without the need of a catalyst. In the same manner as ATRP, this results in excellent control over molecular weight and a narrow distribution. The main limitation of this approach lies in the relatively small range of monomers compatible with this chemistry, as well as the high temperatures required to reliably undergo this reversible nitroxide attachment and detachment.

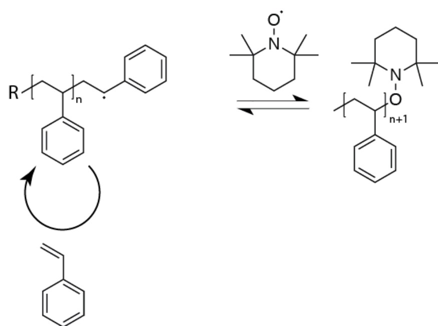

Figure 1.13 NMP equilibrium of Styrene

In RAFT, thiocarbonylthiol compounds such as dithioesters, xanthogenates, and thiocarbamates are commonly employed as reversible chain-transfer agents. Following conventional polymer initiation, chain-transfer to the RAFT agent leads to another polymer initiation. Following that reaction, an equilibrium between active polymer propagation, reactions to the chain transfer agent and fragmentation from the chain transfer agent radical intermediate result in control over the polymer molecular weight and molecular weight distribution. The efficacy of the RAFT agent is strongly dependent on the RAFT agent pendant groups, but does allow for a wide range of monomers. In RAFT, as with all CRP techniques, improper tailoring of the reaction conditions will lead to irreversible polymer termination, chain transfer and radical consumption.

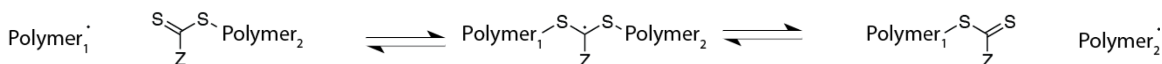

Figure 1.14 RAFT equilibrium between 2 polymers

Controlled inhibition and termination represent powerful tools in preventing undesired polymerization and achieving excellent control over the polymerization process. Recent work and applications of controlled polymerization inhibition in the framework of photopolymerizations is further discussed in Section 1.5.

1.5 Photocontrolled reactions in (stereo)lithography

Aside from chemical control over polymerizations an alternate method of control is spatially through selective exposure of photocurable formulations, this is particularly useful in additive manufacturing. In stereolithography (SLA), a vat of photosensitive resin containing a movable stage is cured selectively through sequential exposure with a laser beam in a layer-by-layer fashion. Following each layer, the stage is moved slightly and resin is replenished. Digital light processing (DLP) proceeds through a similar fashion, as photopolymer resin is cured through a projected image, significantly speeding up the fabrication process relative to SLA Following each exposure, the vertical stage moves up, and the photopolymer resin is renewed.[95]

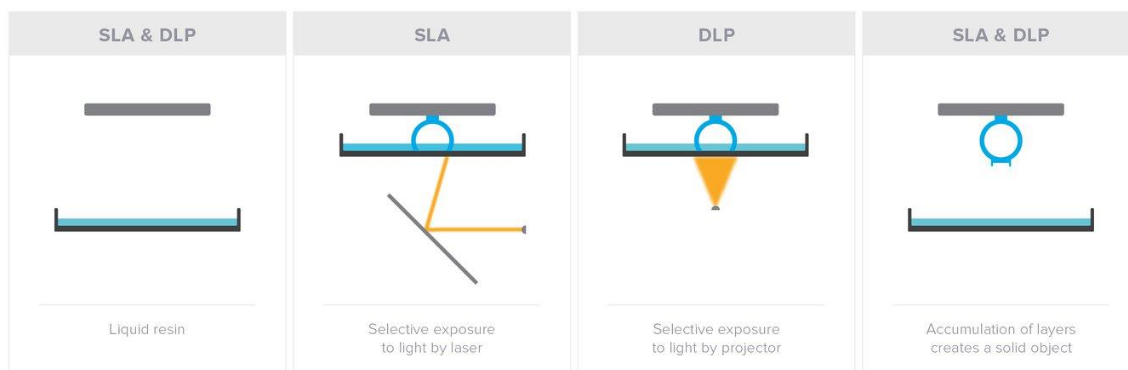

Figure 1.15 Comparison between SLA and DLP irradiation (Formlabs, https://formlabs.com/blog/3d-printing-technology-comparison-sla-dlp/)

The excellent spatial control allowed through SLA and DLP facilitates the rapid production of bespoke objects. Although great strides have been made in stereolithographic 3D printing, the manufacturing of large, dense structures through these techniques remains challenging. Large surface areas limit resin reflow, and stifles delamination from the print window. Large-scale production is further limited by print rates. As layers typically range in height between 10-50 µm, production of tall structures

is significantly time consuming and currently makes this approach undesirable for large-scale manufacturing.

Removing the need for delamination and recoating by preventing adhesion to the curing window would significantly improve production rates. Recently, Carbon described further control over the photopolymerization process through oxygen inhibition of the polymerization. By employing an oxygen-permeable window and an oxygen-rich atmosphere, molecular oxygen diffuses into the photopolymer resin near the window. As molecular oxygen inhibits free-radical polymerizations of (meth)acrylates, solidification of the resin near the window is prevented, allowing for a continuous additive manufacturing process, reaching unprecedented vertical print rates.[96, 97] This approach however is dependent on effective diffusion of oxygen into the monomer, inhibition efficacy is strongly related to monomer viscosity, severely limiting the scope.

Rather than passive inhibition of photopolymerizations, Scott *et al.* described a novel two-color single-photon photoinitiation/photoinhibition chemistry for use in direct-write lithography.[98] This concept employs a visible-light active photoinitiator in combination with a near-UV activated chain-transfer agent to act as a photoinhibitor. Irradiation of the photopolymer resin with near-UV activates the chain-transfer agent, which in turn retards any active photopolymerization reaction and prevents solidification. In contrast, areas exposed to exclusively blue light are not affected by this retardation and cure rapidly. The reliance on chain-transfer agents in this approach results in non-zero polymerization rates under exclusive near-UV irradiation, and severely limits the monomer scope as described by Forman.[99]

Li *et al*. achieved controlled polymerization photoinhibition through deactivation of the photoinitiating species rather than the approach of rapidly consuming active radicals described above.[100] Following activation of the photoinitiator through an 800 nm two-photon process, the activated photoinitiator is deactivated through a continuous wave of the same wavelength. Both this approach and Scott's photoinitiation/photoinhibition approach allow for sub-diffraction direct-write lithography through appropriate focus of the initiating and deactivating wavelengths.

Light activated and deactivated crosslinking of polymeric materials through a light-induced reversible chemical change was demonstrated by Vijayamohanan *et al*.[101, 102] Employing spirothiopyran-bearing methacrylate polymers, activation of these moieties with near-UV light generates a thiolate anion as the spirothiopyran (STP) ring-opens to the merocyanine (MC) isomer. The thiolate anion subsequently reacts to maleimide-functionalized poly(ethylene glycol) in a thiol–Michael reaction (see Figure 1.16). The thiol–Michael reaction is prevented through rapid visible light-induced switching to the spiropyran form. This chemistry was expanded upon and demonstrated to be feasible without the need of a maleimide-bearing polymer.[103] Zwitterionic merocyanine pendant groups lead to supramolecular crosslinking of these materials, and was demonstrated in a direct-write lithography setting.

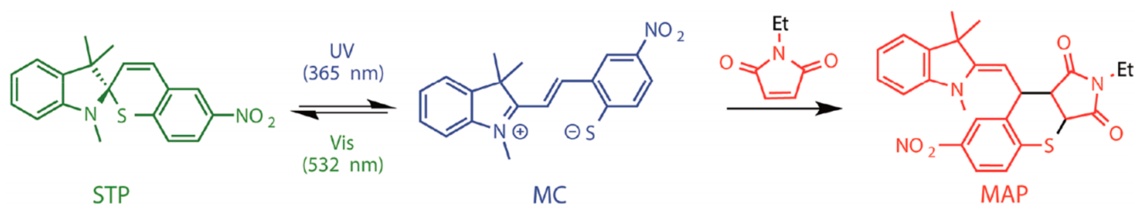

Figure 1.16 Photochromic ring-opening of STP to MC and subsequent thiol–Michael reaction with a maleimide[101]

The potential of photoswitchable molecular structures provides further tools for controlled functionalization of materials. Expanding beyond polymeric materials, Lerch *et al.* demonstrate a system containing azobenzene and donor–acceptor Stenhouse adduct, both of which can be activated and deactivated orthogonally, [104] granting unprecedented light-based control over molecular structure. Orthogonal photoactivated tetrazole and photoenol ligation with maleimides could provide yet another path towards greater control over polymer structures.[105] Independent photoswitching, selective photoinhibition, and orthogonal polymer crosslinking chemistries prove to be extremely powerful tools in light-based additive manufacturing approaches.

1.6 Overview of subsequent chapters

The remaining chapters of this dissertation are organized as follows.

Chapter 2 describes the synthesis of silane- and norbornyl-based thiol–ene monomers and oligomers. These monomers and oligomers are examined for their photopolymerization behavior. The impact of the pre-oligomerized formulations on the thermomechanical properties and polymerization shrinkage stress is evaluated.

Chapter 3 describes further development of the thiol–ene formulations studied in Chapter 2. The effect of allyl sulfide addition-fragmentation chain-transfer additives on photopolymer characteristics is determined. Subsequently, the chemical compatibility of the thiol–ene formulations with acidic monomers is evaluated.

Chapter 4 describes the demonstration of hexaarylbiimidazoles as photoinhibitors of free-radical chain-growth photopolymerizations, and their application in a two-color

continuous additive manufacturing system. Covalently linked hexaarylbiimidazoles are synthesized and evaluated to overcome the shortcomings of conventional hexaarylbiimidazoles for additive manufacturing purposes.

Chapter 5 describes butyl nitrite as an alternative photoinhibitor of free radical photopolymerizations in two-color irradiation schemes. Following a demonstration of two-color photoinitiation/photoinhibition in volumetric 3D printing, a combination of cationic photopolymerization with free radical photopolymerization inhibition is examined for the development of support-free stereolithographic additive manufacturing.

Chapter 6 gives an overall summary and conclusions of this work followed by a discussion of future directions.

1.7 References

1. Bowen, R. L., Properties of a silica-reinforced polymer for dental restorations. *Journal of the American Dental Association* **1963,** *66* (1), 57-64.

2. Ferracane, J. L.; Greener, E. H., Fourier transform infrared analysis of degree of polymerization in unfilled resins-methods comparison. *Journal of Dental Research* **1984,** *63* (8), 1093-1095.

3. Moszner, N.; Salz, U., New developments of polymeric dental composites. *Progress in Polymer Science* **2001,** *26* (4), 535-576.

4. Cramer, N. B.; Stansbury, J. W.; Bowman, C. N., Recent Advances and Developments in Composite Dental Restorative Materials. *Journal of Dental Research* **2011,** *90* (4), 402-416.

5. Leprince, J. G.; Palin, W. M.; Hadis, M. A.; Devaux, J.; Leloup, G., Progress in dimethacrylate-based dental composite technology and curing efficiency. *Dental Materials* **2013,** *29* (2), 139-156.

6. Bayne, S. C.; Ferracane, J. L.; Marshall, G. W.; Marshall, S. J.; van Noort, R., The Evolution of Dental Materials over the Past Century: Silver and Gold to Tooth Color and Beyond. *Journal of Dental Research* **2019,** *98* (3), 257-265.

7. Sadhir, R. K.; Luck, R. M., *Expanding Monomers: Synthesis, Characterization and Applications*. CRC Press: Boca Raton, 1992.

8. Ferracane, J. L.; Mitchem, J. C., Relationship between composite contraction stress and leakage in Class V cavities. *American Journal of Dentistry* **2003,** *16* (4), 239-243.

9. Rosatto, C. M. P.; Bicalho, A. A.; Verissimo, C.; Braganca, G. F.; Rodrigues, M. P.; Tantbirojn, D.; Versluis, A.; Soares, C. J., Mechanical properties, shrinkage stress, cuspal strain and fracture resistance of molars restored with bulk-fill composites and incremental filling technique. *Journal of Dentistry* **2015,** *43* (12), 1519-1528.

10. Ferracane, J. L.; Hilton, T. J., Polymerization stress - Is it clinically meaningful? *Dental Materials* **2016,** *32* (1), 1-10.

11. *Dental Composite Materials for Direct Restorations*. Springer Cham: 2017.

12. Oliveira, L. C. A.; Duarte, S.; Araujo, C. A.; Abrahao, A., Effect of low-elastic modulus liner and base as stress-absorbing layer in composite resin restorations. *Dental Materials* **2010,** *26* (3), E159-E169.

13. Taubock, T. T.; Tarle, Z.; Marovic, D.; Attin, T., Pre-heating of high-viscosity bulk-fill resin composites: Effects on shrinkage force and monomer conversion. *Journal of Dentistry* **2015,** *43* (11), 1358-1364.

14. Sakaguchi, R. L.; Wiltbank, B. D.; Murchison, C. F., Contraction force rate of polymer composites is linearly correlated with irradiance. *Dental Materials* **2004,** *20* (4), 402-407.

15. Pfeifer, C. S. C.; Braga, R. R.; Ferracane, J. L., Pulse-delay curing: Influence of initial irradiance and delay time on shrinkage stress and microhardness of restorative composites. *Operative Dentistry* **2006,** *31* (5), 610-615.

16. Thompson, V. P.; Williams, E. F.; Bailey, W. J., Dental resins with reduced shrinkage during hardening. *Journal of Dental Research* **1979,** *58* (5), 1522-1532.

17. Bailey, W. J. Polycyclic ring-opened polymers. U.S. Patent 4,387,215. June 7, 1983.

18. Stansbury, J. W., Synthesis and evaluation of new oxaspiro monomers for double ring-opening polymerization. *Journal of Dental Research* **1992,** *71* (7), 1408-1412.

19. Sanda, F.; Takata, T.; Endo, T., Synthesis and radical polymerization of spiro orthocarbonates bearing exomethylene groups. *Journal of Polymer Science Part a-Polymer Chemistry* **1994,** *32* (2), 323-332.

20. Belfield, K. D.; Abdelrazzaq, F. B., Photoinitiated cationic cross-linking of 4-methylene-2-phenyl-1,3-dioxolane with 2,2'-(1,4-phenylene)bis(4-methylene-1,3-dioxolane). *Macromolecules* **1997,** *30* (22), 6985-6988.

21. Moszner, N.; Volkel, T.; Rheinberger, V.; Klemm, E., Polymerization of cyclic monomers .3. Synthesis, radical and cationic polymerization of bicyclic 2-methylene-1,3-dioxepanes. *Macromolecular Chemistry and Physics* **1997,** *198* (3), 749-762.

22. Evans, R. A.; Rizzardo, E., Free-radical ring-opening polymerization of cyclic allylic sulfides. 2. Effect of substituents on seven- and eight-membered ring low shrink monomers. *Macromolecules* **2000,** *33* (18), 6722-6731.

23. Evans, R. A.; Rizzardo, E., Free radical ring-opening polymerization of cyclic allylic sulfides: Liquid monomers with low polymerization volume shrinkage. *Journal of Polymer Science Part a-Polymer Chemistry* **2001,** *39* (1), 202-215.

24. Sasaki, H.; Kuriyama, A.; Kakuchi, T., Photoinitiated Cationic Polymerization of 3-Ethyl-3-(phenoxymethyl)-oxetane in Nitrogen Atmosphere. *Journal of Macromolecular Science-Pure and Applied Chemistry* **1995,** *A32* (10), 1699-1707.

25. Nuyken, O.; Bohner, R.; Erdmann, C., Oxetane photopolymerization - A system with low volume shrinkage. *Macromolecular Symposia* **1996,** *107*, 125-138.

26. Weinmann, W.; Thalacker, C.; Guggenberger, R., Siloranes in dental composites. *Dental Materials* **2005,** *21* (1), 68-74.

27. Lu, H.; Carioscia, J. A.; Stansbury, J. W.; Bowman, C. N., Investigations of step-growth thiol–ene polymerizations for novel dental restoratives. *Dental Materials* **2005,** *21* (12), 1129-1136.

28. Carioscia, J. A.; Lu, H.; Stanbury, J. W.; Bowman, C. N., Thiol–ene oligomers as dental restorative materials. *Dental Materials* **2005,** *21* (12), 1137-1143.

29. Hoyle, C. E.; Lee, T. Y.; Roper, T., Thiol–enes: Chemistry of the past with promise for the future. *Journal of Polymer Science Part a-Polymer Chemistry* **2004,** *42* (21), 5301-5338.

30. Cramer, N. B.; Bowman, C. N., Kinetics of thiol–ene and thiol-acrylate photopolymerizations with real-time Fourier transform infrared. *Journal of Polymer Science Part a-Polymer Chemistry* **2001,** *39* (19), 3311-3319.

31. Patel, M. P.; Braden, M.; Davy, K. W. M., Polymerization Shrinkage of Methacrylate Esters. *Biomaterials* **1987,** *8* (1), 53-56.

32. Leung, D.; Bowman, C. N., Reducing Shrinkage Stress of Dimethacrylate Networks by Reversible Addition-Fragmentation Chain Transfer. *Macromolecular Chemistry and Physics* **2012,** *213* (2), 198-204.

33. Park, H. Y.; Kloxin, C. J.; Fordney, M. F.; Bowman, C. N., Stress relaxation of trithiocarbonate-dimethacrylate-based dental composites. *Dental Materials* **2012,** *28* (8), 888-893.

34. Fenoli, C. R.; Wydra, J. W.; Bowman, C. N., Controllable Reversible Addition-Fragmentation Termination Monomers for Advances in Photochemically Controlled Covalent Adaptable Networks. *Macromolecules* **2014,** *47* (3), 907-915.

35. Park, H. Y.; Kloxin, C. J.; Abuelyaman, A. S.; Oxman, J. D.; Bowman, C. N., Stress Relaxation via Addition − Fragmentation Chain Transfer in High T. **2012**, 2551-2556.

36. Park, H. Y.; Kloxin, C. J.; Fordney, M. F.; Bowman, C. N., Stress Reduction and T-g Enhancement in Ternary Thiol-Yne-Methacrylate Systems via Addition-Fragmentation Chain Transfer. *Macromolecules* **2012,** *45* (14), 5647-5652.

37. Scott, T. F.; Schneider, A. D.; Cook, W. D.; Bowman, C. N., Photoinduced plasticity in cross-linked polymers. *Science* **2005,** *308* (5728), 1615-1617.

38. Kloxin, C. J.; Scott, T. F.; Bowman, C. N., Stress Relaxation via Addition-Fragmentation Chain Transfer in a Thiol–ene Photopolymerization. *Macromolecules* **2009,** *42* (7), 2551-2556.

39. Park, H. Y.; Kloxin, C. J.; Scott, T. F.; Bowman, C. N., Stress relaxation by addition-fragmentation chain transfer in highly cross-linked thiol-yne networks. *Macromolecules* **2010,** *43* (24), 10188-10190.

40. Shah, P. K.; Stansbury, J. W.; Bowman, C. N., Application of an addition-fragmentation-chain transfer monomer in di(meth) acrylate network formation to reduce polymerization shrinkage stress. *Polymer Chemistry* **2017,** *8* (30), 4339-4351.

41. Gorsche, C.; Griesser, M.; Gescheidt, G.; Moszner, N.; Liska, R., beta-Allyl Sulfones as Addition-Fragmentation Chain Transfer Reagents: A Tool for Adjusting Thermal and Mechanical Properties of Dimethacrylate Networks. *Macromolecules* **2014,** *47* (21), 7327-7336.

42. Gorsche, C.; Koch, T.; Moszner, N.; Liska, R., Exploring the benefits of beta-allyl sulfones for more homogeneous dimethacrylate photopolymer networks. *Polymer Chemistry* **2015,** *6* (11), 2038-2047.

43. Gauss, P.; Ligon-Auer, S. C.; Griesser, M.; Gorsche, C.; Svajdlenkova, H.; Koch, T.; Moszner, N.; Liska, R., The Influence of Vinyl Activating Groups on beta-Allyl Sulfone-Based Chain Transfer Agents for Tough Methacrylate Networks. *Journal of Polymer Science Part a-Polymer Chemistry* **2016,** *54* (10), 1417-1427.

44. Schoerpf, S.; Catel, Y.; Moszner, N.; Gorsche, C.; Liska, R., Enhanced reduction of polymerization-induced shrinkage stress via combination of radical ring opening and addition fragmentation chain transfer. *Polymer Chemistry* **2019,** *10* (11), 1357-1366.

45. Garant, P. R., *Oral Cells and Tissues*. Quintessence Publishing: Chicago, 2003.

46. Eick, J. D.; Wilko, R. A.; Anderson, C. H.; Sorensen, S. E., Scanning electron microscopy of cut tooth surfaces and identification of debris by use of the electron microprobe. *Journal of dental research* **1970,** *49* (6), Suppl:1359-68.

47. Nakabayashi, N.; Kojima, K.; Masuhara, E., The Promotion of Adhesion by the Infiltration of Monomers into Tooth Substrates. *Journal of Biomedical Materials Research* **1982,** *16* (3), 265-273.

48. Breschi, L.; Mazzoni, A.; Ruggeri, A.; Cadenaro, M.; Di Lenarda, R.; Dorigo, E. D. S., Dental adhesion review: Aging and stability of the bonded interface. *Dental Materials* **2008,** *24* (1), 90-101.

49. De Munck, J.; Mine, A.; Poitevin, A.; Van Ende, A.; Cardoso, M. V.; Van Landuyt, K. L.; Peumans, M.; Van Meerbeek, B., Meta-analytical Review of Parameters Involved in Dentin Bonding. *Journal of Dental Research* **2012,** *91* (4), 351-357.

50. Hashimoto, M.; Nagano, F.; Endo, K.; Ohno, H., A review: Biodegradation of resin–dentin bonds. *Japanese Dental Science Review* **2011,** *47* (3), 5-12.

51. Kumler, W. D.; Eiler, J. J., The acid strength of mono and diesters of phosphoric acid. The n-alkyl esters from methyl to butyl, the esters of biological importance, and the natural guanidine phosphoric acids. *Journal of the American Chemical Society* **1943,** *65*, 2355-2361.

52. De Munck, J.; Van Meerbeek, B.; Satoshi, I.; Vargas, M.; Yoshida, Y.; Armstrong, S.; Lambrechts, P.; Vanherle, G., Microtensile bond strengths of one- and two-step self-etch adhesives to bur-cut enamel and dentin. *American Journal of Dentistry* **2003,** *16* (6), 414-420.

53. Inoue, S.; Vargas, M. A.; Abe, Y.; Yoshida, Y.; Lambrechts, P.; Vanherle, G.; Sano, H.; Van Meerbeek, B., Microtensile bond strength of eleven contemporary adhesives to enamel. *American Journal of Dentistry* **2003,** *16* (5), 329-334.

54. Inoue, S.; Vargas, M. A.; Abe, Y.; Yoshida, Y.; Lambrechts, P.; Vanherle, G.; Sano, H.; Van Meerbeek, B., Microtensile bond strength of eleven contemporary adhesives to dentin. *The journal of adhesive dentistry* **2001,** *3* (3), 237-45.

55. Salz, U.; Burtscher, P.; Vogel, K.; Moszner, N.; Rheinberger, V., New adhesive monomers for dental application. *Abstracts of Papers of the American Chemical Society* **1997,** *214*, 175-POLY.

56. R., D., *Photochemistry, History and Commercial Applications of Hexaarylbiimidazoles*. Elsevier: Amsterdam, 2006.

57. Hayashi, T.; Maeda, K., Preparation of a New Phototropic Substance. *Bulletin of the Chemical Society of Japan* **1960,** *33* (4), 565-566.

58. Cescon, L. A.; Coraor, G. R.; Dessauer, R.; Silversm.Ef; Urban, E. J., Properties of Triarylimidazoyl Radicals and their Dimers. *Journal of Organic Chemistry* **1971,** *36* (16), 2262-2267.

59. White, D. M.; Sonnenbe.J, Oxidation of Triarylimidazoles. Structures of Photochromic and Piezochromic Dimers of Triarylimidazyl Radicals. *Journal of the American Chemical Society* **1966,** *88* (16), 3825-3829.

60. Maeda, K.; Hayashi, T., Mechanism of Photochromism, Thermochromism and Piezochromism of Dimers of Triarylimidazoyl. *Bulletin of the Chemical Society of Japan* **1970,** *43* (2), 429-438.

61. Shi, Y. T.; Yin, J.; Kaji, M.; Yori, H., Photopolymerization of acrylate derivatives initiated by hexaarylbiimidazole with ether groups. *Polymer International* **2006,** *55* (3), 330-339.

62. Shi, Y. T.; Wang, B. H.; Jiang, X. S.; Yin, J.; Kaji, M.; Yori, H., Photoinitiation properties of heterocyclic hexaarylbiimidazoles with high UV-vis absorbance. *Journal of Applied Polymer Science* **2007,** *105* (4), 2027-2035.

63. Kikuchi, A.; Iyoda, T.; Abe, J., Electronic structure of light-induced lophyl radical derived from a novel hexaarylbiimidazole with pi-conjugated chromophore. *Chemical Communications* **2002,** (14), 1484-1485.

64. Iwahori, F.; Hatano, S.; Abe, J., Rational design of a new class of diffusion-inhibited HABI with fast back-reaction. *Journal of Physical Organic Chemistry* **2007,** *20* (11), 857-863.

65. Kishimoto, Y.; Abe, J., A Fast Photochromic Molecule That Colors Only under UV Light. *Journal of the American Chemical Society* **2009,** *131* (12), 4227-4229.

66. Ahn, D.; Sathe, S. S.; Clarkson, B. H.; Scott, T. F., Hexaarylbiimidazoles as visible light thiol–ene photoinitiators. *Dental Materials* **2015,** *31* (9), 1075-1089.

67. Igarashi, H.; Igarashi, T.; Sagawa, M.; Mori, T.; Kotani, Y.; Muroya, Y.; Katsumura, Y.; Yamashita, T., Preparation and photoreactivity of a novel lophine dimer

containing a hydrophilic group. *Journal of Photopolymer Science and Technology* **2007,** *20* (5), 757-762.

68. Berdzinski, S.; Strehmel, N.; Lindauer, H.; Strehmel, V.; Strehmel, B., Extended mechanistic aspects on photoinitiated polymerization of 1,6-hexanediol diacrylate by hexaarylbisimidazoles and heterocyclic mercapto compounds. *Photochemical & Photobiological Sciences* **2014,** *13* (5), 789-798.

69. Eaton, D. F.; Horgan, A. G.; Horgan, J. P., Mechanism of coinitiation of photopolymerization of methyl methacrylate by hexaarylbiimidazole—hydrogen-atom donor combinations. The role of electron transfer v*s.* direct hydrogen-atom abstraction. *Journal of Photochemistry and Photobiology a-Chemistry* **1991,** *58* (3), 373-391.

70. Ahn, D.; Zavada, S. R.; Scott, T. F., Rapid, Photomediated Healing of Hexaarylbiimidazole-Based Covalently Cross-Linked Gels. *Chemistry of Materials* **2017,** *29* (16), 7023-7031.

71. Chen, Y. C.; Kuo, Y. T., Photocuring Kinetic Studies of TMPTMA Monomer by Type II Photoinitiators of Different Weight Ratios of 2-Chlorohexaaryl Biimidazole (o-Cl-HABI) and N- Phenylglycine (NPG). *Journal of Photopolymer Science and Technology* **2018,** *31* (4), 487-492.

72. Chen, Y. C.; Kuo, Y. T.; Ho, T. H., Photo-polymerization properties of type-II photoinitiator systems based on 2-chlorohexaaryl biimidazole (o-Cl-HABI) and various N-phenylglycine (NPG) derivatives. *Photochemical & Photobiological Sciences* **2019,** *18* (1), 190-197.

73. Bendyk, M.; Jedrzejewska, B.; Paczkowski, J.; Linden, L. A., Hexaarylbisimidazoles and ketocyanine dyes as effective electron transfer photoinitiating systems. *Polimery* **2002,** *47* (9), 654-656.

74. Laevee, J.; Morlet-Savary, F.; El Roz, M.; Allonas, X.; Fouassier, J. P., Thiyl Radical Generation in Thiol or Disulfide Containing Photosensitive Systems. *Macromolecular Chemistry and Physics* **2009,** *210* (5), 311-319.

75. Monroe, B. M.; Weed, G. C., Photoinitiators for free-radical-initiated photoimaging systems. *Chemical Reviews* **1993,** *93* (1), 435-448.

76. Peng, Y.; Yu, H. W.; Chen, H. B.; Huang, Z. C.; Li, H. M., Cross-linking and de-cross-linking of triarylimidazole-based polymer. *Polymer* **2016,** *99*, 529-535.

77. Honda, S.; Toyota, T., Photo-triggered solvent-free metamorphosis of polymeric materials. *Nature Communications* **2017,** *8*.

78. Verstraeten, F.; Gostl, R.; Sijbesma, R. P., Stress-induced colouration and crosslinking of polymeric materials by mechanochemical formation of triphenylimidazolyl radicals. *Chemical Communications* **2016,** *52* (55), 8608-8611.

79. Gong, W. L.; Zhang, G. F.; Li, C.; Aldred, M. P.; Zhu, M. Q., Design, synthesis and optical properties of a green fluorescent photoswitchable hexaarylbiimidazole (HABI) with non-conjugated design. *Rsc Advances* **2013,** *3* (24), 9167-9170.

80. Gong, W. L.; Xiong, Z. J.; Li, C.; Zhu, M. Q., Design, synthesis and photoswitching of broad-spectrum fluorescent hexaarylbiimidazoles. *Rsc Advances* **2014,** *4* (109), 64371-64378.

81. Gong, W. L.; Yan, J.; Zhao, L. X.; Li, C.; Huang, Z. L.; Tang, B. Z.; Zhu, M. Q., Single-wavelength-controlled in situ dynamic super-resolution fluorescence imaging for block copolymer nanostructures via blue-light-switchable FRAP. *Photochemical & Photobiological Sciences* **2016,** *15* (11), 1433-1441.

82. Gong, W. L.; Xiong, Z. J.; Xin, B.; Yin, H.; Duan, J. S.; Yan, J.; Chen, T.; Hua, Q. X.; Hu, B.; Huang, Z. L.; Zhu, M. Q., Twofold photoswitching of NIR fluorescence and EPR based on the PMI-N-HABI for optical nanoimaging of electrospun polymer nanowires. *Journal of Materials Chemistry C* **2016,** *4* (13), 2498-2505.

83. Hua, Q. X.; Xin, B.; Xiong, Z. J.; Gong, W. L.; Li, C.; Huang, Z. L.; Zhu, M. Q., Super-resolution imaging of self-assembly of amphiphilic photoswitchable macrocycles. *Chemical Communications* **2017,** *53* (18), 2669-2672.

84. Nakahara, I.; Kikuchi, A.; Iwahori, F.; Abe, J., Photochromism of a novel hexaarylbiimidazole derivative having azobenzene moieties. *Chemical Physics Letters* **2005,** *402* (1-3), 107-110.

85. Satoh, Y.; Ishibashi, Y.; Ito, S.; Nagasawa, Y.; Miyasaka, H.; Chosrowian, H.; Taniguchi, S.; Mataga, N.; Kato, D.; Kikuchi, A.; Abe, J., Ultrafast laser photolysis study on photodissociation dynamics of a hexaarylbiimidazole derivative. *Chemical Physics Letters* **2007,** *448* (4-6), 228-231.

86. Fujita, K.; Hatano, S.; Kato, D.; Abe, J., Photochromism of a radical diffusion-inhibited hexaarylbiimidazole derivative with intense coloration and fast decoloration performance. *Organic Letters* **2008,** *10* (14), 3105-3108.

87. Kawai, S.; Yamaguchi, T.; Kato, T.; Hatano, S.; Abe, J., Entropy-controlled thermal back-reaction of photochromic 2.2 paracyclophane-bridged imidazole dinner. *Dyes and Pigments* **2012,** *92* (2), 872-876.

88. Mutoh, K.; Sliwa, M.; Abe, J., Rapid Fluorescence Switching by Using a Fast Photochromic 2.2 Paracyclophane-Bridged lmidazole Dimer. *Journal of Physical Chemistry C* **2013,** *117* (9), 4808-4814.

89. Kato, M.; Kamigaito, M.; Sawamoto, M.; Higashimura, T., Polymerization of Methyl Methacrylate with the Carbon Tetrachloride/Dichlorotris-(triphenylphosphine)ruthenium(II)/Methylaluminum Bis(2,6-di-tert-butylphenoxide) Initiating System: Possibility of Living Radical Polymerization. *Macromolecules* **1995,** *28* (5), 1721-1723.

90. Wang, J. S.; Matyjaszewski, K., Controlled Living Radical Polymerization - Atom-Transfer Radical Polymerization in the Presence of Transition-Metal complexes. *Journal of the American Chemical Society* **1995,** *117* (20), 5614-5615.

91. Matyjaszewski, K.; Xia, J. H., Atom transfer radical polymerization. *Chemical Reviews* **2001,** *101* (9), 2921-2990.

92. Matyjaszewski, K., Atom Transfer Radical Polymerization (ATRP): Current Status and Future Perspectives. *Macromolecules* **2012,** *45* (10), 4015-4039.

93. Solomon, D. H.; Rizzardo, E.; Cacioli, P. Polymerization process and polymers produced thereby 1986.

94. Hawker, C. J., Molecular-Weight Control by a Living Free-Radical Polymerization Process. *Journal of the American Chemical Society* **1994,** *116* (24), 11185-11186.

95. Ligon, S. C.; Liska, R.; Stampfl, J.; Gurr, M.; Mulhaupt, R., Polymers for 3D Printing and Customized Additive Manufacturing. *Chemical Reviews* **2017,** *117* (15), 10212-10290.

96. Tumbleston, J. R.; Shirvanyants, D.; Ermoshkin, N.; Janusziewicz, R.; Johnson, A. R.; Kelly, D.; Chen, K.; Pinschmidt, R.; Rolland, J. P.; Ermoshkin, A.; Samulski, E. T.; DeSimone, J. M., Continuous liquid interface production of 3D objects. *Science* **2015,** *347* (6228), 1349-1352.

97. Janusziewicz, R.; Tumbleston, J. R.; Quintanilla, A. L.; Mecham, S. J.; DeSimone, J. M., Layerless fabrication with continuous liquid interface production. *Proceedings of the National Academy of Sciences of the United States of America* **2016,** *113* (42), 11703-11708.

98. Scott, T. F.; Kowalski, B. A.; Sullivan, A. C.; Bowman, C. N.; McLeod, R. R., Two-Color Single-Photon Photoinitiation and Photoinhibition for Subdiffraction Photolithography. *Science* **2009,** *324* (5929), 913-917.

99. Forman, D. L. Photoinhibition Superresolution Lithography. Ph.D. dissertation, University of Colorado Boulder, 2014.

100. Li, L. J.; Gattass, R. R.; Gershgoren, E.; Hwang, H.; Fourkas, J. T., Achieving lambda/20 Resolution by One-Color Initiation and Deactivation of Polymerization. *Science* **2009,** *324* (5929), 910-913.

101. Vijayamohanan, H.; Palermo, E. F.; Ullal, C. K., Spirothiopyran-Based Reversibly Saturable Photoresist. *Chemistry of Materials* **2017,** *29* (11), 4754-4760.

102. Vijayamohanan, H.; Bhide, P.; Boyd, D.; Zhou, Z.; Palermo, E. F.; Ullal, C. K., Effect of Chemical Microenvironment in Spirothiopyran Monolayer Direct-Write Photoresists. *Langmuir* **2019,** *35* (11), 3871-3879.

103. Muller, P.; Muller, R.; Hammer, L.; Barner-Kowollik, C.; Wegener, M.; Blasco, E., STED-Inspired Laser Lithography Based on Photoswitchable Spirothiopyran Moieties. *Chemistry of Materials* **2019,** *31* (6), 1966-1972.

104. Lerch, M. M.; Hansen, M. J.; Velema, W. A.; Szymanski, W.; Feringa, B. L., Orthogonal photoswitching in a multifunctional molecular system. *Nature Communications* **2016,** *7*, 12054.

105. Menzel, J. P.; Feist, F.; Tuten, B.; Weil, T.; Blinco, J. P.; Barner-Kowollik, C., Light-Controlled Orthogonal Covalent Bond Formation at Two Different Wavelengths. *Angewandte Chemie (International ed. in English)* **2019,** *58* (22), 7470-7474.

Chapter 2

Development of Novel High T_g, Low Shrinkage Stress Thiol–ene Resins

2.1 Original Publication information

Parts of this chapter are in preparation for publication or have been published or in the following peer-reviewed papers:

H.L. Van der Laan; S.L. Zajdowicz; K. Kuroda; B.J. Bielajew; T.A. Davidson; J. Gardinier; D.H. Kohn; S. Chahal; S. Chang, J. Liu; J. Gerszberg; T.F. Scott; and B.H. Clarkson. Biological and Mechanical Evaluation of Novel Prototype Dental Composites. *Journal of Dental Research,* **2019**, *98,* 91–97

2.2 Abstract

Polymerization-induced shrinkage in dental restorative materials typically leads to significant development of polymerization shrinkage stress accompanied by various deleterious side effects. Thiol–ene resins have emerged as a candidate to replace these methacrylate-based materials, owing significantly to their inherently reduced polymerization shrinkage stress, but are generally limited by subpar glass transition temperatures resulting in rubbery materials. Here, we describe a silane-based, norbornyl-bearing oligomers in thiol–ene dental resins and determine the impact of these materials on the glass transition temperature, polymerization shrinkage stress, and photopolymerization kinetics relative to a thiol–ene standard. Significant improvements in glass transition temperature are obtained through this approach, whilst polymerization-

induced shrinkage stress was reduced to less than half. Biological and mechanical evaluation of filled thiol–ene composites demonstrated these materials to be on par with methacrylate composite materials.

2.3 Introduction

Dental composite materials, consisting of an inorganic filler material dispersed throughout a continuous cross-linked polymeric matrix have a near-ubiquitously use in dental restorations, and have significantly displaced mercury-based amalgam alloys in this application.[1] Methacrylate-based dental composites[2, 3] demonstrate many favorable properties including improved aesthetics, and *in situ* photopolymerization to afford materials with high elastic moduli and glass transition temperatures. Despite the excellent properties exhibited by the composite dental fillings, methacrylate-derived monomers introduce several complications. Volumetric shrinkage of the resin under confinement of the cavity walls[4, 5] leads to the development of a significant amount of volumetric shrinkage stress, which can lead to a variety of deleterious effects such as severe dental pain, tooth deflection,[6] tooth cracking,[7] as well as localized debonding and gap formation.[8] Although gap formation, and subsequent clinical failure of the dental restorative can develop through long-term mechanical and thermal stresses, a direct relationship has been demonstrated between shrinkage stress and marginal integrity. In addition, methacrylate free radical polymerizations proceed through a chain-growth polymerization mechanism, which is inhibited by the presence of oxygen,[9, 10] and as a result the cross-linked materials can exhibit low surface reaction extends, and can contain significant amounts of unreacted, extractable monomer.[11] Finally, the introduction of methacrylate-based polymers unavoidably incorporates ester moieties that are susceptible

to hydrolytic degradation,[12] reducing structural integrity of the polymer, and allows leeching of liberated monomers.

As the development of polymerization shrinkage stress in dental resins has a significant effect on the longevity of the restoration, it has been a topic of high interest to reduce the polymerization shrinkage stress in dental composites. Use of a pre-oligomerization approach reduces the functional group concentration and the resultant shrinkage stress. Alternatively, low shrinkage ring-opening polymerizations bearing spiro- or oxirane moieties reduce shrinkage stress through minimizing the change in free volume upon polymerization. Furthermore, making use of polymerization-induced microphase separation, or modification of the *in situ* processing protocol have shown great potential for reducing polymerization shrinkage stress.

Thiol–ene materials have been extensively studied as a new generation of low shrinkage stress dental resins. In contrast to methacrylate polymerization, a thiol–ene polymerization follows a step-growth polymerization mechanism through alternating addition and chain transfer reactions. [13] Coupling thiols and electron-rich C=C double bonds such that these functional groups are consumed in a 1:1 stoichiometric ratio without generating significant side products. The step-growth polymerization yields materials with a delayed gel point, allowing significant volumetric shrinkage stress to be dissipated through viscous flow of the resin and lower extractable material content. [4, 14-16] Furthermore, it has previously been demonstrated that thiol–ene polymerizations exhibit lower volumetric polymerization shrinkage than methacrylates on a molecular level, where volumetric shrinkage per mole of the double bond decreases from 22.5 cm^3/mol for methacrylates to 12-15 cm^3/mol for thiol–ene systems. Not only does the thiol–ene

polymerization exhibit reduced volumetric shrinkage and shrinkage stress relative to methacrylate resins, it shows nearly all the advantages of the conventional free-radical chain-growth polymerization such as high polymerization rates, polymerization can be performed in bulk, result in optically clear materials, can be readily cured with visible light,[17] and allow for a wide variety of mechanical properties. It is also highly resistant to inhibition by oxygen,[18, 19] preventing tacky surfaces, and reduces unreacted extractable monomer content. In addition, ester-free thiol–ene resins have been demonstrated as hydrolytically stable, and solvent resistant, further reducing leachables. In addition, as the thiol–ene polymerization proceeds through a radical mechanism, the formulations can be easily adapted to current dental infrastructure. Despite these excellent characteristics, thiol–ene formulations are generally limited by their low elastic moduli and glass transition temperature.[20]

Several strategies have been employed to address the deficiencies presented by thiol–ene formulations for dental resins.[14, 21, 22] Thiol–ene/methacrylate formulations can afford materials with increased elastic moduli and glass transition temperatures while simultaneously obtaining relatively low shrinkage stress values. [20, 21, 23-30] However, as a significant amount of methacrylate monomer is required, the disadvantages of methacrylate-based materials start to arise. Moreso, the thiol–ene conversion is limited due to trapping in the methacrylate network, owing to the pseudo two-stage polymerization and phase separation.[20, 28, 31] Alternatively *via* a mixed mode thiol–ene/thiol–epoxy formulation, two step-growth polymerizations are combined to yield a combined rubbery/glassy network, however the stoichiometric balance of this approach, as well as the amines required for the epoxy curing make this method less than desirable.

[21] More recently, success has been achieved through the use of silane-based tetrathiols. These silane-based materials yield increased glass transition temperatures owing to their increased crosslink density.[32] These silane-based materials also lack ester moieties, which are common in thiol–ene resins, giving them increased resistance to hydrolysis. However, it was reported that these monomers display significantly lower rates of polymerization compared to the model thiol–ene systems studied.

Here, rather than employing mixed mode polymerizations, we address the deficiencies of the thiol–ene resins by using the silane-based tetrathiol, and combining it with norbornene-bearing monomers to further increase the glass transition temperature. While these norbornene monomers are poorly miscible with regular thiol–ene resins, we utilize a pre-oligomerization to prepare norbornyl-bearing oligomers, that are miscible with conventional ene monomers. This approach has the added advantages of reducing shrinkage stress *via* pre-oligomerization, and additionally result in low vapor pressure oligomers, curtailing the malodorous silane-based tetrathiols. We expect that this combination of factors will result in significantly improved materials for dental applications.

2.4 Experimental

2.4.1 Materials

Tetravinylsilane was obtained from Gelest (Morrisville, PA), azobisisobutyronitrile, tetrahydrofuran. thioacetic acid, 1,3,5,-triallyl-1,3,5-triazine-2,4,6(1H,3H,5H)-trione (TATATO), dicyclopentadiene, methanol, dioxane, and pentaerythritol tetra-3-mercaptopropionate (PETMP) were obtained from Sigma-Aldrich (St. Louis, MO) , concentrated hydrochloric acid was obtained from Fisher Scientific

(Hampton, NH). Diallyl bisphenol A was obtained from AstaTech (Bristol, PA). Diphenyl (2,4,6-trimethylbenzoyl)-phosphine oxide (TPO) was received from BASF (Florham Park, NJ). tris(N-nitroso-N-phenylhydroxylaminato)aluminum (Q1301) was obtained from Wako Chemicals (Richmond, VA). THF was passed through basic alumina to remove inhibitor prior to use. All other chemicals were used as received.

The monomers PETMP and TATATO were used as a mixture, such that the thiol (i.e., mercapto) and ene (i.e., allyl) functional groups were present at a 1:1 stoichiometric ratio, and used as a model thiol–ene resin. Tetra(2-mercaptoethyl)silane (TMES) was similarly mixed with TATATO in a 1:1 stoichiometric ratio. TMES was also pre-oligomerized with 1,3,5,-trinorbornyl-1,3,5-triazine-2,4,6(1H,3H,5H)-trione (TNTATO), or Dinorbornyl bisphenol A ether (DNBPA) in a 1:0.32 and 1:0.16 ratio prior to formulating with TATATO. Prior to thiol and ene component mixing, 0.01 wt% Q1301 was added to the TATATO as a radical polymerization inhibitor to preclude premature thiol–ene polymerization. Diphenyl (2,4,6-trimethylbenzoyl)-phosphine oxide (Irgacure TPO) was used as visible light-active photoinitiating systems at 1 wt%. the concentrations as indicated in the text. All commercial monomers and photoinitiators were used without further purification, the synthesis of TMES, TNTATO, DNBPA, and their pre-oligomerization is described in reference, and the structures of all materials used are shown in Figure 2.1.

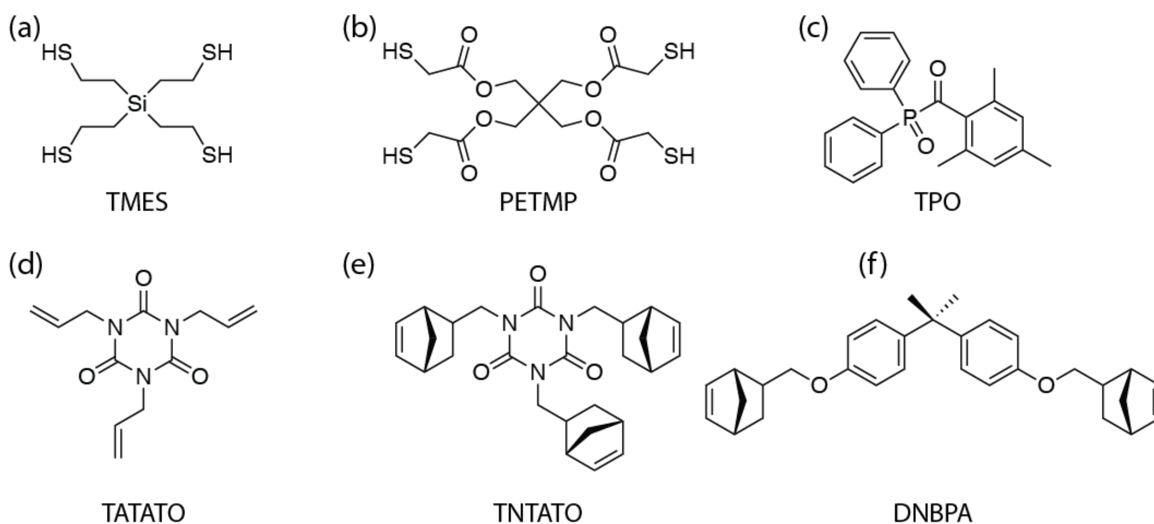

Figure 2.1 Materials used in this study (a) TMES (b) PETMP (c) TPO (d) TATATO (e) TNTATO (f) DNBPA

2.4.2 Methods

2.4.2.1 Light Sources and intensity measurement

Violet light was provided by a collimated, LED-based illumination source (Thorlabs M405L2-C) with an emittance centered at 405 nm (FWHM 13 nm), used in combination with a current-adjustable LED driver (Thorlabs LEDD1B) for intensity control. Irradiation intensities were measured with an International Light IL1400A radiometer equipped with a broadband silicon detector (model SEL033), a 10× attenuation neutral density filter (model QNDS1), and a quartz diffuser (model W).

2.4.2.2 FTIR Spectroscopy

Photopolymerization reaction kinetics were examined using a Thermo Scientific Nicolet 6700 FT-IR spectrometer equipped with a horizontal transmission accessory, as described elsewhere, recording spectra from 2000 cm^{-1} to 7000 cm^{-1} at a rate of approximately 2 every second. Resins were mixed in 1:1 thiol:ene stoichiometric ratios, formulated with 1 wt% Irgacure TPO, and introduced between two glass microscope

slides separated by 50 μm thick spacers. The functional group conversions upon irradiation were determined by monitoring the disappearance of the peak area centered at 2571 cm^{-1} corresponding to the thiol group stretch and 3083 cm^{-1} corresponding to the allylic vinyl group stretch. All experiments were conducted in triplicate, and the irradiation intensities were as indicated in the figure captions.

2.4.2.3 Dynamic Mechanical Analysis

Cross-linked polymer films were prepared from thiol–ene formulations containing 1 wt% Irgacure TPO which were polymerized between glass microscope slides separated by 250 μm thick spacers for 30 minutes at room temperature under 405 nm irradiation at 10 $mW\cdot cm^{-2}$. Samples of approximately 15 mm × 5 mm × 0.25 mm were cut from the cured films and mounted in a TA Instruments Q800 dynamic mechanical analyzer equipped with a film tension clamp. Experiments were performed at a strain and frequency of 0.1% and 1 Hz, respectively, scanning the temperature from −25°C to 200°C twice at $2°C\cdot min^{-1}$, and the storage modulus (E′) and tan δ curves were recorded. All experiments were conducted in triplicate. The repeated temperature scan was used to determine the influence of dark polymerization at temperatures greater than the glass transition temperature (T_g). The T_g was assigned as the temperature at the tan δ curve peak.

2.4.2.4 Polymerization Shrinkage Stress

Polymerization-induced shrinkage stress was determined using a tensometer. Resins formulated in 1:1 thiol:ene stoichiometric ratios, containing 1 wt% Irgacure TPO as the photoinitiator were introduced between 2 polished quartz rods (6mm diameter) spaced 1 mm apart. The samples were irradiated from below through the quartz rod and

the polymerization-induced shrinkage stress was monitored through cantilever deflection and recorded at a rate of 10 per second. All experiments were conducted in triplicate, and the irradiation intensities were as indicated in the figure captions.

2.4.2.5 FA Synthesis

Briefly, a solution containing 0.25M EDTA-Ca-Na_2, 0.15M $NaH_2PO_4 \cdot H_2O$, and 0.05M NaF was subjected to mild hydrothermal conditions (121 °C, 2 atm) for 10 h to dissociate the Ca^{2+} and allow its slow release from EDTA-Ca complex. The resultant crystals were washed 3 times in distilled water. They were then ground with a SpeedMixer (FlackTek Inc.) resulting in a crystal length of approximately 600 nm to 1 µm. Even dispersion and wetting of the FA crystals in the resins were carried out with a SpeedMixer.

2.4.2.6 Composite Specimen Composition for all Tests

Composites made from TMES-TNTATO/TATATO and TMESDNBPA/TATATO were tested and benchmarked against bisGMA (70 wt%) and TEGDMA (30 wt%) composites. The resins contained 1% Irgacure TPO as the photoinitiator and were cured at 405 nm with Thorlabs M405L2 LED at an intensity of 10 mW/cm2 for 30 min. The samples reached 70% conversion. Each resin was filled with either 1) 50% w/w silanated glass (hybrid of 40% 700 nm barium borosilicate glass filler [BBAS] + 60% 2 µm BBAS) or 2) 50% w/w glass + FA (hybrid of 30% 700 nm BBAS + 40% 2 µm BBAS + 30% 600 nm–1 µm FA).

2.4.2.7 Material Cytotoxicity

Following ISO 10993-12 and ISO 10993-5 protocol, human dental pulp stem cells were used to evaluate the toxicity of the synthesized polymers (TMES-TNTATO/TATATO, TMES-DNBPA/TATATO, and bisGMA/TEGDMA) and their glass- or glass + FA–filled composites. The leachables were extracted from 4.5 specimens (5 × 25 × <0.5 mm each) after their incubation in 1-mL Dulbecco's modified Eagle's medium (DMEM) with the addition of 10% fetal bovine serum at pH 7.4 for 24 h. After 5 × 104 dental pulp stem cells were seeded into 96-well plates, they were cultured for 24 h and then treated with serially diluted leachables from the composites for 24 h. XTT solutions, or 2,3-bis-(2-methoxy-4-nitro-5-sulfophenyl)-2H-tetra-zolium5-carboxanilide, were added to each test well, and the plate was incubated for 5 h. Optical density (OD) values were measured at 450 nm. Statistical analysis by 2-way analysis of variance (ANOVA) was based on GraphPad Prism 6, and significance was considered at $P < 0.05$.

2.4.2.8 Mechanical Property Evaluation

Composite beams (25 × 2 × 2 mm) were fabricated in stainless steel split molds and specimens light cured in 5 overlapping sections for maximum conversion on the top and bottom surfaces, according to ISO 4049 protocol. Flexural tests ($n = 5$ per condition) were conducted on an Admet eXpert 450 Universal Testing Machine at 0.01-mm/s until failure. During each test, load and deflection were recorded, and stress and strain were calculated from standard 3-point beam-bending equations: preyield, postyield, and total toughness were calculated per the area under the elastic, plastic, and total stress-strain curve at fracture, respectively. Due to the brittle nature of the composites, postyield

toughness was negligible, and preyield toughness was equal to total toughness and therefore not reported.

2.4.2.9 Biofilm Evaluation

Biofilms were formed with a monospecies biofilm model containing a luciferase-expressing Streptococcus mutans. Briefly, composite discs 7 mm in diameter and 1 mm thickness were sterilized in 70% alcohol containing 0.5% triclosan for 30 min; 3 experiments were conducted with 3 discs for each sample, yielding a total 9 discs per sample. Following sterilization, discs were rinsed in sterile saline and brain-heart infusion (BHI) broth for at least 1 h. S. mutans firefly was grown in BHI broth overnight at 37 °C with 5% CO_2. Following incubation, the OD at 600 nm (OD600) was measured, and cultures were diluted to an OD600 of 0.05 into fresh BHI broth supplemented with 1% sucrose. Discs were transferred to sterile white opaque 24-well plates (Fisher Scientific); 1 mL of the bacterial dilution was added to each well; and the plates were incubated with static conditions at 37 °C with 5% CO2 for 24 h to allow for mature biofilm formation. Controls were also prepared (no bacteria added), where only BHI + 1% sucrose were added to the wells containing discs. After incubation, all discs were transferred to fresh BHI + 1% sucrose and incubated for 1 h to allow for repletion of ATP. To measure luciferase activity, 2mM D-luciferin (Fisher Scientific) was added, and luminescence was measured at 2-min intervals up to 10 min (FilterMax F5; Molecular Devices). Statistical analysis was performed with a Student’s t test and ANOVA. After luciferase activity was measured, biofilms on each resin were disrupted through sonication with a water bath sonicator (Ultrasonic Bath 1.9L; Thermo Fisher Scientific) for 10 min, followed by agitation by vortexing for 3 min. The bioburden on discs was enumerated as colony-

forming units per milliliter (CFU/mL), and statistical analysis was performed with a Student's t test and ANOVA.

2.4.3 Synthesis

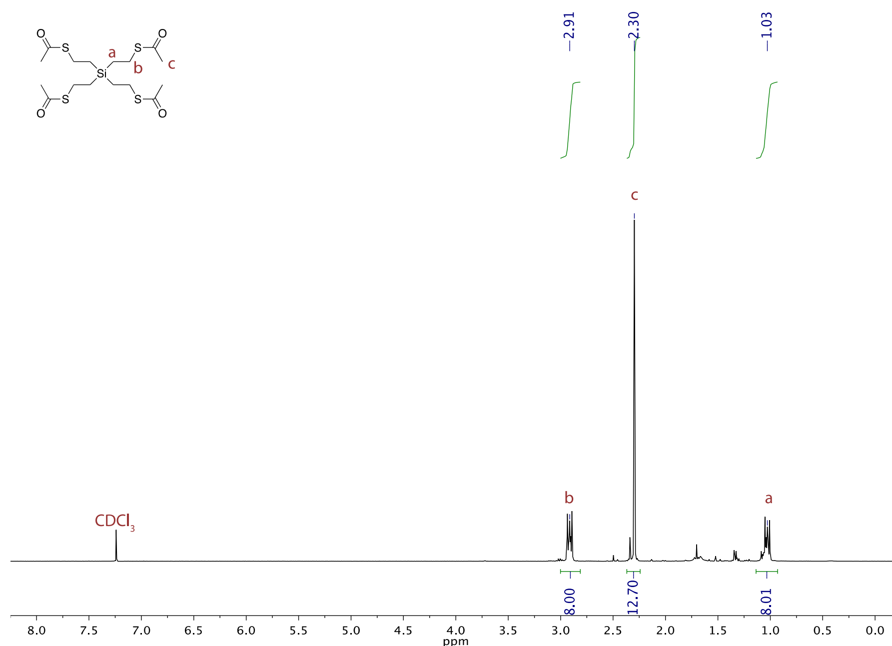

Figure 2.2 ^{1}H-NMR Spectrum of Tetra(S-ethylethanethioate)silane

2.4.3.1 Tetra(S-ethylethanethioate)silane.

Tetravinylsilane (50g), azobisisobutyronitrile (8g), and thioacetic acid (120 mL) were dissolved in Tetrahydrofuran (500 mL) in a 1L round-bottom flask equipped with a reflux condenser. The solution was heated to 70°C, and stirred overnight. The solution was allowed to cool to room temperature, and the solvent was removed under reduced pressure to yield a yellow oil. The obtained material was used in the next step without further purification. ^{1}H NMR (400 MHz, $CDCl_3$): δ = 2.90-2.95 (m, 8H, -SC**H**$_2$-), 2.31 (s, 12H, -C**H**$_3$), 1.02-1.06 (m, 8H, -C**H**$_2$-Si).

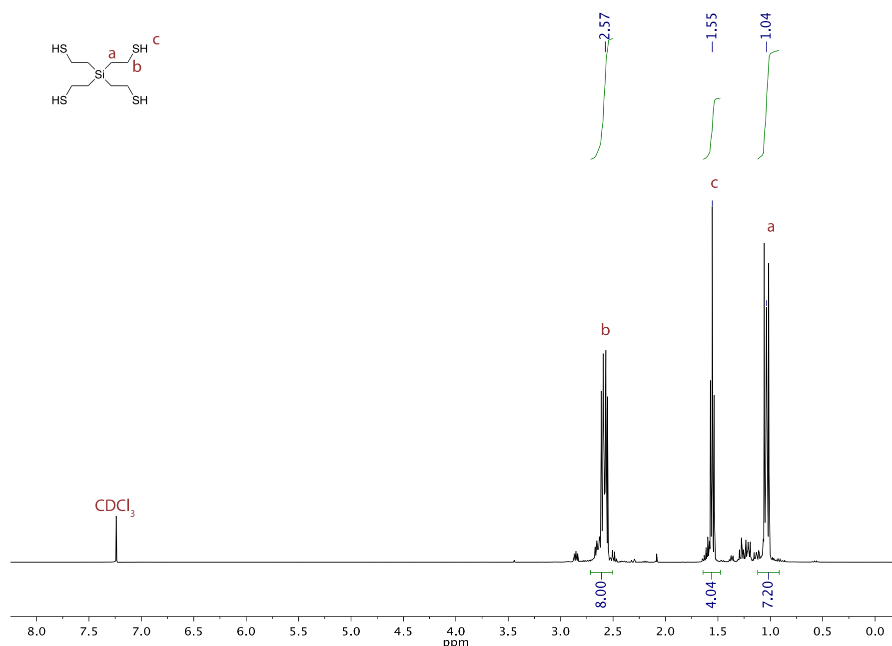

Figure 2.3 ¹H-NMR Spectrum of Tetra(2-mercaptoethyl)silane (TMES)

2.4.3.2 Tetra(2-mercaptoethyl)silane.

The Tetra(S-ethylethanethioate)silane obtained from the previous step was dissolved in a mixture of methanol (200 mL) and 1,4-dioxane (300 mL) in a 2-neck flask equipped with a reflux condenser. To this was added concentrated hydrochloric acid (100 mL), and the solution was heated to 65°C, and stirred over the weekend. The solution was allowed to cool to room temperature, and the solvent was removed under reduced pressure. To the resultant oil was added water (200 mL), and the aqueous phase was extracted 3 times with methylene chloride (150 mL). The combined organic phases were dried over magnesium sulfate, and the solvent removed under reduced pressure. The residual oil was distilled under vacuum (200°C, 0.4 Torr), and the first fraction product was collected and redistilled under the same conditions 2 additional times to afford TMES as a colorless, malodorous oil. ^{1}H NMR (400 MHz, $CDCl_3$): δ = 2.58-2.69 (m, 8H, -SC**H**$_2$-), 1.56-1.62 (m, 4H, -S**H**), 1.04-1.16 (m, 8H, -C**H**$_2$-Si).

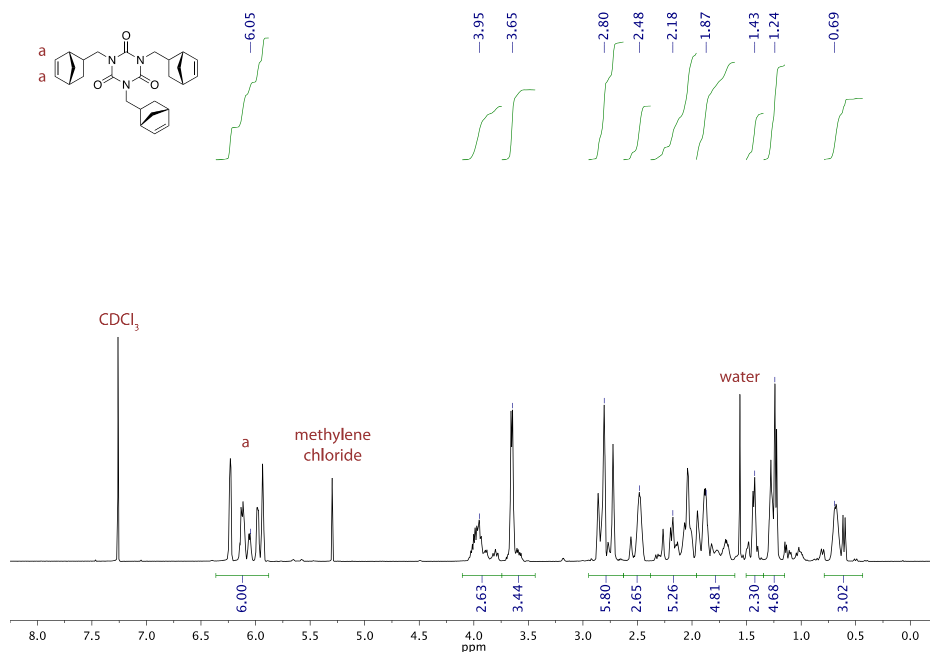

Figure 2.4 ^{1}H-NMR Spectrum of Trinorbornyl triazine trione (TNTATO)

2.4.3.3 Trinorbornyl triazine trione (TNTATO).

Dicyclopentadiene (8.75 g) and triallyl triazine trione (5.5 g) were added to a 50 mL glass bomb flask. The flask was sealed and heated to 190°C for 2 days. The mixture was allowed to cool to room temperature, and was dissolved in methylene chloride (100 mL). The solution was filtered over a pad of celite, and the solvent removed under reduced pressure. The product loaded on a silica column, and after washing with hexanes, was purified through silica column chromatography (hexanes:methylene chloride = 2:1). Removal of the solvent under reduced pressure yielded the product as a mixture of *endo* and *exo* adducts as a white powder. ^{1}H NMR (400 MHz, $CDCl_3$): δ 6.36-5.88 (m, 6H), 3.74-4.11 (m), 3.74-3.44 (m), 2.95-2.63 (m), 2.63-2.38 (m), 2.38-1.96 (m), 1.96-1.61 (m), 1.50-1.34 (m), 1.34-1.15 (m), 0.79-0.44 (m)

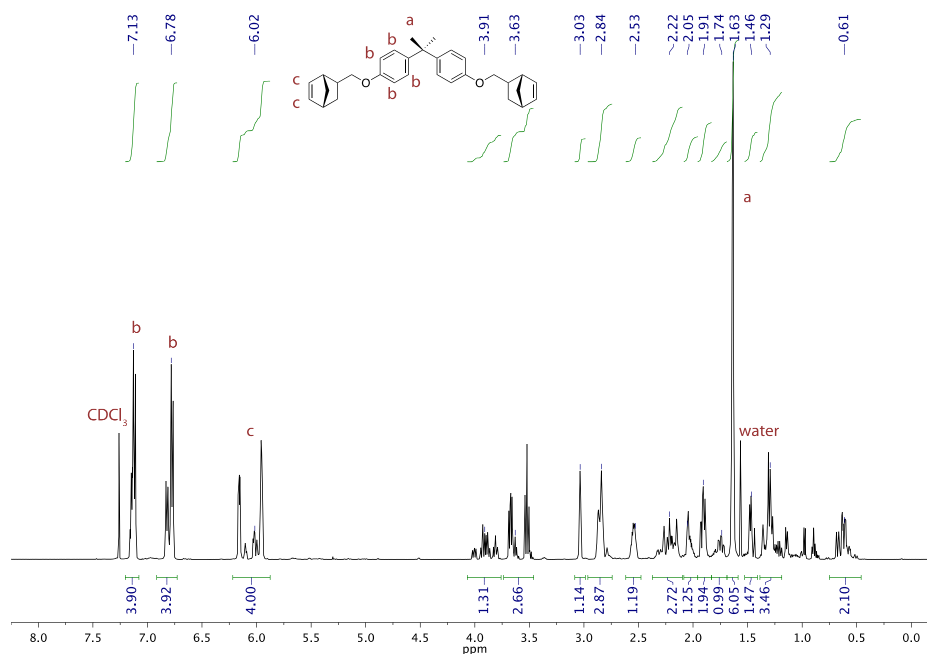

Figure 2.5 ^{1}H-NMR Spectrum of Dinorbornyl bisphenol A (DNBPA)

2.4.3.4 Dinorbornyl bisphenol A (DNBPA)

Dicyclopentadiene (6.1 g) and diallyl bisphenol A (7.2 g) were added to a 50 mL glass bomb flask. The flask was sealed and heated to 190°C for 2 days. The mixture was allowed to cool to room temperature, and was dissolved in methylene chloride (100 mL). The solution was filtered over a pad of celite, and the solvent removed under reduced pressure. The product loaded on a silica column, and after washing with hexanes, was purified through silica column chromatography (hexanes:methylene chloride = 2:1). Removal of the solvent under reduced pressure yielded the product as a mixture of *endo* and *exo* adducts as a white powder. ^{1}H NMR (400 MHz, $CDCl_3$): δ 7.20-7.08 (m, 4H), 6.92-6.73 (m, 4H), 6.22-5.88 (m, 4H), 4.07-3.76 (m), 3.74-3.46 (m), 3.08-2.99 (m), 2.96-2.74 (m), 2.62-2.48 (m), 2.37-2.10 (m), 2.08-1.96 (m), 1.96-1.83 (m), 1.83-1.69 (m), 1.69-1.59 (s, 6H), 1.53-1.41 (m), 1.39-1.19 (m), 0.75-0.46 (m)

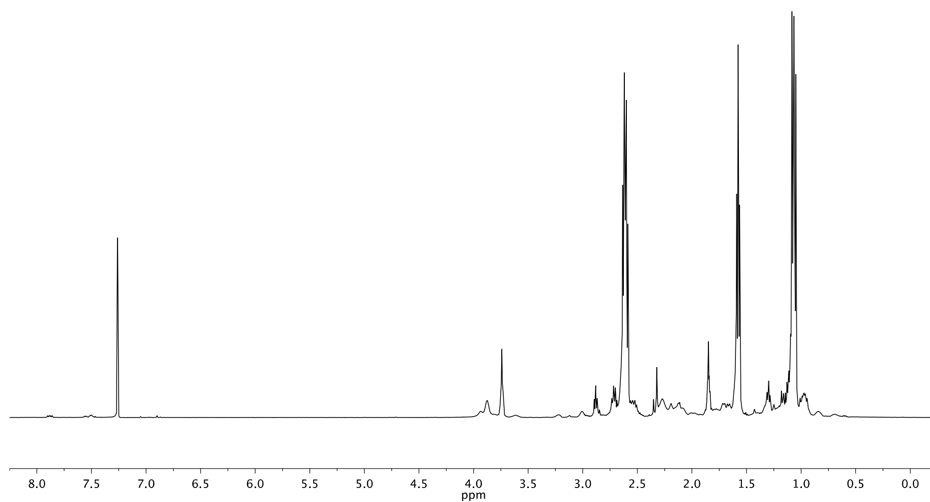

Figure 2.6 ^{1}H-NMR Spectrum of TMES-TNTATO oligomer

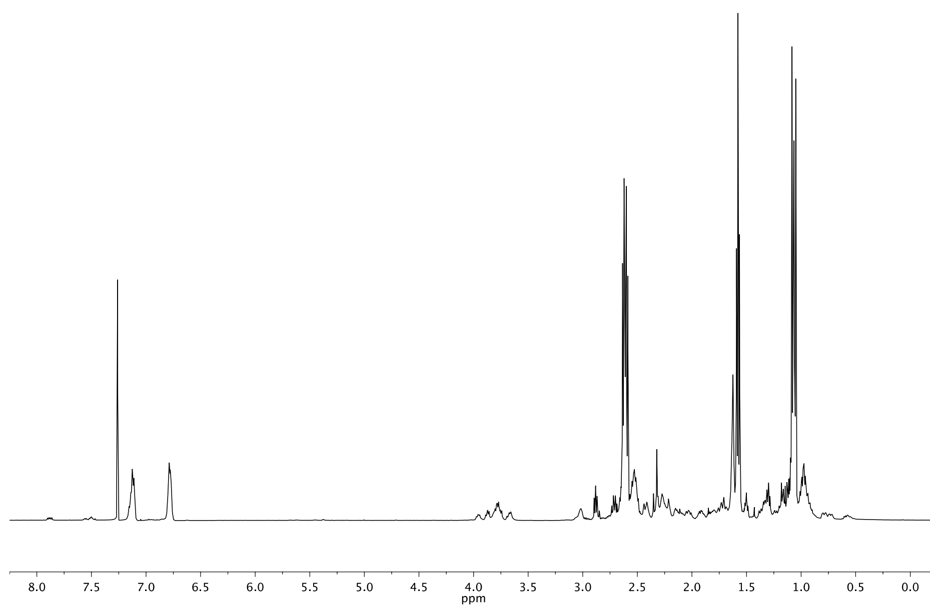

Figure 2.7 ^{1}H-NMR Spectrum of TMES-DNBPA oligomer

2.4.3.5 TMES-TNTATO and TMES-DNBPA Oligomers

The monomers were mixed in a 1:0.16 and 1:0.32 thiol–ene stoichiometric ratios for TMES-TNTATO and TMES-DNBPA, respectively, formulated with 1 wt% Irgacure TPO, and approximately 5 grams of the monomer mixture was dissolved in 50 mL THF. The solution was stirred overnight under irradiation with 405 nm at 15 mW/cm^2 using a Thorlabs M405L2 LED. After removal of the solvent under reduced pressure a golden, mildly odorous oil was obtained. Excess solvent was removed under reduced pressure, and through heating under a strong vacuum.

2.5 Results and Discussion

Rapid polymerization rates, required for clinically acceptable dental material processing times, are a hallmark of the contemporary, methacrylate-based dental restorative resins. The PETMP/TATATO monomer system formulated in a 1:1 stoichiometric ratio has been widely studied as a thiol–ene alternative to the methacrylate resins, as it displays polymerization rates comparable to the methacrylate monomers, and will be used as the benchmark resin in this study. The photopolymerization behavior and consumption of vinyl and thiol moieties of PETMP with TATATO, TMES with TATATO, TMES-TNTATO oligomer with TATATO, and TMES-DNBPA oligomer with TATATO, all containing 1 wt% TPO were examined using FTIR spectroscopy (See Figure 2.8). Of these, PETMP/TATATO reference saw the highest rates of polymerization and final thiol and ene conversions, followed by TMES/TATATO, and the pre-oligomerized formulations. In contrast to previous reports, it was demonstrated that the silane-based lower MW tetrathiol TMES polymerizes with TATATO at rates

comparable to the PETMP/TATATO. The discrepancy is likely attributable to residual impurities following the preparation of TMES. Initial photopolymerization experiments showed results comparable to those previously reported. Consistent, improved photopolymerization was observed following rigorous and consecutive fractional distillation of TMES.

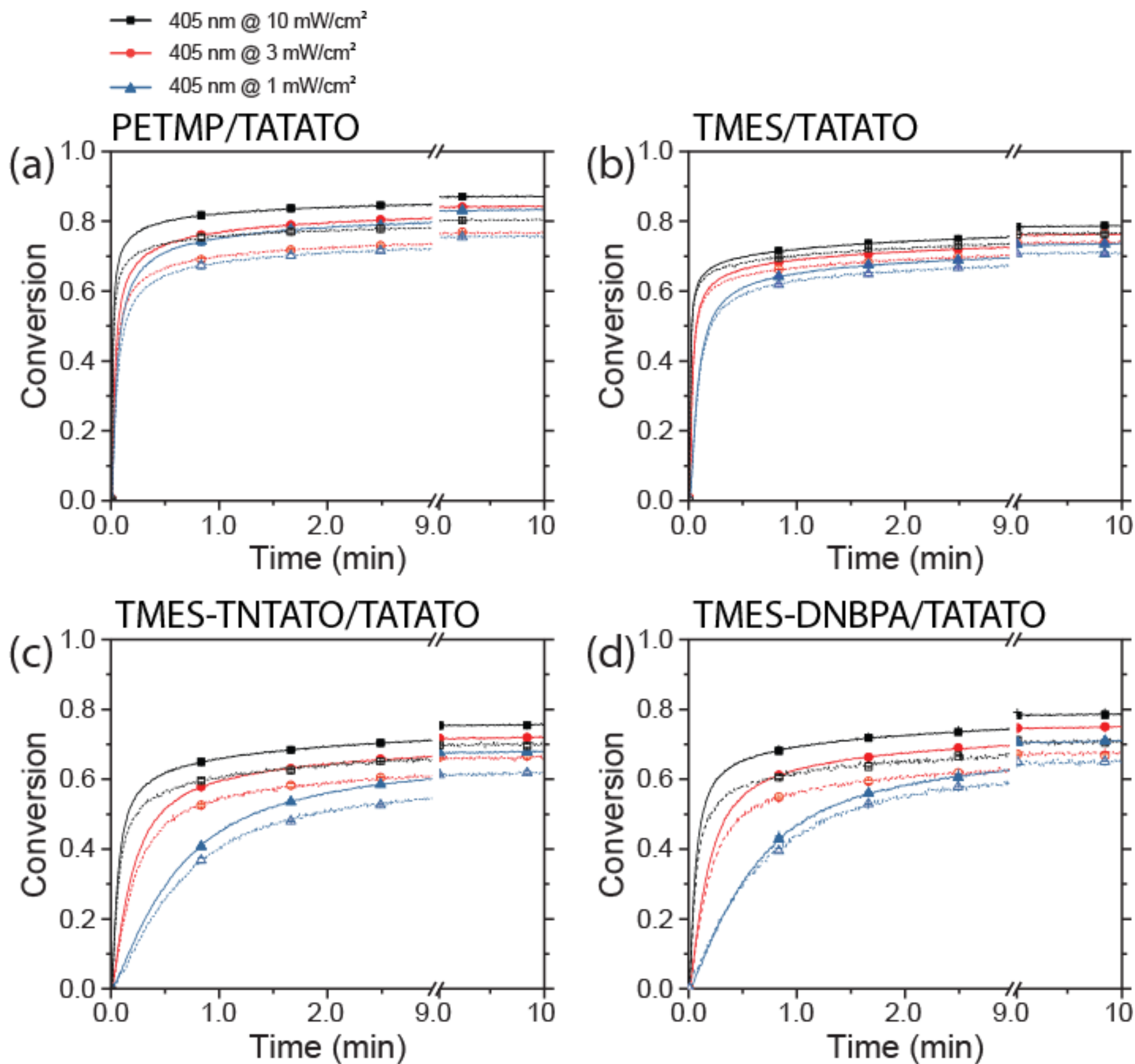

Figure 2.8 Photopolymerization kinetics Conversion versus time for the photopolymerizations of (a) PETMP/TATATO, (b) TMES/TATATO, (c) TMES-TNTATO/TATATO, and (d) TMES-DNBPA/TATATO. Continuous irradiation with 405 nm at intensities of 1 (blue triangles), 3 (red circles), and 10 (black squares) mW/cm^2. TATATO ene conversions are displayed as solid lines and symbols, whereas thiol conversions are dashed lines and open symbols

Attempts to identify the impurities through ^{1}H-NMR spectroscopy and mass spectrometry were unsuccessful. Having established the photopolymerization behavior of TMES, TMES was oligomerized in solution with the norbornyl-bearing monomers TNTATO and DNBPA in a 1:0.16 and 1:0.32 thiol–ene stoichiometry respectively to allow maximum conversion prior to gelation. Complete consumption of the norbornyl moieties is confirmed through ^{1}H-NMR spectroscopy as shown in Figure 2.9.

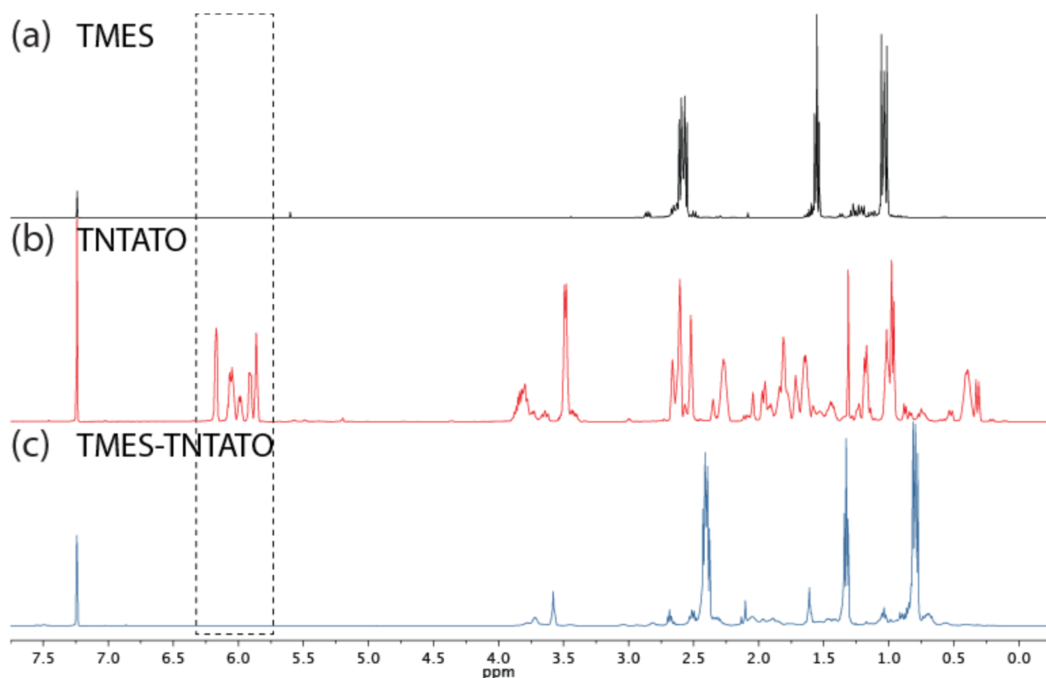

Figure 2.9 ^{1}H-NMR spectra of (a) TMES, (b) TNTATO, and (c) TMES-TNTATO oligomer Complete incorporation of TNTATO in the oligomer is confirmed by the disappearance of the norbornyl signal centered at 6 ppm highlighted in the dashed box

The pre-oligomerized formulations demonstrate rapid polymerization following exposure to 405nm irradiation. While rapid photopolymerization occurs at increased irradiation intensities, the rate of thiol and ene consumption is significantly reduced compared to both TMES/TATATO and PETMP/TATATO at lower irradiation intensities, with a lower overall conversion. As the concentration of both thiol and ene in the oligomeric formulation is significantly reduced relative to the monomeric

TMES/TATATO formulations, the reduction in polymerization rates was not unexpected. While TMES-TNTATO/TATAO saw more rapid TATATO consumption and final conversion than TMES-DNBPA/TATATO, higher rates of thiol consumption and increased final thiol conversion was observed in TMES-DNBPA/TATATO. As the incident irradiation intensity was raised, increased thiol and ene polymerization was observed. Additionally, while the resins were formulated in a 1:1 stoichiometric thiol/ene ratio, TATATO consumption proceeded faster and to greater extend than that of the thiols in all formulations. Polymerization initiated readily upon irradiation with no noticeable induction period. When considering overall conversion of the various photopolymers the reduction in final conversion of the TMES-based formulations is lower than the PETMP/TATATO formulation. The decrease is likely related to the increased glass transition temperature (See Figure 2.11 and Table 2.1) of the resultant polymer, and resultant vitrification trapping radicals and preventing further conversion of the monomers. Although thiol–ene polymerizations are often described as ideal alternating copolymerizations, where the thiol and ene moieties are consumed at equal rates as these polymerizations proceed, the allyl functional group was consistently consumed more rapidly than the thiol under all irradiation conditions for each of the examined formulations, attributable to a limited amount of allylic homopolymerization during each reaction. While these systems do show reduced rates of polymerization, they nevertheless cure rapidly at increased incident irradiation intensities. As the irradiation intensity emitted by the light guide of conventional dental lamps usually approaches or exceeds 1 $W \cdot cm^{-2}$ this is not a cause of concern for these oligomeric formulations.

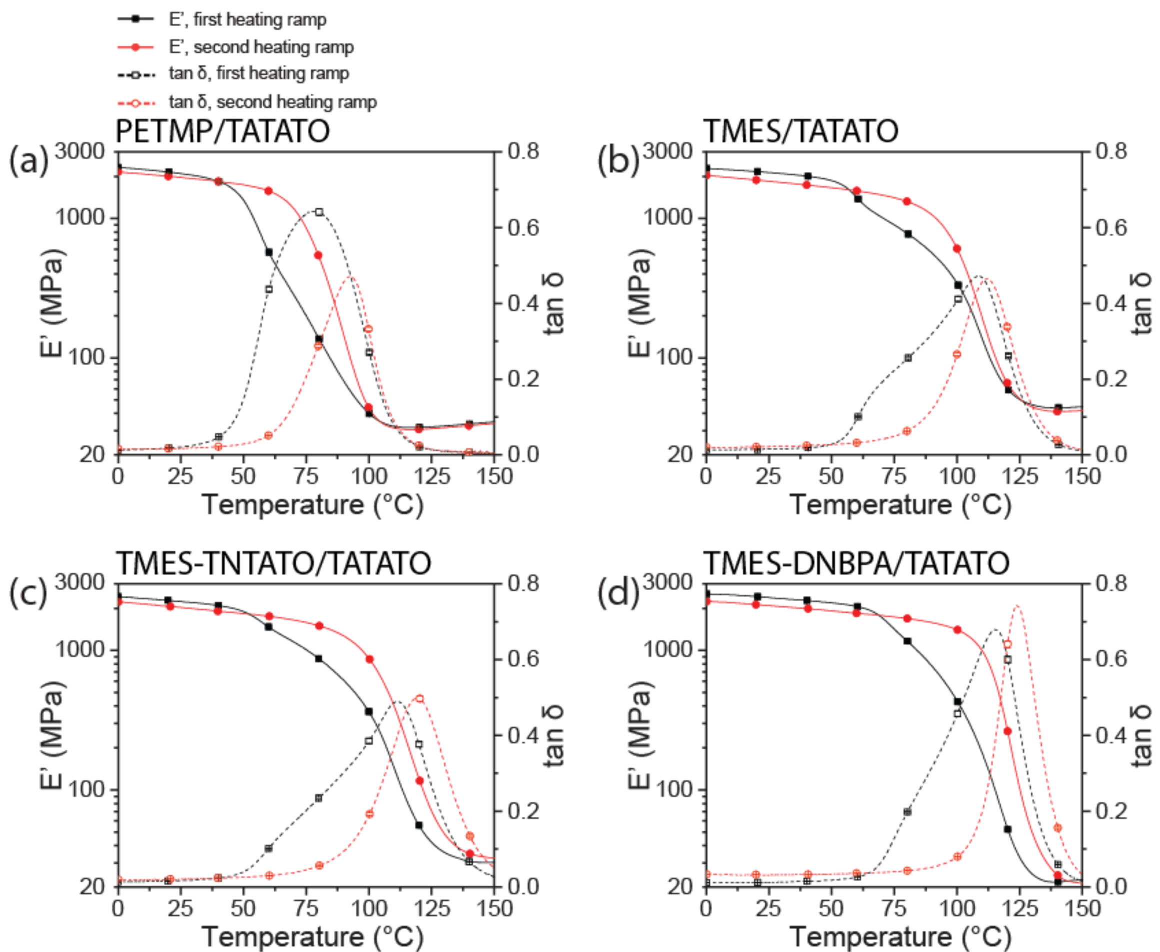

Figure 2.10 Dynamic Mechanical Analysis traces of storage modulus (E', solid lines) and tan δ (dashed lines) as a function of temperature (a) PETMP/TATATO, (b) TMES/TATATO, (c) TMES-TNTATO/TATATO, and (d) TMES-DNBPA/TATATO, irradiated with 405 nm at 10 mW·cm^{-2}. First heating ramp is in black, and second heating ramp is in red. Storage modulus is displayed as solid lines and symbols, whereas tan δ is displayed as dashed lines and open symbols

For resins to be acceptable for clinical dental applications, one requirement to be met is a sufficiently high glass transition temperature of the cured resin, generally needing to exceed 100°C. The viscoelastic properties of the 4 different thiol–ene resins cured at 10 mW/cm^2 of 405 nm light were determined using dynamic mechanical analysis (See Figure 2.10. summarized in Table 2.1). The storage modulus (E′) prior to the glass transition onset was lower for the second temperature ramp than for the first ramp for all samples, whereas the E′ was consistently higher in the rubbery regime for the

second ramp than for the first. Whereas the observed glass transition temperature (T_g), as determined by the peak in the tan δ curve, was higher for the second temperature ramp than the first for all samples.

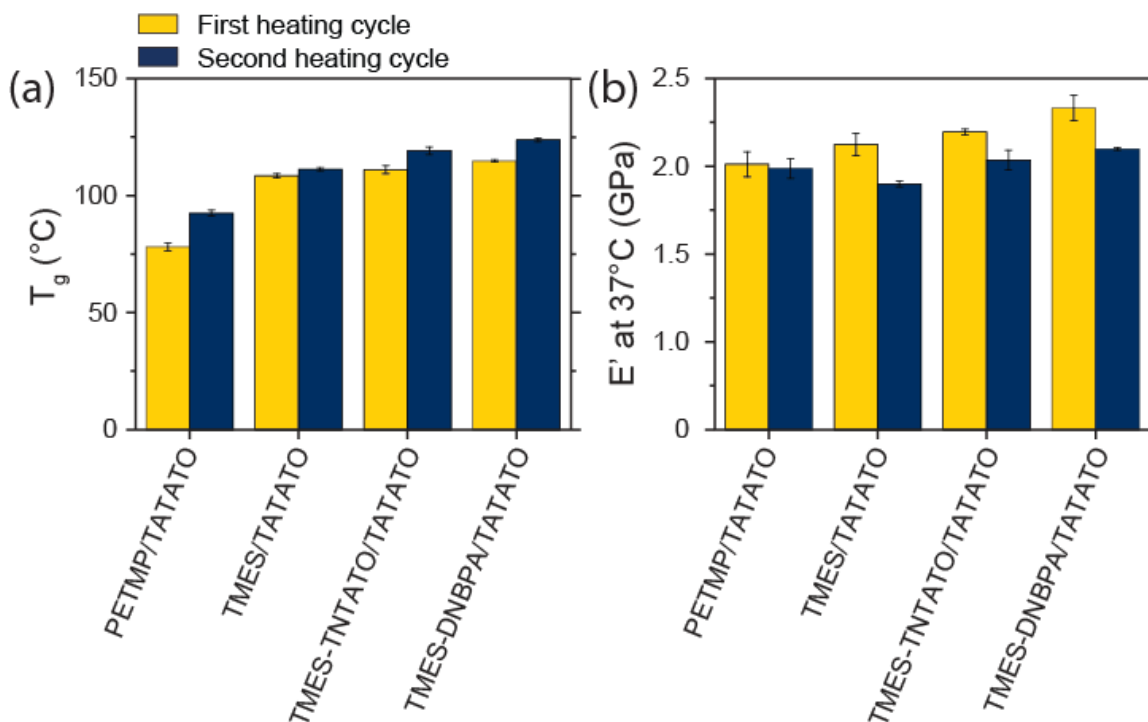

Figure 2.11 Dynamic Mechanical Analysis comparison of cured thiol–ene monomeric and oligomeric resins as indicated and irradiated with 405 nm at 10 mW·cm^{-1} in the first (maize) and second (blue) heating cycles (a) glass transition temperature as indicated by tan δ, and (b) storage modulus at 37 °C.

The PETMP/TATATO formulation when cured under these conditions displays a glass transition temperature of 78.6°C, while this increased to 92.5°C in the second heating ramp, the lowest T_g of the studied thiol–ene materials. During the heating cycle of the DMA, the cured material softens and allows for trapped radicals to further advance monomer conversion. The increased conversion is more representative of the dental clinical practice as the irradiation intensities delivered by light guides of conventional dental lights results in an increased monomer conversion compared to those used in this

study. The hypothesis that the increased crosslinking density obtained from using the lower MW TMES to replace PETMP would increase the glass transition temperature of the resultant polymer is confirmed by DMA. The T_g of the TMES/TATATO polymer was increased in both the first and second heating ramps, with an observed T_g of 108.5°C and 111.3°C respectively. As expected, the inclusion of the norbornyl monomers in the TMES/TATATO formulations through pre-oligomerization resulted in a further increase of the glass transition temperature of the resultant polymer films. TMES-TNTATO/TATATO saw an increase in T_g to 111.1°C in the first heating ramp and 119.2°C in the second heating ramp. The T_g of the DNBPA-containing formulations increased to 114.9°C and 123.8°C in the first and second heating ramps respectively, demonstrating that the inclusion of norbornyl-containing monomers in thiol–ene photopolymers yields an increase in the glass transition temperature as summarized in Figure 2.11 and Table 2.1, reaching T_g values comparable to contemporary methacrylate-based dental resins.

Table 2.1 DMA Summary thiol–ene formulations as indicated and irradiated with 405 nm at 10 mW·cm^{-1} for 10 minutes

Formulation	**Tg (°C), ramp 1**	**E′ at 37°C (GPa), ramp 1**	**Tg (°C), ramp 2**	**E′ at 37°C (GPa), ramp 2**
PETMP/TATATO	78.1 ± 1.6	1.89 ± 0.09	92.5 ± 1.3	1.86 ± 0.07
TMES/TATATO	108.5 ± 0.9	2.03 ± 0.08	111.3 ± 0.7	1.75 ± 0.02
TMES-TNTATO/ TATATO	111.1 ± 1.7	2.12 ± 0.02	119.2 ± 1.6	1.92 ± 0.07
TMES-DNBPA/ TATATO	114.9 ± 0.4	2.29 ± 0.09	123.8 ± 0.8	2.00 ± 0.01

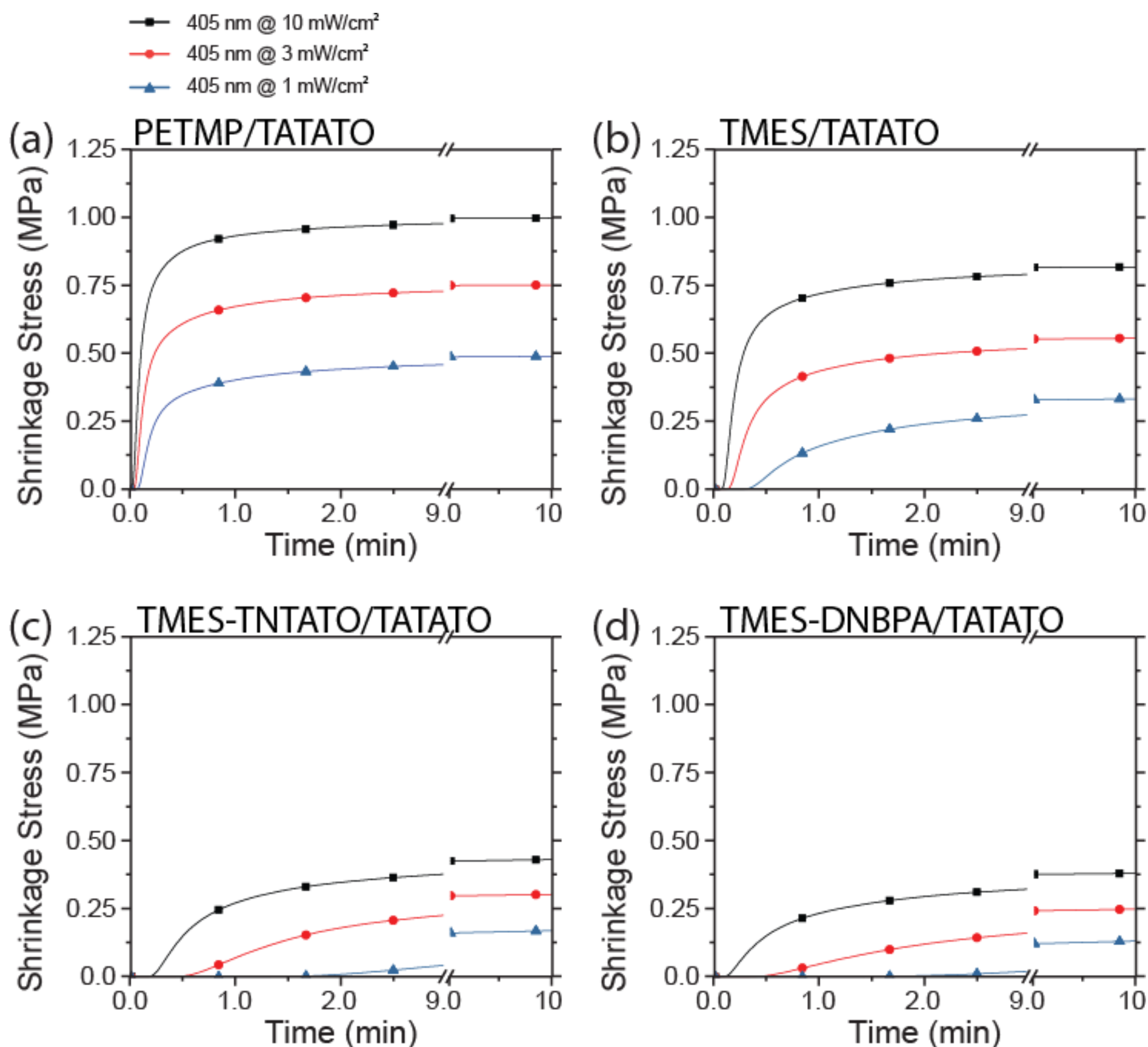

Figure 2.12 Tensometry Polymerization Shrinkage stress versus time for the photocuring of (a) PETMP/TATATO, (b) TMES/TATATO, (c) TMES-TNTATO/TATATO, and (d) TMES-DNBPA/TATATO. Continuous irradiation with 405 nm at intensities of 1 (blue triangles), 3 (red circles), and 10 (black squares) mW·cm^{-2}.

A strong motivation for the development of thiol–ene dental resin lies in their significant reduction in the observed polymerization-induced shrinkage stress relative to methacrylate-based dental resins, owing to both the inherently lower volumetric shrinkage, and the delayed gelation following from the step-growth polymerization mechanism. The PETMP/TATATO formulation displays a five-fold reduction in polymerization-induced shrinkage stress relative to the bisGMA/TEGDMA methacrylate

reference. In this study tensometry experiments to determine polymerization shrinkage stress were carried out at light intensities matching those of the photopolymerization kinetics. As demonstrated in Figure 2.12 the development of polymerization-induced shrinkage stress of the PETMP/TATATO develops rapidly, while in the TMES/TATATO formulation, both the rate of shrinkage stress development as well as final observed shrinkage stress are significantly decreased.

Table 2.2 Shrinkage stress comparison of thiol–ene monomeric and oligomeric resins as indicated and irradiated with 405 at the noted intensity for 10 minutes

Formulation	**Final shrinkage Stress at 1 mW/cm^2 @ 405nm**	**Final shrinkage Stress at 3 mW/cm^2**	**Final shrinkage Stress at 10 mW/cm^2**
PETMP/TATATO	0.49 ± 0.02	0.75 ± 0.01	1.00 ± 0.02
TMES/TATATO	0.34 ± 0.02	0.56 ± 0.05	0.82 ± 0.01
TMES-TNTATO/ TATATO	0.17 ± 0.01	0.30 ± 0.01	0.43 ± 0.04
TMES-DNBPA/ TATATO	0.13 ± 0.01	0.25 ± 0.01	0.38 ± 0.01

Previously reported oligomerization of PETMP/TATATO formulations prior to resin curing leads to a further decrease in the observed polymerization-induced shrinkage stress, as the volumetric shrinkage that occurs as a result of the pre-oligomerization is dissipated through viscous flow in solution. Similarly, it was hypothesized that among other benefits the pre-oligomerization of TMES with TNTATO and DNBPA would result in an overall decrease in the observed polymerization shrinkage stress.

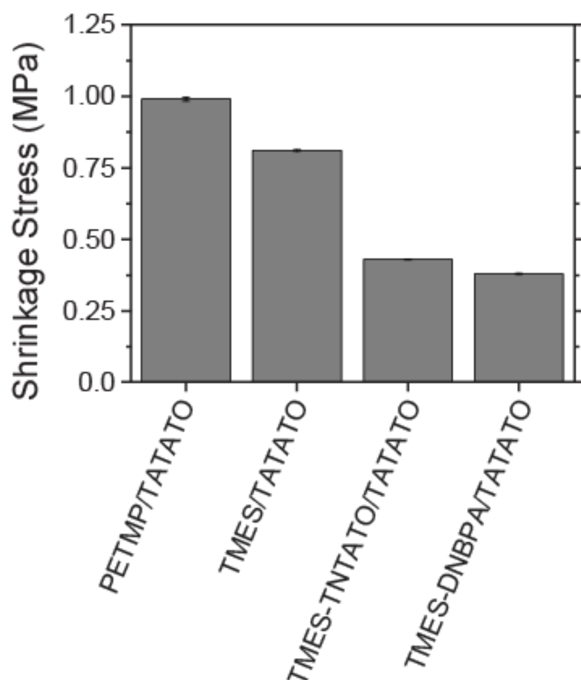

Figure 2.13 Shrinkage stress comparison of thiol–ene monomeric and oligomeric resins as indicated and irradiated with 405 nm at 10 mW·cm^{-1} for 10 minutes.

Photopolymerization of the TMES-TNTATO/TATATO and TMES-DNBPA/TATATO formulations show a significant delay in the development of polymerization shrinkage stress, as well as a slower development of said shrinkage stress. As summarized in Figure 2.13, the final observed polymerization-induced shrinkage stress of the oligomeric resins cured at 10 mW/cm^2 is reduced to half for both oligomeric resins. In accordance with previous literature the development of shrinkage stress, as well as the final observed shrinkage stress is significantly decrease at lowered incident light irradiation intensities, as is summarized in Table 2.2. Importantly, this reduction in observed shrinkage stress is not a result of decreased curing of the resins, as Figure 2.8 demonstrates that the conversion in all formulations reaches a similar level. Through correlation of monomer conversion (Figure 2.8) with shrinkage stress (Figure 2.12) as shown in Figure 2.14, it is demonstrated this observation holds true for all the studied

formulations and irradiation intensities, further indicating the potential for pre-oligomerized thiol–ene formulations for dental restorative resins.

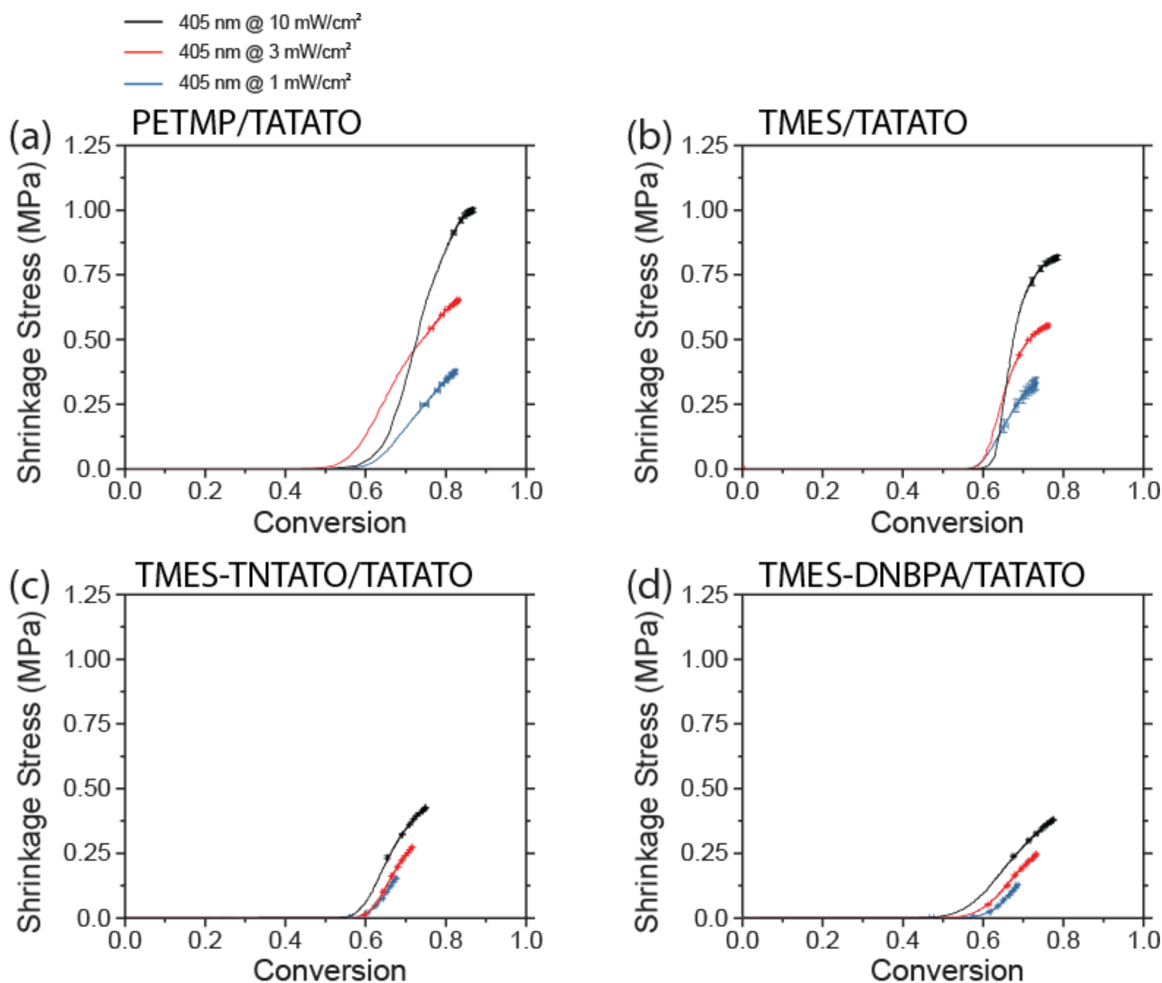

Figure 2.14 Correlation of TATATO double bond conversion with the observed polymerization shrinkage stress of (a) PETMP/TATATO, (b) TMES/TATATO, (c) TMES-TNTATO/TATATO, and (d) TMES-DNBPA/TATATO. Continuous irradiation with 405 nm at intensities of 1 (blue), 3 (red), and 10 (black) mW·cm^{-2}. Data from Figure 2.8 and Figure 2.12.

In all occasions, increasing the light irradiation intensity resulted in earlier onset of polymerization shrinkage stress development, and increased overall polymerization-induced shrinkage stress. The PETMP/TATATO thiol–ene reference showed the highest shrinkage stress values, followed by TMES/TATATO, TMES-TNTATO/TATATO, and with TMES-DNBPA/TATATO showing the lowest shrinkage stress. Polymerization

shrinkage stress data was correlated to photopolymerization kinetics data to provide insight in the conversion-shrinkage stress relationship.

Following the demonstration of rapid photopolymerization of the TMES/TATATO and the oligomeric TMES-derived formulations, these formulations were further examined in glass, and glass & fluoroapetite crystal filled composites and compared for their performance to a similarly filled bisGMA/TEGDMA composite for their cytotoxicity and mechanical properties by collaborators.

When extracted under the DMEM culture media conditions, at the highest leachable concentrations (10x dilution) and the more diluted concentrations (100x and 1000x dilutions), all three filled resins, i.e. TMES-TNTATO/TATATO, TMES-DNBPA/TATATO and bisGMA/TEGDMA, filled with glass, with and without FA crystals, did not show toxic effects compared to the cell only controls.

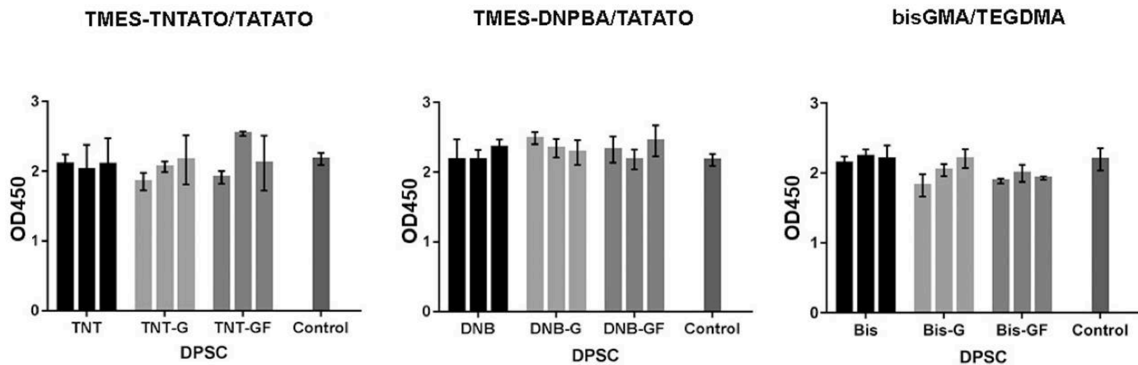

Figure 2.15 Cell viability testing

Composites made from the new resins, TMES-DNBPA/TATATO and TMES-TNTATO/TATATO exhibited a trend toward greater total toughness than composites made from bisGMA/TEGDMA. The increase in toughness did not come at the expense of

strength or stiffness, as is typical, as these properties were not significantly different from those of bisGMA/TEGDMA based composites, and trended towards higher values. Introduction of FA reduced the strength but not the modulus, compared to the same composite filled with glass only. This is expected, given the non-silated nature of the FA/resin coupling and resultant inferior bonding of FA to the matrix compared, and the greater dependence of strength on the resin/filler bond. However, the magnitude of these properties exceeds that of bisGMA/TEGDMA composites containing FA fillers.

Table 2.3 Mechanical testing results of composite formulations

Composite	**Flexural Modulus (GPa)**	**Flexural Strength (MPa)**	**Yield Strength (MPa)**	**Post-Yield Toughness (MPa)**	**Total Toughness (MPa)**
Bis-GMA 50% glass	5.94 ± 1.35	73.34 ± 16.13	73.34 ± 16.13	0.00 ± 0.00	0.53 ± 0.26
Bis-GMA 50% glass + FA	4.22 ± 1.08	51.21 ± 12.87	51.21 ±12.87	0.00 ± 0.00	0.37 ± 0.22
TMES-DNBPA 50% Glass	3.56 ± 0.85	68.60 ± 16.75	68.60 ± 16.75	0.00 ± 0.00	0.73 ± 0.28
TMES-DNBPA 50% Glass+FA	3.44 ± 0.16	59.22 ± 2.71	59.22 ± 2.71	0.00 ± 0.00	0.58 ± 0.09
TMES-TNTATO 50% Glass	3.24 ± 0.61	67.11 ± 15.14	67.11 ± 15.14	0.00 ± 0.00	0.81 ± 0.33
TMES-TNTATO 50% Glass+FA	3.26 ± 0.56	46.17 ± 7.17	46.17 ± 7.17	0.00 ± 0.00	0.36 ± 0.09

2.6 Conclusion

In this work, we compared the PETMP/TATATO model thiol–ene resin to the ester-free silane-based alternative TMES, and 2 different TMES-derived norbornyl-containing oligomers of TNTATO, and DNBPA for the formulation of dental restorative resins. The resultant resins cure rapidly under moderate intensity visible light irradiation, resulting in highly cross-linked materials. These cross-linked materials all show an improved T_g in both the first and second heating ramp of the dynamic mechanical testing,

increasing the T_g up to 36°C relative to PETMP/TATATO. Furthermore, the polymerization-induced shrinkage stress was reduced by employing TMES to replace PETMP, and pre-oligomerization of TMES with either TNTATO or DNBPA slowed down the shrinkage stress development, and significantly lowered the final observed shrinkage stress. Furthermore, oligomeric resins filled with glass and glass + fluoroapetite behave similarly to the methacrylate control in terms of cytotoxicity, flexural modulus and toughness. Through a combination of silane-based based monomers, and pre-oligomerization, we have developed novel ester-free norbornyl-containing thiol–ene resins with improved glass transition temperatures, significantly reduced shrinkage stresses, while still curing rapidly and to high conversions.

2.7 Acknowledgements

The author thanks Harrison Cheng, Jun Liu, and professor Brian Clarkson at the University of Michigan School of Dentistry for preparing the composite filled materials, biological and mechanical evaluation thereof, and interpretation of the results.

2.8 References

1. Sadowsky, S. J., An overview of treatment considerations for esthetic restorations: A review of the literature. *Journal of Prosthetic Dentistry* **2006,** *96* (6), 433-442.

2. Peutzfeldt, A., Resin composites in dentistry: The monomer systems. *Eur. Journal of Oral Sciences* **1997,** *105* (2), 97-116.

3. Ferracane, J. L., Resin composite-State of the art. *Dental Materials* **2011,** *27* (1), 29-38.

4. Lu, H.; Carioscia, J. A.; Stansbury, J. W.; Bowman, C. N., Investigations of step-growth thiol–ene polymerizations for novel dental restoratives. *Dental Materials* **2005,** *21* (12), 1129-1136.

5. Kleverlaan, C. J.; Feilzer, A. J., Polymerization shrinkage and contraction stress of dental resin composites. *Dental Materials* **2005,** *21* (12), 1150-1157.

6. Alomari, Q. D.; Reinhardt, J. W.; Boyer, D. B., Effect of Liners on Cusp Deflection and Gap Formation in Composite Restorations. *Operational Dentistry* **2001,** *26* (1), 406-411.

7. Kanca, J.; Suh, B. I., Pulse activation: Reducing resin-based composite contraction stresses at the enamel cavosurface margins. *American Journal of Dentistry* **1999,** *12* (3), 107-112.

8. Hannig, M.; Friedrichs, C., Comparative In Vivo and In Vitro Investigation of Interfacial Bond Variability. *Operational Dentistry* **2001,** *26* (1), 3-11.

9. Gauthier, M. A.; Stangel, I.; Ellis, T. H.; Zhu, X. X., Oxygen inhibition in dental resins. *Journal of Dental Research* **2005,** *84* (8), 725-729.

10. Shawkat, E. S.; Shortall, A. C.; Addison, O.; Palin, W. M., Oxygen inhibition and incremental layer bond strengths of resin composites. *Dental Materials* **2009,** *25* (11), 1338-1346.

11. Spahl, W.; Budzikiewicz, H.; Geurtsen, W., Determination of leachable components from four commercial dental composites by gas and liquid chromatography mass spectrometry. *Journal of Dentistry* **1998,** *26* (2), 137-145.

12. Munksgaard, E. C.; Freund, M., Enzymatic hydrolysis of (di)methacrylates and their polymers. *Scandinavian Journal of Dental Research* **1990,** *98* (3), 261-267.

13. Scott, T. F.; Furgal, J. C.; Kloxin, C. J., Expanding the Alternating Propagation-Chain Transfer-Based Polymerization Toolkit: The Iodo–ene Reaction. *ACS Macro Letters* **2015,** *4* (12), 1404-1409.

14. Fairbanks, B. D.; Scott, T. F.; Kloxin, C. J.; Anseth, K. S.; Bowman, C. N., Thiol-Yne Photopolymerizations: Novel Mechanism, Kinetics, and Step-Growth Formation of Highly Cross-Linked Networks. *Macromolecules* **2009,** *42* (1), 211-217.

15. Adzima, B. J.; Tao, Y. H.; Kloxin, C. J.; DeForest, C. A.; Anseth, K. S.; Bowman, C. N., Spatial and temporal control of the alkyne-azide cycloaddition by photoinitiated Cu(II) reduction. *Nature Chemistry* **2011,** *3* (3), 256-259.

16. Gong, T.; Adzima, B. J.; Baker, N. H.; Bowman, C. N., Photopolymerization Reactions Using the Photoinitiated Copper (I)-Catalyzed Azide-Alkyne Cycloaddition (CuAAC) Reaction. *Advanced Materials* **2013,** *25* (14), 2024-2028.

17. Ahn, D. W.; Sathe, S. S.; Clarkson, B. H.; Scott, T. F., Hexaarylbiimidazoles as Visible Light Thiol–Ene Photoinitiators. *Dental Materials* **2015**.

18. Hoyle, C. E.; Lowe, A. B.; Bowman, C. N., Thiol-click chemistry: a multifaceted toolbox for small molecule and polymer synthesis. *Chemical Society Reviews* **2010,** *39* (4), 1355-1387.

19. O'Brien, A. K.; Cramer, N. B.; Bowman, C. N., Oxygen inhibition in thiol-acrylate photopolymerizations. *Journal of Polymer Science Part A: Polymer Chemistry* **2006,** *44* (6), 2007-2014.

20. Cramer, N. B.; Couch, C. L.; Schreck, K. M.; Carioscia, J. A.; Boulden, J. E.; Stansbury, J. W.; Bowman, C. N., Investigation of thiol–ene and thiol–ene-methacrylate based resins as dental restorative materials. *Dental Materials* **2010,** *26* (1), 21-28.

21. Carioscia, J. A.; Stansbury, J. W.; Bowman, C. N., Evaluation and control of thiol–ene/thiol-epoxy hybrid networks. *Polymer* **2007,** *48* (6), 1526-1532.

22. Carioscia, J. A.; Schneidewind, L.; O'Brien, C.; Ely, R.; Feeser, C.; Cramer, N.; Bowman, C. N., Thiol-norbornene materials: Approaches to develop high T-g thiol–ene polymers. *Journal of Polymer Science Part A: Polymer Chemistry* **2007,** *45* (23), 5686-5696.

23. Beigi, S.; Yeganeh, H.; Atai, M., Evaluation of fracture toughness and mechanical properties of ternary thiol–ene-methacrylate systems as resin matrix for dental restorative composites. *Dental Materials* **2013,** *29* (7), 777-787.

24. Ye, S.; Cramer, N. B.; Smith, I. R.; Voigt, K. R.; Bowman, C. N., Reaction Kinetics and Reduced Shrinkage Stress of Thiol-Yne-Methacrylate and Thiol-Yne-Acrylate Ternary Systems. *Macromolecules* **2011,** *44* (23), 9084-9090.

25. Park, H. Y.; Kloxin, C. J.; Scott, T. F.; Bowman, C. N., Covalent adaptable networks as dental restorative resins: Stress relaxation by

additionfragmentation chain transfer in allyl sulfide-containing resins. *Dental Materials* **2010,** *26* (10), 1010-1016.

26. Wei, H. Y.; Senyurt, A. F.; Jonsson, S.; Hoyle, C. E., Photopolymerization of ternary thiol–ene/acrylate systems: Film and network properties. *Journal of Polymer Science Part A: Polymer Chemistry* **2007,** *45* (5), 822-829.

27. Senyurt, A. F.; Wei, H. Y.; Hoyle, C. E.; Piland, S. G.; Gould, T. E., Ternary thiol–ene/acrylate photopolymers: Effect of acrylate structure on mechanical properties. *Macromolecules* **2007,** *40* (14), 4901-4909.

28. Lee, T. Y.; Carioscia, J.; Smith, Z.; Bowman, C. N., Thiol-allyl ether-methacrylate ternary systems. Evolution mechanism of polymerization-induced shrinkage stress and mechanical properties. *Macromolecules* **2007,** *40* (5), 1473-1479.

29. Cramer, N. B.; Couch, C. L.; Schreck, K. M.; Boulden, J. E.; Wydra, R.; Stansbury, J. W.; Bowman, C. N., Properties of methacrylate-thiol–ene formulations as dental restorative materials. *Dental Materials* **2010,** *26* (8), 799-806.

30. Boulden, J. E.; Cramer, N. B.; Schreck, K. M.; Couch, C. L.; Bracho-Troconis, C.; Stansbury, J. W.; Bowman, C. N., Thiol–ene-methacrylate composites as dental restorative materials. *Dent. Mater.* **2011,** *27* (3), 267-272.

31. Senyurt, A. F.; Wei, H.; Phillips, B.; Cole, M.; Nazarenko, S.; Hoyle, C. E.; Piland, S. G.; Gould, T. E., Physical and mechanical properties of photopolymerized thiol–ene/acrylates. *Macromolecules* **2006,** *39* (19), 6315-6317.

32. Podgórski, M.; Becka, E.; Chatani, S.; Claudino, M.; Bowman, C. N., Ester-free thiol-X resins: new materials with enhanced mechanical behavior and solvent resistance. *Polymer Chemistry* **2015,** *6* (12), 2234-2240.

Chapter 3

Further Development of Thiol–ene Dental Resins Through Addition-Fragmentation Chain-Transfer Chemistry and Adhesive Monomers

3.1 Abstract

Methacrylate-based dental composite resins have long suffered from high polymerization-induced shrinkage stress, and poor adhesion to mineralized tissues. Consequently, novel chemistries have been developed for these materials to improve on these aspects. With the recent development of high glass transition, low shrinkage stress thiol–ene polymers for dental restorative purposes the need arises for further development of these materials to be competitive with methacrylate composites. Here, we examine allyl sulfide addition-fragmentation chain-transfer chemistry as a means of reducing polymerization-induced shrinkage stress in glassy thiol–ene polymers and determine the impact of this chemistry on reaction kinetics and thermomechanical properties. To improve adhesion of the thiol–ene resins to mineralized tissue, acid-containing allyl monomers were prepared and evaluated for their effect on the thiol–ene photopolymerization and glass transition temperature. Further reduction of shrinkage stress in glassy thiol–ene materials was achieved, and carboxylic acid-containing monomers demonstrate good compatibility with thiol–ene photopolymerizations.

3.2 Introduction

3.2.1 Addition-fragmentation chain-transfer chemistry in thiol–ene systems

Rapid photopolymerization reactions of vinyl monomers through free radical chain-growth polymerizations is frequently observed with a significant decrease in volume. In the case of methacrylate-based dental restorative materials the development of shrinkage stress as a result of this can lead to various deleterious effects such as marginal gap formation[1], tooth cracking,[2] and post-operative sensitivity. Among the approaches to reduce polymerization-induced shrinkage stress in dental formulations, thiol–ene chemistry has emerged as a potential candidate to this end.[3] Through a combination of inherently lower shrinkage and delayed gelation, thiol–ene polymers show very favorable attributes. While historically limited by their low glass transition temperatures, the previous chapter discusses the successful development of low shrinkage stress, high T_g thiol–ene polymers. While the obtained results are promising, additional avenues towards improving on these materials are available.

A well-established approach towards reduction of polymerization-induced shrinkage stress lies in stress relaxation of the crosslinked polymeric network.[4] This can be achieved through free-radical mediated rearrangement *via* addition-fragmentation chain-transfer (AFCT) reactions. AFCT agents containing β-quaternary carbon centers[5] and β-allyl sulfones[6] allow for single-use stress relaxation, as these necessitate a nearby double bond for successful AFCT. Allyl sulfide AFCT agents in contrast demonstrate the ability to undergo addition and fragmentation multiple times without loss of active radicals or allyl sulfide as demonstrated in Scheme 3.1. In addition, the allyl disulfide network rearrangement mechanism provied a means of stress relaxation without change

in thermomechanical properties, as the crosslinking density of the material is preserved.[4, 7] The allyl disulfide AFCT approach is particularly well-suited for stress relaxation in thiol–ene-based crosslinked polymers. As Scheme 3.2 shows, the thiyl radicals involved in the thiol–ene polymerization are interchangable with AFCT-derived thiyl radicals in the network rearrangement.[8, 9] Thus, the thiyl radical acts as a central intermediate in the thiol–ene/AFCT cascade reactions.

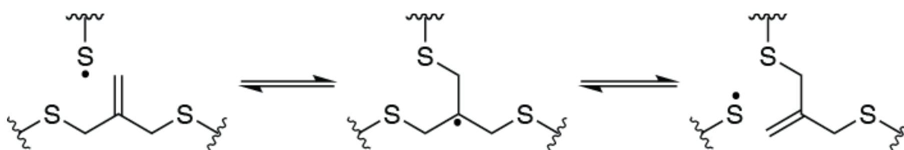

Scheme 3.1 Addition-fragmentation chain-transfer mechanism demonstrating network rearrangement through thiyl radical addition to an allyl disulfide and subsequent fragmentation

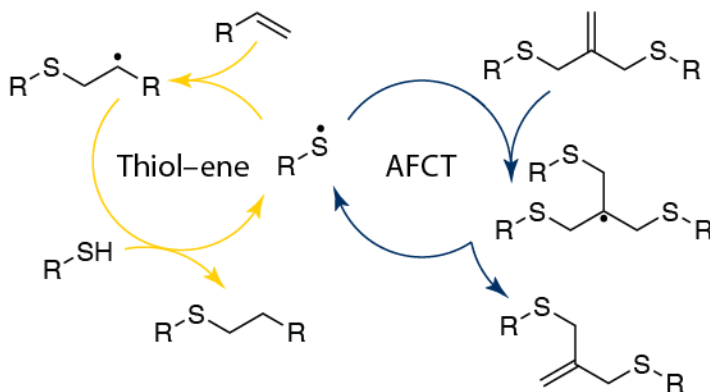

Scheme 3.2 The thiol–ene/AFCT cascade reaction mechanism in which the central thiyl radical takes part in either the thiol–ene polymerization (left, maize cycle), or addition-fragmentation chain-transfer through an allyl disulfide (right, blue cycle).

Owing to their ubiquitous use in contemporary dental restorations, methacrylate have been the main focus of AFCT chemistries for shrinkage stress reduction. Allyl sulfides as AFCT agents in dimethacrylate formulations have lead to significant reduction in observed polymerization shrinkage stress.[10, 11] However, as the AFCT is irreversible methacrylate-only resins, greater shrinkage stress reduction was observed in dual thiol-

methacrylate formulations,[12] as a result of both the increased step-growth polymerization character of the curing, as well as decreased consumption of the allyl sulfides. Despite these successes, the inherently high shrinkage stress of dimethacrylates resins is limiting to reducing the total shrinkage stress. Thiol–ene polymerizations on the other hand display a signifcantly lower shrinkage stress, a combination of delayed gelation and inherently lower shrinkage per monomer consumed.[3, 13] A significant deterrent to the use of thiol–ene formulations in dental resins lies in the generally lower T_g[3] of the polymeric materials. Especially the subpar T_gs exhibited by previously described thiol–ene/AFCT formulations rendered them ill-suited as dental restoratives.[8] However, the silane-based oligomers described in the previous chapter provide high T_g thiol ene-based materials. Additionally, while other AFCT chemistries are limited in their use, thiol–ene polymerizations in conjuction with allyl sulfide AFCT is not limited by this as the allyl sulfide is regenerated following AFCT. Here, we examine the impact of incorporating allyl sulfide AFCT agents on the previously developed silane-based oligomeric resins. The effects on polymerization shrinkage stress profiles, thiol–ene photopolymerization kinetics, and thermomechical properties are studied. Propyl sulfide bearing additives unable to undergo AFCT were studied in tandem as a control.

3.2.2 Acidic monomers to improve adhesion to mineralized tissues

Excellent adhesion of the dental formulations to the tooth is essential for the longevity of the restoration. For methacrylate-based dental composites typically following preparation of the cavity, the exposed enamel and dentin is subjected to a phosphoric acid-based etchant. Subsequently the etchant is rinsed away, and an adhesive resin, typically consisting of solvent, hydroxyethylmethacrylate (HEMA) and

dimethacrylates is applied,[14-16] after which the actual restorative composite is placed. The phosphoric acid-based etchant serves to remove the smear layer, increase enamel surface area, and demineralize the dentin leaving behind a collagen matrix.[17, 18] The adhesive resin then infiltrates the prepared tissue, penetrating into the collagen matrix, dental tubules in dentin,[19] and the rough enamel surface. Adhesion is achieved through a combination of chemical bonding between the tissue and adhesive, and mechanical interlocking of the crosslinked polymers with the enamel surface and collagen matrix. While this “etch-and-rinse” or “total etch” approach has been a staple in promoting restoration adhesion, the results are highly technique dependent. Poorly application of the etchant can result in various deleterious effects including significant post-operative sensitivity[20-22] and incomplete penetration of the adhesive into the tissue.[23, 24] Additionally the influence of the smear layer on adhesion is highly debated and it might have a positive impact on restoration longevity.

With the demand for a less technique sensitive approach, self-etch adhesives were developed. In contrast to the total etch approach; no strong etchant is applied following cavity preparation. Instead, the adhesive resin contains acid curable monomers. These monomers contain a polymerizable moiety and an active acidic group,[15] typically a carboxylic acid,[25] phosphoric acid,[14] or phosphonate acid.[26, 27] These acidic moieties serve to demineralize the tooth tissue, and promote adhesion to the hydroxyapatite and collagen in the tissue through either covalent or ionic bonding. In the reduced concentration in the resin the acids are typically significantly weaker than the phosphoric acid etchant, and as a result demineralization of dentin is significantly limited, resulting in a decreased hybrid adhesive/tissue layer. As the etching characteristics of the adhesive

are intrinsic to the formulation, more consistent results can be achieved independent of the practitioner.

Notwithstanding the success of self-etch adhesives, the monomers display several disadvantageous properties. The most significant consequence of the monomer design is a decrease in the adhesive lifetime, both in bottle and in restoration.[25, 28, 29] The general concern of methacrylate hydrolysis is amplified by these monomers. As ester hydrolysis is catalyzed at low and high pH, the inherent presence of acidic moieties leads to auto-catalyzed hydrolysis. This is further amplified by the common use of water as a solvent in adhesive resins. In the case of phosphate ester monomers, additional hydrolysis is possible at the phosphate ester bonds.[30]

Efforts to improve hydrolytic resistance of acid-containing monomers commonly focus on either the monomer hydrophobicity or replacement of methacrylates by more resistant moieties. Exchanging the methacrylate ester group for methacrylamides,[31] ether linkages,[26] or acrylonitriles[32] significantly improves hydrolytic resistance, and have been successfully demonstrated with multiple acidic moieties. Increasing steric hindrance near the methacrylate or incorporation of a more hydrophobic spacer similarly leads to improvements in hydrolytic resistance.[33, 34] Nevertheless, this latter approach fails to address the inherent issue of methacrylate susceptibility to hydrolysis,[25, 35] as even the decylene spacer in the phosphate ester-bearing methacryloyldecylphosphate does not completely prevent methacrylate hydrolysis.[25] While hydrolytic resistance is an important aspect of these self-etch monomers, some excellently stable monomers are nevertheless ill-suited for applications in dental adhesive resins as they suffer from slow polymerization rates, poor tissue wettability and weak adhesion to the tooth tissue.[36, 37]

Design of self-etch monomers can improve the stability of these particular compounds, this approach fails to take into account their impact on the resin as a whole. A significant portion of the self-etch adhesive is commonly made up of HEMA and dimethacrylates. Whilst monomer design increases the self-etch adhesive, the methacrylates used in contemporary adhesive formulations remain ever susceptible to the acid-catalyzed hydrolysis. In contrast, the silane-based oligomeric thiol–ene resins described previously are devoid of hydrolysis-susceptible ester moieties, and the silane thiol core has been demonstrated to form hydrolysis-resistant thiol–ene polymers.[38] Combination of thiol–ene chemistry with methacrylate-free thiol–ene compatible acidic monomers would potentially allow for combining the advantages of low shrinkage stress thiol–ene polymers with the benefits of improved adhesion from self-etch. In here, the synthetic approach to carboxylate-, phosphate-, phosphonate-, and trimellitic anhydride-containing monomers is described. The characterization of the successfully prepared monomers, and photopolymerization behavior of these methacrylate-free thiol–ene compatible acidic monomers to improve adhesion to mineralized tissue is described. The cured materials are further examined for the impact of the acidic monomers on the thermomechanical properties of the thiol–ene polymers. To the best of our knowledge, acidic, adhesion-promoting self-etch monomers have not been previously described for thiol–ene polymers.

3.3 Experimental

3.3.1 Materials

Tetra(2-mercaptoethyl)silane (TMES) and 1,3,5,-trinorbornyl-1,3,5-triazine-2,4,6(1H,3H,5H)-trione (TNTATO) were prepared as described in the previous chapter.

Dicyclopentadiene, allyl bromide, Potassium ethyl xanthogenate, ethylene diamine, sodium, trimethylolpropane diallyl ether, pentaerythrithol allyl ether (technical grade 70%), phosphorous (V) oxychloride were obtained from Sigma-Aldrich (St. Louis, MO). 2-methylpropan-1,3-diol was obtained from TCI America (Portland, OR). Sodium Bromide, potassium *tert*-butoxide, bromoacetic acid, triethyl amine, absolute ethanol, methanol, sulfuric acid, and *tert*-butanol were obtained from Fisher Scientific (Hampton, NH). 1,3-dichloro-2-methylenepropane was obtained from AK Scientific (Union City, CA)

3.3.2 Methods

3.3.2.1 Light Sources and intensity measurement

Violet light was provided by a collimated, LED-based illumination source (Thorlabs M405L2-C) with an emittance centered at 405 nm (FWHM 13 nm), used in combination with a current-adjustable LED driver (Thorlabs LEDD1B) for intensity control. Irradiation intensities were measured with an International Light IL1400A radiometer equipped with a broadband silicon detector (model SEL033), a 10× attenuation neutral density filter (model QNDS1), and a quartz diffuser (model W).

3.3.2.2 FTIR Spectroscopy

Photopolymerization reaction kinetics were examined using a Thermo Scientific Nicolet 6700 FT-IR spectrometer equipped with a horizontal transmission accessory, as described elsewhere, recording spectra from 2000 cm^{-1} to 7000 cm^{-1} at a rate of approximately 2 every second. Resins were mixed in 1:1 thiol:ene stoichiometric ratios, formulated with 1 wt% Irgacure TPO, and introduced between two glass microscope slides separated by 50 μm thick spacers. The functional group conversions upon

irradiation were determined by monitoring the disappearance of the peak area centered at 2571 cm^{-1} corresponding to the thiol group stretch and 3083 cm^{-1} corresponding to the allylic vinyl group stretch. All experiments were conducted in triplicate, and the irradiation intensities were as indicated in the figure captions.

3.3.2.3 Dynamic Mechanical Analysis

Cross-linked polymer films were prepared from thiol–ene formulations containing 1 wt% Irgacure TPO which were polymerized between glass microscope slides separated by 250 μm thick spacers for 30 minutes at room temperature under 405 nm irradiation at 10 $mW{\cdot}cm^{-2}$. Samples of approximately 15 mm × 5 mm × 0.25 mm were cut from the cured films and mounted in a TA Instruments Q800 dynamic mechanical analyzer equipped with a film tension clamp. Experiments were performed at a strain and frequency of 0.1% and 1 Hz, respectively, scanning the temperature from −25°C to 200°C twice at $2°C{\cdot}min^{-1}$, and the storage modulus (E′) and tan δ curves were recorded. All experiments were conducted in triplicate. The repeated temperature scan was used to determine the influence of dark polymerization at temperatures greater than the glass transition temperature (T_g). The T_g was assigned as the temperature at the tan δ curve peak.

3.3.2.4 Polymerization Shrinkage Stress

Polymerization-induced shrinkage stress was determined using a tensometer. Resins formulated in 1:1 thiol:ene stoichiometric ratios, containing 1 wt% Irgacure TPO as the photoinitiator were introduced between 2 polished quartz rods (6mm diameter) spaced 1 mm apart. The samples were irradiated from below through the quartz rod and the polymerization-induced shrinkage stress was monitored through cantilever deflection

and recorded at a rate of 10 per second. All experiments were conducted in triplicate, and the irradiation intensities were as indicated in the figure captions.

3.3.3 Synthesis

3.3.3.1 Norbornyl bromide

Dicyclopentadiene (4.73 g), allyl bromide (10.73 g), and Q-1301 (16 mg) were added to a 50 mL glass bomb flask. The flask was sealed and heated to 170°C for 20 hours. The flask was allowed to cool to room temperature, and the excess allyl bromide was removed by heating the opened flask to 100°C for several hours. The resultant material was distilled under reduced pressure (40°C, 300 mTorr) to yield the desired material in a mixture of *endo* and *exo* isomers (85:15) as a colorless oil. ^{1}H NMR (400 MHz, $CDCl_3$) δ 6.21 (d, 1H), 6.00 (d, 1H), 3.22 (t, 1H), 3.05 (t, 1H), 3.00 (m, 1H), 2.88 (s, 1H), 2.52 (bm, 1H), 1.95 (m, 1H), 1.49 (m, 1H), 1.32 (m, 1H), 0.61 (d, 1H)

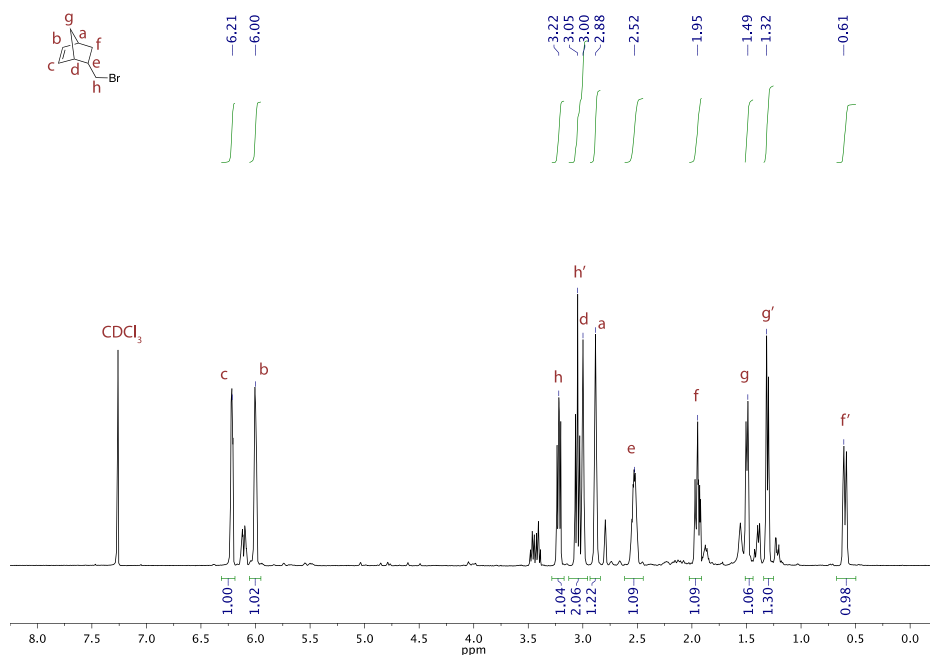

Figure 3.1 ^{1}H-NMR Spectrum of endo-Norbornyl bromide (major isomer)

3.3.3.2 2-methylenepropane-1,3-di(ethylxanthogenate)

Potassium ethyl xanthogenate (27 g) was added to absolute ethanol (300 mL) in a 500 mL 2-neck round-bottom flask equipped with an addition funnel. 1,3-dichloro-2-methylenepropane (10 g) was dissolved in ethanol (10 mL) added dropwise, and the solution was stirred at room temperature overnight. The solvent was removed under reduced pressure and water (200 mL) was added. The mixture was extracted 3 times with ethyl ether (100 mL), and the combined organic phases were washed with brine (100 mL). The organic phase was dried over magnesium sulfate and the solvent removed under reduced pressure. The obtained material was used without further purification ^{1}H NMR (400 MHz, $CDCl_3$) δ 5.26 (s, 2H), 4.64 (qt, 4H), 3.91 (s, 4H), 1.43 (t, 6H)

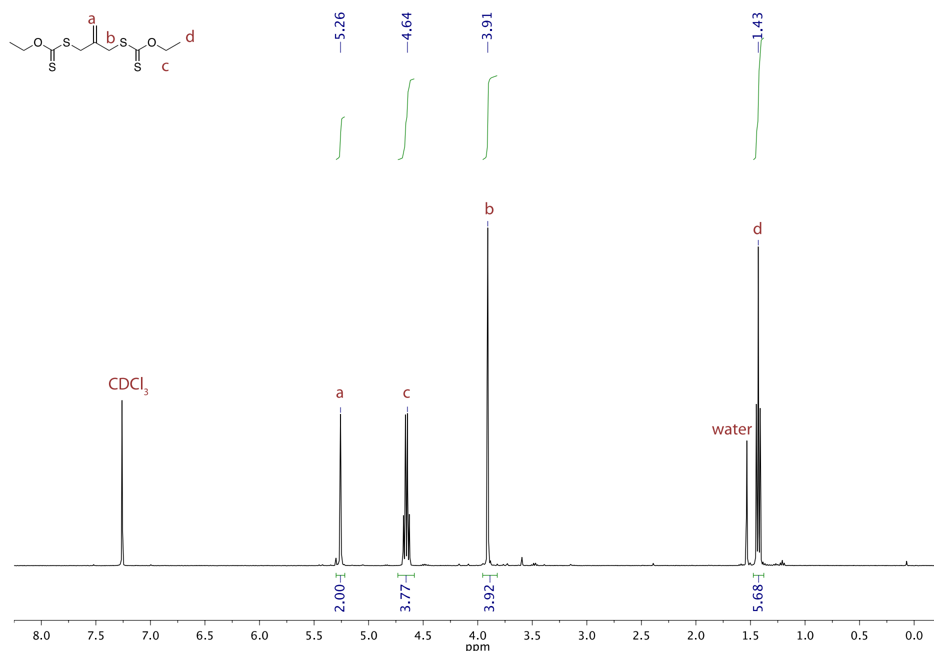

Figure 3.2 ^{1}H-NMR of 2-methylenepropane-1,3-di(ethylxanthogenate)

3.3.3.3 2-methylenepropane-1,3-dithiol

2-methylenepropane-1,3-di(ethylxanthogenate) (20 g) was added dropwise to ethylene diamine (40 mL) cooled on ice. The mixture was stirred on ice for 2 hours after which it was very carefully added to a mixture of sulfuric acid (100 mL) and ice (500 g) and stirred for 30 minutes. The mixture was extracted 3 times with ethyl ether (125 mL) and the combined organic phases were washed with 2M aqueous sulfuric acid (250 mL) and brine (250 mL). The solution was dried over magnesium sulfate, filtered, and the solvent removed under reduced pressure. The obtained material was distilled under reduced pressure (41°C, 0.4 Tor) to obtain the desired product as a malodorous colorless oil. ^{1}H NMR (400 MHz, $CDCl_3$) δ 4.99 (s, 1H), 1.32 (m, 1H), 0.61 (d, 1H)

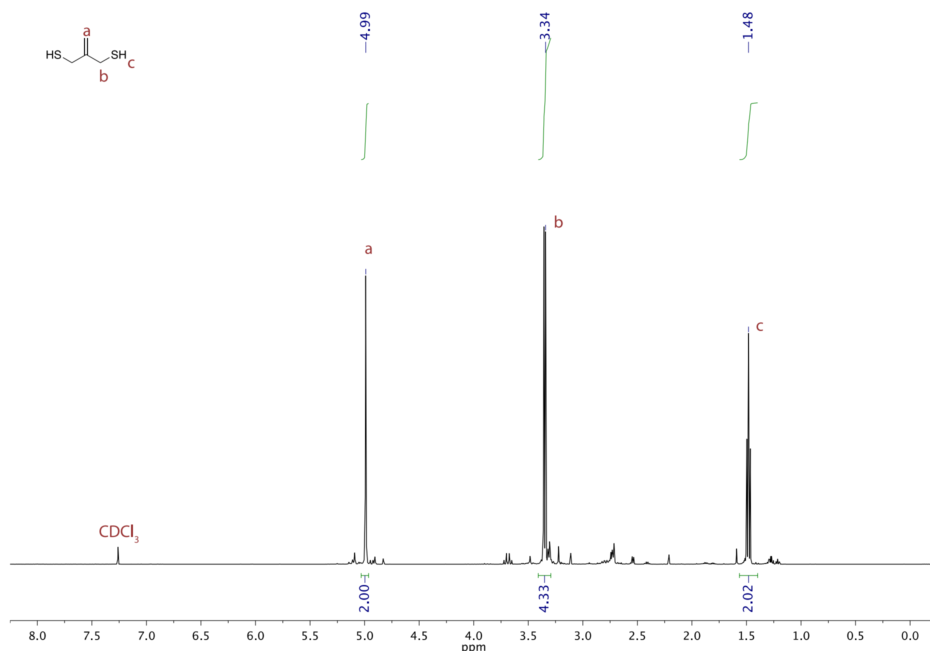

Figure 3.3 ^{1}H-NMR Spectrum of 2-methylenepropane-1,3-dithiol

3.3.3.4 2-Methylenepropane-1,3-di(norbornene sulfide) (NAS)

To a 250 mL 3-neck round bottom flask equipped with a reflux condenser and an addition funnel was added to 80 mL anhydrous methanol in an argon atmosphere elemental sodium (1.34g). The solution was heated to 75°C for 1 hour. Then, a mixture of norbornyl bromide (5.10g) and 2-methylenepropane-1,3-dithiol (2.76g) in a minimal amount of anhydrous methanol was added dropwise, and the solution was left to stir overnight. The next morning, the solution was allowed to cool to room temperature, and the solvent was removed under reduced pressure. Water was added to the residue, and the mixture was extracted 4 times with ethyl ether (80 mL). The combined organic phases were washed with brine, dried over magnesium sulfate and the solvent removed under reduced pressure. The resultant material was distilled under reduced pressure (210°C, 0.2 Torr) to obtain the desired material as a waxy solid.

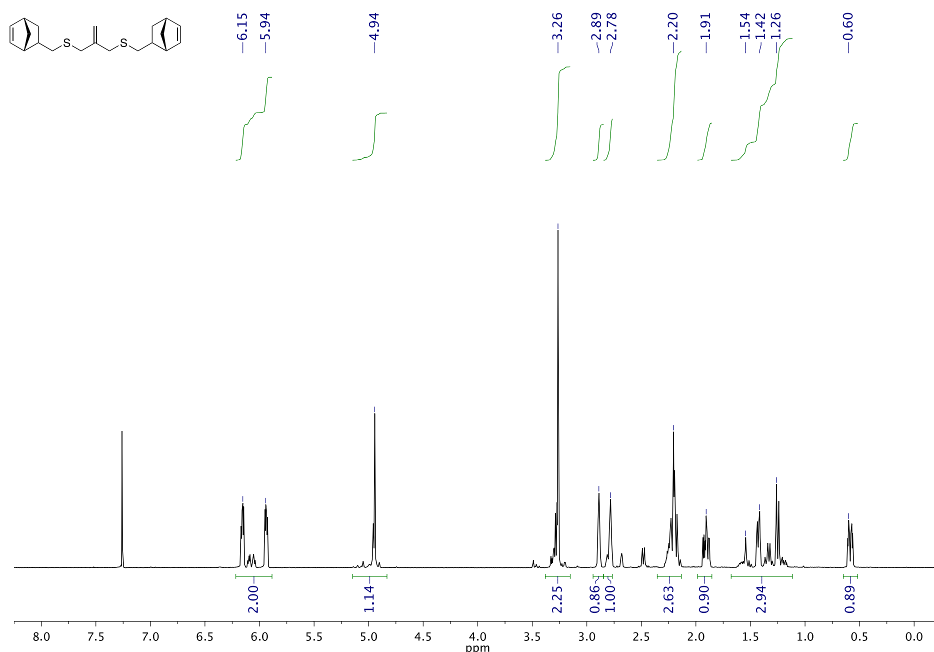

Figure 3.4 ***^{1}H-NMR Spectrum of NAS***

3.3.3.5 1,3-dibromo-2-methylpropane

Sodium bromide (215g and 2-methylpropan-1,3-diol (74 mL) were dissolved in deionized water (74 mL) in a 500 mL round-bottom flask equipped with a reflux condenser. Sulfuric acid (190 mL) was added dropwise, and the solution was heated to 140°C, and stirred for 2 hours. The solution was allowed to cool to room temperature, and was extracted 3 times with methylene chloride (100 mL). The combined organic phases were washed with 1M aqueous sodium carbonate solution (100 mL) and brine (100 mL). The solution was dried over magnesium sulfate and the solvent was removed under reduced pressure. The resultant material was distilled under reduced pressure (105°C, 10 Torr) to yield the desired product as a colorless liquid. ^{1}H NMR (400 MHz, $CDCl_3$) δ 3.51 (m, 4H), 2.18 (m, 1H), 1.15 (d, 3H)

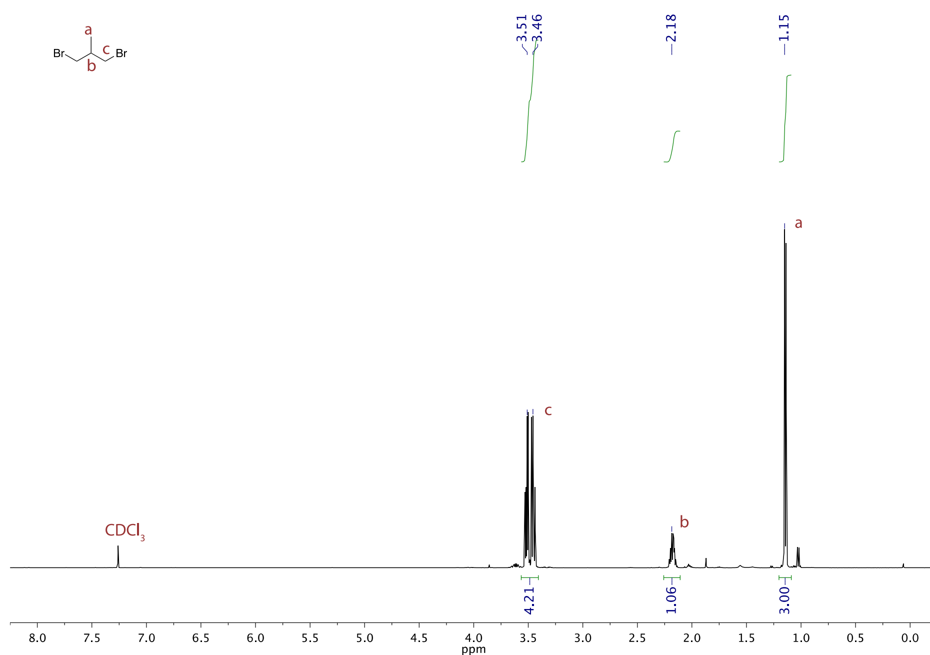

Figure 3.5 ^{1}H-NMR Spectrum of 1,3-dibromo-2-methylpropane

3.3.3.6 2-methylpropane-1,3-di(ethylxanthogenate)

Potassium ethyl xanthogenate (150g) was added to absolute ethanol (250 mL) in a 500 mL 2-neck round-bottom flask equipped with an addition funnel. The 1,3-dibromo-2-methylpropane obtained from the previous step was added dropwise, and the solution was stirred at room temperature for 2 days. Water (200 mL) was added to the solution, and the mixture was extracted 3 times with ethyl ether (100 mL). The organic phases were combined and dried over magnesium sulfate and the solvent removed under reduced pressure. The obtained material was purified using silica column chromatography (hexanes:ethyl acetate = 8:2) to obtain the desired product as a… ^{1}H NMR (400 MHz, $CDCl_3$) δ 4.66 (q, 4H), 3.00-3.30 (ddd, 4H), 2.26 (m, 1H), 1.42 (t, 6H), 1.13 (d, 3H)

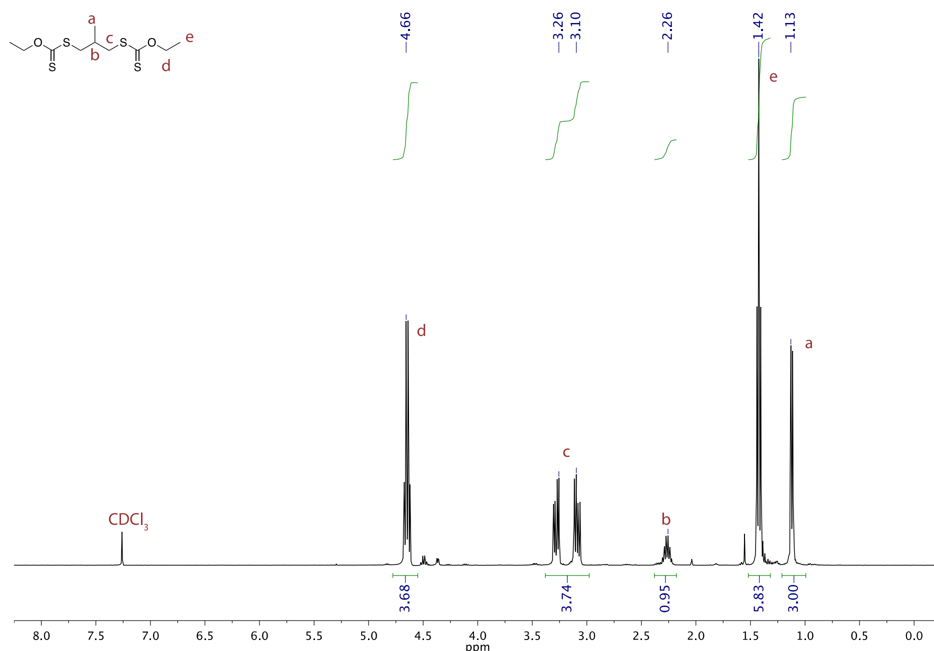

Figure 3.6 ^{1}H-NMR Spectrum of 2-methylpropane-1,3-di(ethylxanthogenate)

3.3.3.7 2-methylpropane-1,3-dithiol

2-methylpropane-1,3-di(ethylxanthogenate) (20 g) was added dropwise to ethylene diamine (40 mL) cooled on ice. The mixture was stirred on ice for 2 hours after which it was very carefully added to a mixture of sulfuric acid (100 mL) and ice (400 g) and stirred for 30 minutes. The mixture was extracted 3 times with ethyl ether (125 mL) and the combined organic phases were washed with 2M aqueous sulfuric acid (250 mL) and brine (250 mL). The solution was dried over magnesium sulfate, filtered, and the solvent removed under reduced pressure. The obtained material was distilled under reduced pressure (50°C, 0.5 Torr) to obtain the desired product as a malodorous colorless oil. ^{1}H NMR (400 MHz, $CDCl_3$) δ 2.59 (m, 4H), 1.80 (m, 1H), 1.25 (t, 2H), 1.02 (d, 3H)

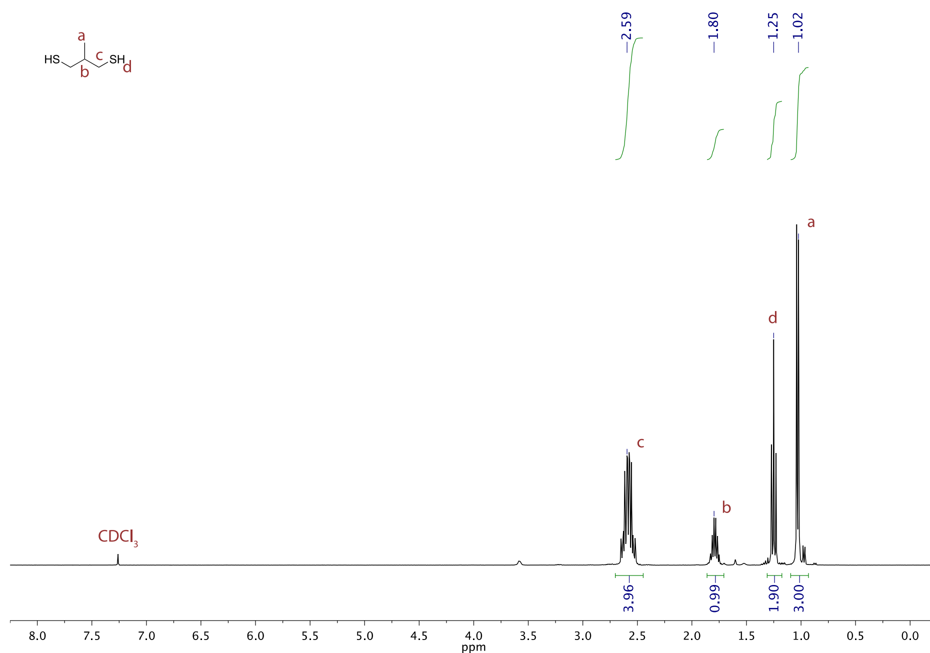

Figure 3.7 ^{1}H-NMR Spectrum of 2-methylpropane-1,3-dithiol

3.3.3.8 2-Methylpropane-1,3-di(norbornene sulfide) (NPS)

To a 250 mL 3-neck round bottom flask equipped with a reflux condenser and an addition funnel was added to 80 mL anhydrous methanol in an argon atmosphere elemental sodium (1.34g). The solution was heated to 75°C for 1 hour. Then, a mixture of norbornyl bromide (5.10g) and 2-methylpropane-1,3-dithiol (2.76g) in a minimal amount of anhydrous methanol was added dropwise, and the solution was left to stir overnight. The next morning, the solution was allowed to cool to room temperature, and the solvent was removed under reduced pressure. Water was added to the residue, and the mixture was extracted 4 times with ethyl ether (80 mL). The combined organic phases were washed with brine, dried over magnesium sulfate and the solvent removed under reduced pressure. The resultant material was distilled under reduced pressure (210°C, 0.2 Torr) to obtain the desired material as a colorless oil.

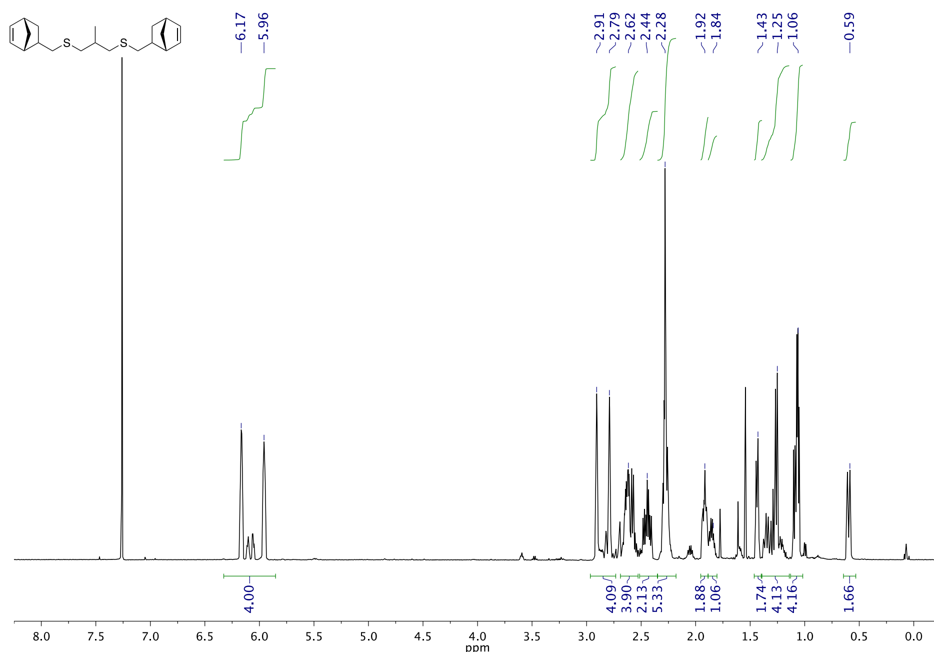

Figure 3.8 ^{1}H-NMR Spectrum of NPS

3.3.3.9 Trimethylolpropanediallyl ethermonoacetic acid (DAC)

Potassium tert-butoxide (22g) and trimethylolpropane diallyl ether (20 mL) were added to tert-butanol (160 mL) in a 500 mL 2-neck round bottom flask equipped with a reflux condenser and an addition funnel. The solution was heated to 90°C and stirred for 1 hour. A solution of bromoacetic acid (13.2 g) in tert-butanol (40 mL) was added dropwise to the solution. Immediately following addition, a white precipitate started to form. Following complete addition, the reaction was stirred at 90°C for another 2 days. The solution was allowed to cool to room temperature, and most solvent was removed under reduced pressure. Water (120 mL) was added to the residue, and the precipitate dissolved. The alkaline aqueous phase was extracted 2 times with diethyl ether (120 mL). To the aqueous phase was carefully added 200 mL of hydrochloric acid (1 M), and the pH was confirmed to be near 1. The acidic aqueous phase was extracted 4 times with methylene chloride (75 mL), and the combined methylene chloride phases were washed with brine (100 mL). The organic phase was dried over magnesium sulfate, and the solvent was removed under reduced pressure. Further purification through fractional Kugelrohr distillation (First fraction 100°C (tBuOH), second fraction 160°C 0.4 Torr) yielded the product as a colorless, viscous oil. ^{1}H NMR (400 MHz, $CDCl_3$) δ 5.89 (m, 2H), 5.21 (dd, 4H), 4.01 (s, 2H), 3.98 (m, 4H), 3.45 (s, 2H), 3.38 (qt, 4H), 1.44 (qt, 2H), 0.85 (t, 3H)

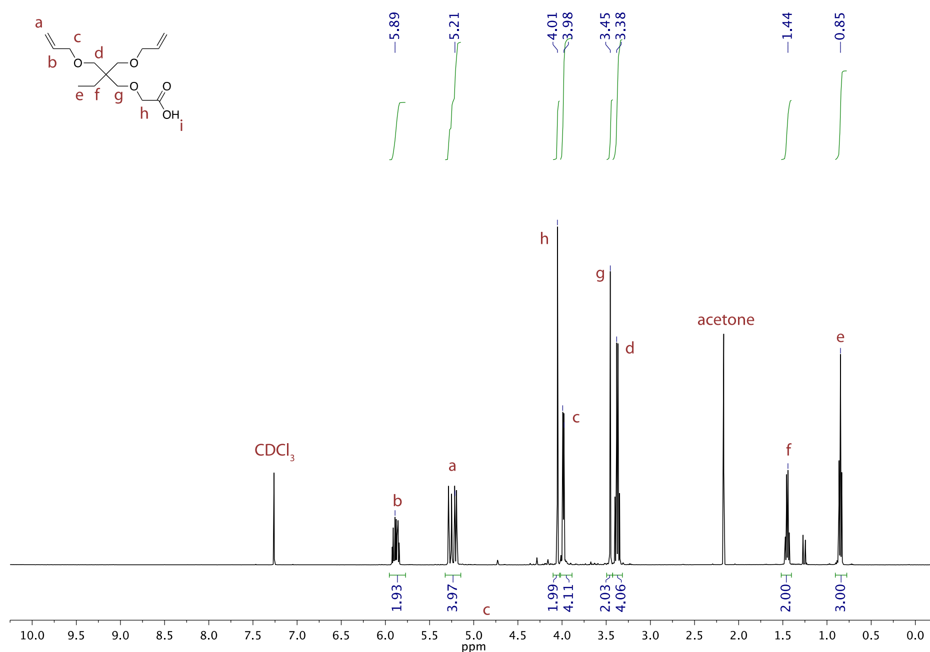

Figure 3.9 ^{1}H-NMR Spectrum of DAC

3.3.3.10 Pentaerythritoltriallyl ethermonoacetic acid (TAC)

Potassium tert-butoxide (22g) and pentaerythritol allyl ether (70%) (24.8 g) were added to tert-butanol (160 mL) in a 500 mL 2-neck round bottom flask equipped with a reflux condenser and an addition funnel. The solution was heated to 90°C and stirred for 1 hour. A solution of bromoacetic acid (13.2 g) in tert-butanol (40 mL) was added dropwise to the solution. Immediately following addition, a white precipitate started to form. Following complete addition, the reaction was stirred at 90°C for another 2 days. The solution was allowed to cool to room temperature, and most solvent was removed under reduced pressure. Water (120 mL) was added to the residue, and the precipitate dissolved. The alkaline aqueous phase was extracted 2 times with diethyl ether (120 mL). To the aqueous phase was carefully added 200 mL of hydrochloric acid (1 M), and the pH was confirmed to be near 1. The acidic aqueous phase was extracted 4 times with methylene chloride (75 mL), and the combined methylene chloride phases were washed with brine

(100 mL). The organic phase was dried over magnesium sulfate, and the solvent was removed under reduced pressure. Further purification through fractional Kugelrohr distillation (First fraction 100°C (tBuOH), second fraction 180°C 0.4 Torr) yielded the product as a colorless, viscous oil. ^{1}H NMR (400 MHz, $CDCl_3$) δ 5.88 (m, 3H), 5.23 (dd, 6H), 4.05 (s, 2H), 3.97 (m, 6H), 3.56 (s, 2H), 3.47 (s, 6H), 1.44 (qt, 2H), 0.85 (t, 3H)

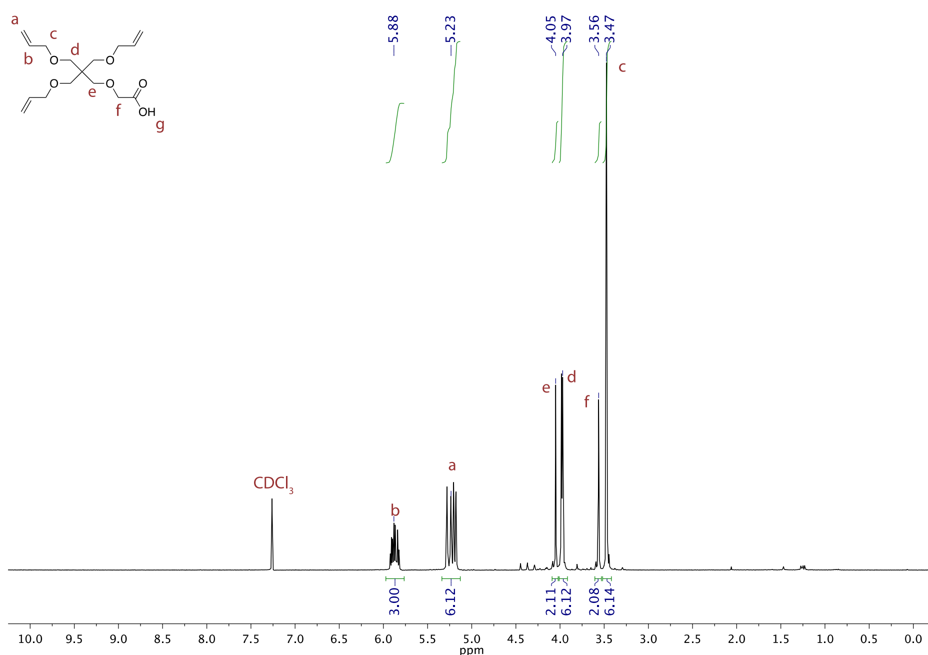

Figure 3.10 ^{1}H-NMR Spectrum of TAC

3.3.3.11 Trimethylolpropane diallyl ether monophosphoric acid (DAP)

Triethylamine (1.3g) and trimethylolpropane diallyl ether (2.76 g) were added to anhydrous diethyl ether (20 mL) in a 100 mL round bottom flask equipped with an addition funnel. The solution was cooled on ice and stirred for 1 hour. A solution of phosphorous(V) oxychloride (1.77 g) in anhydrous diethyl ether (15 mL) was added dropwise to the solution. Following complete addition, the solution was allowed to slowly warm up to room temperature and stirred overnight, during which a white

precipitate formed. The precipitate was filtered off, and the remaining solution was added dropwise to 50 mL of vigorously stirring, ice cold water. Then, a solution of sodium carbonate (250 g/L) was added and the aqueous phase was extracted 3 times with diethyl ether (50 mL). The aqueous phase was brought to a pH of 3 through careful addition of concentrated hydrochloric acid. The acidic aqueous phase was extracted three times with diethyl ether (50 mL). The combined ethereal phases were dried over sodium sulfate, and the solvent removed under reduced pressure to yield the desired product as a slightly yellow, viscous oil. ^{1}H NMR (400 MHz, $CDCl_3$) δ 9.00-9.20 (m, 2H), 5.86 (m, 2H), 5.20-5.30 (m, 4H), 3.96 (m, 6H), 3.33 (s, 4H), 1.45 (m, 2H), 0.86 (t, 3H) ^{31}P NMR (400 MHz, $CDCl_3$) δ 1.78 (s)

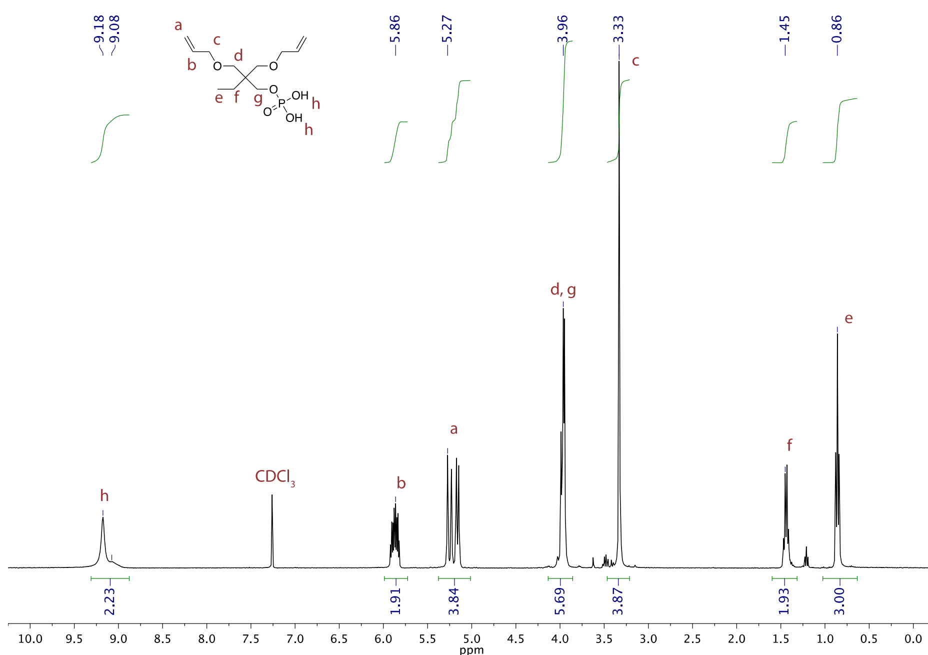

Figure 3.11 ^{1}H-NMR Spectrum of DAP

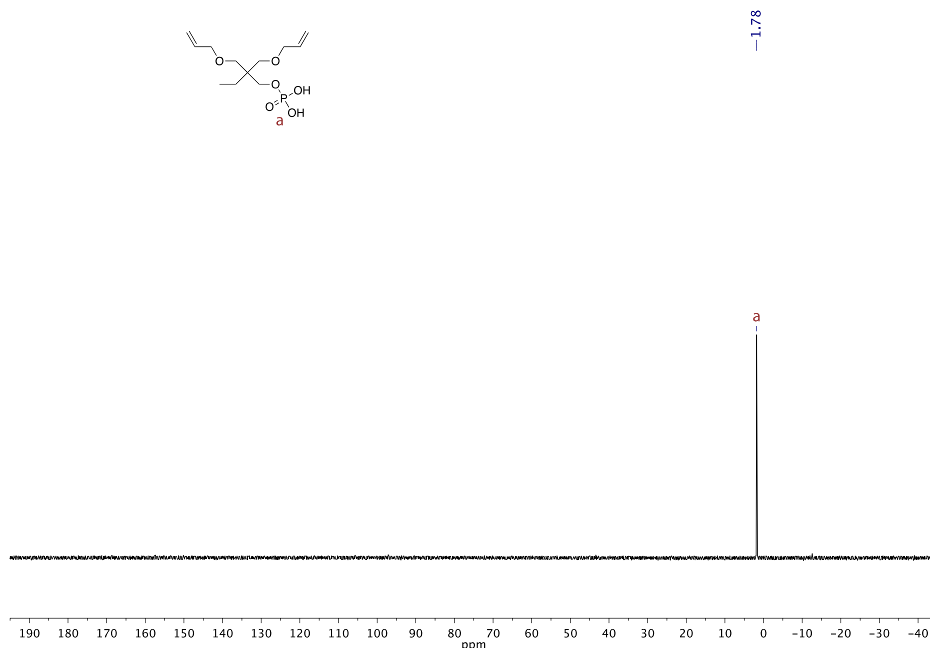

Figure 3.12 ^{31}P-NMR Spectrum of DAP

3.3.3.12 Pentaerythritol triallyl ethermonophosphoric acid (TAP)

Triethylamine (1.9g) and pentaerythritol allyl ether (70%) (4.95 g) were added to anhydrous diethyl ether (30 mL) in a 100 mL round bottom flask equipped with an addition funnel. The solution was cooled on ice and stirred for 1 hour. A solution of phosphorous(V) oxychloride (2.65 g) in anhydrous diethyl ether (30 mL) was added dropwise to the solution. Following complete addition, the solution was allowed to slowly warm up to room temperature and stirred for 2 days, during which a white precipitate formed. The precipitate was filtered off, and the remaining solution was added dropwise to 100 mL of vigorously stirring, ice cold water. Then, a solution of sodium carbonate (250 g/L) was added and the aqueous phase was extracted 3 times with diethyl ether (100 mL). The aqueous phase was brought to a pH of 3 through careful addition of concentrated hydrochloric acid. The acidic aqueous phase was extracted twice with

diethyl ether (50 mL). The combined ethereal phases were dried over magnesium sulfate, and the solvent removed under reduced pressure to yield the desired product as a slightly yellow, viscous oil. ^{1}H NMR (400 MHz, $CDCl_3$) δ 7.75-8.25 (bs, 2H), 5.84 (m, 3H), 5.10-5.32 (m, 6H), 4.11 (m, 2H), 3.96 (m, 6H), 3.47 (s, 6H), 0.86 (t, 3H) ^{31}P NMR (400 MHz, $CDCl_3$) δ 2.01 (s)

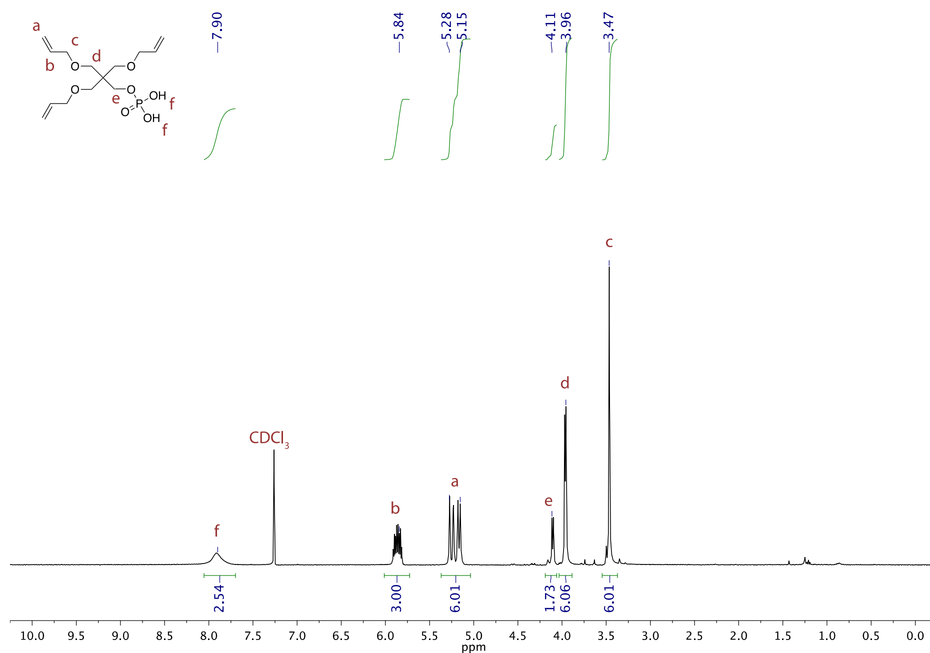

Figure 3.13 ^{1}H-NMR Spectrum of TAP

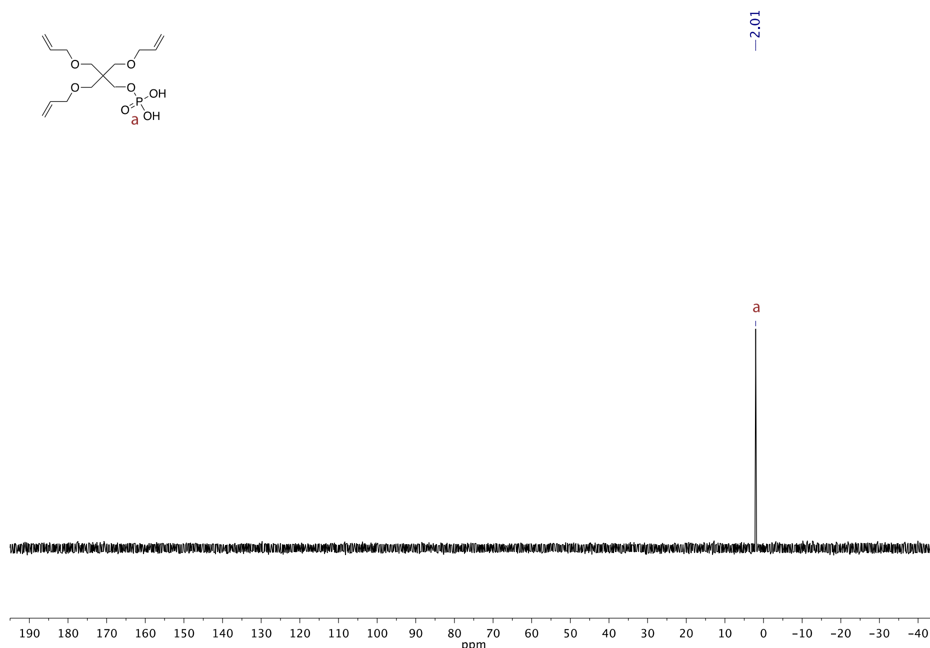

Figure 3.14 ^{31}P-NMR Spectrum of TAP

3.4 Results and discussion

3.4.1 Effect of Addition-Fragmentation CT on thiol–ene resins

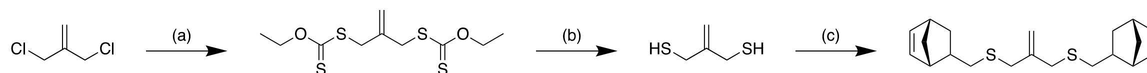

Scheme 3.3 Synthesis of NAS Reagents and conditions: (a) Potassium ethyl xanthogenate, r.t. overnight, EtOH,(b) ethylene diamine, 0°C, 2h, (c) Na, norbornyl bromide, 75°C, overnight, MeOH

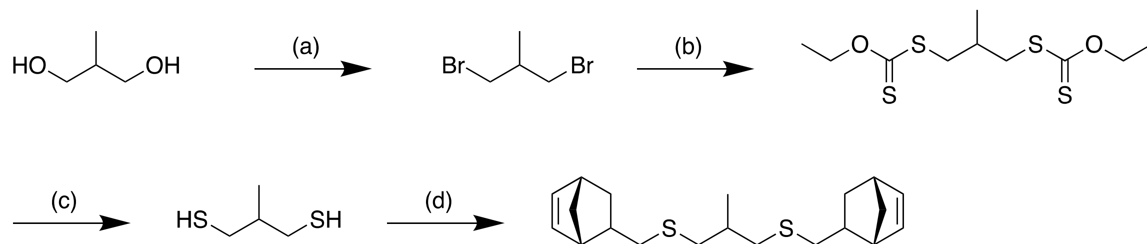

Scheme 3.4 Synthesis of NPS Reagents and conditions: (a) H_2SO_4, NaBr, reflux, water (b) Potassium ethyl xanthogenate, r.t. overnight, EtOH,(c) ethylene diamine, 0°C, 2h, (d) Na, norbornyl bromide, 75°C, overnight, MeOH

The addition-fragmentation chain transfer (AFCT) additive norbornyl allyl sulfide (NAS) (see Scheme 3.3) was prepared as previously described in literature. In order to evaluate the effects of AFCT versus the effect of the addition of a new monomer in the system, a negative control, which reacts in the thiol–ene reaction as NAS, but cannot undergo the AFCT, norbornyl propyl sulfide (NPS) (see Scheme 3.4) was also prepared. As shown in Chapter 1, the TMES/TATATO, and TMES-TNTATO/TATATO formulations serve as low shrinkage stress ester-free high T_g alternatives for thiol–ene dental restorative resins. To evaluate the effect of AFCT chemistry on the photopolymerizations of these resins NAS was added at various concentrations (5-15%) and NPS at a single concentration (10%) to these resins. In the photopolymerization of TMES/TATATO with NAS & NPS (see Figure 3.16) the effect of NAS on the thiol–ene polymerization is significant. Relative to the pristine TMES/TATATO formulation (Figure 2.8b) the rate of consumption of both the thiol and ene is significantly reduced, with a more pronounced effect as higher NAS content. As the thiyl radical in the thiol–ene reaction takes part in the AFCT mechanism, the competing reaction is expected to reduce the rate of polymerization, this is in agreement with the observed decrease in polymerization rates as the NAS concentration increases. Furthermore, the formulation containing NPS (Figure 3.16d) shows photopolymerization behavior similar to the pristine TMES/TATATO resin. Of interest is the increased thiol consumption relative to TATATO in the NAS-containing formulations. It is possible that the carbon-centered radical intermediate of the AFCT reaction can undergo a chain-transfer reaction with a free thiol, thus consuming the thiols as shown in Figure 3.15.

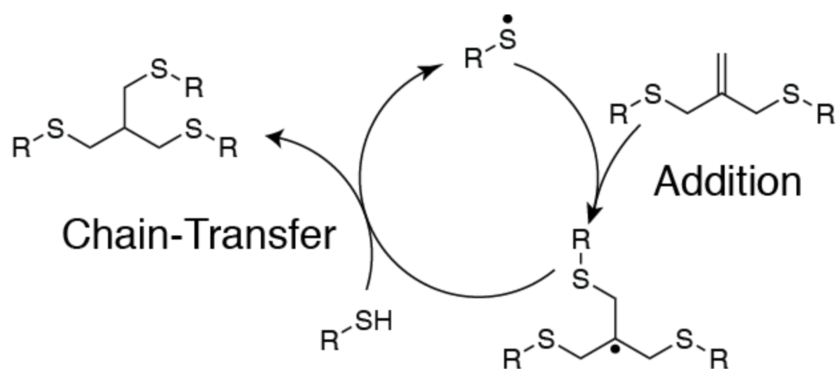

Figure 3.15 Possible mechanism for thiol consumption in AFCT

Unfortunately, unlike previously reports, the allyl sulfide moiety could not be monitored through FTIR spectroscopy in this system, as the signal overlaps with other signals in the spectrum.[8] Incorporation of NAS/NPS into the crosslinked polymer network was achieved though the thiol–ene reaction with the pendant norbornene moieties, in which the thiol–norbornene reaction proceeds more rapidly than the thiol–TATATO reaction, demonstrated by Figure 3.17. The favored thiol–ene reaction with the norbornene moieties provides another alternative avenue for the increased thiol consumption in these formulations. It is however unlikely to be a major factor, as the NPS-formulated resins displayed thiol and ene conversions akin to those of pristine TMES/TATATO.

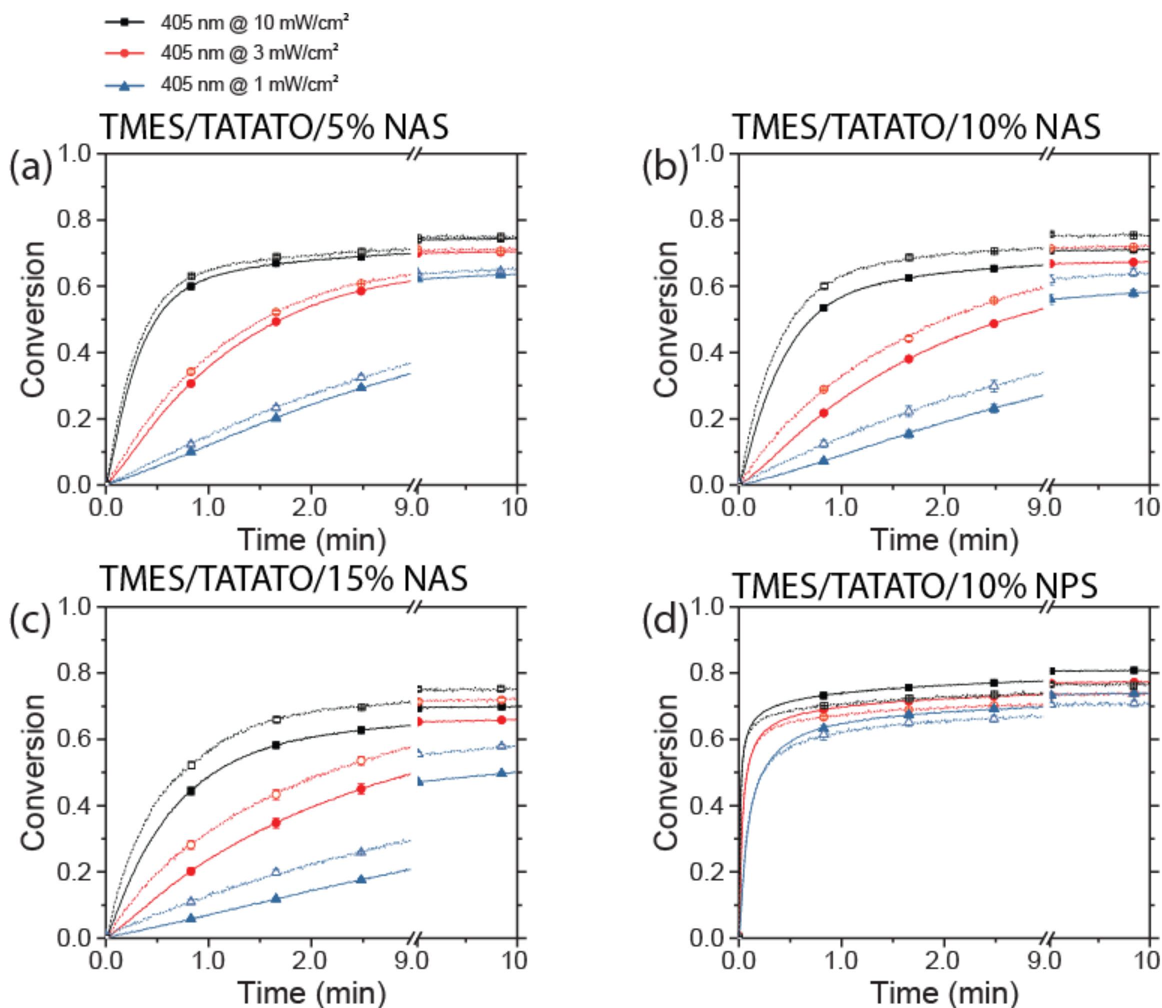

Figure 3.16 Photopolymerization kinetics Conversion versus time for the photopolymerizations of TMES/TATATO formulated with (a) 5% NAS, (b) 10% NAS, (c) 15% NAS, and (d) 10% NPS Continuous irradiation with 405 nm at intensities of 10 (black squares), 3 (red circles), and 1 (blue triangles) mW·cm^{-2}. TATATO ene conversions are displayed as solid lines and symbols, whereas thiol conversions are dashed lines and open symbols

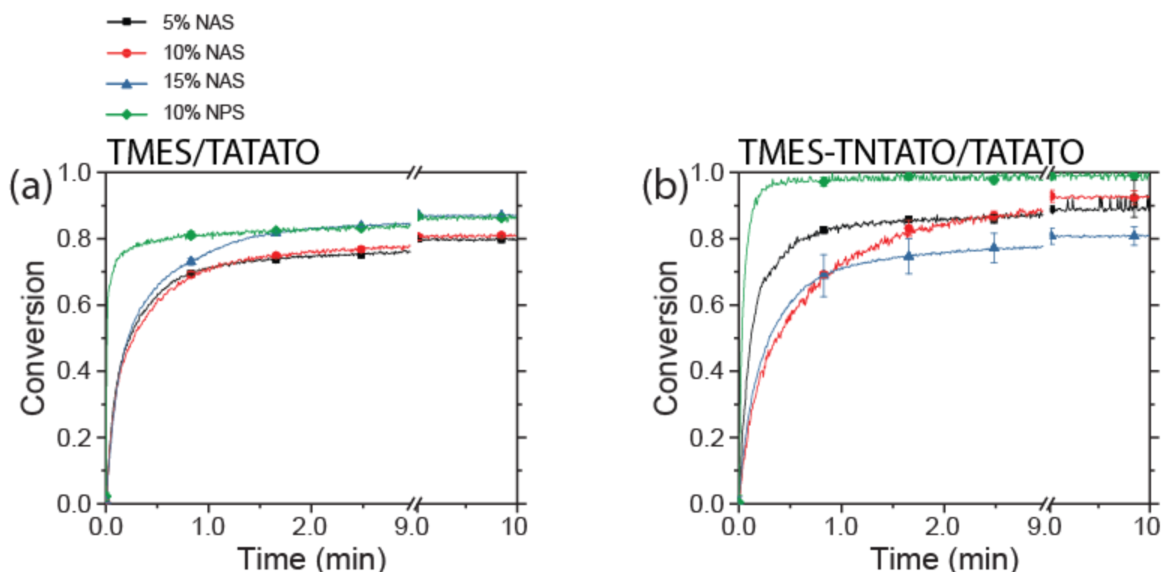

Figure 3.17 NAS and NPS norbornene photopolymerization kinetics versus time in formulations of (a) TMES/TATATO, and (d) TMES-TNTATO/TATATO. Continuous irradiation with 405 nm at 10 mW·cm^{-2} of formulation containing 5% NAS (black squares), 10% NAS (red circles), 15% NAS (blue triangles), and 10% NPS (green diamonds)

The observations made in the TMES-TNTATO/TATATO formulations follow the same trends as the TMES/TATATO-based formulations. The discrepancy between thiol and ene polymerization however, is observed to be much greater in the pre-oligomerized systems, particularly at high NAS concentrations (see Figure 3.18). The relative concentration of allyl sulfide and norbornyl moieties is significantly higher in the pre-oligomerized formulations, as a substantial fraction of the total enes has been consumed in the pre-oligomerization. With the rapid incorporation of norbornenes into the resin, coupled with the proposed addition/chain-transfer reaction in Figure 3.15 the elevated thiol consumption can be explained. Overall, the addition-fragmentation chain-transfer monomers are compatible with the previously developed thiol–ene and oligomeric thiol–ene formulations, as the reduction in polymerization rates can be overcome through increasing light intensities.

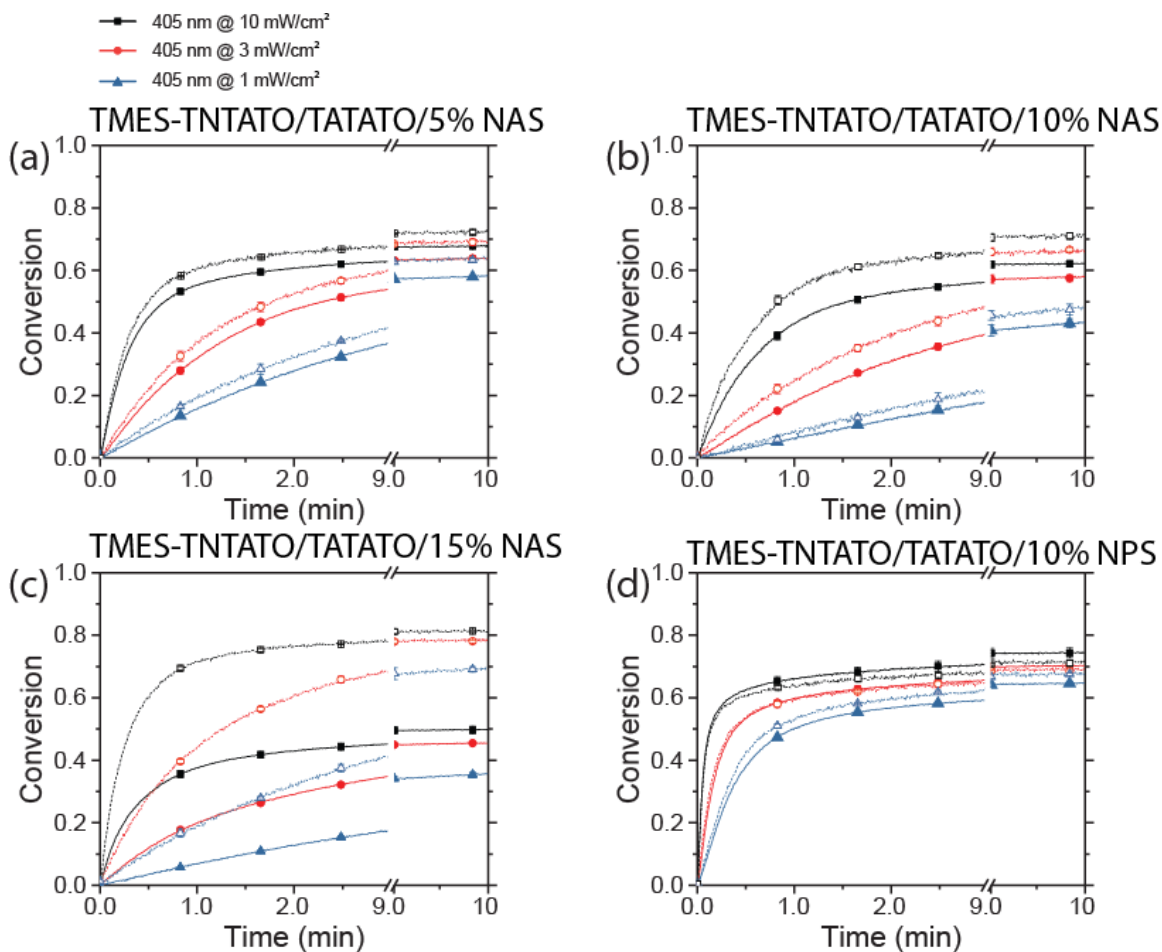

Figure 3.18 Photopolymerization kinetics Conversion versus time for the photopolymerizations of TMES-TNTATO/TATATO formulated with (a) 5% NAS, (b) 10% NAS, (c) 15% NAS, and (d) 10% NPS. Continuous irradiation with 405 nm at intensities of 10 (black squares), 3 (red circles), and 1 (blue triangles) mW·cm^{-2}. TATATO ene conversions are displayed as solid lines and symbols, whereas thiol conversions are dashed lines and open symbols

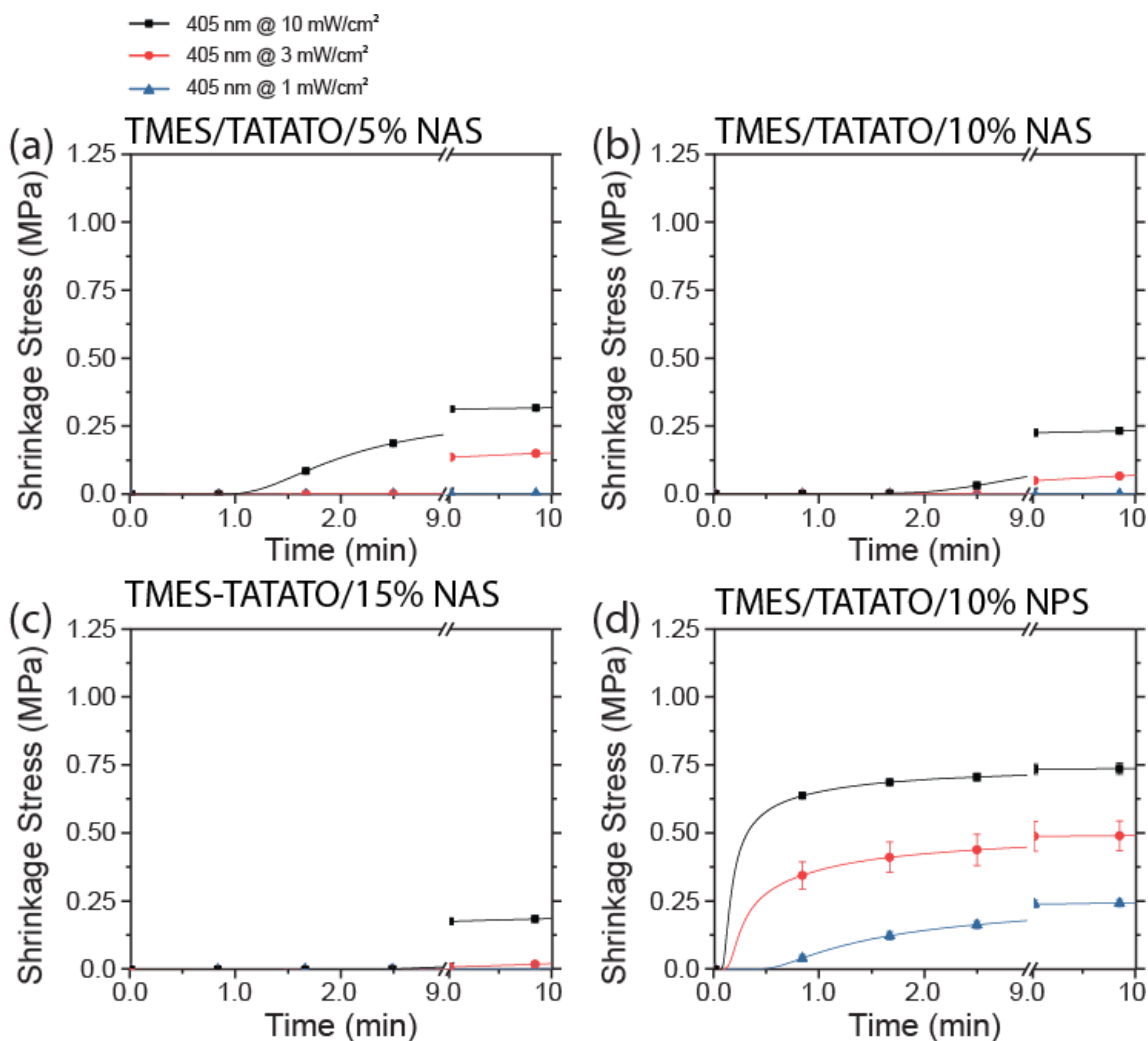

Figure 3.19 Polymerization-induced shrinkage stress versus time for the photopolymerizations of TMES/TATATO formulated with (a) 5% NAS, (b) 10% NAS, (c) 15% NAS, and (d) 10% NPS. Continuous irradiation with 405 nm at intensities of 10 (black squares), 3 (red circles), and 1 (blue triangles) mW·cm^{-2}.

The impact of NAS on the polymerization-induced shrinkage stress was evaluated through tensometry. The shrinkage stress observed in TMES/TATATO formulations was impacted significantly by the inclusion of NAS. Whereas in the pristine TMES/TATATO formulation shrinkage stress rapidly developed shortly following irradiation (see Figure 2.12b), the TMES/TATATO formulations containing NAS (see Figure 3.19) saw a significant delay in the development of shrinkage stress, coupled with an overall decrease

in the observed value, with no significant stress observed at the lowest irradiation intensities. Incremental increase in the NAS content lead to a steady decrease in the onset, rate, and final shrinkage stress. Conversely, inclusion of the negative control NAS did not result in a significant change in polymerization-induced shrinkage stress.

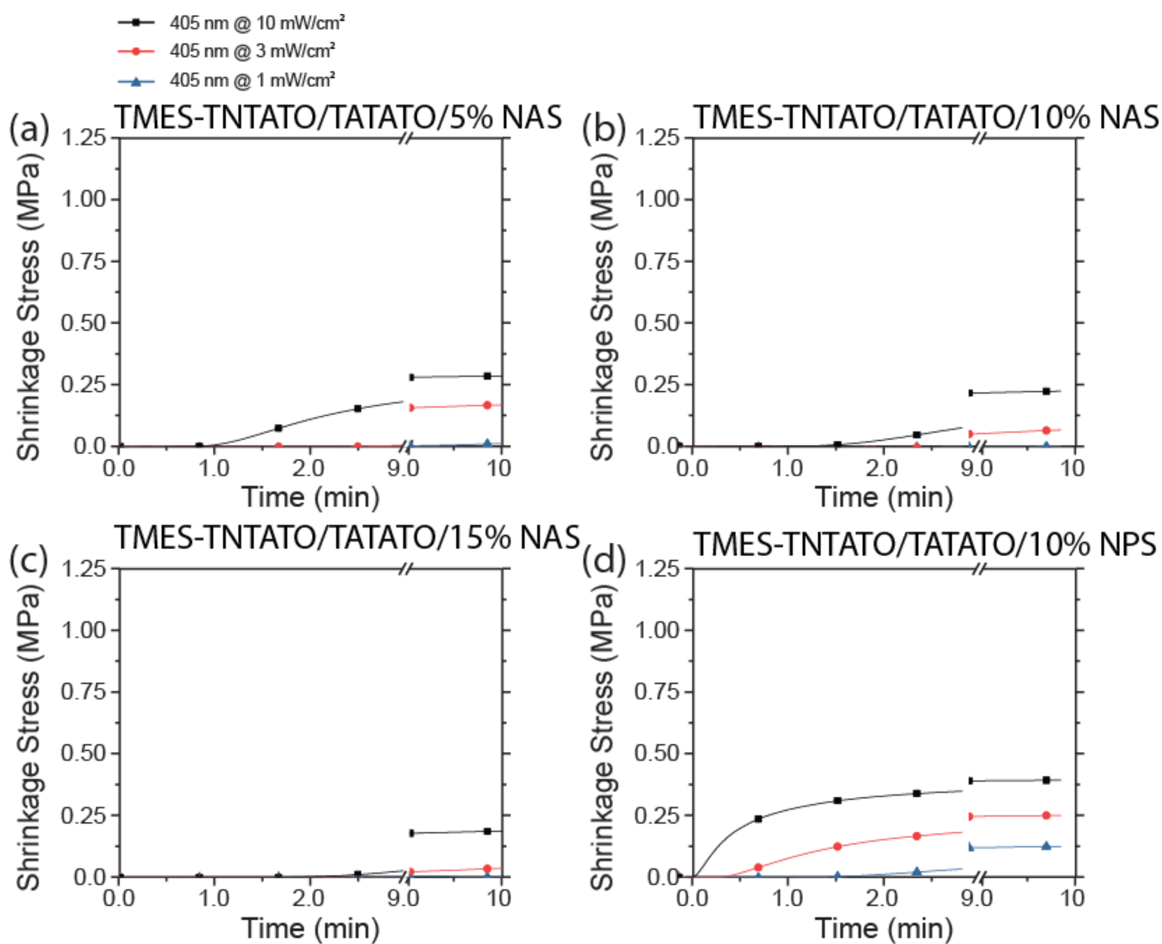

Figure 3.20 Polymerization-induced shrinkage stress versus time for the photopolymerizations of TMES-TNTATO/TATATO formulated with (a) 5% NAS, (b) 10% NAS, (c) 15% NAS, and (d) 10% NPS. Continuous irradiation with 405 nm at intensities of 10 (black squares), 3 (red circles), and 1 (blue triangles) mW·cm^{-2}.

Similar to the TMES/TATATO formulations, inclusion of NAS into the pre-oligomerized TMES-TNTATO/TATATO formulations lead to a further decrease in the observed shrinkage stress. The impact of NAS on the oligomeric formulations however was much less pronounced (see Figure 3.20). Rather, the onset, rate, and final shrinkage

stress were very similar to those observed in the TMES/TATATO-based formulations (summarized in Figure 3.21 and Table 3.1). This observation demonstrates that the AFCT chemistry, which rearranges the crosslinked polymeric network, dominates the development of shrinkage stress rather than the initial reduction from the pre-oligomerization. Correlating polymerization shrinkage stress with TATATO ene conversion further visualizes the limited effect of NAS on conversion while significantly reducing shrinkage stress.

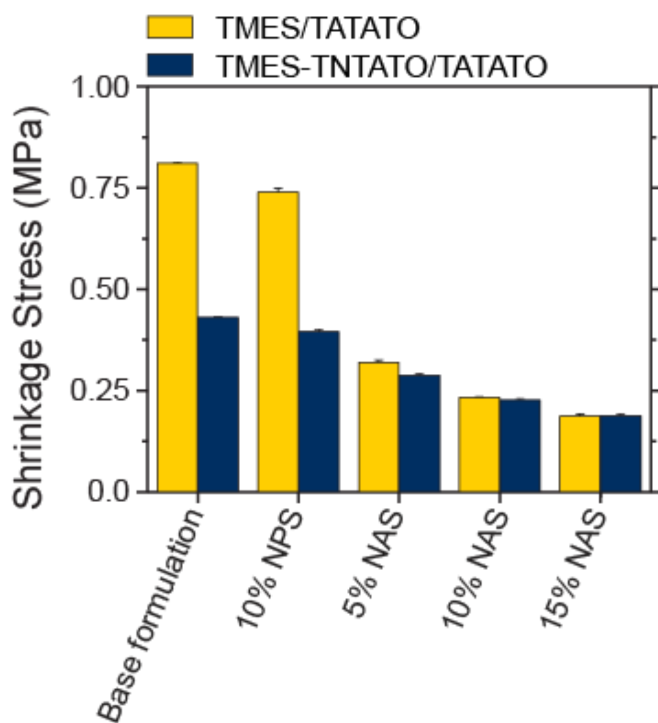

Figure 3.21 Polymerization shrinkage stress versus allyl sulfide (NAS) content for TMES/TATATO (maize) and TMES-TNTATO/TATATO (blue) based formulations containing 1% TPO as the photoinitiator and irradiated for 10 minutes with 405nm light @ 10 mW/cm^2.

Table 3.1 Summary of polymerization-induced shrinkage stress of thiol–ene formulations based on TMES/TATATO and TMES-TNTATO/TATATO after constant irradiation for 10 minutes with 405nm light at the indicated light intensity.

Formulation	**Final shrinkage Stress at 1 mW/cm^2 (MPa)**	**Final shrinkage Stress at 3 mW/cm^2 (MPa)**	**Final shrinkage Stress at 10 mW/cm^2 (MPa)**
TMES/TATATO	0.34 ± 0.02	0.56 ± 0.05	0.82 ± 0.01
TMES-TNTATO/ TATATO	0.17 ± 0.01	0.30 ± 0.01	0.43 ± 0.04
TMES/TATATO/ NAS (5%)	0.004 ± 0.003	0.15 ± 0.01	0.32 ± 0.01
TMES-TNTATO/ TATATO/NAS (5%)	0.012 ± 0.005	0.170 ± 0.005	0.287 ± 0.004
TMES/TATATO/ NAS (10%)	0.000 ± 0.001	0.069 ± 0.003	0.233 ± 0.009
TMES-TNTATO/ TATATO/NAS (10%)	0.00 ± 0.03	0.069 ± 0.004	0.226 ± 0.004
TMES/TATATO/ NAS (15%)	0.002 ± 0.002	0.02 ± 0.01	0.187 ± 0.003
TMES-TNTATO/ TATATO/NAS (15%)	0.002 ± 0.005	0.037 ± 0.005	0.188 ± 0.004
TMES/TATATO/ NPS (10%)	0.25 ± 0.01	0.49 ± 0.06	0.72 ± 0.01
TMES-TNTATO/ TATATO/ NPS (10%)	0.126 ± 0.006	0.251 ± 0.006	0.394 ± 0.006

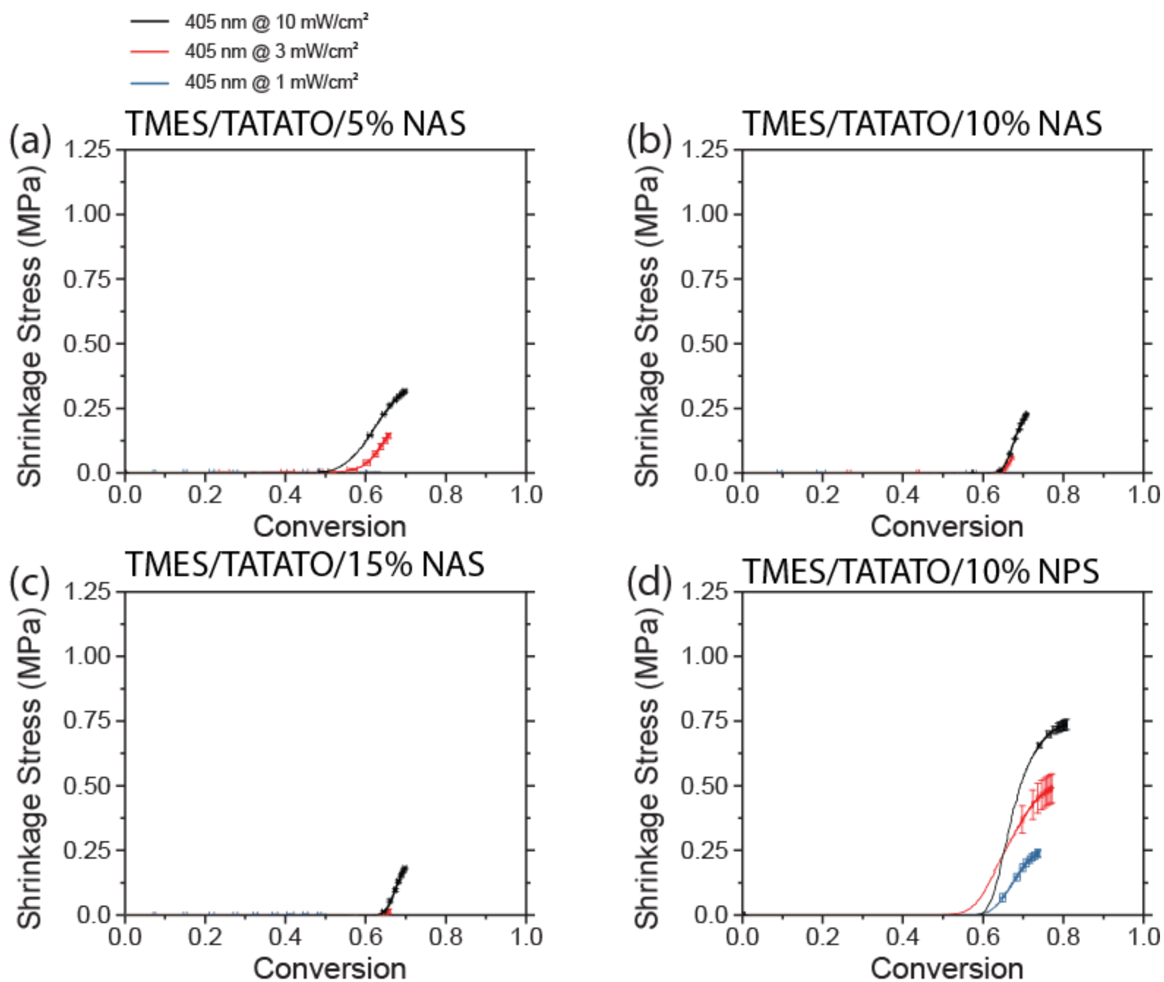

Figure 3.22 Correlation between monomer conversion and polymerization-induced shrinkage stress of TMES/TATATO formulated with (a) 5% NAS, (b) 10% NAS, (c) 15% NAS, and (d) 10% NPS Continuous irradiation with 405 nm at intensities of 10 (black squares), 3 (red circles), and 1 (blue triangles) mW·cm^{-2}. TATATO ene conversions are displayed as solid lines and symbols, whereas thiol conversions are dashed lines and open symbols

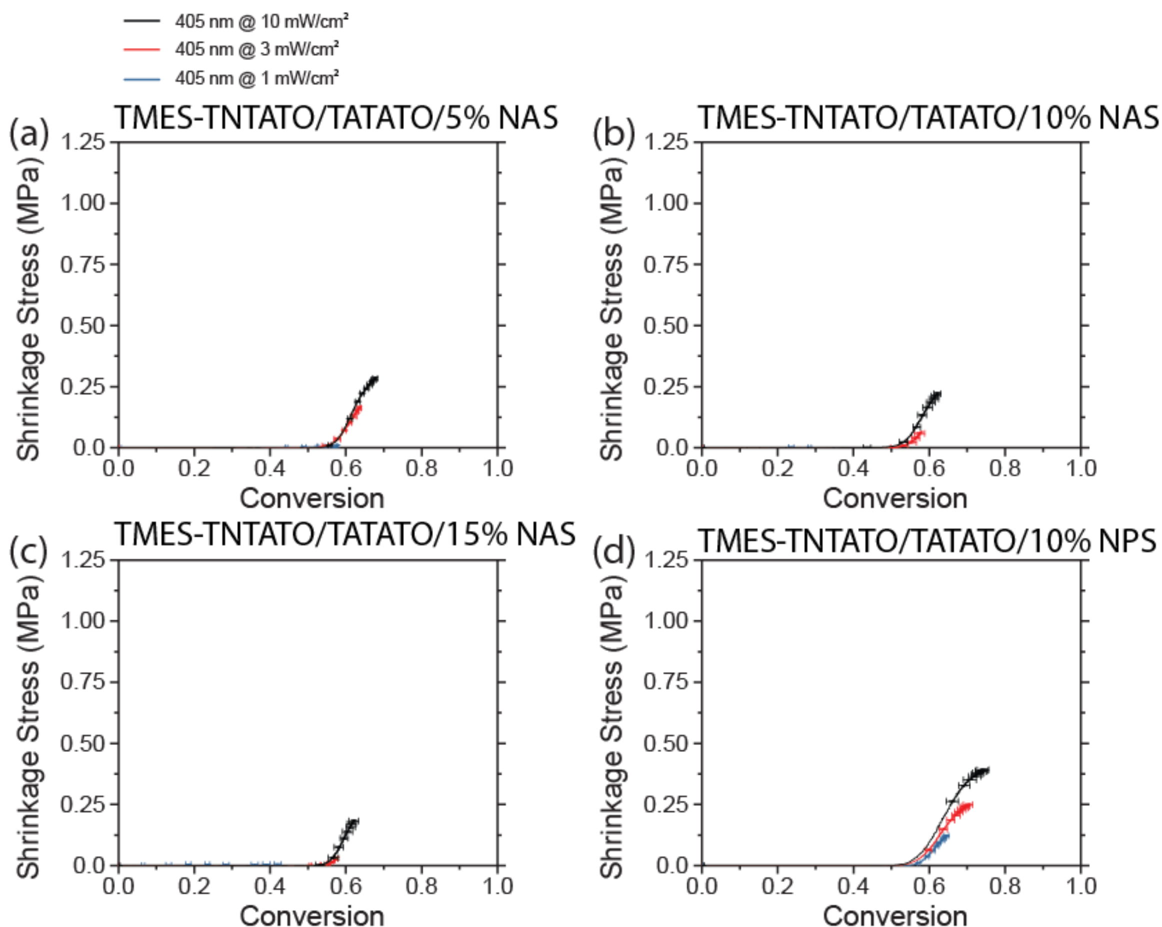

Figure 3.23 Correlation between monomer conversion and polymerization-induced shrinkage stress of TMES-TNTATO/TATATO formulated with (a) 5% NAS, (b) 10% NAS, (c) 15% NAS, and (d) 10% NPS Continuous irradiation with 405 nm at intensities of 10 (black squares), 3 (red circles), and 1 (blue triangles) mW·cm^{-2}. TATATO ene conversions are displayed as solid lines and symbols, whereas thiol conversions are dashed lines and open symbols

The inclusion of NAS into the thiol–ene formulations is expected to result in a decrease of the crosslinking density of the resultant polymer network, as the trifunctional TATATO is replaced by the difunctional AFCT monomer. To evaluate the effect of changing the monomers, as well as the impact of AFCT on the T_g of the resultant polymeric materials, TMES/TATATO and TMES-TNTATO/TATATO crosslinked polymers containing NAS, as well as formulations containing the negative control NPS were examined through dynamic mechanical analysis with the results shown in Figure

3.24 and Figure 3.25. The T_g of the polymers including NAS and NPS was decreased relative to their parent resins. With the changes highlighted in Figure 3.26 and Table 3.2, the decrease in crosslinking density appears to be the major factor in this change. The AFCT chemistry has little impact on the resultant T_g as is indicated by a minor difference in T_g between the formulations containing NAS and those containing NPS. Furthermore, at ambient temperatures the polymeric materials exhibited moduli well into the glassy regime. While the broadness of the glass transition in the first heating ramp in these resins could be a cause for concern, the second heating ramp is more representative of the actual dental practice since the light intensities used in this study are significantly lower compared to the dental clinical practice (10 mW/cm^2 vs <1 W/cm^2) the increased polymerization exotherm and extend.

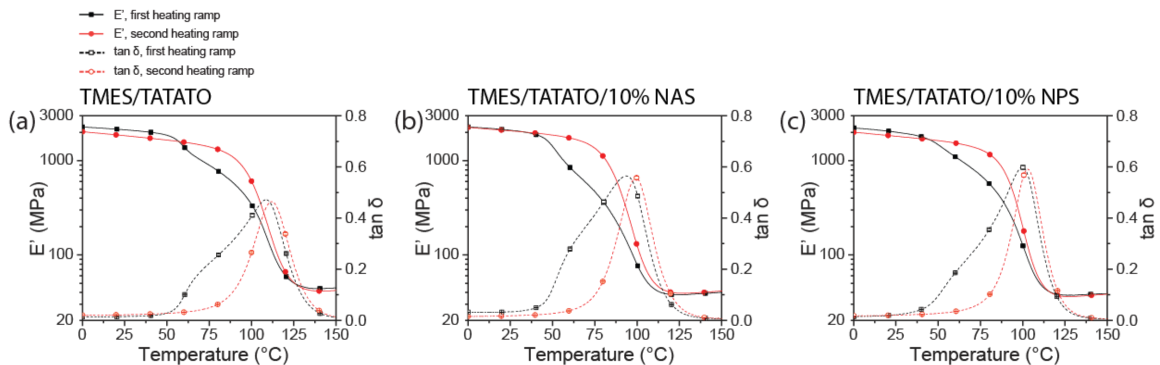

Figure 3.24 Dynamic Mechanical Analysis traces of storage modulus (E', solid lines) and tan δ (dashed lines) as a function of temperature (a) TMES/TATATO, (b) TMES/TATATO/NAS (10%), (c) TMES/TATATO/NPS (10, irradiated with 405 nm at 10 mW·cm^{-2}. First heating ramp is in black, and second heating ramp is in red. Storage modulus is displayed as solid lines and symbols, whereas tan δ is displayed as dashed lines and open symbols

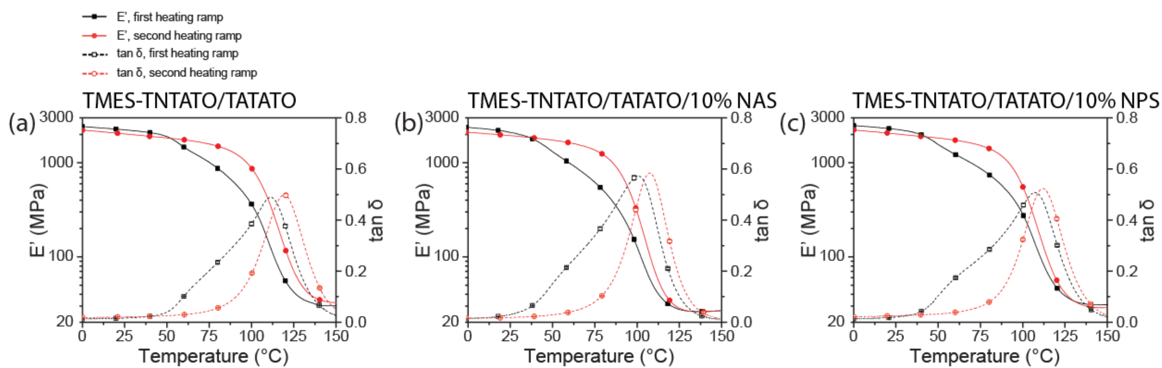

Figure 3.25 Dynamic Mechanical Analysis traces of storage modulus (E', solid lines) and tan δ (dashed lines) as a function of temperature (a) TMES-TNTATO/TATATO, (b) TMES-TNTATO/TATATO/NAS (10%), (c) TMES-TNTATO/TATATO/NPS (10%), irradiated with 405 nm at 10 mW·cm^{-2}. First heating ramp is in black, and second heating ramp is in red. Storage modulus is displayed as solid lines and symbols, whereas tan δ is displayed as dashed lines and open symbols

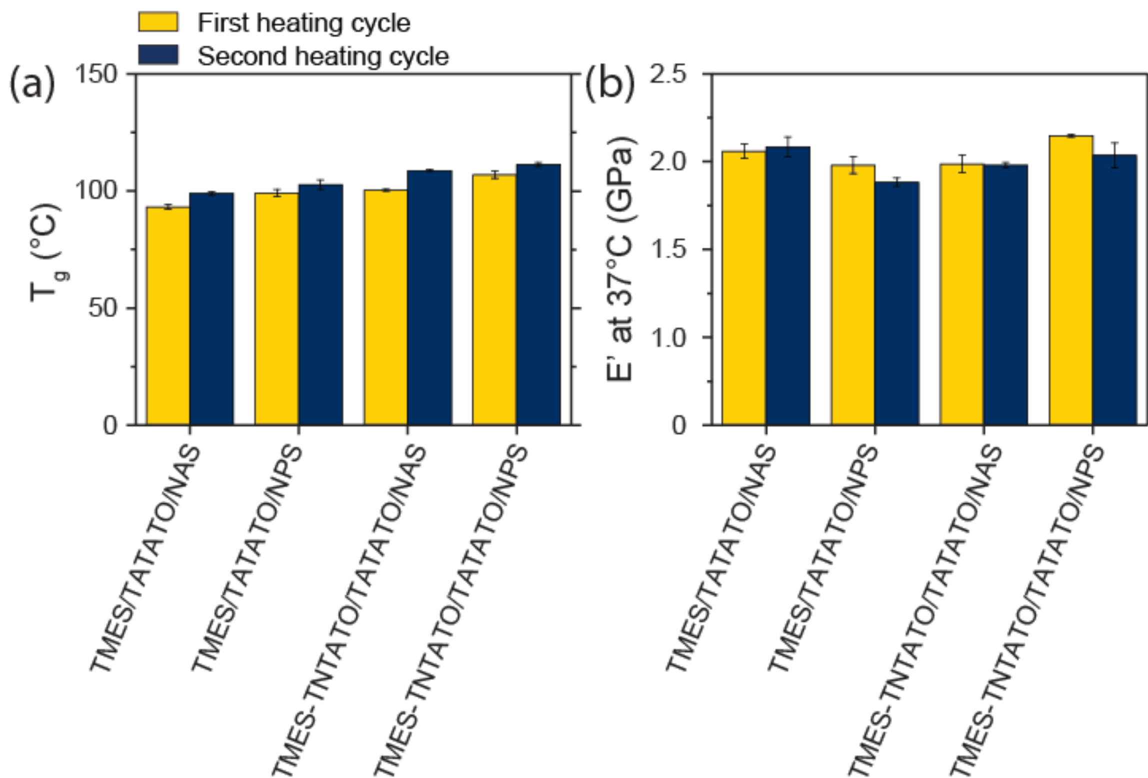

Figure 3.26 Dynamic Mechanical Analysis comparison of cured TMES/TATATO and TMES-TNTATO/TATATO resins formulated with AFCT monomer NAS and negative control NPS at 10 wt% as indicated and irradiated with 405 nm at 10 mW·cm^{-1} in the first (maize) and second (blue) heating cycles (a) glass transition temperature as indicated by tan δ, and (b) storage modulus at 37 °C

Table 3.2 Compilation glass transition temperatures and storage moduli at 37°C in both heating ramps of TMES/TATATO and TMES-TNTATO/TATATO-based formulations irradiated with 405 nm at 10 mW·cm^{-2}

Formulation	**T_g (°C), ramp 1**	**E′ at 37°C (GPa), ramp 1**	**T_g (°C), ramp 2**	**E′ at 37°C (GPa), ramp 2**
TMES/TATATO	108.5 ± 0.9	2.03 ± 0.08	111.3 ± 0.7	1.75 ± 0.02
TMES/TATATO/ NAS (10%)	93.2 ± 0.8	1.95 ± 0.02	99.0 ± 0.9	1.98 ± 0.03
TMES/TATATO/ NAS (10%)	99.2 ± 1.1	1.85 ± 0.03	102.47 ± 1.1	1.73 ± 0.02
TMES-TNTATO/ TATATO	111.1 ± 1.7	2.12 ± 0.02	119.2 ± 1.6	1.92 ± 0.07
TMES-TNTATO/ TATATO/NAS (10%)	101.4 ± 1.1	1.86 ± 0.04	108.2 ± 0.8	1.85 ± 0.03
TMES-TNTATO/ TATATO/NPS (10%)	106.9 ± 1.3	2.06 ± 0.03	111.5 ± 1.1	1.92 ± 0.03

3.4.2 Acidic monomers for improved tissue adhesion

To promote adhesion of the developed thiol–ene dental restorative resins to mineralized tissue, a library of acid-containing allylic monomers based on methacrylate adhesive monomers was proposed. The monomers containing carboxylates, phosphates, phosphonates, and anhydride adhesive moieties contain a central trimethylolpropane diallyl ether or pentaerythritol triallyl ether core (Figure 3.27), allowing for further insight into how the degree of functionality affects the resultant thiol–ene polymers.

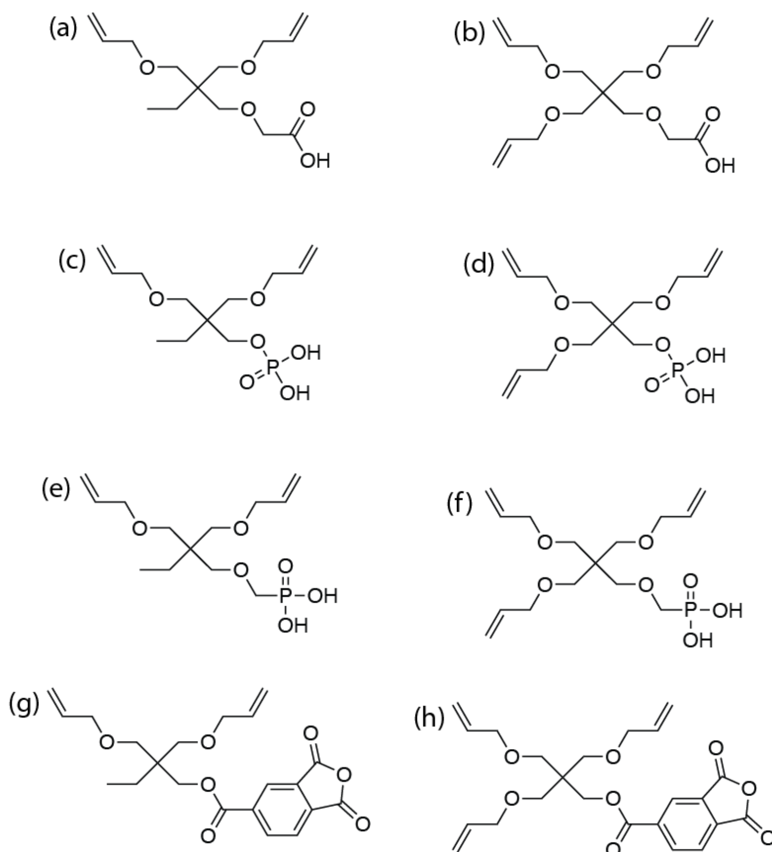

Figure 3.27 Structures of proposed self-etching monomers

The synthesis of the diallylcarboxylate and triallylcarboxylate (Figure 3.27a and b) was performed according to an adjusted literature procedure, and the materials were purified through vacuum distillation. Similarly, the diallylphosphate and triallylphosphate (Figure 3.27c and d) synthesis was successful, though attempts at purification through vacuum distillation proved unsuccessful. Despite this, ^{1}H-NMR and ^{31}P-NMR suggested these materials to be of high purity.

The diallyl phosphonate and triallyl phosphonate (Figure 3.27e and f) synthesis however was significantly more challenging. The reactions involving the phosphonate as the electrophile were unsuccessful, despite previous success in the preparation of the carboxylate-bearing monomers. In an alternate approach, trimethylolpropane diallyl ether

was successfully functionalized with bromine, triflate, and sulfonate leaving groups, but attempts to further react these materials with hydroxy-functionalized phosphonates also proved unsuccessful. Similarly, attempts were made to react trimethylolpropane diallyl ether and pentaerythritol triallyl ether with trimellitic anhydride chloride to yield the desired anhydride functionalized monomers (Figure 3.27g and h).

The difficulty in preparing these acid-containing monomers was unexpected. While the carboxylate and phosphate monomers could be obtained in sufficient purity, the yield of the reaction was low. It is likely, that despite the nucleophile in this system being a primary alcohol, the allylic and aliphatic groups surrounding the reactive group are effective at shielding this moiety from reagents. Only when used with highly reactive reagents such as phosphorous (V) oxychloride, triflic anhydride, or exposure to harsh conditions with stable reagents like reflux overnight in strongly basic conditions with bromoacetic acid, this barrier can be overcome and the desired product obtained.

Following the successful preparation of the carboxylate and phosphate monomers their compatibility with thiol–ene chemistry was evaluated through FTIR photopolymerization kinetics. The baseline TMES/TATATO formulation was formulated with 10% and 20% concentrations of the carboxylate replacing TATATO. As shown in Figure 3.28 the carboxylate monomers show a minimal impact on the photopolymerization of TMES/TATATO in the case of both the diallylcarboxylate and the triallylcarboxylate.

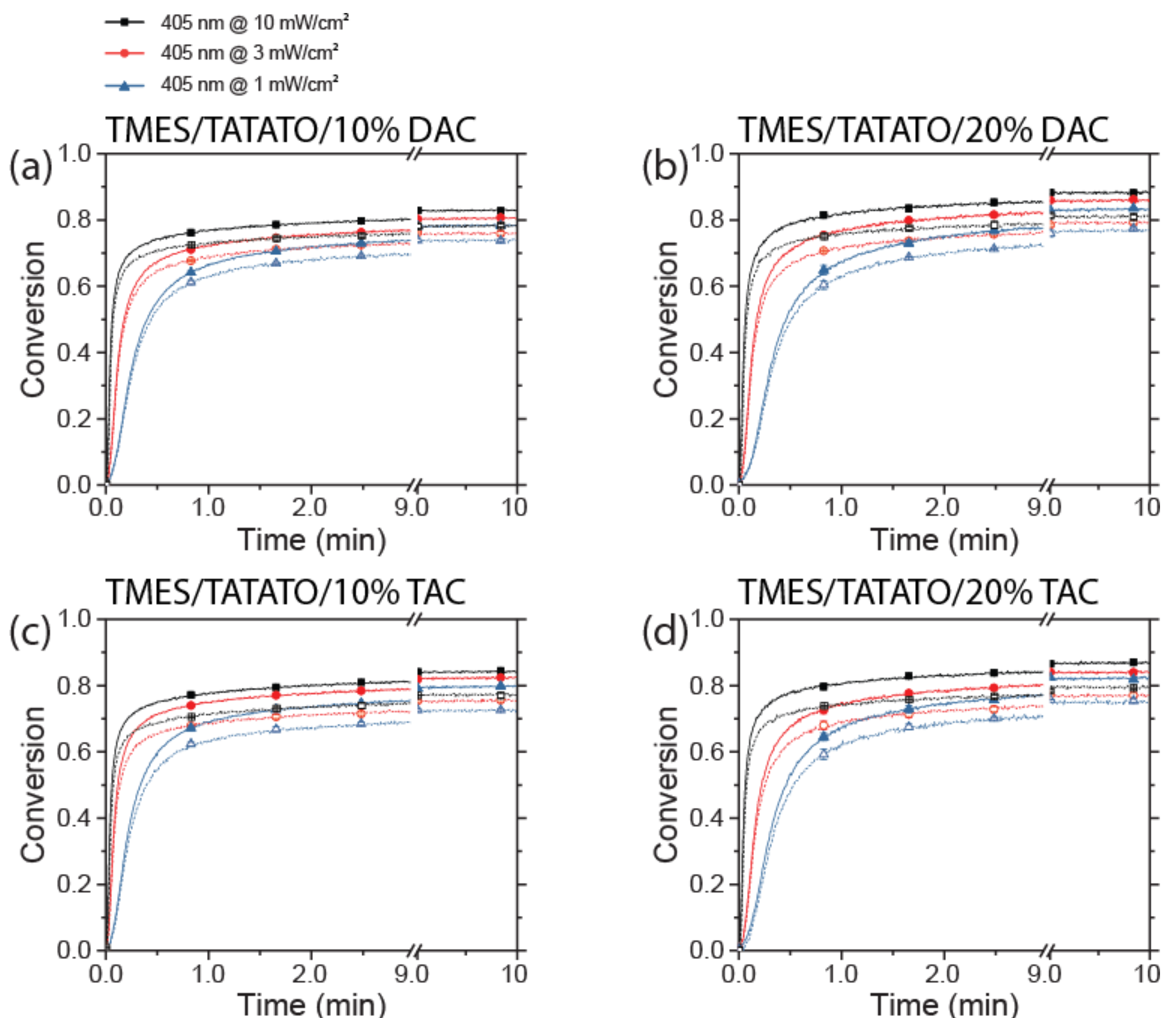

Figure 3.28 Photopolymerization kinetics conversion versus time for the photopolymerizations of TMES/TATATO formulated with (a) 10% DAC, (b) 20% DAC, (c) 10% TAC, and (d) 20% TAC. Continuous irradiation with 405 nm at intensities of 10 (black squares), 3 (red circles), and 1 (blue triangles) mW·cm^{-2}. TATATO ene conversions are displayed as solid lines and symbols, whereas thiol conversions are dashed lines and open symbols

Inclusion of the phosphate-bearing monomers in the TMES/TATATO formulation has a profound effect on the thiol–ene photopolymerization. As Figure 3.29 shows, the phosphate-bearing monomers significantly reduce the rate of thiol and ene consumption, and lead to lower overall conversions, especially at higher concentration. It is possible for an impurity following the monomer synthesis to persist in the purification process, as this process is based solely on acid-base extractions to remove impurities.

Silica column chromatography and vacuum distillation were attempted, but did not result in successful purification of the product. However both the ^{1}H-NMR and ^{31}P-NMR of both phosphate monomers suggest pure material was obtained. Alternatively as organophosphoric materials have been described previously as stabilizers for thiol–ene formulations, it is possible for the phosphate-bearing monomers to act in this fashion. Organic phosphonates, as well as inorganic phosphates have been demonstrated to act in this fashion, although organic phosphate esters have not been described as such.[39] Despite this the thiol–ene photopolymerization with the phosphate monomers did result in glassy material post-irradiation. The TMES/TATATO polymers formulated with the diallylcarboxylate and triallylcarboxylate showed an overall decrease in both the T_g and the storage modulus relative to TMES/TATATO in both heating ramps of the dynamic mechanical analyzer. As expected the diallylcarboxylate polymers display a decrease in T_g relative to the triallylcarboxylate counterparts as a result of the reduction in crosslinking density. Additionally, as both monomer are increased in molecular weight relative to TATATO, this serves to further reduce the crosslinking density and subsequent T_g. In the second heating ramp the polymeric materials exhibit slightly reduced storage moduli compared to TMES/TATATO. The possibility of increased chain movement as a result of monomer structure could be an explanation for this. Despite this, the materials still show moduli well into the GPa range.

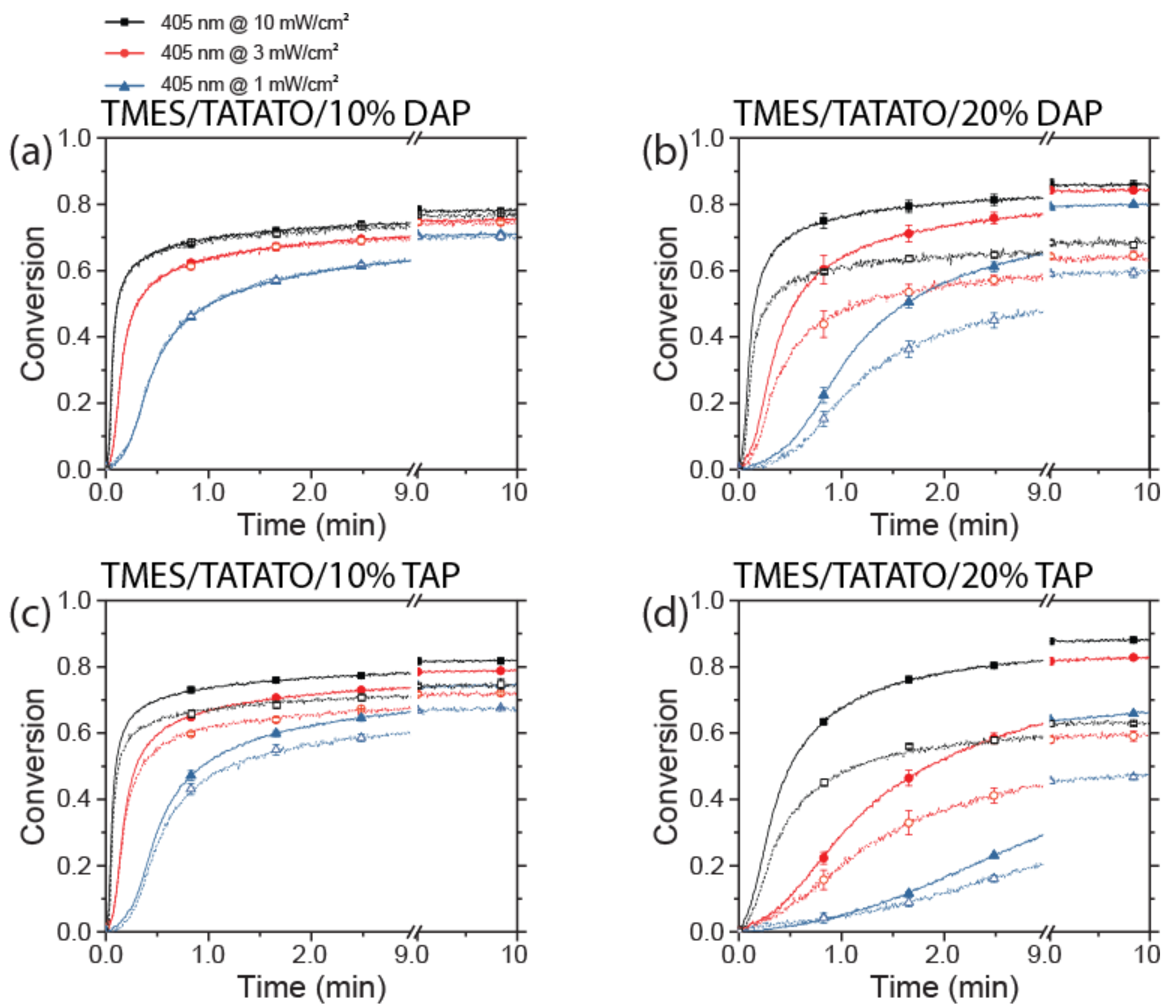

Figure 3.29 Photopolymerization kinetics conversion versus time for the photopolymerizations of TMES/TATATO formulated with (a) 10% DAP, (b) 20% DAP, (c) 10% TAP, and (d) 20% TAP. Continuous irradiation with 405 nm at intensities of 10 (black squares), 3 (red circles), and 1 (blue triangles) mW·cm^{-2}. TATATO ene conversions are displayed as solid lines and symbols, whereas thiol conversions are dashed lines and open symbols

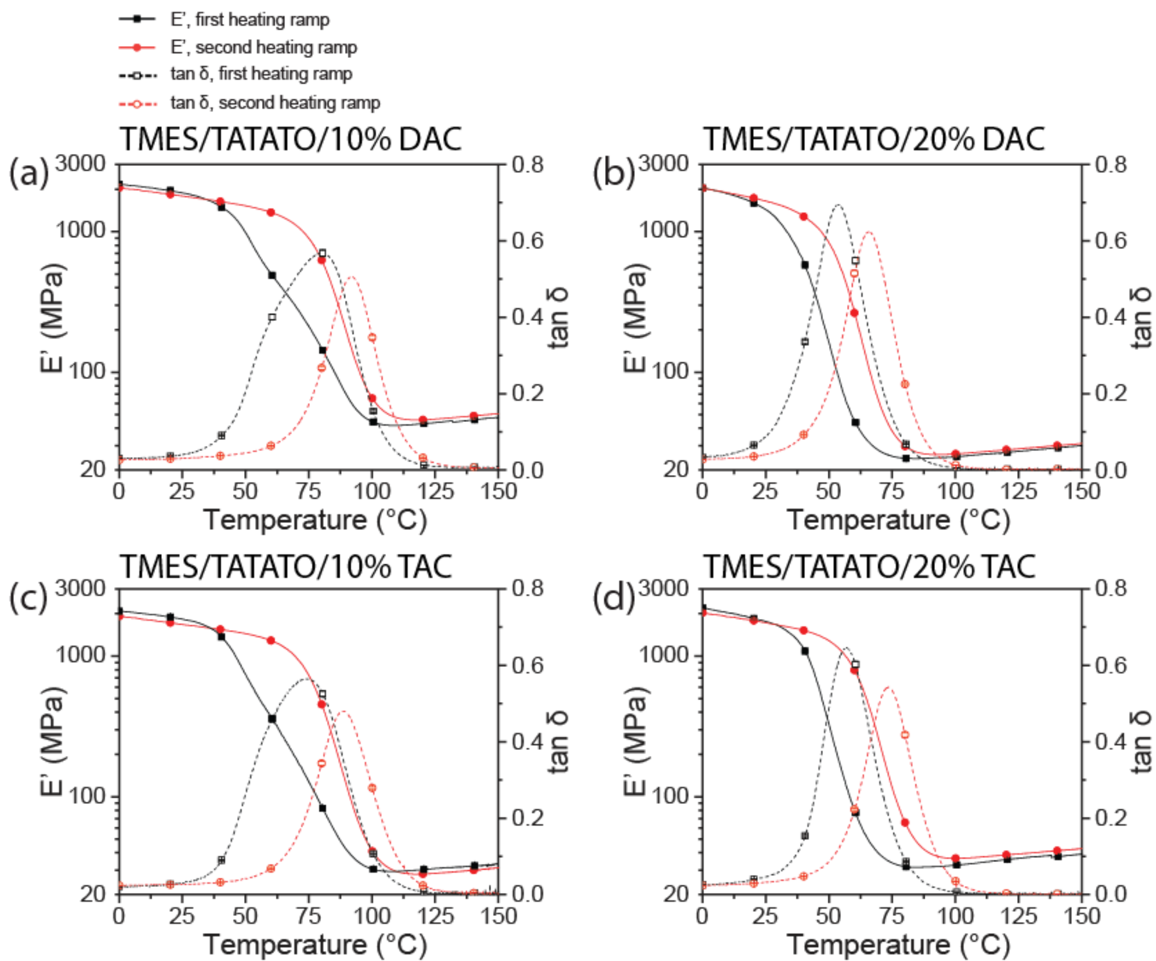

Figure 3.30 Dynamic Mechanical Analysis traces of storage modulus (E', solid lines) and tan δ (dashed lines) as a function of temperature OF TMES/TATATO formulated with (a) 10% DAC, (b) 20% DAC, (c) 10% TAC, and (d) 20% TAC), irradiated with 405 nm at 10 mW·cm^{-2}. First heating ramp is in black, and second heating ramp is in red. Storage modulus is displayed as solid lines and symbols, whereas tan δ is displayed as dashed lines and open symbols

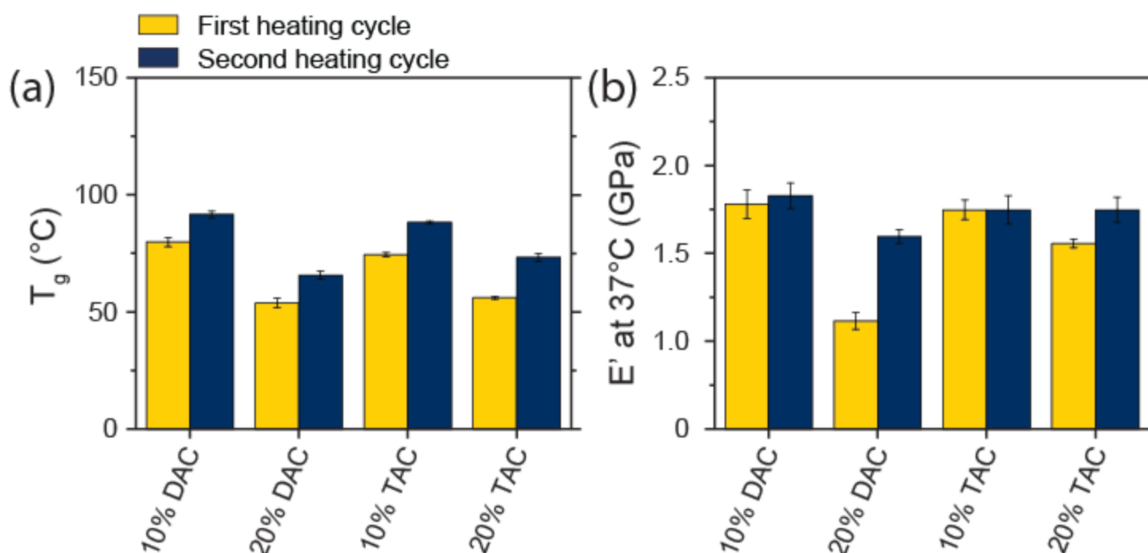

Figure 3.31 Dynamic Mechanical Analysis comparison of cured TMES/TATATO resins formulated with carboxylic acid monomer as indicated and irradiated with 405 nm at 10 mW·cm^{-1} in the first (maize) and second (blue) heating cycles (a) glass transition temperature as indicated by tan δ, and (b) storage modulus at 37 °C

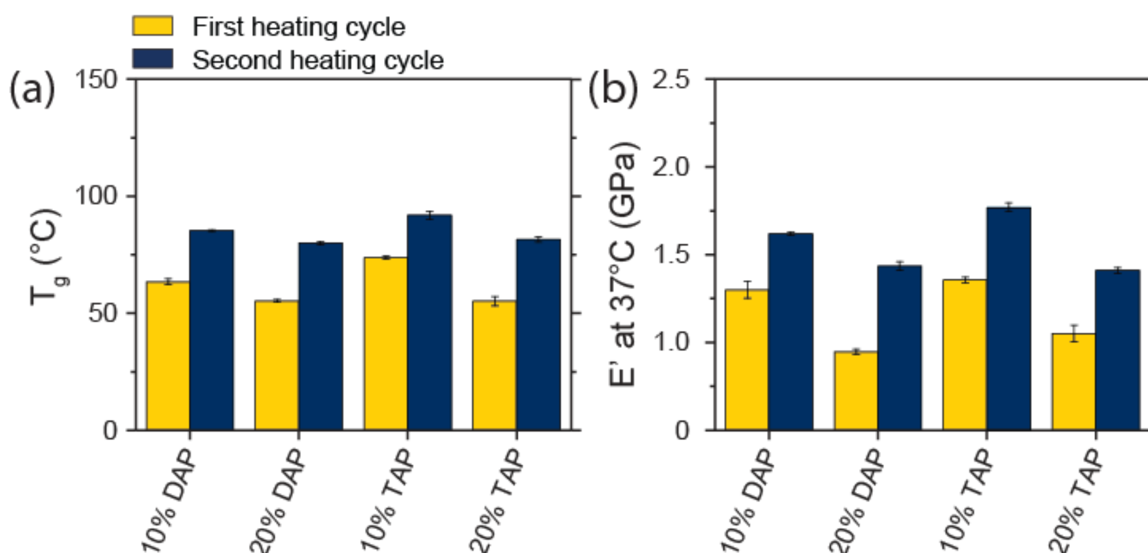

Figure 3.32 Dynamic Mechanical Analysis comparison of cured TMES/TATATO resins formulated with phosphoric acid monomer as indicated and irradiated with 405 nm at 10 mW·cm^{-1} in the first (maize) and second (blue) heating cycles (a) glass transition temperature as indicated by tan δ, and (b) storage modulus at 37 °C

Similar to the carboxylate-containing formulations the TMES/TATATO resins formulated with the diallylphosphate and triallylphosphate display a reduced T_g and

modulus relative to the parent TMES/TATATO resin. All formulations show a 15-20°C increase in their T_g in the second heating ramp resulting in T_g values between 80.0 and 92.0°C. Relative to their carboxylate counterparts, the phosphate-containing formulations generally show an increased T_g with storage moduli in the same regime. As a result of the decreased thiol–ene conversion and increased molecular weight of the phosphate-bearing monomers relative to the carboxylate formulations, the crosslinking density and resultant T_g was expected to be decreased. A possible explanation for this unexpectedly high T_g could lie in the improved hydrogen-bonding abilities of the phosphates relative to the carboxylates generating a secondary network in the covalently crosslinked polymer.

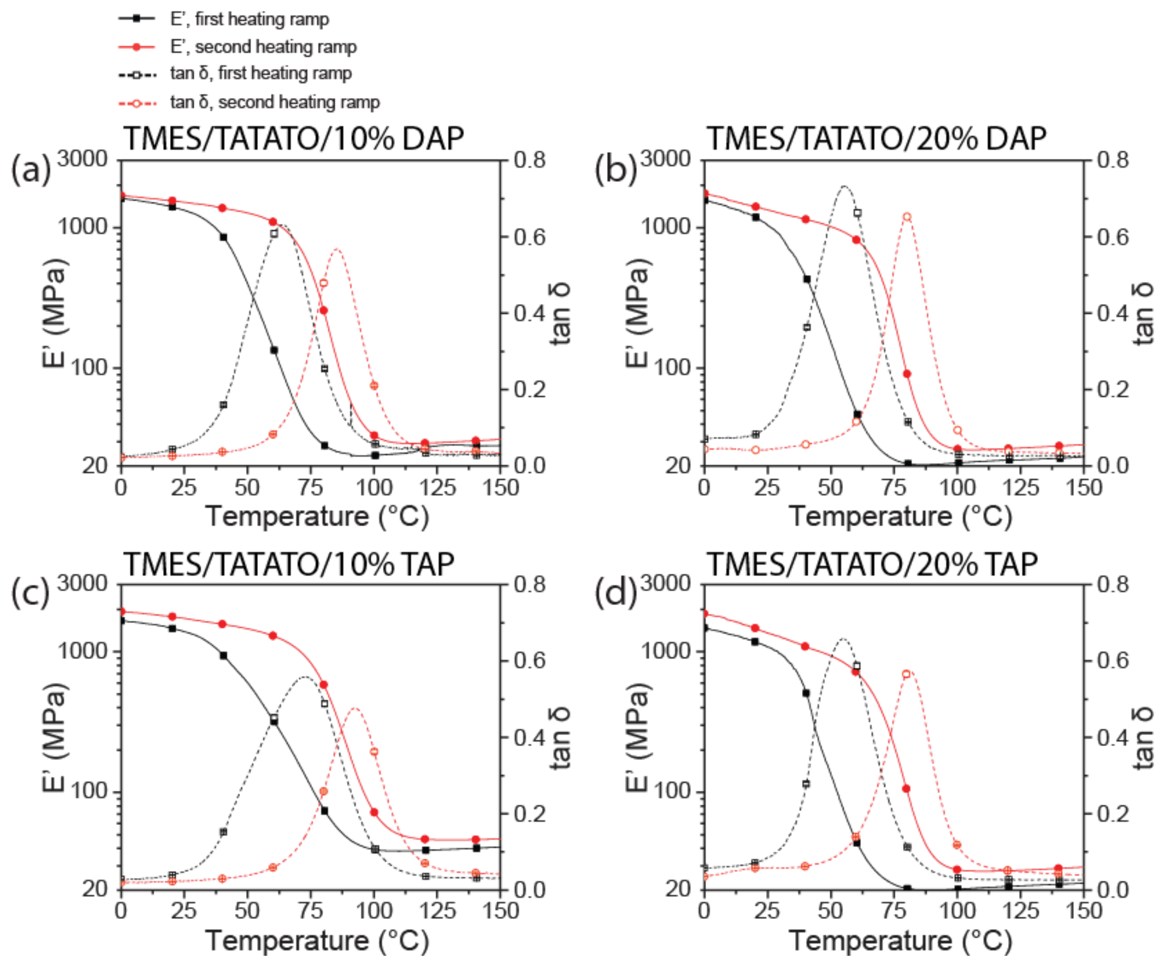

Figure 3.33 Dynamic Mechanical Analysis traces of storage modulus (E', solid lines) and tan δ (dashed lines) as a function of temperature OF TMES/TATATO formulated with (a) 10% DAP, (b) 20% DAP, (c) 10% TAP, and (d) 20% TAP), irradiated with 405 nm at 10 mW·cm^{-2}. First heating ramp is in black, and second heating ramp is in red. Storage modulus is displayed as solid lines and symbols, whereas tan δ is displayed as dashed lines and open symbols

Table 3.3 Compilation glass transition temperatures and storage moduli at 37°C in both heating ramps of TMES/TATATO formulated with acidic and irradiated with 405 nm at 10 mW·cm^{-2}

Acid monomer content	*T_g (°C), ramp 1*	*E' at 37°C (GPa), ramp 1*	*T_g (°C), ramp 2*	*E' at 37°C (GPa), ramp 2*
10% DAC	79.7	1.61 ± 0.02	91.6	1.66 ± 0.03
20% DAC	53.5	0.77 ± 0.01	65.7	1.37 ± 0.02
10% TAC	74.5	1.56 ± 0.02	88.6	1.56 ± 0.02
20% TAC	56.8	1.32 ± 0.02	73.3	1.56 ± 0.02
10% DAP	63.5	1.00 ± 0.01	85.2	1.40 ± 0.02
20% DAP	55.3	0.56 ± 0.01	80.0	1.17 ± 0.02
10% TAP	72.2	1.07 ± 0.02	92.0	1.59 ± 0.02
20% TAP	55.4	0.69 ± 0.01	81.3	1.14 ± 0.01

3.5 Conclusion

Incorporation of the addition-fragmentation chain-transfer (AFCT) monomer norbornyl allyl sulfide (NAS) lead to a significant reduction in the observed polymerization-induced shrinkage stress in TMES/TATATO-based formulations. A reduction in T_g of the formulations was observed, however this was determined to be unrelated to the AFCT mechanism. Competition between the thiol–ene reaction and AFCT resulted in a decrease in the rate of polymerization, the degree of which increased at increasing additive content. In addition to polymerization rate reduction, a relative increase in thiol consumption was observed, likely due to a combination of a favored

thiol–norbornene reaction and chain-transfer with the addition-fragmentation intermediate. Pre-oligomerized TMES-TNTATO/TATATO formulations displayed the same trends as the TMES/TATATO formulations. As the NAS content in the formulations increased, the decrease in observed shrinkage stress resulting from TMES & TNTATO is nearly completely mitigates, as the TMES-TATATO formulations display very similar shrinkage stress profiles and final observed stresses.

Carboxylate- and phosphate-functionalized allyl monomers were successfully prepared. Inclusion of the phosphate-bearing monomers into TMES/TATATO formulations lead to a reduction in the rate of polymerization, especially at higher concentrations while the carboxylate monomer did not negatively affect the thiol–ene polymerization. All acidic monomers lead to a reduction in both the modulus and the T_g of the TMES/TATATO-based polymeric films. Overall, the formulations containing phosphate-bearing monomers show favorable mechanical and thermal properties compared to the carboxylate monomers.

3.6 References

1. Ferracane, J. L.; Mitchem, J. C., Relationship between composite contraction stress and leakage in Class V cavities. *American Journal of Dentistry* **2003,** *16* (4), 239-243.

2. Rosatto, C. M. P.; Bicalho, A. A.; Verissimo, C.; Braganca, G. F.; Rodrigues, M. P.; Tantbirojn, D.; Versluis, A.; Soares, C. J., Mechanical properties, shrinkage stress, cuspal strain and fracture resistance of molars restored with bulk-fill

composites and incremental filling technique. *Journal of Dentistry* **2015,** *43* (12), 1519-1528.

3. Lu, H.; Carioscia, J. A.; Stansbury, J. W.; Bowman, C. N., Investigations of step-growth thiol–ene polymerizations for novel dental restoratives. *Dental Materials* **2005,** *21* (12), 1129-1136.

4. Scott, T. F.; Schneider, A. D.; Cook, W. D.; Bowman, C. N., Photoinduced plasticity in cross-linked polymers. *Science* **2005,** *308* (5728), 1615-1617.

5. Shah, P. K.; Stansbury, J. W.; Bowman, C. N., Application of an addition-fragmentation-chain transfer monomer in di(meth) acrylate network formation to reduce polymerization shrinkage stress. *Polymer Chemistry* **2017,** *8* (30), 4339-4351.

6. Gauss, P.; Ligon-Auer, S. C.; Griesser, M.; Gorsche, C.; Svajdlenkova, H.; Koch, T.; Moszner, N.; Liska, R., The Influence of Vinyl Activating Groups on beta-Allyl Sulfone-Based Chain Transfer Agents for Tough Methacrylate Networks. *Journal of Polymer Science Part A: Polymer Chemistry* **2016,** *54* (10), 1417-1427.

7. Ligon, S. C.; Seidler, K.; Gorsche, C.; Griesser, M.; Moszner, N.; Liska, R., Allyl Sulfides and alpha-Substituted Acrylates as Addition-Fragmentation Chain Transfer Agents for Methacrylate Polymer Networks. *Journal of Polymer Science Part A: Polymer Chemistry* **2016,** *54* (3), 394-406.

8. Kloxin, C. J.; Scott, T. F.; Bowman, C. N., Stress Relaxation via Addition-Fragmentation Chain Transfer in a Thiol–ene Photopolymerization. *Macromolecules* **2009,** *42* (7), 2551-2556.

9. Park, H. Y.; Kloxin, C. J.; Scott, T. F.; Bowman, C. N., Stress relaxation by addition-fragmentation chain transfer in highly cross-linked thiol-yne networks. *Macromolecules* **2010,** *43* (24), 10188-10190.

10. Park, H. Y.; Kloxin, C. J.; Scott, T. F.; Bowman, C. N., Covalent adaptable networks as dental restorative resins: Stress relaxation by addition-fragmentation chain transfer in allyl sulfide-containing resins. *Dental Materials* **2010,** *26* (10), 1010-1016.

11. Park, H. Y.; Kloxin, C. J.; Fordney, M. F.; Bowman, C. N., Stress relaxation of trithiocarbonate-dimethacrylate-based dental composites. *Dental Materials* **2012,** *28* (8), 888-893.

12. Park, H. Y.; Kloxin, C. J.; Abuelyaman, A. S.; Oxman, J. D.; Bowman, C. N., Stress Relaxation via Addition − Fragmentation Chain Transfer in High Tg, High Conversion Methacrylate-based Systems. *Macromolecues* **2012,** *45* (14), 5640-5646.

13. Cramer, N. B.; Bowman, C. N., Kinetics of thiol–ene and thiol-acrylate photopolymerizations with real-time Fourier transform infrared. *Journal of Polymer Science Part A: Polymer Chemistry* **2001,** *39* (19), 3311-3319.

14. Chigira, H.; Yukitani, W.; Hasegawa, T.; Manabe, A.; Itoh, K.; Hayakawa, T.; Debari, K.; Wakumoto, S.; Hisamitsu, H., Self-etching Dentin Primers Containing Phenyl-P. *Journal of Dental Research* **1994,** *73* (5), 1088-1095.

15. Van Landuyt, K. L.; Snauwaert, J.; De Munck, J.; Peurnans, M.; Yoshida, Y.; Poitevin, A.; Coutinho, E.; Suzuki, K.; Lambrechtsa, P.; Van Meerbeek, B.,

Systematic review of the chemical composition of contemporary dental adhesives. *Biomaterials* **2007,** *28* (26), 3757-3785.

16. Van Landuyt, K. L.; Snauwaert, J.; Peumans, M.; De Munck, J.; Lambrechts, P.; Van Meerbeek, B., The role of HEMA in one-step self-etch adhesives. *Dental Materials* **2008,** *24* (10), 1412-1419.

17. Pashley, D. H.; Tay, F. R., Aggressiveness of contemporary self-etching adhesives - Part II: etching effects on unground enamel. *Dental Materials* **2001,** *17* (5), 430-444.

18. Van Landuyt, K. L.; Kanumilli, P.; De Munck, J.; Peumans, M.; Lambrechts, P.; Van Meerbeek, B., Bond strength of a mild self-etch adhesive with and without prior acid-etching. *Journal of Dentistry* **2006,** *34* (1), 77-85.

19. Nakabayashi, N.; Kojima, K.; Masuhara, E., The Promotion of Adhesion by the Infiltration of Monomers into Tooth Substrates. *Journal of Biomedical Materials Research* **1982,** *16* (3), 265-273.

20. Perdigao, J.; Geraldeli, S.; Hodges, J. S., Total-etch versus self-etch adhesive - Effect on postoperative sensitivity. *Journal of the American Dental Association* **2003,** *134* (12), 1621-1629.

21. Unemori, M.; Matsuya, Y.; Akashi, A.; Goto, Y.; Akamine, A., Self-etching adhesives and postoperative sensitivity. *American Journal of Dentistry* **2004,** *17* (3), 191-195.

22. Yousaf, A.; Aman, N.; Manzoor, M. A.; Shahl, J. A.; Dilrasheed, Postoperative Sensitivity of Self Etch Versus Total Etch Adhesive. *Jcpsp-Journal of the College of Physicians and Surgeons Pakistan* **2014,** *24* (6), 383-386.

23. Breschi, L.; Mazzoni, A.; Ruggeri, A.; Cadenaro, M.; Di Lenarda, R.; Dorigo, E. D. S., Dental adhesion review: Aging and stability of the bonded interface. *Dental Materials* **2008,** *24* (1), 90-101.

24. De Munck, J.; Mine, A.; Poitevin, A.; Van Ende, A.; Cardoso, M. V.; Van Landuyt, K. L.; Peumans, M.; Van Meerbeek, B., Meta-analytical Review of Parameters Involved in Dentin Bonding. *Journal of Dental Research* **2012,** *91* (4), 351-357.

25. Salz, U.; Zimmermann, J.; Zeuner, F.; Mozner, N., Hydrolytic stability of self-etching adhesive systems. *Journal of Adhesive Dentistry* **2005,** *7* (2), 107-116.

26. Moszner, N.; Zeuner, F.; Pfeiffer, S.; Schurte, I.; Rheinberger, V.; Drache, M., Monomers for adhesive polymers, 3 - Synthesis, radical polymerization and adhesive properties of hydrolytically stable phosphonic acid monomers. *Macromolecular Materials and Engineering* **2001,** *286* (4), 225-231.

27. Catel, Y.; Fischer, U. K.; Moszner, N., Monomers for Adhesive Polymers, 10-Synthesis, Radical Photopolymerization and Adhesive Properties of Methacrylates Bearing Phosphonic Acid Groups. *Macromolecular Materials and Engineering* **2013,** *298* (7), 740-756.

28. Inoue, S.; Koshiro, K.; Yoshida, Y.; De Munck, J.; Nagakane, K.; Suzuki, K.; Sano, H.; Van Meerbeek, B., Hydrolytic stability of self-etch adhesives bonded to dentin. *Journal of Dental Research* **2005,** *84* (12), 1160-1164.

29. Fukuoka, A.; Koshiro, K.; Inoue, S.; Yoshida, Y.; Tanaka, T.; Ikeda, T.; Suzuki, K.; Sano, H.; Van Meerbeek, B., Hydrolytic Stability of One-step Self-etching Adhesives Bonded to Dentin. *Journal of Adhesive Dentistry* **2011,** *13* (3), 243-248.

30. Salz, U.; Burtscher, P.; Vogel, K.; Moszner, N.; Rheinberger, V., New adhesive monomers for dental application. *Abstracts of Papers of the American Chemical Society* **1997,** *214*, 175-POLY.

31. Nishiyama, N.; Suzuki, K.; Yoshida, H.; Teshima, H.; Nemoto, K., Hydrolytic stability of methacrylamide in acidic aqueous solution. *Biomaterials* **2004,** *25* (6), 965-969.

32. Moszner, N.; Zeuner, F.; Angermann, J.; Fischer, U. K.; Rheinberger, V., Monomers for adhesive polymers, 4 - Synthesis and radical polymerization of hydrolytically stable crosslinking monomers. *Macromolecular Materials and Engineering* **2003,** *288* (8), 621-628.

33. Zeuner, F.; Quint, S.; Geipel, F.; Moszner, N., A simple method for the preparation of functionalized steric hindered methacrylic acid esters and amides. *Synthetic Communications* **2004,** *34* (5), 767-774.

34. Moszner, N., New monomers for dental application. *Macromolecular Symposia* **2004,** *217* (1), 63-75.

35. Moszner, N.; Salz, U.; Zimmermann, J., Chemical aspects of self-etching enamel-dentin adhesives: A systematic review. *Dental Materials* **2005,** *21* (10), 895-910.

36. Van Meerbeek, B.; De Munck, J.; Yoshida, Y.; Inoue, S.; Vargas, M.; Vijay, P.; Van Landuyt, K.; Lambrechts, P.; Vanherle, G., Buonocore Memorial Lecture - Adhesion to enamel and dentin: Current status and future challenges. *Operative Dentistry* **2003,** *28* (3), 215-235.

37. Sezinando, A., Looking for the ideal adhesive - A Review. *Rev Port Estomatol Med Dent Cir Maxilofac.* **2014,** *55* (4), 194-206.

38. Podgórski, M.; Becka, E.; Chatani, S.; Claudino, M.; Bowman, C. N., Ester-free thiol-X resins: new materials with enhanced mechanical behavior and solvent resistance. *Polym. Chem.* **2015,** *6* (12), 2234-2240.

39. Esfandiari, P.; Ligon, S. C.; Lagref, J. J.; Frantz, R.; Cherkaoui, Z.; Liska, R., Efficient Stabilization of Thiol–ene Formulations in Radical Photopolymerization. *Journal of Polymer Science Part A: Polymer Chemistry* **2013,** *51* (20), 4261-4266.

Chapter 4

Hexaarylbiimidazoles as Efficient Photoinhibitors of Free-Radical Chain-Growth Photopolymerizations

4.1 Original Publication information

Parts of this chapter have been published in the following peer-reviewed publication: M.P. De Beer*; **H.L. Van der Laan***; M.A. Cole; R.J. Whelan; M.A. Burns; and T.F. Scott; Rapid, continuous additive manufacturing by volumetric polymerization inhibition patterning. *Science Advances,* **2019**, *5,* eaau8723

*M.P. De Beer and H.L. Van der Laan contributed equally.

4.2 Abstract

Contemporary, layer-wise stereolithographic additive manufacturing approaches afford sluggish print rates and often yield structures with ridged surfaces; in contrast continuous stereolithographic 3D printing overcomes the layer-wise operation of conventional devices, greatly increasing achievable print speeds and generating objects with smooth surfaces. Here, we develop and demonstrate a novel chemistry for rapid and continuous stereolithographic additive manufacturing by employing two-color irradiation of resin formulations containing complementary photo-initiator and photo-inhibitor species. In this approach, photo patterned polymerization inhibition volumes generated by irradiation at one wavelength spatially confine the region photopolymerized by a second, concurrent

irradiation wavelength. To address the limitations presented by the hexaarylbiimidazole photoinhibitor diffusion-limited covalently linked hexaarylbiimidazole photoinhibitors were prepared. Through these species, sharper photoinhibition transitions were achieved, at the cost of inhibition efficacy.

4.3 Introduction

Additive manufacturing (AM) methods enable facile fabrication of exceptionally complex objects with internal features unobtainable by conventional methods.[1] Commonly called 3D printing, these technologies typically produce three-dimensional structures by successive addition of thin layers of material. The simple operation and near limitless design choice has made AM very attractive for producing custom and prototype parts finding utility in applications ranging from the fabrication of bespoke medical devices[2-4] and athletic equipment tailored to an individual's anatomy,[5] to the low volume production of automotive and aerospace components[6]. A wide variety of materials, including thermoplastics, polymeric resins and inorganic powders, have been employed as AM media for methods ranging from material extrusion[7-9] to powder bed fusion[10] and binder jetting.[11] A particular method of interest, stereolithographic AM (SL or SLA),[12, 13] uses photopolymer resin and a patterned illumination source to cure cross-sectional layers of the desired geometry. The speed of many layer-by-layer SLA devices is, depending on the build platform translation direction, limited either by adhesion of cured polymer to the projection window or by resin surface disturbances, necessitating time-consuming separation or recoating steps between successive layers. Consequently, the print speeds in these systems range from only a few millimeters to several centimeters per hour. The recently-described continuous liquid interface production (CLIP) technique [14-16]

addresses this deficiency by employing an oxygen-permeable projection window to create a thin, polymerization-free resin layer (dead zone) adjacent to the projection window, enabling continuous part production at translation speeds of several hundred millimeters per hour. Unfortunately, the dependency on diffusion of molecular oxygen into the photopolymer resin dictates the success of formulations, as the dead zone thickness strongly depends on monomer viscosity and reactivity, which in turn limits vertical print rates through diminished resin reflow capability. Ultimately contemporary AM techniques prove to be ill-suited for high-throughput manufacturing through stereolithography.

HABIs exhibit several attributes favoring their potential as universal photoinhibitors of radical-mediated, chain-growth polymerizations, including their favorable absorbance spectra and the inability of HABI-derived lophyl radicals to directly initiate polymerization of (meth)acrylates,[17, 18] greatly expanding the compatible monomer palette. As negligible polymerization is observed, this suggests that the HABI does not produce polymerization rate-retarding chain transfer reactions. Note that other two-color irradiation schemes have been demonstrated previously for sub-diffraction, direct-write photolithography[19-21]. These systems used CQ and EDAB as a blue light photoinitiator system and tetraethylthiuram disulfide (TETD) as a UV-active photoinhibitor. Unfortunately, the utility of TETD in rapid additive manufacturing is hindered by its participation in chain transfer reactions with propagating radical species,[22] resulting in significantly reduced photopolymerization rates at raised TETD concentrations even under exclusively photoinitiating irradiation, while co-irradiation at the photoinhibition wavelength yields reduced polymerization rates but does not

completely cease polymerization.[19] Moreover, TETD has only been shown to effectively inhibit methacrylate resins, limiting the palette of compatible monomers.

In order to address the deficiencies presented by time-consuming delamination, recoating, and repositioning in contemporary stereolithographic AM without the limitations imposed by oxygen inhibition, we hypothesized that the two-color photoinitiation/photoinhibition schemes employed previously could serve to create a polymerization-free “inhibition zone” through dual projection of near-UV and blue light. Whilst TETD is ill-suited for this purpose, we propose that HABIs could serve this purpose well owing to their inability to directly initiate (meth)acrylate formulations while generating stable, long-lived organic free radicals.

4.4 Experimental

4.4.1 Materials

Triethylene glycol divinyl ether (TEGDVE), Ethoxylayed bisphenol A diacrylate (BPAEDA), 2-mercaptobenzothiazole (2-MBT) benzil, 1,8-diiodonapthtalene, potassium ferricyanide, α,α-dichloromethyl methyl ether, lithium aluminum hydride, and Tetrahydrofuran were obtained from Sigma-Aldrich, (St. Louis, MO), 4-formylphenylboronic acid, and palladium(0) tetrakis(triphenylphosphine) were obtained from Oakwood Products (Estill, SC), ammonium acetate, acetic acid, potassium hydroxide, benzene, ethanol, titanium(IV)chloride, DDQ, chlorobenzene, aluminum chloride, oxalyl chloride, N-(n-propyl)maleimide (NPM), and methylene chloride were obtained from Fisher Scientific (Hampton, NH), [2.2] paracyclophane was obtained from AK Scientific (Union City, CA), 2-chloro-4-formylphenylboronic acid was obtained from AOBChem (Los Angeles, CA), 2,2’-Bis(2-chlorophenyl)-4,4’,5,5’-tetraphenyl-1,2’-

biimidazole (*o*-Cl-HABI) was obtained from TCI America (Portland, OR), (±)-camphorquinone (CQ), ethyl 4-dimethylaminobenzoate (EDAB), triethylene glycol dimethacrylate (TEGDMA), and bisphenol A glycidyl methacrylate (bisGMA) were obtained as a sample from EssTech (Essington, PA). Anhydrous solvents were dried over 20% (w/v%) molecular sieves for at least 24 hours prior to use. All further chemicals were used as received.

TEGDMA and bisGMA were formulated as a mixture of 50 weight % (wt%) TEGDMA and 50 wt% bisGMA. NPM and TEGDVE were formulated in a manner such that the maleimide and vinyl ether groups were present in a 1:1 stoichiometric ratio. CQ and EDAB were used as the photoinitiator system, and HABIs as the photoinhibitors at the concentrations indicated. Owing to poor solubility in the monomers, the HABIs were dissolved in THF as a ~30 wt% solution before formulating the resins.

4.4.2 Methods

4.4.2.1 Photoinitiator & photoinhibitor formulations

The bisGMA/TEGDMA monomer mixture was formulated with 0.2 wt % CQ, 0.5 wt % EDAB, and 3 wt % *o*-Cl-HABI, or 0.2 wt % CQ, 0.5 wt % EDAB, and 5 wt % cyclophane HABI. BPAEDA was formulated with 0.2 wt % CQ, 0.5 wt % EDAB, and 2 wt % *o*-Cl-HABI. The TEGDVE/NPM monomer mixture was formulated with 1.0 wt % CQ, 0.5 wt % EDAB, and 5 wt % o-Cl-HABI. All monomer quantities were adjusted to account for the THF, in which o-Cl-HABI was dissolved. For the *o*-Cl-HABI photoinitiation testing, bisGMA/TEGDMA was formulated with 1 wt % *o*-Cl-HABI and either no co-initiator or 0.5 wt % of either EDAB or 2-MBT.

4.4.2.2 UV-Vis spectroscopy

UV-visible spectrophotometry was performed on 1 wt% solutions of the analyte in tetrahydrofuran using an Agilent Technologies Cary 60 UV-Vis spectrophotometer. Spectra were collected from 200 to 800 nm with 1 nm spacing on solutions using a 1 mm path length quartz cuvette in the dark.

4.4.2.3 Time-resolved Fourier Transform Infrared Spectroscopy

FTIR photopolymerization kinetics were performed on resin formulations introduced between NaCl crystal windows (International Crystal Laboratories) separated by spacers as indicated to maintain constant sample thickness during polymerization. Each sample was placed in a Thermo Scientific Nicolet 6700 FTIR spectrometer equipped with a horizontal transmission accessory, as described previously, and spectra were collected from 650 to 4000 cm^{-1} at a rate of 2 per second. The functional group conversion upon irradiation was determined by monitoring the disappearance of the peak area centered at 1635 cm^{-1} for the methacrylate stretch, 1636 cm^{-1} for the acrylate stretch, 1618 cm^{-1} for the vinyl ether stretch, and 829 cm^{-1} for the maleimide C=C double bond stretch. The respective sample thicknesses for the formulations were chosen to ensure that the functional group peaks remained within the linear regime of the instrument detector while affording good signal to noise and maintaining optically thin and isothermal polymerization conditions. All experiments were performed in triplicate, and the photoinitiator and photoinhibitor concentrations and irradiation intensities were as indicated.

4.4.2.4 Light source and intensity

Blue light was provided by a collimated, LED-based illumination source (Thorlabs M470L3-C1) with an emittance centered at 470 nm (FWHM 25 nm), used in combination with a current-adjustable LED driver (Thorlabs LEDD1B) for intensity control. UV light was provided by a UV spot curing system (Omnicure LX500, Excelitas Technologies) equipped with an Omnicure LED MAX head with an emittance centered at 365 nm. Irradiation intensities were measured with an International Light IL1400A radiometer equipped with a GaAsP Detector (model SEL005), a 10× attenuation neutral density filter (model QNDS1), and a quartz diffuser (model W).

4.4.2.5 NMR Spectroscopy

^{1}H-NMR spectra of the synthesized materials were acquired in $CDCl_3$ or DMSO-d6 as noted on a Varian MR400 spectrometer operating at 400 MHz. The chemical shift data are reported in units of δ (ppm) relative to tetramethylsilane (TMS) and referenced to residual solvent.

4.4.3 Synthesis

4.4.3.1 4,5-diphenyl-2-(4'-phenylboronic acid)imidazole.

4-Formylphenylboronic acid (3.37g), benzil (4.73g) , and ammonium acetate (26g) were dissolved in glacial acetic acid (150 mL) in a round bottom flask equipped with a reflux condenser. The solution was heated to 125°C stirred for 24 hours and was allowed to cool to room temperature. Shortly following the heating, a white precipitate formed, which was no longer present after 24 hours. Most solvent was removed under reduced pressure, and the mixture was transferred to an Erlenmeyer flask in an ice bath. Concentrated ammonium hydroxide solution was added dropwise to neutralize the

solution until a pH value of 8 was observed, and a precipitate formed. Ethyl acetate (200 mL) was added to the slurry and the yellow solution was washed 5 times with brine (100 mL). The organic phase was dried over sodium sulfate, and the solvent was removed under reduced pressure and high vacuum to yield a white powder. This powder was purified using silica column chromatography (ethyl acetate:hexanes = 7:3) to yield the desired product. ^{1}H NMR (400 MHz, $(CD_3)_2SO$) δ 12.73 (bs, 1H), 8.18-8.07 (m, 2H), 8.06-7.98 (m, 2H), 7.91-7.81 (d, 2H), 7.59-7.46 (m, 4H), 7.45-7.19 (m, 6H)

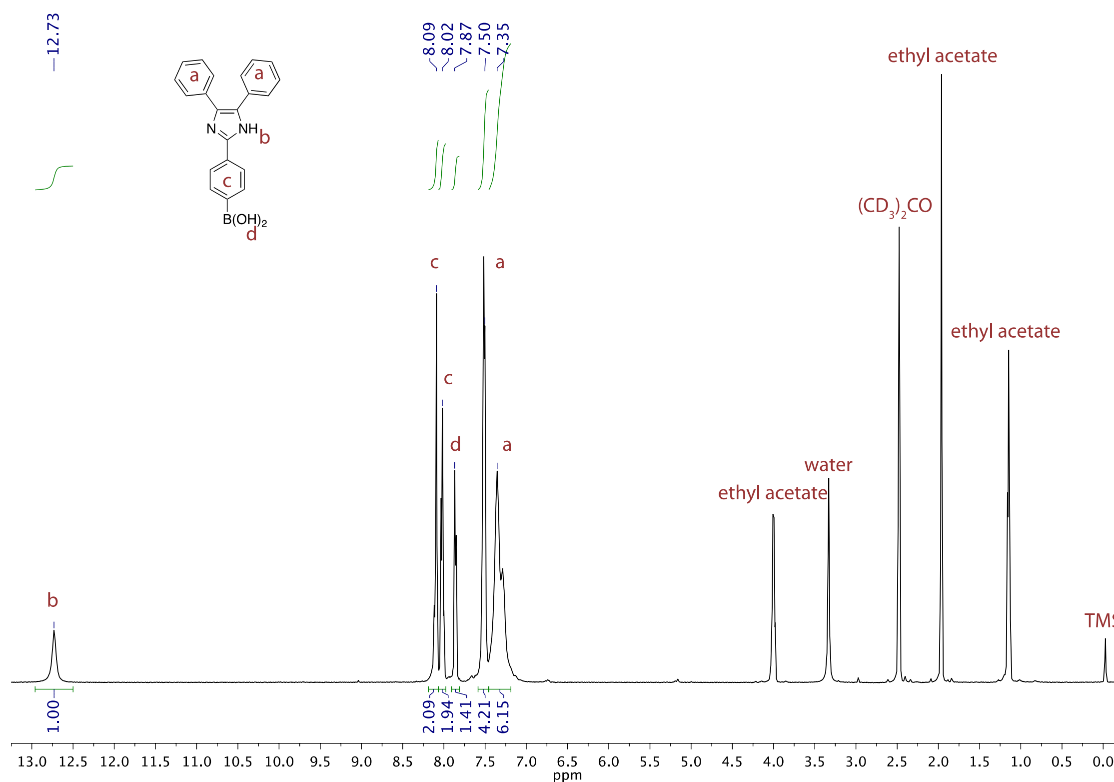

Figure 4.1 ^{1}H-NMR of 4,5-diphenyl-2-(4'-phenylboronic acid)imidazole

4.4.3.2 1,8-bislophine-naphthalene.

1,8-diiodonaphthalene (520 mg) was dissolved in 108 mL of a 1:1 mixture of benzene and ethanol in a 250 mL Schlenk flask equipped with a reflux condenser. To the mixture were added 4,5-diphenyl-2-(4'-phenylboronic acid)imidazole (1360 mg) and

palladium tetrakis(triphenylphosphine) (222 mg). The flask was wrapped in aluminum foil to exclude light and placed in an oil bath before purging with N_2 for 20 minutes. A solution of sodium carbonate (876 mg) in deionized water (35 mL) was added and the mixture was purged with N_2 for another 40 minutes. The solution was heated to 95°C and stirred overnight under inert atmosphere. The solution was then allowed to cool to room temperature, was added to 200 mL brine and 200 mL chloroform. The aqueous phase was extracted 3 times with chloroform (100 mL), and the combined organic phases were washed with water (200 mL) and brine (200 mL). The organic phase was briefly dried over sodium sulfate and the solvent was removed under reduced pressure. The resultant material was purified using silica column chromatography (hexanes:ethyl acetate = 7:3) to yield the desired diimidazole product as a yellow powder.

4.4.3.3 1,8-(2,4,5-triphenylimidazoyl)-naphthalene.

Potassium ferricyanide (1.9g) and potassium hydroxide (1.3g) were dissolved in 9 mL deionized water in a 20 mL vial equipped with a stir bar and a solvent-resistant cap. To this was added a solution of the diimidazole (137 mg) in benzene (9 mL). The vial was wrapped in aluminum foil to exclude light, and the mixture was stirred vigorously at room temperature for 2 hours. The organic phase turned a dark blue color shortly following stirring. Subsequently, the organic and aqueous phases were separated, and the organic phase was washed with water until the aqueous phase remained colorless, and the organic phase was then washed with brine. The organic phase was dried over sodium sulfate and the solvent was removed under reduced pressure to yield a green solid. Following purification through silica column chromatography, the green material turned yellow.

4.4.3.4 4,5-diphenyl-2-(2'-chloro-4'-phenylboronic acid)imidazole.

2-Chloro-4-formylphenylboronic acid (1.02), benzil (0.99g) , and ammonium acetate (3.07g) were dissolved in glacial acetic acid (30 mL) in a 2-neck flask equipped with a reflux condenser & bubbler. The solution was purged with N_2 for 1 hour, and the solution was heated to 100°C and stirred overnight. The reaction mixture was allowed to cool to room temperature, and most solvent was removed under reduced pressure. The mixture was transferred to an Erlenmeyer flask in an ice bath. Concentrated ammonium hydroxide solution was added dropwise to neutralize the solution until a pH value of 8 was observed, and a precipitate formed. Ethyl acetate (25 mL) was added to the slurry and separated. The aqueous phase was extracted 3 more times with ethyl acetate (30 mL), the combined organic phases were washed with brine (100 mL) and dried over sodium sulfate to yield a yellow powder. This powder was purified using silica column chromatography (hexanes: ethyl acetate = 8:2 followed by pure ethyl acetate) to yield the desired product as a yellow powder.

4.4.3.5 1,8-(2-(2'-chlorophenyl)lophine)-naphthalene.

1,8-diiodonaphthalene (1.02g) was dissolved in 200 mL of a 1:1 mixture of benzene and ethanol in a 500 mL Schlenk flask equipped with a reflux condenser. To the mixture were added 4,5-diphenyl-2-(2'-chloro-4'-phenylboronic acid)imidazole (3.2 g) and palladium tetrakis(triphenylphosphine) (250 mg). The flask was wrapped in aluminum foil to exclude light and placed in an oil bath before purging with N_2 for 1 hour. A solution of sodium carbonate (2 g) in deionized water (80 mL) was added and the mixture was purged with N_2 for another 30 minutes. The solution was heated to 100°C and stirred overnight under inert atmosphere. The solution was then allowed to cool to

room temperature, was added to 150 mL brine and 150 mL methylene chloride. The aqueous phase was extracted 3 times with methylene chloride (100 mL), and the combined organic phase was washed 2 times with brine (150 mL). The organic phase was briefly dried over sodium sulfate and the solvent was removed under reduced pressure. The resultant material was purified using silica column chromatography (hexanes:ethyl acetate = 8:2) to yield the desired diimidazole product as a yellow powder.

4.4.3.6 1,8-(4,5-diphenyl-2-(2'-chlorophenyl)imidazoyl)-naphthalene.

Potassium ferricyanide (1.9g) and potassium hydroxide (1.3g) were dissolved in 9 mL deionized water in a 20 mL vial equipped with a stir bar and a solvent-resistant cap. To this was added a solution of the diimidazole (137 mg) in benzene (9 mL). The vial was wrapped in aluminum foil to exclude light, and the mixture was stirred vigorously at room temperature for 2 hours. The organic phase turned a dark blue color shortly following stirring. Subsequently, the organic and aqueous phases were separated, and the organic phase was washed with water until the aqueous phase remained colorless, and the organic phase was then washed with brine. The organic phase was dried over sodium sulfate and the solvent was removed under reduced pressure to yield a green solid. Following purification through silica column chromatography, the green material turned yellow.

4.4.3.7 [2.2]paracyclophane-4-glyoxylacid chloride.

Aluminum chloride (10.5 g) was added to anhydrous methylene chloride (120 mL) in a 500 mL 3-neck flask equipped with a liquid addition funnel, a solids addition funnel, and a bubbler. The suspension was cooled to -10°C. A solution of oxalyl chloride (10.06 g) in anhydrous methylene chloride (9 mL) was added dropwise over 10 minutes.

After an additional 10 minutes, [2.2]paracyclophane was added slowly through a solids addition funnel, and the solution immediately turned a dark red color. Following complete addition the mixture was stirred an additional 20 minutes at -10°C. The mixture was then poured onto ice (200 g) in a separation funnel. The red solution turned yellow upon contact with the ice, the ice was allowed to melt, the aqueous and organic phases separated, and the aqueous phase was extracted 4 times with methylene chloride (100 mL). The combined organic phase was dried over sodium sulfate, and the solvent was removed under reduced pressure to yield the desired product as a yellow powder. The product was used without further purification.

4.4.3.8 [2.2]Paracyclophane-4-carboxylate methyl ester.

[2.2]paracyclophane-4-glyoxylacid chloride obtained from the previous reaction was dissolved in chlorobenzene (100 mL) in a 250 mL round bottom flask equipped with a reflux condenser. The solution was heated to 150°C and stirred for 3 hours. Significant gas development was observed upon heating. After cooling to room temperature the solvent was removed under reduced pressure. 100 mL of methanol was added to the flask, and the mixture was stirred under reflux for 3 hours. After cooling to room temperature the solvent was removed under reduced pressure, and the product was purified through silica column chromatography (toluene) to yield desired product was an off-white powder.

4.4.3.9 [2.2]Paracyclophane-4-carbaldehyde-9-carboxylate methyl ester.

[2.2]Paracyclophane-4-carboxylate methyl ester (5 g) was dissolved in anhydrous methylene chloride (300 mL) in a 1 L 3-neck flask equipped with 2 addition funnels and a bubbler. The solution was cooled to -10°C and purged with N_2 for 45 minutes.

Titanium(IV) chloride (9 mL) was added dropwise over 10 minutes. The solution turned brown immediately following contact with the titanium(IV) chloride. Following complete addition, α,α-dichloromethyl methyl ether (7.5 mL) was added dropwise over 30 minutes. The solution was stirred overnight and allowed to warm up to room temperature. The solution was poured onto 100g ice in a separation funnel. The reaction mixture reacted violently with the ice and resulted in the formation of a white precipitate. The ice was allowed to melt, and the organic and aqueous phases were separated. The aqueous phase was extracted twice with methylene chloride (50 mL), and the combined organic phase was washed with saturated sodium bicarbonate (100 mL), water (100 mL), and brine (100 mL). The organic phase was dried over sodium sulfate, filtered, and concentrated under reduced pressure. The concentrate was filtered over a silica plug with methylene chloride. The solvent was removed under reduced pressure, and the resultant powder was recrystallized from cyclohexane (170 mL).

4.4.3.10 [2.2]Paracyclophane-4,9-dimethylene alcohol.

[2.2]Paracyclophane-4-carbaldehyde-9-carboxylate methyl ester (3.75 g) was dissolved in anhydrous THF (250 mL) in a 500 mL 2-neck flask equipped with a bubbler and a reflux condenser. The solution was purged with N_2 for 30 minutes, after which lithium aluminum hydride (1.25 g) was added. The suspension was heated to 60°C and was stirred for 6 hours. The suspension was allowed to cool to room temperature, and the excess lithium aluminum hydride was quenched through careful addition of wet ethyl acetate. Hydrochloric acid (3M) was added until all precipitate was dissolved. The aqueous phase was extracted 3 times with methylene chloride (100 mL), the combined

organic phase was dried over sodium sulfate, and removal of the solvent under reduced pressure yielded a white powder, which was used without further purification.

4.4.3.11 [2.2]Paracyclophane-4,9-dicarbaldehyde.

[2.2]Paracyclophane-4,9-dimethylene alcohol was dissolved in anhydrous 1,4-dioxane (100 mL) in a 500 mL 2-neck flask equipped with an addition funnel. A solution of 2,3-dichloro-5,6-dicyano-1,4-benzoquinone (2.5 g) in 1,4-dioxane (100 mL) was added dropwise over the course of 30 minutes. A precipitate formed following addition of DDQ, and the suspension was stirred at room temperature for 3 hours. The reaction mixture was filtered, and the solvent removed under reduced pressure to yield a yellow powder. The yellow powder was purified using silica column chromatography (cyclohexane: ethyl acetate = 5:1) to yield the desired dialdehyde.

4.4.3.12 Pseudogem-Bis(4,5-diphenyl-1H-imidazol-2-yl)[2.2]paracyclophane.

[2.2]Paracyclophane-4,9-dicarbaldehyde (442 mg), benzil (707 mg), and ammonium acetate (3328 mg) were dissolved in glacial acetic acid (16 mL) in a 20 mL vial equipped with a stir bar and a solvent-resistant cap. The vial was wrapped in aluminum foil to exclude light, placed in an oil bath, and heated to 90°C. After stirring for 2 days, the solution was cooled on ice, neutralized to pH = 8 with concentrated ammonium hydroxide. The formed precipitate was filtered off and washed with water. Following unsuccessful recrystallization of the residue from ethanol, the product was purified through silica column chromatography (hexanes:ethyl acetate = 7:3), which yielded the desired diimidazole as a yellow powder.

4.4.3.13 Pseudogem-Bis(diphenylimidazole)[2.2]paracyclophane

Pseudogem-Bis(4,5-diphenyl-1H-imidazol-2-yl)[2.2]paracyclophane (44 mg) was dissolved in benzene (40 mL) in a 100 mL 2-neck flask equipped with a bubbler. The solution was purged with N2 for 30 minutes, after which a solution of potassium ferricyanide (2.8 g) and potassium hydroxide (1.3 g) in water (30 mL) was added. The resultant emulsion was stirred vigorously under protective atmosphere and in the dark for 2 hours. Then, the organic and aqueous phases were separated, and the aqueous phase was washed several times with benzene until the organic phase remained colorless. The combined organic phase was washed several times with brine until the brine remained colorless. The organic phase was dried over sodium sulfate, and removal of the solvent under reduced pressure yielded a yellow powder. This material was further purified using silica column chromatography (hexanes:ethyl acetate = 7:3) to yield the desired hexaarylbiimidazole as a yellow powder.

4.5 Results and Discussion

4.5.1 o-Cl-HABI as a photoinhibitor of free-radical chain-growth polymerizations

Two-color photoinhibition of free-radical chain-growth photopolymerizations was explored by establishing optical compatibility between the candidate photoinhibiting agents and the photoinitiators. Independent control over photoinitiation and photoinhibition necessitates that the candidate agents have complementary absorbance spectra. As Figure 4.2 indicates, *o*-Cl-HABI exhibits very weak absorbance in the blue region of the spectrum and moderate absorbance in the near UV, complementing the absorbance spectrum of the photoinitiator CQ which absorbs blue light (λ_{max} = 470 nm) but absorbs poorly in the near UV. This minimal overlap in the absorbance spectra of CQ

and *o*-Cl-HABI in the near UV to blue region of the spectrum enables selective activation of CQ though blue light irradiation (λ ≈ 470 nm), while *o*-Cl-HABI can be exclusively activated through near-UV irradiation (λ ≈ 365 nm).

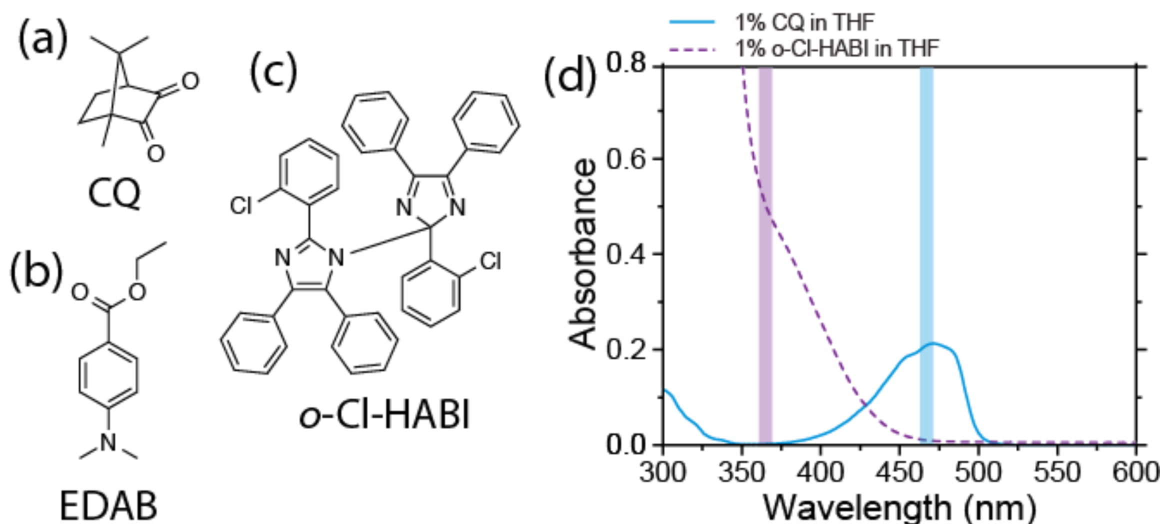

Figure 4.2 Structures of (a) photoinitiator CQ, (b) co-initiator EDAB, (c) photoinhibitor o-Cl-HABI. (d) UV-Vis absorbance spectrum of CQ (blue solid line) and o-Cl-HABI (violet dashed line) in THF. The UV and blue wavelengths used in the two-color irradiation system are highlighted by the violet and blue vertical bars, respectively.

Previous work has demonstrated that *o*-Cl-HABI by itself is unable to photoinitiate the chain-growth polymerizations of methacrylates.[18, 23] Despite this, *o*-Cl-HABI was commercialized as a photoinitiator by DuPont in their Dylux products as in the presence of a suitable, hydrogen-donating co-initiator *o*-Cl-HABI can effectively and efficiently photoinitiate chain-growth polymerizations. The transient lophyl radical species that forms upon photoexcitation of *o*-Cl-HABI (Figure 4.3a) displays a characteristic UV-Vis absorbance spectrum with a maximum absorbance at 554 nm.[24] Through monitoring the absorbance at this wavelength, a convenient assessment of the lophyl radicals in solution can be made. Through irradiating *o*-Cl-HABI in solution by itself, in combination with EDAB, and in combination with the hydrogen-donating co-

initiator 2-mercaptobenzothiazole[25] (2-MBT) it is observed that *o*-Cl-HABI under irradiation does not appear to interact with EDAB, as the absorbance decay profile is similar to that of *o*-Cl-HABI. In contrast, the solution containing 2-MBT did not show significant absorbance at 554 nm under near-UV irradiation.

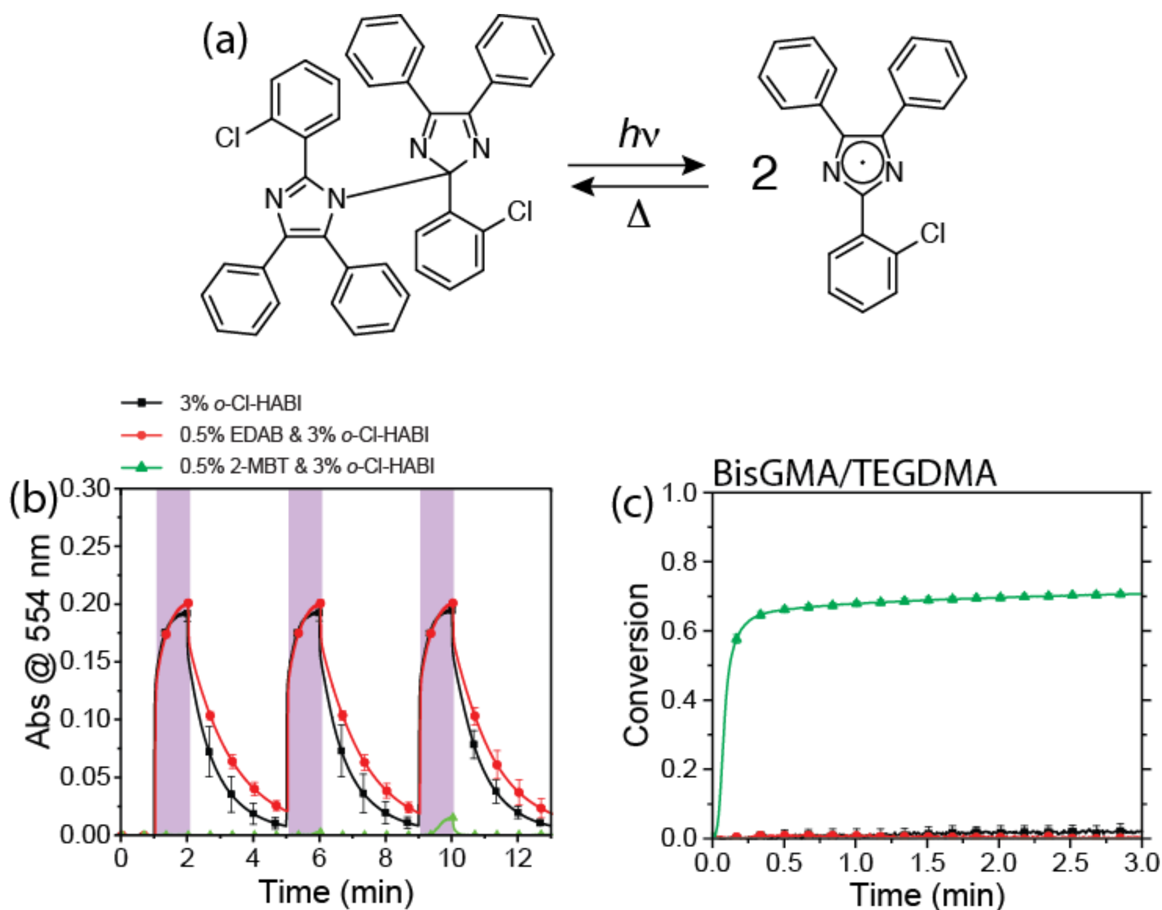

Figure 4.3 (a) Photodissociation and thermal recombination reaction of o-Cl-HABI (b) absorbance at 554 nm of o-Cl-HABI, o-Cl-HABI and EDAB, and o-Cl-HABI and 2-MBT under irradiation with 365 nm @ 30 mW/cm² as indicated by the vertical violet bars, and (b) methacrylate conversion vs time under continuous irradiation with 365 nm @ 30 mW/cm² for formulations containing o-Cl-, o-Cl-HABI and EDAB, and o-Cl-HABI and 2-MBT

A further examination of the *o*-Cl-HABI interaction with co-initiators was performed through monitoring conversion of *o*-Cl-HABI/co-initiator methacrylate formulations with time-resolved FTIR spectroscopy. Lacking a co-initiator, or in the

presence of EDAB, no significant bisGMA/TEGDMA conversion was observed under continuous near-UV irradiation (Figure 4.3c). Inversely, the formulation containing 2-MBT showed efficient photoinitiation and rapid polymerization following near-UV irradiation. Thus demonstrating *o*-Cl-HABI as a very effective photoinitiator with an appropriate co-initiator, but unable to photoinitiate this methacrylate formulation with EDAB.

Following the optical and chemical compatibility of *o*-Cl-HABI with the CQ/EDAB photoinitiator system, the components were formulated together to explore the efficacy of *o*-Cl-HABI as a photoinhibitor of free-radical chain-growth photopolymerizations. In these formulations, CQ was activated through irradiation at 470 nm, and in the excited state undergoes an electron-transfer/hydrogen abstraction reaction resulting in initiating free radicals. Irradiation with near-UV light on the other hand, photocleaves *o*-Cl-HABI, which subsequently dissociates into lophyl radicals, which serve to terminate active polymer chains. The monomers shown in Figure 4.4a-e were examined, and include acrylates, methacrylates, and an electron acceptor/electron donor maleimide/vinyl ether formulation. Through time-resolved FTIR spectroscopy, the double bond conversion profiles were obtained. For each of the monomer types, photopolymerization proceeded rapidly under blue light irradiation, demonstrating that under these conditions *o*-Cl-HABI does not interfere with the free radical photopolymerization. Exposure of these formulations to near-UV irradiation leads to negligible polymerization of the acrylate and methacrylate monomers. Notably, this is in stark contrast to the system developed by Scott *et al.*, whom observed non-zero methacrylate conversion following activation of their TETD photoinhibitor.[19] Minor

curing of the maleimide/vinyl ether was observed. Following exposure of the formulations to blue and near-UV light concurrently, polymerization rates are significantly decreased relative to exclusive blue irradiation. While the polymerization of the acrylate and methacrylate approaches zero, efficacy of photoinhibition in the maleimide/vinyl ether formulation is decreased. A likely explanation for this observation is the *N*-(n-propyl)maleimide serving as a co-initiator to both *o*-Cl-HABI and CQ. NPM is known as a co-initiator for CQ through an electron transfer/hydrogen abstraction mechanism. With *o*-Cl-HABI capable of photoinitiating with hydrogen donating coinitiators,[25-27] it is likely that the high concentration of NPM in the formulation leads to some initiation by the lophyl radicals.

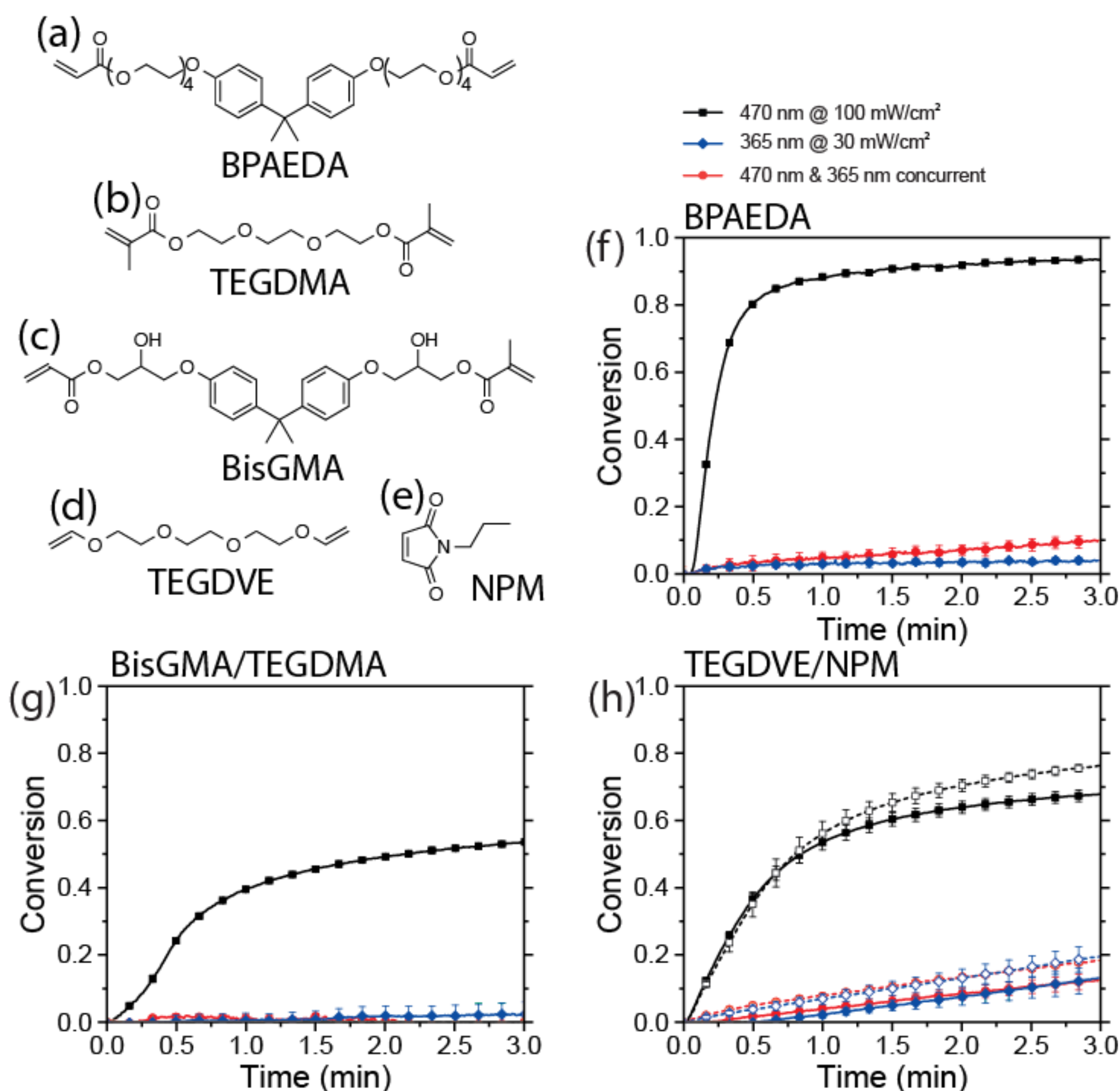

Figure 4.4 Structures of monomers examined (a) Bisphenol A ethoxylate diacrylate (BPAEDA; n=4), (b) triethylene glycol dimethacrylate (TEGDMA), (c) bisphenol A glycidyl dimethacrylate (bisGMA), (d) triethylene glycol divinyl ether (TEGDVE), (e) N-(n-propyl)maleimide (NPM), Alkene conversion versus time for resin formulations of (f) BPAEDA (g), bisGMA/TEGDMA, and (h) TEGDVE/NPM (vinyl ether and maleimide conversions denoted by solid and dashed lines, respectively). Continuous irradiation with exclusively 470 nm @ 100 mW/cm^2, 470 nm @ 100 mW/cm^2 & 365 nm @ 30 mW/cm^2, and 365 nm @ 30 mW/cm^2 as indicated.

Nevertheless, the potential and broad applicability of *o*-Cl-HABI as a free-radical chain-growth photopolymerization photoinhibitor is demonstrated by the variety of compatible monomer types. Further expansion of this chemistry to commercial acrylate and methacrylate resins is demonstrated in Figure 4.5. This two-color irradiation scheme

for photoinhibition has been explored previously. However the efficacy of TETD in that scheme was hindered by its participation in chain-transfer reactions with the propagating and non-zero polymerization upon exclusive near-UV irradiation. The resin scope was further limited by the inability of TETD to photoinhibit other monomer species, only being viable for the TEGDMA dimethacrylate.

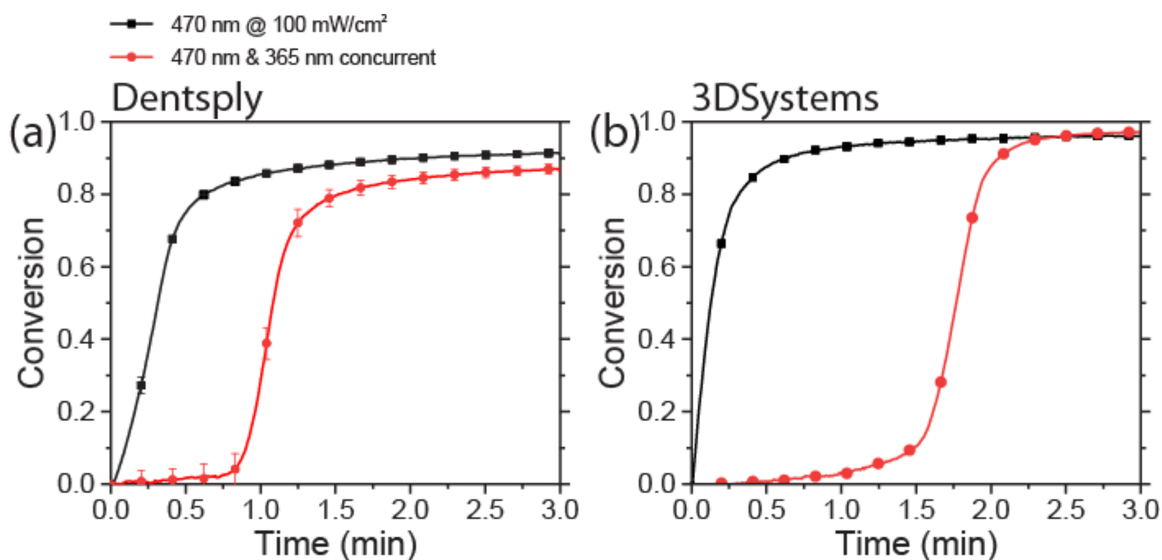

Figure 4.5 Alkene conversion versus time for commercial resin formulations received from, and (a) Dentsply, and (b) 3D systems. Continuous irradiation with exclusively 470 nm, and concurrent 470 nm & 365 nm

The concept of *o*-Cl-HABI photoinhibition in larger structures was demonstrated by using a photomask lithographic approach with an acrylate-based resin as shown in Figure 4.6. Resin contained between parallel glass slides was irradiated uniformly though a transparent substrate with the initiating wavelength. On the opposite site, the photoinhibiting wavelength was patterned through a photomask. As a result, resin not exposed to the near-UV light in the masked region cures and becomes a crosslinked and insoluble polymer network. The unmasked region however, is prevented from curing by

the lophyl radicals generated as a result of the near-UV light exposure, and the uncured resin can be washed away.

Figure 4.6 Schematic diagram of the photoinitiation-photoinhibition system using mask-based photolithography. The photomask used to pattern the photoinhibiting wavelength and a sample produced by using the photoinitiation-photoinhibition system.

With the successful demonstration of *o*-Cl-HABI as a photoinhibitor of free-radical chain-growth photopolymerizations through time-resolved FTIR spectroscopy and mask-based photolithography the photoinhibition system was adapted to function in a two-color continuous additive manufacturing setup, as shown in Figure 4.7a.

A unique aspect of this system is the use of a multi-color system to achieve volumetric patterning by the photochemical generation of both polymerization initiation

and polymerization inhibition species. Common amongst all contemporary SLA devices is the use of a single wavelength of light to initiate polymerization patterned in a plane. In contrast, we use one wavelength to photochemically activate polymerization and a second wavelength to inhibit that reaction. As demonstrated previously the lophyl radicals generated upon HABI photolysis efficiently inhibit radical-mediated, chain-growth polymerization and thus could be used to prevent polymerization adjacent to the illumination window.

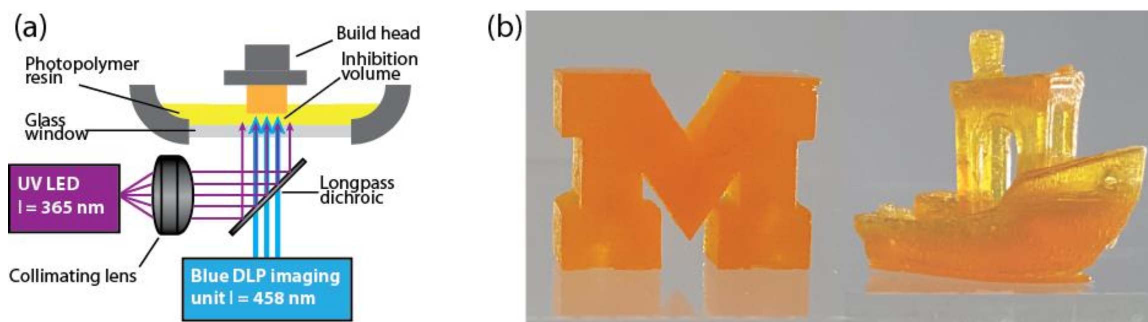

Figure 4.7 (a) Optical setup for two-color, stereolithographic AM by concurrent photopolymerization and photoinhibition. Near UV (365 nm) is superimposed onto patterned blue (458 nm) with a dichroic mirror and projected through a transparent window into a photopolymerizable resin vat. (b) A solid block M (left) and a 3DBenchy (right) printed using the two-color, stereolithographic AM. *Images courtesy of Martin de Beer.*

The thickness of the polymerization inhibition volume can be controlled by varying the ratio of the intensities of the two illuminating light sources. When both UV and blue light are supplied to the resin, an inhibition volume with no polymerization is generated adjacent to the window. Above this region, polymerization occurs allowing the continuous printing of objects, such as those shown in Figure 4.7 without deleterious window adhesion. Importantly, the inhibition volume thickness (i.e., the vertical distance into the resin from the transparent window in which no polymerization occurs) is dependent on the incident initiating and inhibiting light intensities. The development of

this two-color stereolithographic additive manufactring has various advantages. It allows for tailoring the inhibition zone to the reactivity of the resin, is compatible with various filler materials, and is not limited by diffusion rates of small molecules into the resin, which in turn enables higher viscosity resins to be printed.

Although the discussion on further developing the continuous additive manufacturing process is outside the scope of this work, evaluation and further development of the chemistry is not. As Figure 4.3b shows, the transient lophyl radicals originating from *o*-Cl-HABI photocleavage persist for minutes in solution post-irradiation. The impact of this lifetime on photopolymerizations can be seen in Figure 4.8 as demonstrated through time-resolved FTIR spectroscopy of a methacrylate-based resin under constant blue light irradiation with intermittent exposure to near-UV irradiation. Rapid polymerization proceeds upon visible light irradiation, while the accumulation of lophyl radicals during the 30-second UV irradiation window afford decreased polymerization rates. Upon cessation of UV irradiation, the polymerization rates recover after induction times of approximately 30 seconds owing to the relatively slow consumption of lophyl radicals by recombination. In a continuous additive manufacturing setting this behavior leads to a less defined inhibition volume and as a result sacrifices on resolution and vertical print rates, thus it would be desirable to employ related CQ/EDAB-compatible photoinhibitors that display significantly shorter lifetimes of the inhibiting species.

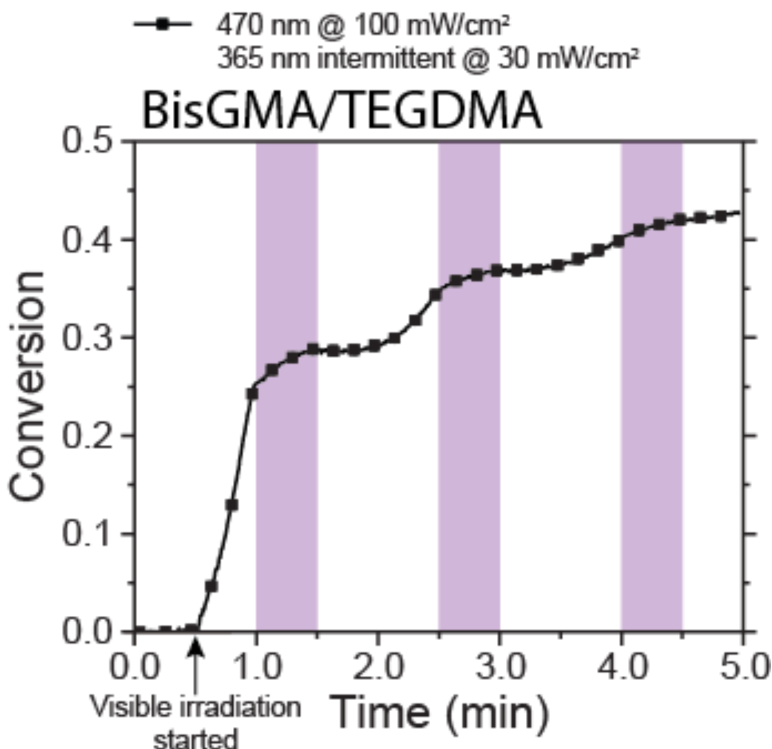

Figure 4.8 Wavelength selective photoinitiation and transient photoinhibition of methacrylate polymerization. Methacrylate conversion versus time for bisGMA/TEGDMA formulated with CQ/EDAB and o-Cl-HABI under continuous irradiation, starting at 0.5 minutes, with 470 nm @ 100 mW/cm^2 and intermittent irradiation with 365 nm @ 30 mW/cm^2 during the shaded periods as indicated.

4.5.2 Covalently linked, diffusion-limited HABIs as photoinhibitors

As the lifetime of the transient lophyl radical generated by photocleavage of *o*-Cl-HABI is limiting the rapid transition between polymerization and inhibition an alternative photoinhibitor was sought. Due to their relative inertness to the CQ/EDAB photoinitiation system, HABIs and lophyl radical chemistry lends itself well for this application. Unfortunately, dependence on diffusion of these stable radicals to recombine significantly prolongs their presence following irradiation. In recent years various covalently linked, diffusion-limited HABIs such as those in Figure 4.9 have been described in literature with half-lives in the order from microseconds to seconds.[28-32] The forced proximity and orientation of these HABIs through bridging moieties significantly

reduces their lifetimes in solution while maintaining the desired properties of lophyl radicals the photoinitiation/photoinhibition system.

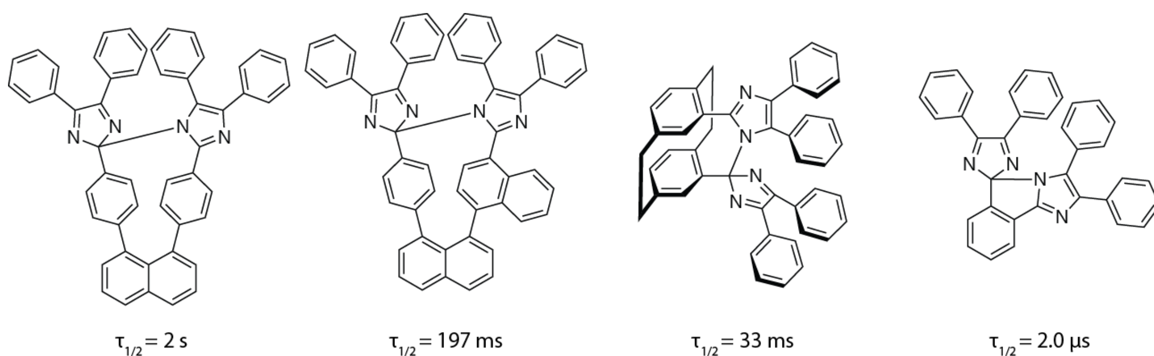

Figure 4.9 Covalently bound HABIs with different transient radical lifetimes[28-32]

Among the reported diffusion-limited HABIs, the naphthalene-linked 1,8-TPID-naphthalene was hypothesized to be a suitable replacement owing to its synthetic accessibility and seemingly suitable lifetime of 2 seconds.

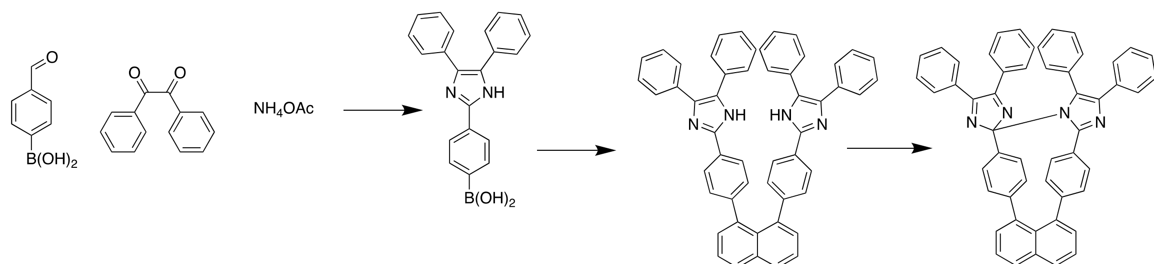

Scheme 4.1 Synthesis of 1,8-TPID-naphthalene. Reagents and conditions: (a) benzil, NH_4OAc, 125°C 24h, glacial acetic acid (b) 1,8-diiodonaphthalene, $Pd(PPh_3)_4$, Na_2CO_3, benzene/ethanol, (c) $K_3Fe(CN)_6$, KOH, 2h RT, benzene, water

The preparation of 1,8-TPID-naphthalene proved to be somewhat challenging. A major loss in yield and increased difficulty occurred as a result of unreported deboronylation of either 4-formylphenylboronic acid or 4,5-diphenyl-2-(4'-phenylboronic acid)imidazole. Attempts to circumvent this through a Suzuki coupling of 4-formylphenylbronic acid with 1,8-diiodonaphthalene were unsuccessful, likely as a

result of unfavorable electronics of the 4-formylphenylbronic acid for this reaction. The desired dilophine was eventually obtained and subsequently oxidized to the target HABI. The oxidation was near-quantitative as per ESI mass spectrometry, but it was observed that following either purification attempts through silica column chromatography or storage of the product lead to a change in color from green to yellow. Closer examination of the ESI mass spectrum suggested the addition of oxygen to 1,8-TPID-naphthalene, indicated by a mass increase of 32 as shown in Figure 4.10.

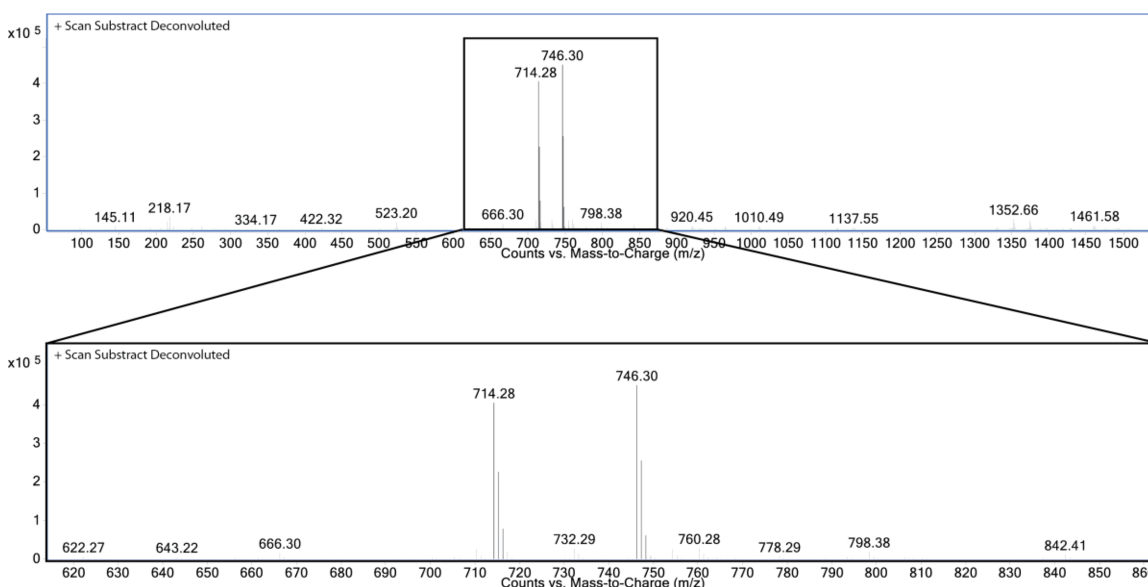

Figure 4.10 ESI mass spectrum of oxidated pincer showing 1,8-TPID-naphthalene at 714.28 and the oxidized species at 746.30 m/z

The oxidation and chemiluminescense of HABIs is a well-known and widely studied phenomenon.[33] Under ambient conditions however, most HABIs and their derived lophyl radicals do not show significant reactivity towards molecular oxygen, as the lophyl radicals lack the required proximity for a peroxidation with O_2. Hatano *et al.*[34] studied and reported on the peroxidation of 1,8-TPID-naphthalene, suggesting a degradation mechanism as shown in Figure 4.11. Following further studies of diffusion-

limited HABI reactions with O_2, it was suggested that a balance between lophyl radical proximity, orientation, and lifetime exists with regards to oxygen sensitivity.

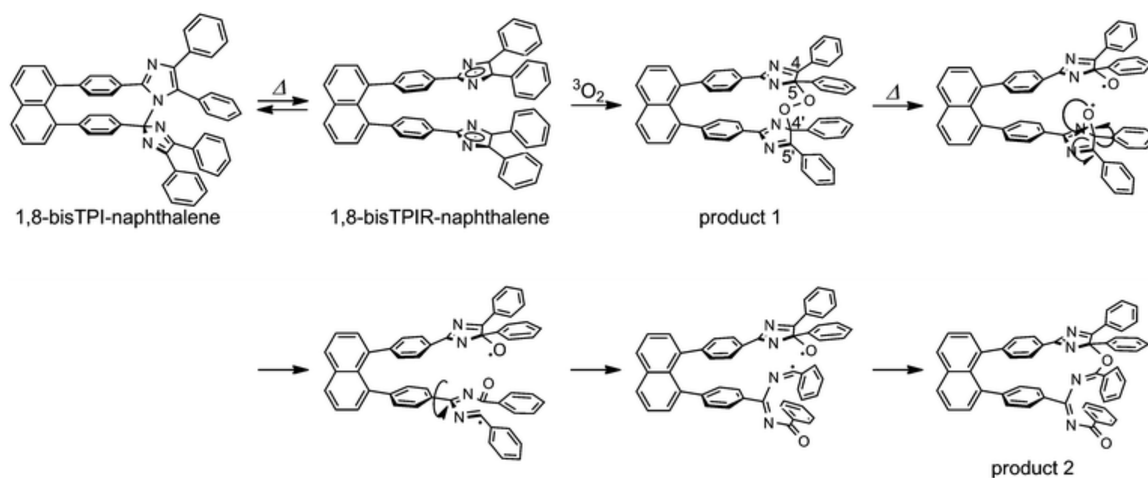

Figure 4.11 Proposed reaction of the naphthalene linked HABIs with molecular oxygen [34]

Thermal cleavage of 1,8-TPID-naphthalene into the lophyl radical was suspected to be the leading cause for the peroxidation and degradation. As the equilibrium of HABI to lophyl radical is influenced by substituents on the aryl groups, it was hypothesized that introducing such a moiety could lead to increased stability. As the dimerization of lophyl radicals is favored in *o*-Cl-HABI relative to unfunctionalized HABI,[35] a 1,8-TPID-naphthalene alternative bearing chlorines in the *ortho* position was prepared as described by Scheme 4.2.

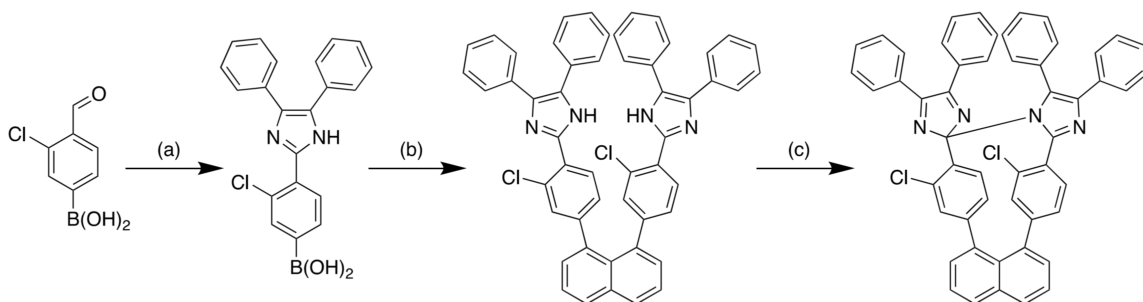

Scheme 4.2 Synthesis of o-chloro-1,8-TPID-naphthalene Reagents and conditions: (a) benzil, NH_4OAc, 125°C 24h, glacial acetic acid (b) 1,8-diiodonaphthalene, $Pd(PPh_3)_4$, Na_2CO_3, benzene/ethanol, (c) $K_3Fe(CN)_6$, KOH, 2h r.t., benzene, water

Unfortunately, the chlorine-bearing naphthalene-linked HABI displayed a similar sensitivity to O_2 as 1,8-TPID-naphthalene, preventing purification and study of this HABI as a photoinhibitor. Following the results obtained from the naphthalene-linked HABIs, a HABI linked through a cyclophane core was synthesized as an alternative. This cyclophane HABI was reported to be exceedingly insensitive to the presence of O_2,[29] being able to undergo thousands of cycles without degradation. The reported lifetime of this species lies in the order of tens of milliseconds which, while short, could allow for a significant contrast improvement in the continuous additive manufacturing process. The synthetic route towards the cyclophane HABI is shown in Scheme 4.3.

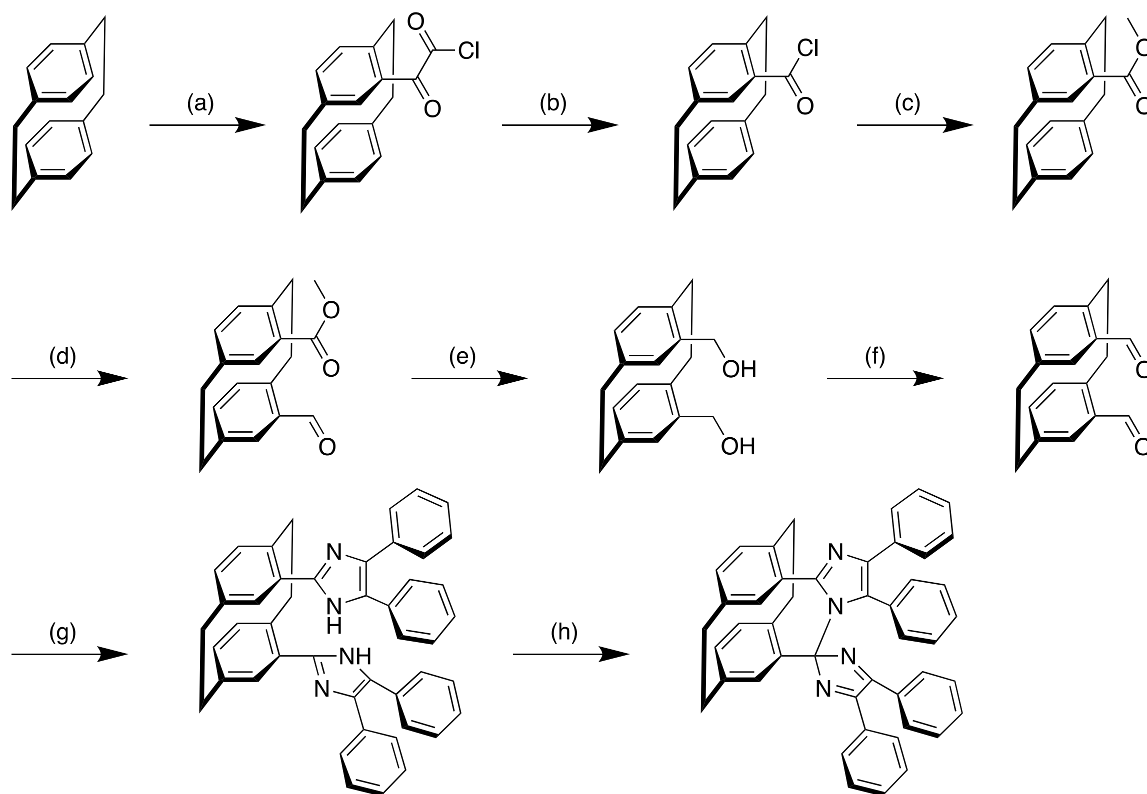

Scheme 4.3 Synthesis of cyclophane-linked pincer. Reagents and conditions: (a) oxalyl chloride, $AlCl_3$, -10°C, anhydrous methylene chloride (b) reflux 3h, chlorobenzene (c) reflux 3h, methanol (d) $TiCl_4$, α,α-dichloromethyl methyl ether, -10°C anhydrous methylene chloride (e) $LiAlH_4$, reflux 6h, anhydrous THF (f) DDQ, r.t. 3h, anhydrous 1,4-dioxane (g) benzil, NH_4OAc, 90°C 48h, glacial acetic acid (h) $K_3Fe(CN)_6$, KOH, 2h r.t., benzene, water

The preparation of the cyclophane HABI, although lengthy, mostly proceeded without issue. Of note is the reduction of [2.2]Paracyclophane-4-carbaldehyde-9-carboxylate methyl ester to [2.2]Paracyclophane-4,9-dimethylene alcohol. This reaction was monitored through disappearance of the methyl ester and aldehyde signals through ^{1}H-NMR. Following reaction completion and subsequent oxidation, two new signals appeared in the aldehyde region of the ^{1}H-NMR spectrum, as opposed to the expected single signal. Condensation to the lophines through the Debus-Radziszewski reaction yielded two distinct products, the expected dilophine, and an impurity with an m/z of 440 in ESI mass spectrometry. It appears there is a delicate balance between the rigorous

conditions required to reduce the [2.2]paracyclophane-4-carbaldehyde-9-carboxylate methyl ester and prevent excessive reduction of the obtained alcohols as in Scheme 4.4. Purification of the reduced cyclophane was ultimately successful and the subsequent condensation and oxidation into the hexaarylbiimidazole proceeded without further issues.

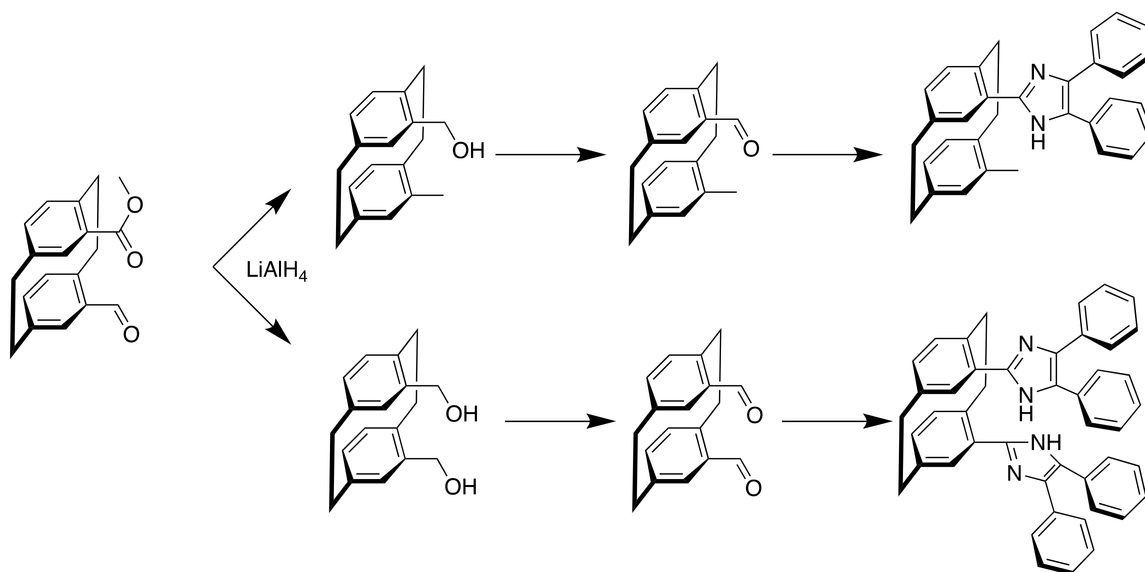

Scheme 4.4 Reaction pathways following $LiAlH_4$ reduction to diol and reduction to alcohol and methyl

As with *o*-Cl-HABI, the potential of the cyclophane HABI as a photoinhibitor was examined through UV-Vis spectroscopy and time-resolved FTIR spectroscopy. In the dark, the cyclophane HABI in THF shows an absorbance spectrum similar to *o*-cl-HABI, with minimal absorbance in the 470nm region, while showing moderate absorbance in the near-UV region. The strongly decreased lifetime of the cyclophane HABI lead to difficulty in determining the absorbance spectrum of the generated lophyl radicals following photocleavage as indicated in Figure 4.12.

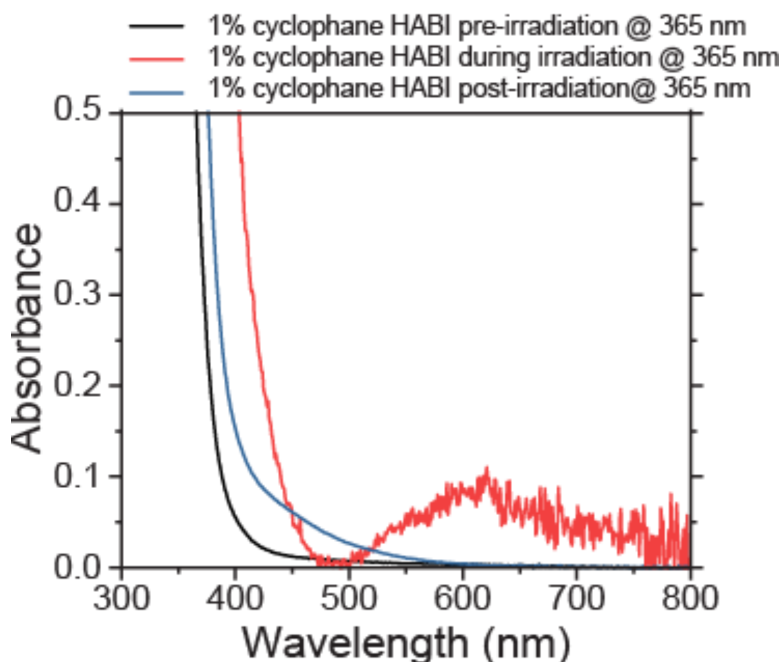

Figure 4.12 UV-Vis Spectra of (a) cyclophane HABI and (b) cyclophane HABI during irradiation and (c) post irradiation (both low and high intensity)

Only at high (>200 mW/cm^2) irradiation intensities at 365 nm the lophyl radical spectrum could be observed, as a result of limitations from the UV-Vis spectrometer used. The obtained spectra during irradiation showed a poor signal-noise ratio, likely due to the rapidly changing concentration in the sample. Furthermore, extended intense irradiation in order to obtain these spectra lead to rapid photobleaching of the cyclophane HABI, causing it to lose all photochromic activity. Due to the challenges faced, UV-Vis spectrometric demonstration of the lophyl radical lifetime, as shown for o-Cl-HABI Figure 4.3b could not be obtained.

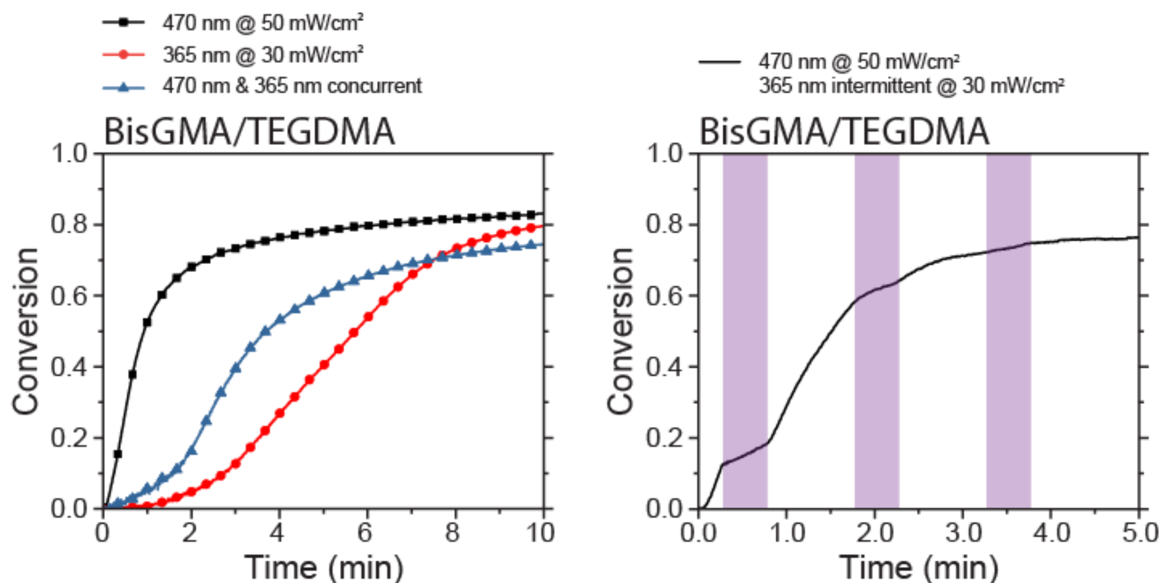

Figure 4.13 Kinetics experiments of cyclophane HABI as a photoinhibitor

Although unable to directly observe the lophyl radicals, the effect of the cyclophane HABI on photopolymerizations could be studied. TEGDMA/bisGMA formulations formulated with CQ, EDAB, and cyclophane HABI were subjected to blue and near-UV irradiation. As observed previously with *o*-Cl-HABI, the cyclophane HABI does not interfere with the CQ-initiated photopolymerization. Unlike *o*-Cl-HABI, extended irradiation with near-UV light did result in significant conversion of the methacrylate formulation, albeit following an induction period. Under concurrent blue and near-UV irradiation, the cyclophane HABI-derived lophyl radicals did demonstrate inhibitive behavior, but the formulation did show more significant conversion than in previous observations. While irradiated intermittently with near-UV under constant blue irradiation, the cyclophane HABI did demonstrate a significantly sharper transition from active inhibition to lack of inhibition. In less than a second following the cessation of near-UV irradiation, the methacrylate photopolymerization resumes. It should be noted that the conditions for photoinhibition in these formulations were far more favorable to

photoinhibition than those employed in the examination of *o*-Cl-HABI as the HABI content was increased from 3 to 5% and the blue irradiation intensity was lowered from 100 to 50 mW/cm^2. Additionally, the overall yield following eight synthetic steps in the preparation of the cyclophane HABI disfavors the potential of cyclophane HABI in continuous additive manufacturing as a result of the amount of HABI required.

4.6 Conclusion

Through a combination of UV-Vis spectroscopy and time-resolved FTIR spectroscopy, the hexaarylbiimidazole *o*-Cl-HABI was demonstrated as an efficient photoinhibitor of acrylate, methacrylate, and maleimide/vinyl ether photopolymerizations initiated by camphorquinone. In contrast to previously reported photoinhibitors *o*-Cl-HABI does not interact with the photopolymerization without prior activation. Following 2D photopatterning, this chemistry was successfully adopted in a rapid continuous additive manufacturing setup, allowing for vertical print rates up to 2 meters per hour. Diffusion-limited covalently linked HABIs were synthesized to address the extended lifetimes of the transient inhibiting lophyl radicals. These HABIs were successfully prepared, and demonstrated significantly sharper changes in polymerization rates through photopolymer kinetics. The increased recombination rates ultimately limited the efficacy of these diffusion-limited HABIs, demonstrating a clear balance between transient lophyl radical lifetime and photoinhibition potential.

4.7 Acknowledgements

The author thanks Martin de Beer and professor Mark Burns at the University of Michigan department of Chemical Engineering for the data and figures concerning the continuous two-color stereolithographic additive manufacturing.

4.8 References

1. Lipson, H.; Kurman, M., *Fabricated: The new world of 3D printing*. Wiley: Indianapolis, USA, 2013.

2. Liu, Q. B.; Leu, M. C.; Schmitt, S. M., Rapid prototyping in dentistry: technology and application. *International Journal of Advanced Manufacturing Technology* **2006,** *29* (3-4), 317-335.

3. Ventola, C. L., Medical Applications for 3D Printing: Current and Projected Uses. *Pharmacy and Therapeutics* **2014,** *39*, 704-711.

4. Chia, H. N.; Wu, B. M., Recent advances in 3D printing of biomaterials. *Journal of Biological Engineering* **2015,** *9*.

5. Wohlers, T.; Caffrey, T., Additive Manufacturing: Going Mainstream. *Manufacturing Engineering* **2013,** *150* (6), 67-73.

6. Manyika, J.; Chui, M.; Bughin, P.; Dobbs, R.; Bisson, P.; Marrs, A., Disruptive Technologies: Advances That Will Transform Life, Business, and the Global Economy. McKinsey Global Institute: 2013.

7. Belter, J. T.; Dollar, A. M., Strengthening of 3D Printed Fused Deposition Manufactured Parts Using the Fill Compositing Technique. *Plos One* **2015,** *10* (4).

8. Chen, H.; Yang, X.; Chen, L. T.; Wang, Y.; Sun, Y. C., Application of FDM three-dimensional printing technology in the digital manufacture of custom edentulous mandible trays. *Scientific Reports* **2016,** *6*.

9. Takagishi, K.; Umezu, S., Development of the Improving Process for the 3D Printed Structure. *Scientific Reports* **2017,** *7*.

10. Frazier, W. E., Metal Additive Manufacturing: A Review. *Journal of Materials Engineering and Performance* **2014,** *23* (6), 1917-1928.

11. Gao, W.; Zhang, Y. B.; Ramanujan, D.; Ramani, K.; Chen, Y.; Williams, C. B.; Wang, C. C. L.; Shin, Y. C.; Zhang, S.; Zavattieri, P. D., The status, challenges, and future of additive manufacturing in engineering. *Computer-Aided Design* **2015,** *69*, 65-89.

12. Sun, C.; Fang, N.; Wu, D. M.; Zhang, X., Projection micro-stereolithography using digital micro-mirror dynamic mask. *Sensors and Actuators a-Physical* **2005,** *121* (1), 113-120.

13. Bertsch, A.; Yezequel, J. Y.; Andre, J. C., Study of the spatial resolution of a new 3D microfabrication process: the microstereophotolithography using a dynamic mask-generator technique. *Journal of Photochemistry and Photobiology a-Chemistry* **1997,** *107* (1-3), 275-281.

14. Tumbleston, J. R.; Shirvanyants, D.; Ermoshkin, N.; Janusziewicz, R.; Johnson, A. R.; Kelly, D.; Chen, K.; Pinschmidt, R.; Rolland, J. P.; Ermoshkin, A.; Samulski, E. T.; DeSimone, J. M., Continuous liquid interface production of 3D objects. *Science* **2015,** *347* (6228), 1349-1352.

15. Janusziewicz, R.; Tumbleston, J. R.; Quintanilla, A. L.; Mecham, S. J.; DeSimone, J. M., Layerless fabrication with continuous liquid interface production.

Proceedings of the National Academy of Sciences of the United States of America **2016,** *113* (42), 11703-11708.

16. Zhu, W.; Tringale, K. R.; Woller, S. A.; You, S. T.; Johnson, S.; Shen, H. X.; Schimelman, J.; Whitney, M.; Steinauer, J.; Xu, W. Z.; Yaksh, T. L.; Nguyen, Q. T.; Chen, S. C., Rapid continuous 3D printing of customizable peripheral nerve guidance conduits. *Materials Today* **2018,** *21* (9), 951-959.

17. Allonas, X.; Obeid, H.; Fouassier, J. P.; Kaji, M.; Ichihashi, Y.; Murakami, Y., Photochemistry and polymerization efficiency of bis-imidazole based photoinitiator systems. *Journal of Photopolymer Science and Technology* **2003,** *16* (1), 123-128.

18. Ahn, D.; Sathe, S. S.; Clarkson, B. H.; Scott, T. F., Hexaarylbiimidazoles as visible light thiol–ene photoinitiators. *Dental Materials* **2015,** *31* (9), 1075-1089.

19. Scott, T. F.; Kowalski, B. A.; Sullivan, A. C.; Bowman, C. N.; McLeod, R. R., Two-Color Single-Photon Photoinitiation and Photoinhibition for Subdiffraction Photolithography. *Science* **2009,** *324* (5929), 913-917.

20. Fischer, J.; Wegener, M., Three-dimensional optical laser lithography beyond the diffraction limit. *Laser & Photonics Reviews* **2013,** *7* (1), 22-44.

21. Gan, Z. S.; Cao, Y. Y.; Evans, R. A.; Gu, M., Three-dimensional deep sub-diffraction optical beam lithography with 9 nm feature size. *Nature Communications* **2013,** *4*, 2061.

22. Lovell, L. G.; Elliott, B. J.; Brown, J. R.; Bowman, C. N., The effect of wavelength on the polymerization of multi(meth)acrylates with disulfide/benzilketal combinations. *Polymer* **2001,** *42* (2), 421-429.

23. Berdzinski, S.; Strehmel, N.; Lindauer, H.; Strehmel, V.; Strehmel, B., Extended mechanistic aspects on photoinitiated polymerization of 1,6-hexanediol diacrylate by hexaarylbisimidazoles and heterocyclic mercapto compounds. *Photochemical & Photobiological Sciences* **2014,** *13* (5), 789-798.

24. Sathe, S. S.; Ahn, D.; Scott, T. F., Re-examining the Photomediated Dissociation and Recombination Kinetics of Hexaarylbiimidazoles. *Industrial & Engineering Chemistry Research* **2015,** *54* (16), 4203-4212.

25. Eaton, D. F.; Horgan, A. G.; Horgan, J. P., Mechanism of coinitiation of photopolymerization of methyl methacrylate by hexaarylbiimidazole—hydrogen-atom donor combinations. The role of electron transfer v*s.* direct hydrogen-atom abstraction. *Journal of Photochemistry and Photobiology a-Chemistry* **1991,** *58* (3), 373-391.

26. Cescon, L. A.; Coraor, G. R.; Dessauer, R.; Deutsch, A. S.; Jackson, H. L.; Maclachl.A; Marcali, K.; Potrafke, E. M.; Read, R. E.; Silversm.Ef; Urban, E. J., Reactions of Triarylimidazoyl Free Radicals. *Journal of Organic Chemistry* **1971,** *36* (16), 2267-2272.

27. Monroe, B. M.; Weed, G. C., Photoinitiators for free-radical-initiated photoimaging systems. *Chemical Reviews* **1993,** *93* (1), 435-448.

28. Iwahori, F.; Hatano, S.; Abe, J., Rational design of a new class of diffusion-inhibited HABI with fast back-reaction. *Journal of Physical Organic Chemistry* **2007,** *20* (11), 857-863.

29. Kishimoto, Y.; Abe, J., A Fast Photochromic Molecule That Colors Only under UV Light. *Journal of the American Chemical Society* **2009,** *131* (12), 4227-4229.

30. Yamashita, H.; Abe, J., Photochromic Properties of 2.2 Paracyclophane-Bridged Imidazole Dimer with Increased Photosensitivity by Introducing Pyrenyl Moiety. *Journal of Physical Chemistry A* **2011,** *115* (46), 13332-13337.

31. Mutoh, K.; Sliwa, M.; Abe, J., Rapid Fluorescence Switching by Using a Fast Photochromic 2.2 Paracyclophane-Bridged lmidazole Dimer. *Journal of Physical Chemistry C* **2013,** *117* (9), 4808-4814.

32. Yamashita, H.; Abe, J., Pentaarylbiimidazole, PABI: an easily synthesized fast photochromic molecule with superior durability. *Chemical Communications* **2014,** *50* (62), 8468-8471.

33. Edkins, R. M.; Probert, M. R.; Fucke, K.; Robertson, C. M.; Howard, J. A. K.; Beeby, A., The formation of peroxide degradation products of photochromic triphenylimidazolyl radical-dimers. *Physical Chemistry Chemical Physics* **2013,** *15* (20), 7848-7853.

34. Hatano, S.; Abe, J., A peroxide-bridged imidazole dimer formed from a photochromic naphthalene-bridged imidazole dimer. *Physical Chemistry Chemical Physics* **2012,** *14* (16), 5855-5860.

35. Cescon, L. A.; Coraor, G. R.; Dessauer, R.; Silversm.Ef; Urban, E. J., Properties of Triarylimidazoyl Radicals and their Dimers. *Journal of Organic Chemistry* **1971,** *36* (16), 2262-2267.

Chapter 5

Dual-Wavelength Volumetric Photopolymerization Confinement Through Butyl Nitrite Free-Radical Photoinhibition

5.1 Original Publication Information

Parts of this chapter are in preparation for publication or have been published or in the following peer-reviewed papers:

H.L. Van der Laan; M.A. Burns, and T.F. Scott. Volumetric photopolymerization confinement through dual-wavelength photoinitiation and photoinhibition. *Manuscript in preparation*

5.2 Abstract

Conventional photolithographic rapid prototyping approaches typically achieve reaction confinement in depth through patterned irradiation of a photopolymer resin at a wavelength where the resin strongly absorbs such that only a very thin layer of material is solidified. Consequently, three-dimensional objects are fabricated by progressive, two-dimensional addition of material, curtailing fabrication rates and necessitating the incorporation of support structures to ensure the integrity of overhanging features. Here, we examine butyl nitrite as a UV-active photoinhibitor of blue light-induced radical-mediated photopolymerizations and explore its utilization to confine in depth the region polymerized in a volume of resin. Three-dimensional photopolymerization patterning in bulk resin is achieved through perpendicular irradiation patterns with blue and near-UV

light, complementing emergent volumetric 3D printing approaches. This system was expanded upon by inclusion of cationic photoinitiators and monomers to pave a way for support-free stereolithographic additive manufacturing and volumetric 3D printing.

5.3 Introduction

Although rapid prototyping by photolithography is generally achieved through two-dimensional material addition *via* either layer-wise[1, 2] or continuous[3-6] fabrication techniques, several alternative approaches have been described whereby photopolymerized objects are generated in bulk resin. For example, two-photon lithography has been extensively employed for the generation of intricate objects with sub-100 nm feature sizes;[7, 8] however, the high irradiation intensities necessary for two-photon absorption generally requires a focused, pulsed laser source, resulting in slow translation speeds[9] and correspondingly tedious fabrication rates. In contrast, interference lithography has been utilized to rapidly yield three-dimensional objects,[10] although the attainable geometries are limited to those afforded by periodic interference patterns. Recently, approaches to fabricate three dimensional, aperiodic objects by projecting patterned irradiation into a volume of photopolymer resin described.[11-13] These approaches, termed volumetric 3D printing, potentially eliminate the necessity of supports for overhanging features owing to the near-neutral buoyancy of the solidified material within the monomeric liquid; nevertheless, the fabrication of dense, complex structures remains challenging owing to the cumulative irradiation in non-target regions, leading to progressive loss of polymerization confinement. Nevertheless, as noted by Loterie *et al*., irradiation of the resin at a second wavelength to effect polymerization inhibition, concurrent with the patterned irradiation employed to induce

photopolymerization, would curtail this loss of polymerization confinement by accumulation of non-target light exposure.[12]

As noted by Junkers et al., the identification of a photo-cleavable, radical polymerization terminator that does not initiate polymerization is challenging owing to the necessary photolytic generation of a highly stabilized radical;[14] nevertheless, several examples have been described. Holdcroft and Guillet employed the laser flash photolysis of 2-naphthylmethyl 1-naphthylacetate at 308 nm to generate non-initiating naphthylmethyl radicals and terminate the radical-mediated polymerization of styrene.[15, 16] Having examined several photoinhibitor candidates, Karatekin et al. similarly utilized arylmethyl sulfone-based photoinhibitors to terminate and end-label growing polymer chains upon photolysis at 308 nm. Scott et al. previously reported a two-color irradiation scheme for sub-diffraction, direct-write photolithography whereby initiating species were generated by irradiation at one wavelength while inhibiting species were generated by irradiation at a second, independent wavelength, thereby reducing the rate of a radical-medicated polymerization upon co-irradiation at the second wavelength.[17] Unfortunately, although the photoinhibitor employed in that study, tetraethylthiuram disulfide (TETD), exhibited a favorable absorbance spectrum, it participated in a chain transfer reaction with propagating radical species,[18] resulting in reduced photopolymerization rates with raised TETD concentrations under exclusively photoinitiating irradiation. Moreover, although co-irradiation at the photoinhibition wavelength yielded reduced methacrylate polymerization rates, the photoinhibition did not completely cease polymerization.[17] To address these deficiencies, we sought alternative photoinhibitors that generated non-initiating radicals upon irradiation without being susceptible to chain transfer. In a recent

study on rapid, continuous stereolithographic additive manufacturing,[6] we established bis[2-(o-chlorophenyl)-4,5-diphenyl imidazole] (*o*-Cl-HABI) as an effective photoinhibitor of radical-mediated chain-growth photopolymerizations. Similar to TETD, the UV-vis absorbance spectrum of *o*-Cl-HABI complements that of camphorquinone (CQ), a blue light-active photoinitiator commonly employed in composite dental restorative materials.[19] Moreover, whereas lophyl radicals generated upon HABI photolysis have previously been found incapable of directly initiating (meth)acrylate polymerizations,[20, 21] we confirmed that *o*-Cl-HABI did not affect visible light photopolymerization absent UV photoactivation.[6] Nevertheless, while *o*-Cl-HABI was well suited for this purpose, the low recombination rates and visible light absorptivity of HABI-derived lophyl radicals may affect the utility of HABIs as photoinhibitors for multi-exposure, long pathlength applications.

Nitrites, both inorganic[22, 23] and organic,[24] are known to be inhibitors or retarders of free-radical chain-growth polymerization. Inorganic nitrite salts can react with water to form nitric oxide and nitrous oxide species,[23] while organic nitrites reportedly require activation to effect polymerization inhibition. Thermal decomposition of organic nitrites results in the formation of nitric oxide, an efficient inhibitor of radical-mediated polymerizations, and alkoxide radicals which can initiate polymerization. Higher molecular weight nitrites have been explored to inhibit styrene and butadiene polymerization during distillation, generally requiring low concentrations (0.0001-0.1%) to be effective.[24] Although alkyl nitrite photolysis has been extensively investigated,[22, 25, 26] studies into their use as photoinhibitors have been limited to an examination of butyl nitrite (BN) as a UV-activated inhibitor of thermally-initiated, radical-mediated chain-

growth polymerization. As summarized in Scheme 1, this UV-induced photoinhibition was attributed to the photolysis of BN, generating nitric oxide (1) which in turn affords a nitroso spin trap upon chain termination (2). This spin trap subsequently terminates a second propagating polymer chain (3), and the generated nitroxide radical terminates another active radical center (4). Thus, although the alkoxy radical also generated by alkyl nitrite photolysis acts to initiate polymerization (5), one photolysis event affords a net two inhibition events.

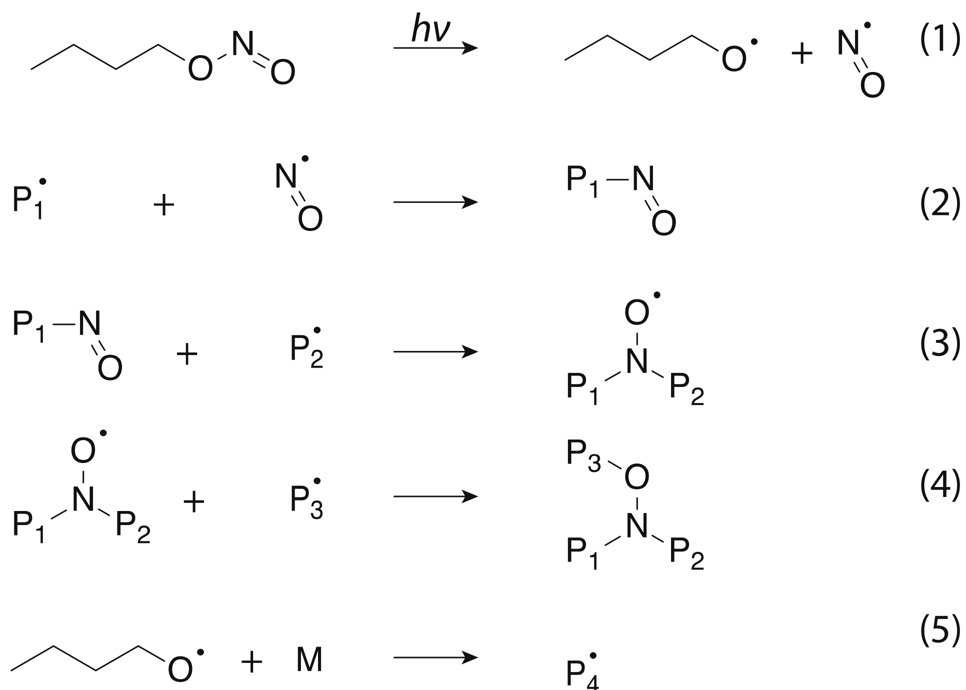

Scheme 5.1 Mechanism for radical-mediated polymerization initiation and termination upon butyl nitrite photolysis, affording a net two termination events.

Following the discovery of *o*-Cl-HABI in two-color photoinitiation/photoinhibition schemes we hypothesized that employing this type of irradiation patterns could improve the resolution and print times in volumetric

tomographic 3D printing approaches. Notably, the tomographic reconstruction approach relies on photopolymer exposure to a critical dose of curing light. As the two-color irradiation increases the threshold of solidification through blue light exposure, this scheme is very well suited for these techniques. However, the prolonged lifetime of the transient inhibiting lophyl radical species makes HABIs ill-suited for this purpose. Alkyl nitrites show no transient species and all fragments are consumed post-irradiation, and thus were hypothesized to be suitable substituents for *o*-Cl-HABI in volumetrically confined 3D printing.

Furthermore, as mentioned we recently developed a two-color irradiation approach to continuous stereolithographic additive manufacturing through *o*-Cl-HABI.[6] Most commonly 3D printing of photopolymers is achieved using stereolithography (SLA) in a layer-by-layer fashion. In order to obtain complex geometries with this approach, temporary support structures are added to the part to be printed. The dependency on such supports requires sufficient clearance to allow removal upon completion, and the printing of large overhangs and voids often leads to sagging or collapse of these structures. In extrusion 3D printing such as fused deposition manufacturing (FDM), as well as inkjet approaches support structures which are removed post-production through dissolution in solvent circumvent this need for sparse breakaway supports, and thus can be applied throughout the entire part and significantly eases printing overhangs and voids. However, within the of SLA of photopolymers, similar approaches to support structures are not practiced, not in the least due to the challenge to cure different materials using only a single exposure to one wavelength of light.

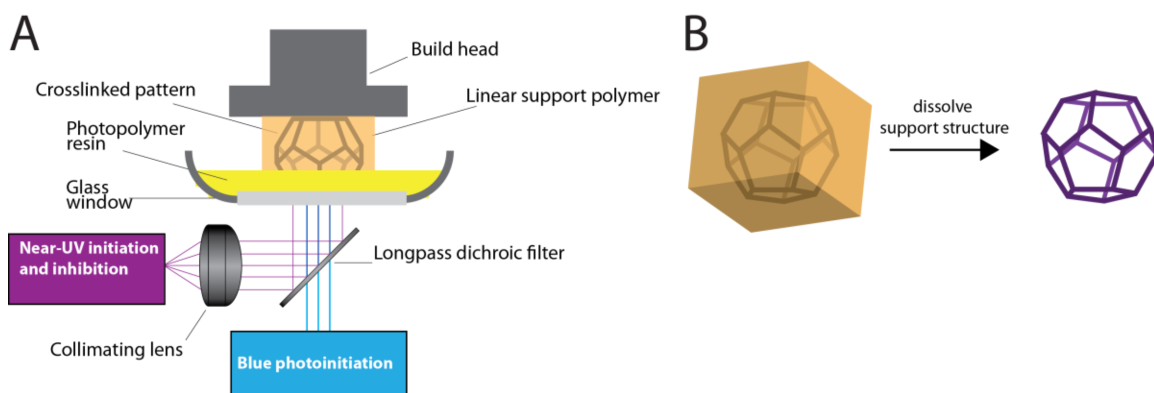

Figure 5.1 (a) SLA setup for two-color SLA support-free printing and (b) scheme for solvent removal of supports in complex, sparse structures

Employing photoinhibition chemistry in conjunction with cationic photopolymerization, could allow 3D multimaterial[27, 28] printing in combined cationic/free radical resins. Notably, through a 2-color irradiation scheme and choice of monomers, a system containing orthogonal free radical and cationic compatible monomers could selectively inhibit one type of polymerization mechanism. This would result in a 2-polymer system, of which a linear polymer would be soluble in solvent, whilst crosslinked polymer would not be. As a consequence, in a 3D printed structure, patterned light could allow for structurally stable supports that can be readily dissolved away following completion.

5.4 Experimental

5.4.1 Materials

2-color photoinitiation/photoinhibition was performed using (±)-Camphorquinone (CQ; Esstech Inc., Essington, PA) was used as a visible light-active photoinitiator in conjunction with ethyl 4-(dimethylamino)benzoate (EDAB; Esstech) as a co-initiator. Butyl nitrite (BN; Sigma-Aldrich, St. Louis, MO) was employed as a UV-active photoinhibitor. Triethylene glycol dimethacrylate (TEGDMA; Esstech) and bisphenol A

glycidyl methacrylate (bisGMA; Esstech) were formulated in a mixture as a 50/50 ratio by mass. Trimethylolpropane trimethacrylate (TMPTMA; Esstech), trimethylolpropane triacrylate (TMPTA; Alfa Aesar, Haverhill, MA), and bisphenol A ethoxylate diacrylate, EO/phenol 4.0 (BPAEDA, Sigma-Aldrich) were all used without comonomers.

2-color cationic & radical curing experiments were performed using using CQ and EDAB as visible light radical photoinitiatiors. Sylanto 7-MS (Synthos specialties; Krakow Poland) was employed as a near-UV active cationic photoinitiator, and BN was employed as a UV-active radical photoinhibitor. Methacrylates TMPTMA and methyl methacrylate (MMA; Sigma-Aldrich) were used in a 50/50 ratio by mass with either cyclohexene oxide (CO; Sigma-Aldrich) or 3,4-Epoxycyclohexylmethyl-3',4'-epoxycyclohexane carboxylate (ECC; Sigma-Aldrich). 2-propenoic acid-2-methyl-7oxabicyclo[4.1.0]hept-3-ylmethyl ester (COMA; AstaTech, Bristol, PA) was used without comonomers. All chemicals were used as received without further purification.

5.4.2 Methods

5.4.2.1 Light sources and intensity measurement

Blue light was provided by a collimated, LED-based illumination source (Thorlabs M470L3-C1) with an emittance centered at 470 nm (FWHM 25 nm), used in combination with a current-adjustable LED driver (Thorlabs LEDD1B) for intensity control. Near-UV light was provided by a UV spot curing system (Omnicure LX500) equipped with an Omnicure LED MAX head with an emittance centered at 365 nm. Irradiation intensities were measured with an International Light IL1400A radiometer equipped with a UV-visible GaAsP detector (model SEL005), a 10× attenuation neutral density filter (model QNDS1), and a quartz diffuser (model W).

5.4.2.2 UV-Vis spectrophotometry

UV-visible spectrophotometry was performed on 8.7×10^{-2} M and 5.4×10^{-2} M solutions of BN and CQ, respectively, in tetrahydrofuran using an Agilent Technologies Cary 60 UV–Vis spectrophotometer. Spectra were collected from 200 to 800 nm with 1 nm spacing on solutions using a 1 mm path length quartz cuvette in the dark.

5.4.2.3 FTIR spectroscopy

Resin formulations were introduced between NaCl salt crystals (International Crystal Laboratories) separated by spacers (13 μm thick) to maintain constant sample thickness during polymerization. Each sample was placed in a Thermo Scientific Nicolet 6700 FTIR spectrometer equipped with a horizontal transmission accessory, as described previously, and spectra were collected from 650 to 4000 cm^{-1} at a rate of 2 per second. The functional group conversion upon irradiation was determined by monitoring the disappearance of the peak area centered at 1635 cm^{-1} for the methacrylate stretch, and 1636 cm^{-1} for the acrylate stretch, and 817 cm^{-1} for the epoxide stretch. The sample thicknesses for the formulations were chosen to ensure that the functional group peaks remained within the linear regime of the instrument detector while affording good signal to noise and maintaining optically thin and isothermal polymerization conditions. Resins were formulated containing 0.2% CQ and 0.5% EDAB as the photoinitiator. The BN photoinhibitor concentration and irradiation intensities are as indicated in the figure insets. Dual curing radical/cationic resins were formulated with 1.0% CQ, 0.5% EDAB, 1.0% Sylanto 7-MS, and 2% BN. All conversion samples were formulated and measured in triplicate, and the presented data represent the mean and standard error of three runs.

5.4.2.4 Photopatterning

The 2D photopatterning was carried out using a formulation of 1.0% CQ, 0.5% EDAB, and 1.0% BN in TMPTA. The resin was introduced between 2 glass slides, spaced 1.0 mm apart. The bottom slide was acrylic coated to improve adhesion, while the top slide was treated with Rain-X water repellent as a release agent to prevent adhesion. The photomask was placed on top, and the formulation was irradiated concurrently with 470 nm light at 100 mW/cm^2 from the bottom, and with 365 nm at 30 mW/cm^2 from the top for 30 seconds. The top glass slide was then removed and the sample was rinsed thoroughly with methanol to remove excess monomer. Reducing the concentration of CQ and BN to 0.2% each, allowed for inhibition through up to 5 mm of resin, while maintaining adequate curing.

The 3D photopatterning was carried out using a formulation of 0.2% CQ, 0.5% EDAB, and 0.2% BN in TMPTA. The resin was introduced to a quartz fluorescence cuvette with a path length of 2 mm, and a width of 10mm, and the cuvette was treated with Rain-X. Triangular photomasks were placed on the 2 mm wide edge, while circular photomasks were placed on the perpendicular side. The resin was irradiated from 2 sides by blue light at 250 mW/cm^2, and perpendicular from 1 side by UV light at 120 mW/cm^2 for 20 seconds. The cured structure was removed from the cuvette and rinsed with methanol to remove any unreacted monomer.

5.5 Results & discussion

While *o*-Cl-HABI and cyclophane HABI are effective photoinhibitors of free-radical chain-growth photopolymerizations, the lifetime of the transient *o*-Cl-HABI-derived lophyl radical, and the synthetic accessibility of cyclophane HABI ultimately

limit their potential. Furthermore in order for HABIs to be dissolved in the monomers, significant amounts of organic solvent were required.

Alkyl nitrite photolysis has been extensively investigated, but their exploration as photoinhibitors has been limited to butyl nitrite (BN) as a photoinhibitor of thermally initiated free-radical chain-growth polymerizations.[29] By itself, BN was reported not to affect initiated polymerizations, while activation of BN by near-UV irradiation would lead to very efficient inhibition. Photolysis of BN (Scheme 5.1) generates an inhibiting nitric oxide species (1), which upon chain termination of an active polymer chain results in the formation of a spin trap (2). This spin trap subsequently terminates a second propagating polymer chain (3), and the generated nitroxide radical will deactivate a third polymerization (4). The alkoxy radical generated upon photolysis is likely to initiate a polymerization, but the combination with 3 inhibition events results in an overall inhibition of polymerization.

Similar to the previously established TETD and *o*-Cl-HABI photoinhibitors, BN exhibits very weak absorbance in the blue region of the UV-Vis spectrum, while having moderate absorbance in the near-UV, thus complimenting the UV-Vis absorbance spectrum of CQ (Figure 5.2D). Allowing for exclusive activation of either the photoinitiator, or the photoinhibitor through irradiation with blue light or near-UV light respectively.

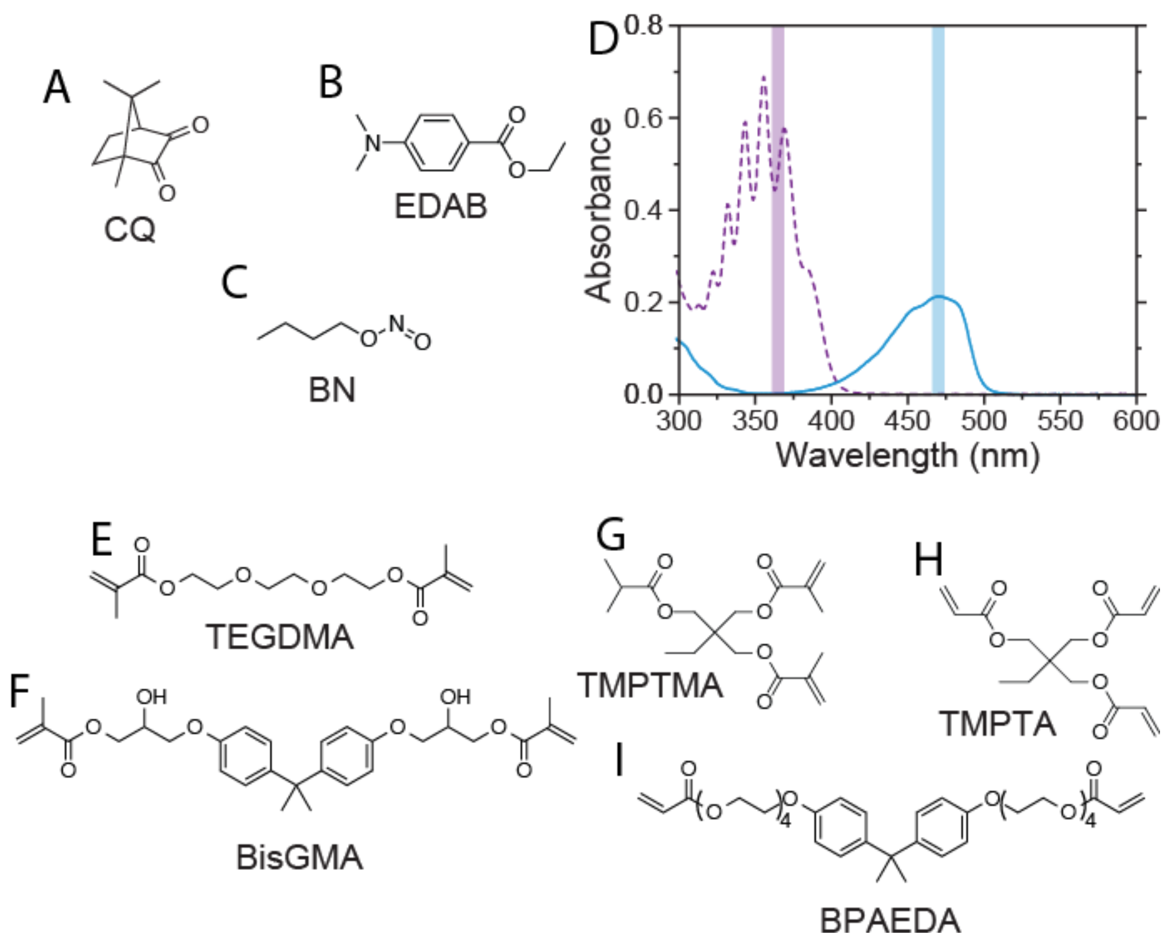

Figure 5.2 Structures of (A) photoinitiator CQ, (B) co-initiator EDAB, (C) near-UV photoinhibitor BN, (C) UV-Visible absorbance spectrum of CQ (solid blue line) and BN (dashed purple line) in THF. The near-UV and visible wavelengths used in this study are highlighted. Monomer structures of (E) TEGDMA, (F) bisGMA, (G) TMPTMA, (H) TMPTA, (I) BPAEDA.

With the optical compatibility between BN and CQ established, the capacity of BN-derived radicals to inhibit free radical chain-growth photopolymerizations was explored by formulating BN, CQ, and EDAB in several different (meth)acrylate-bearing monomers and monitored through time-resolved FTIR spectroscopy.

Having established the optical compatibility between BN and CQ, we explored the capacity of BN photolysis to inhibit free radical chain-growth photopolymerizations by formulating BN, CQ, and ethyl 4-(dimethylamino)benzoate (EDAB, a tertiary amine

coinitiator commonly used in conjunction with CQ[30]) in (meth)acrylate resins. The conversion of (meth)acrylate functional groups was monitored by Fourier transform infrared (FTIR) spectroscopy during the irradiation of formulated resins under irradiation with blue (470 nm) and near UV (365 nm) light.[21] Negligible polymerization was observed for triethyleneglycol dimethacrylate (TEGDMA)/bisphenol A glycidyl dimethacrylate (bisGMA) resin formulations containing BN upon irradiation at 365 nm (see Figure 5.3 and Table 5.1); an extended induction period occurred even in the absence of BN (Figure 5.3A), demonstrating the low initiating radical generation rate afforded by the CQ/EDAB photoinitiator system under near UV irradiation. Sadykov *et al.* reported that, whereas BN acts as a photoinhibitor of the thermal bulk polymerization of methyl methacrylate under near UV irradiation,[29] it does not affect the polymerization without photoactivation. In contrast, both the polymerization rate and overall conversion of the methacrylate formulations examined here under exclusively blue irradiation progressively decreased with raised BN concentration (see Figure 5.3), with negligible polymerization observed for the formulation containing 3 wt% BN. For resins formulated with low BN concentrations, concurrent irradiation under both blue and near UV light yielded significantly reduced polymerization rates relative to those attained under blue irradiation alone (Figure 5.3B and Figure 5.3C), demonstrating the ability of alkyl nitrites to act as photoinhibitors for radical-mediated methacrylate polymerizations.

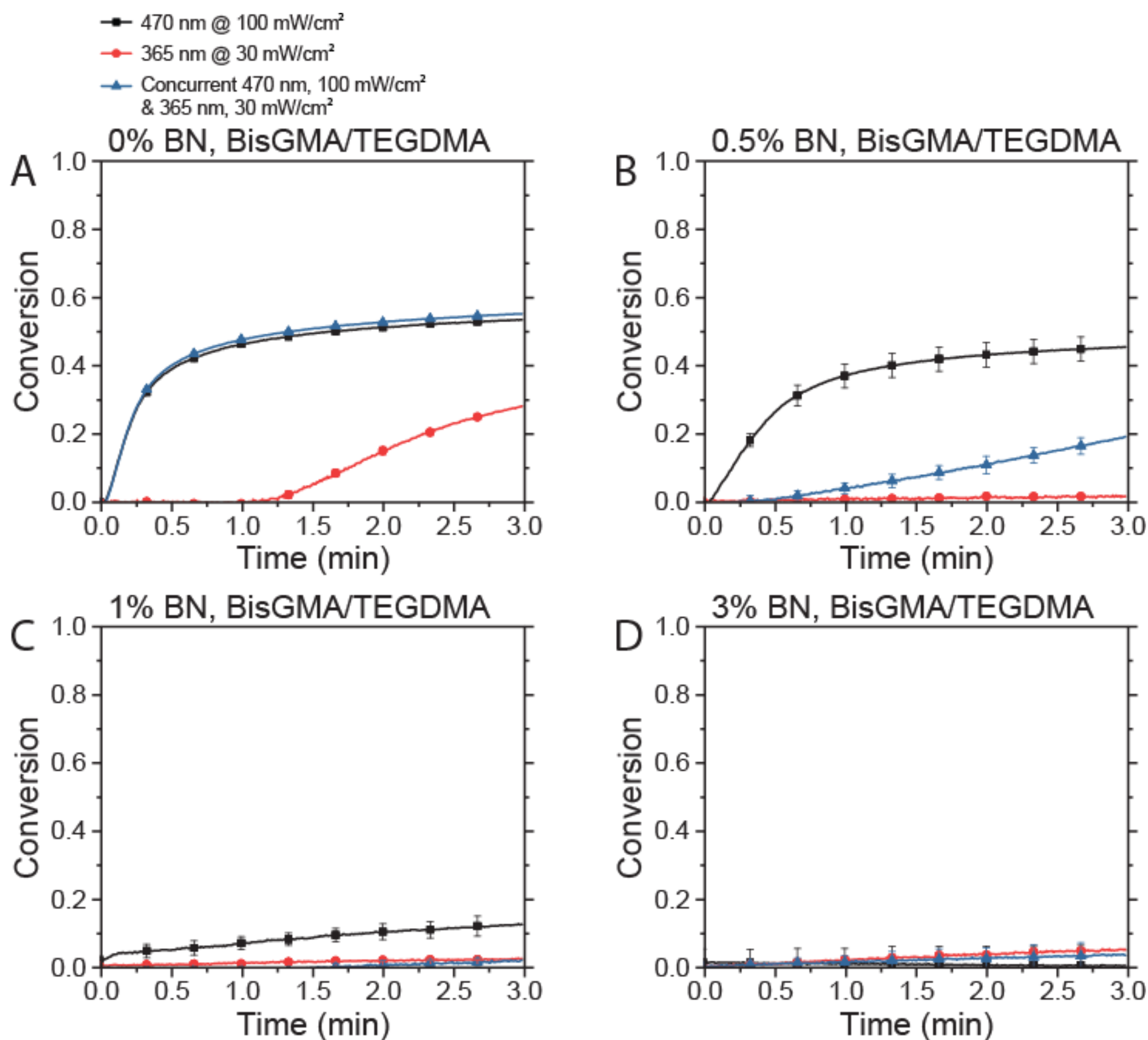

Figure 5.3 Methacrylate conversion versus time for the photopolymerization of bisGMA/TEGDMA resins formulated with 0.2 wt% CQ/0.5 wt% EDAB and (A) 0 wt% BN, (B) 0.5 wt% BN, (C) 1.0 wt% BN, and (D) 3.0 wt% BN. Formulations were irradiated with 470 nm light at an intensity of 100 mW/cm^2 (black, squares), 365 nm light at an intensity of 30 mW/cm^2 (red, circles), or concurrent 470 nm and 365 nm light at intensities of 100 and 30 mW/cm^2 (blue, triangles).

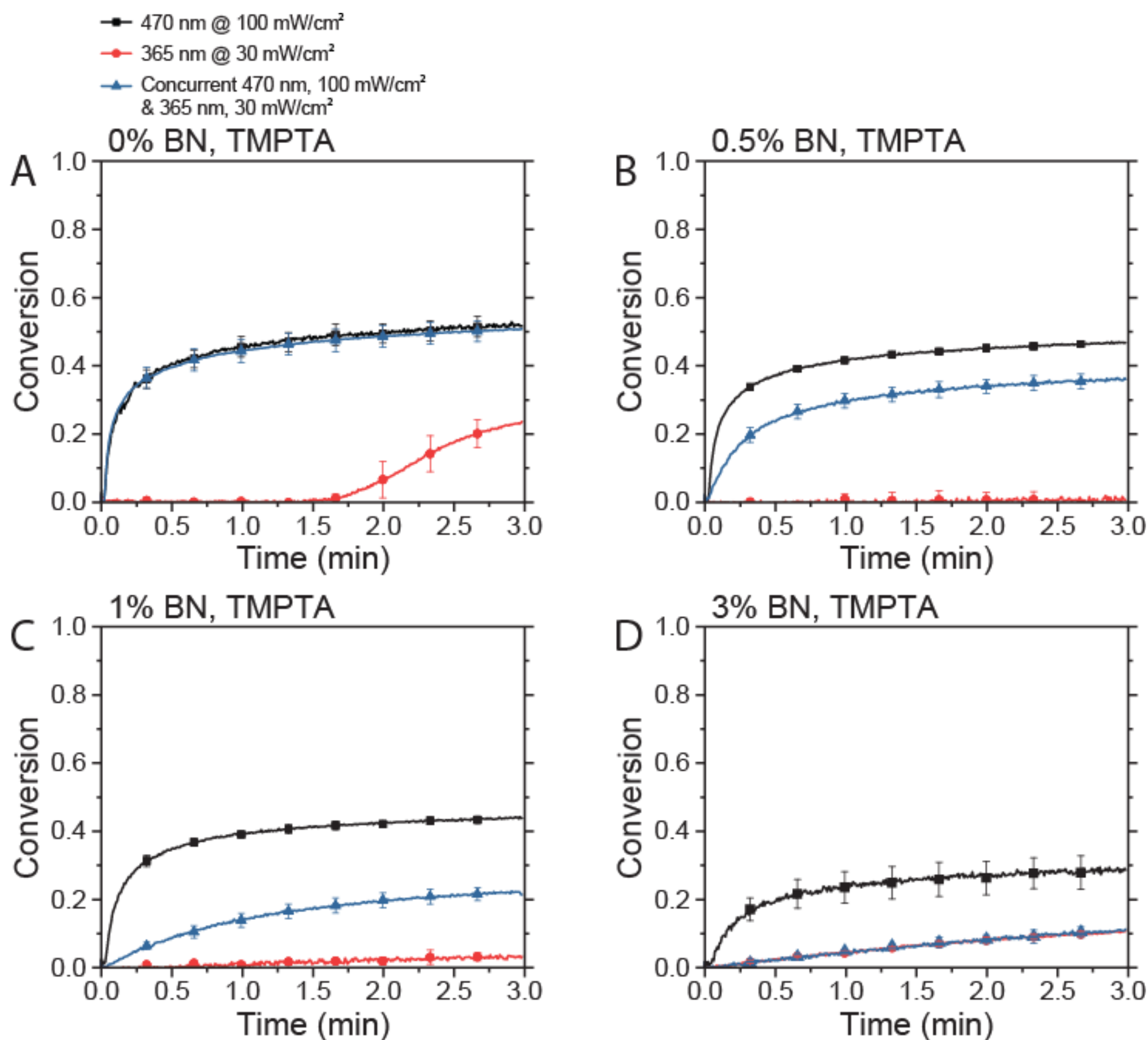

Figure 5.4 Acrylate conversion versus time for the photopolymerization of TMPTA resins formulated with 0.2 wt% CQ/0.5 wt% EDAB and (A) 0 wt% BN, (B) 0.5 wt% BN, (C) 1.0 wt% BN, and (D) 3.0 wt% BN. Formulations were irradiated with 470 nm light at an intensity of 100 mW/cm^2 (black, squares), 365 nm light at an intensity of 30 mW/cm^2 (red, circles), or concurrent 470 nm and 365 nm light at intensities of 100 and 30 mW/cm^2 (blue, triangles).

Table 5.1 Maximum C=C conversion rates for the photopolymerization of bisGMA/TEGDMA resins formulated with 0.2 wt% CQ/0.5 wt% EDAB and varying concentrations of BN as shown.

Irradiation conditions	**C=C conversion rate @ 0 wt% BN ($M.s^{-1}$)**	**C=C conversion rate @ 0.5 wt% BN ($M.s^{-1}$)**	**C=C conversion rate @ 1.0 wt% BN ($M.s^{-1}$)**	**C=C conversion rate @ 3.0 wt% BN ($M.s^{-1}$)**
Blue (470 nm, 100 mW/cm^2)	0.156±0.005	0.0620±0.0139	0.0033±0.0018	-0.0003±0.0012
Near UV (365 nm, 30 mW/cm^2)	0.0191±0.0004	0.0008±0.0002	0.0007±0.0002	0.0017±0.0005
Concurrent blue (470 nm, 100 mW/cm^2) & near UV (365 nm, 30 mW/cm^2)	0.145±0.003	0.0075±0.0008	0.0010±0.0002	0.0011±0.0013

Table 5.2 Maximum C=C conversion rates for the photopolymerization of TMPTA resins formulated with 0.2 wt% CQ/0.5 wt% EDAB and varying concentrations of BN as shown.

Irradiation conditions	**C=C conversion rate @ 0 wt% BN ($M.s^{-1}$)**	**C=C conversion rate @ 0.5 wt% BN ($M.s^{-1}$)**	**C=C conversion rate @ 1.0 wt% BN ($M.s^{-1}$)**	**C=C conversion rate @ 3.0 wt% BN ($M.s^{-1}$)**
Blue (470 nm, 100 mW/cm^2)	0.583±0.077	0.590±0.004	0.534±0.086	0.194±0.053
Near UV (365 nm, 30 mW/cm^2)	0.0546±0.0091	0.0147±0.0670	0.0024±0.0002	0.0057±0.0006
Concurrent blue (470 nm, 100 mW/cm^2) & near UV (365 nm, 30 mW/cm^2)	0.585±0.067	0.139±0.019	0.0274±0.0068	0.0060±0.0008

To further evaluate the breadth of alkyl nitrite photoinhibition capacity, trimethylolpropane triacrylate (TMPTA)-based acrylate resins were similarly formulated with BN, CQ, and EDAB, and their photopolymerization behavior examined under blue and near UV irradiation (see Figure 5.4 and Table 5.2). Under near UV irradiation, an extended induction period was again observed in the absence of BN (Figure 5.4A); however, whereas negligible polymerization was observed under exclusively near UV

irradiation for formulations containing low BN concentrations, some curing did proceed at 3 wt% BN (Figure 5.4D). Notably, under exclusively blue light irradiation, only a modest decrease in polymerization rate and extent was observed with raised BN concentration. Concurrent irradiation with both blue and near UV light afforded photopolymerization rates up to an order of magnitude lower than those observed under exclusively blue irradiation.

The utilization of BN as a photoinhibition species in trimethylolpropane trimethacrylate (see Figure 5.5 and Table 5.3) and bisphenol A ethoxylate diacrylate monomer formulations (Figure 5.6 and Table 5.4) reveals significant variation between different monomers despite bearing the same reactive functional groups. For example, whereas the photopolymerization rate under exclusively blue irradiation for an acrylate-based TMPTA resin formulated with 1 wt% BN was approximately 10% lower than that for a BN-free TMPTA formulation (Table 5.3), the photopolymerization rate under blue light for the bisphenol A ethoxylate diacrylate (BPAEDA) resin formulated with 1 wt% BN was over five-fold lower than that for a BN-free BPAEDA formulation (Table 5.4). Thus, although BN does allow for effective photoinhibition of various monomer formulations, its effectiveness as a photoinhibitor is strongly monomer-dependent.

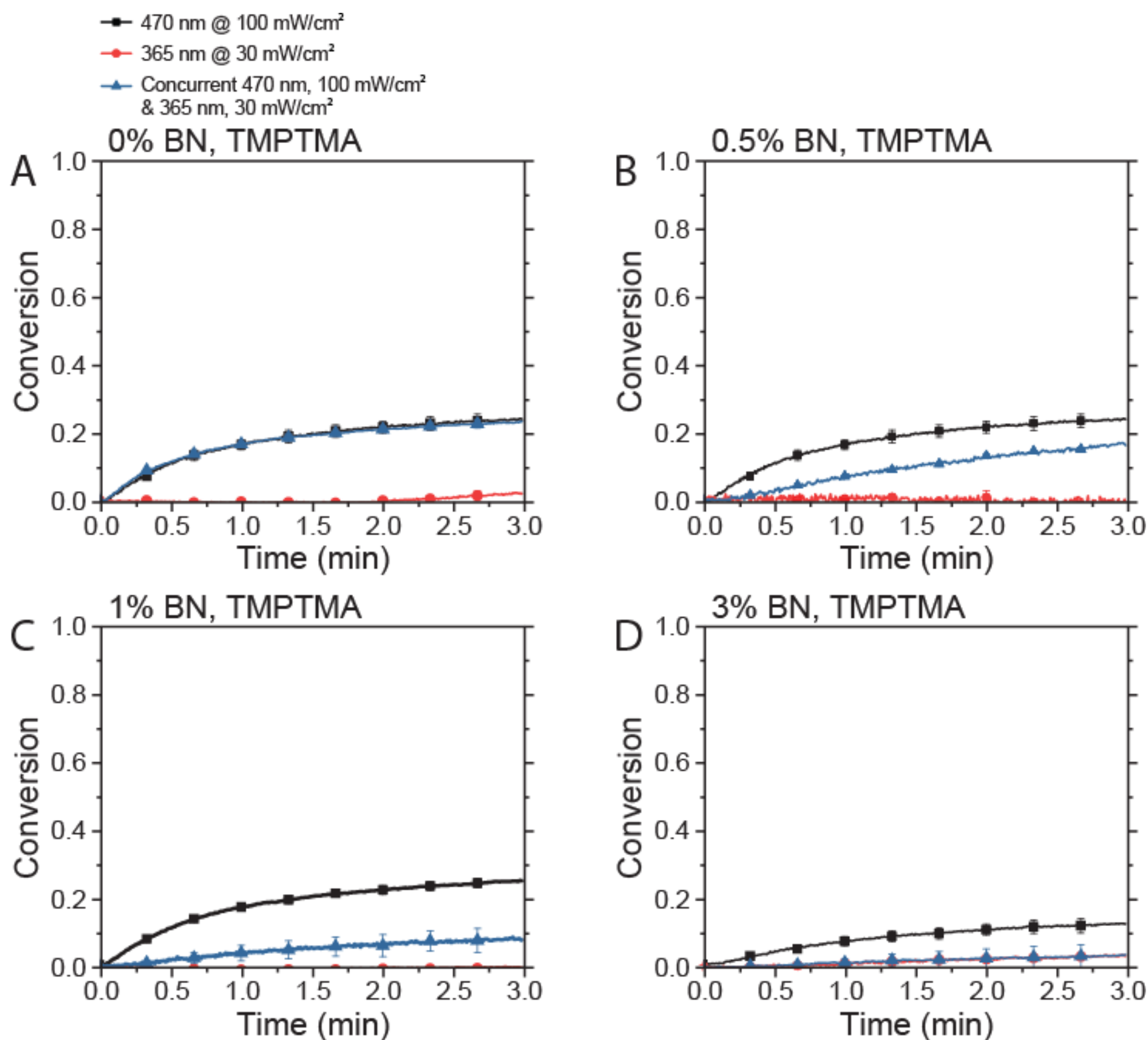

Figure 5.5 Methacrylate conversion versus time for the photopolymerization of TMPTMA resins formulated with 0.2 wt% CQ/0.5 wt% EDAB and (A) 0 wt% BN, (B) 0.5 wt% BN, (C) 1.0 wt% BN, and (D) 3.0 wt% BN. Formulations were irradiated with 470 nm light at an intensity of 100 mW/cm^2 (black, squares), 365 nm light at an intensity of 30 mW/cm^2 (red, circles), or concurrent 470 nm and 365 nm light at intensities of 100 and 30 mW/cm^2 (blue, triangles).

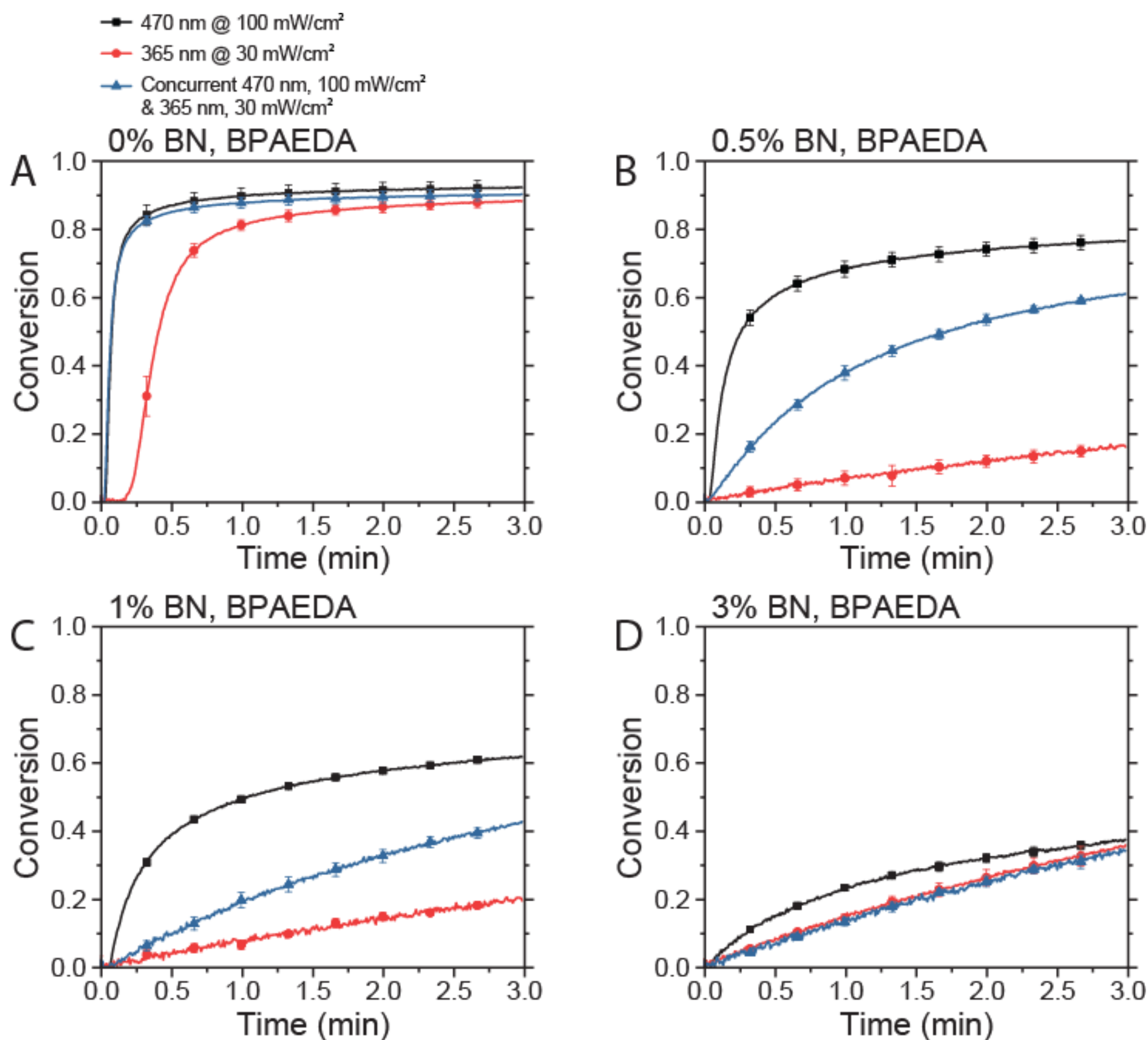

***Figure 5.6** Acrylate conversion versus time for the photopolymerization of BPAEDA resins formulated with 0.2 wt% CQ/0.5 wt% EDAB and (A) 0 wt% BN, (B) 0.5 wt% BN, (C) 1.0 wt% BN, and (D) 3.0 wt% BN. Formulations were irradiated with 470 nm light at an intensity of 100 mW/cm^2 (black, squares), 365 nm light at an intensity of 30 mW/cm^2 (red, circles), or concurrent 470 nm and 365 nm light at intensities of 100 and 30 mW/cm^2 (blue, triangles).*

Table 5.3 Maximum C=C conversion rates for the photopolymerization of TMPTMA resins formulated with 0.2 wt% CQ/0.5 wt% EDAB and varying concentrations of BN as shown.

Irradiation conditions	**C=C conversion rate @ 0 wt% BN ($M.s^{-1}$)**	**C=C conversion rate @ 0.5 wt% BN ($M.s^{-1}$)**	**C=C conversion rate @ 1.0 wt% BN ($M.s^{-1}$)**	**C=C conversion rate @ 3.0 wt% BN ($M.s^{-1}$)**
Blue (470 nm, 100 mW/cm^2)	0.0224±0.0040	0.0278±0.0025	0.0285±0.0024	0.0128±0.0020
Near UV (365 nm, 30 mW/cm^2)	0.0010±0.0012	0.0001±0.0014	0.0001±0.0012	0.0022±0.0008
Concurrent blue (470 nm, 100 mW/cm^2) & near UV (365 nm, 30 mW/cm^2)	0.0155±0.0023	0.0093±0.0002	0.0047±0.0023	0.0028±0.0025

Table 5.4 Maximum C=C conversion rates for the photopolymerization of BPAEDA resins formulated with 0.2 wt% CQ/0.5 wt% EDAB and varying concentrations of BN as shown.

Irradiation conditions	**C=C conversion rate @ 0 wt% BN ($M.s^{-1}$)**	**C=C conversion rate @ 0.5 wt% BN ($M.s^{-1}$)**	**C=C conversion rate @ 1.0 wt% BN ($M.s^{-1}$)**	**C=C conversion rate @ 3.0 wt% BN ($M.s^{-1}$)**
Blue (470 nm, 100 mW/cm^2)	0.653±0.033	0.229±0.006	0.0951±0.0060	0.0167±0.0024
Near UV (365 nm, 30 mW/cm^2)	0.106±0.014	0.0051±0.0023	0.0042±0.0006	0.0073±0.0010
Concurrent blue (470 nm, 100 mW/cm^2) & near UV (365 nm, 30 mW/cm^2)	0.675±0.020	0.0287±0.0015	0.0106±0.0004	0.0072±0.0010

In our previous study employing the photolysis of *o*-Cl-HABI under near UV irradiation to inhibit radical-mediated, chain growth photopolymerizations for stereolithographic additive manufacturing,[6] we found that the polymerization inhibition persisted for several seconds after cessation of irradiation with the photolysis wavelength, attributable to the low recombination rate of the HABI-derived lophyl radicals.[21] Consequently, as the application of photoinhibition to improve photopolymerization

confinement in volumetric additive manufacturing by tomographic reconstruction requires rapid elimination of the inhibitor species in the dark, photoinhibitors based on conventional, non-diffusion-inhibited HABIs are ill-suited for this purpose. To evaluate the impact of BN-derived radicals during and post-irradiation, the methacrylate conversion for a CQ/EDAB/BN-formulated bisGMA/TEGDMA resin was monitored upon constant exposure to blue light and intermittent periods of near UV irradiation (see Figure 5.7). Whereas the photopolymerization proceeded rapidly upon blue light irradiation from t = 0, an immediate 18-fold reduction in the polymerization rate was observed at t = 0.5 min upon the superimposition of near UV irradiation (See Table 5.5). Moreover, the polymerization rate increased promptly after cessation of near UV exposure at t = 1 min, indicating rapid consumption of BN-derived inhibiting radicals in the absence of BN photolysis. Sadykov *et al.*[29] reported extended post-irradiation induction times for the thermal polymerization at 60°C of methyl methacrylate formulations containing benzoyl peroxide as a thermal initiator and BN, potentially attributable to the low radical generation rate under the conditions used. Nevertheless, under the conditions used here, photoinhibition of free-radical chain-growth photopolymerization via BN photolysis can be rapidly switched on and off by cycling the incident near UV light.

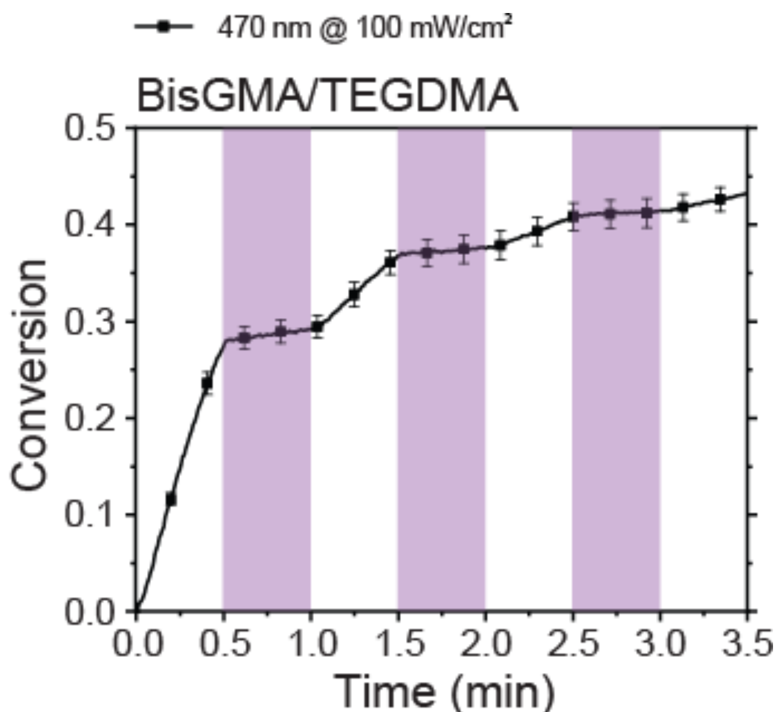

Figure 5.7 Methacrylate conversion versus time for the photopolymerization of a bisGMA/TEGDMA resin formulated with 0.2 wt% CQ/0.5 wt% EDAB/0.5 wt% BN and subject to continuous blue light irradiation (470 nm, 100 mW/cm^2) starting at t = 0 and intermittent near UV light irradiation (365 nm, 30 mW/cm^2) for 0.5 minute periods as indicated by the violet vertical bars.

Table 5.5 C=C conversion rates for the photopolymerization of bisGMA/TEGDMA resins formulated with 0.2 wt% CQ/0.5 wt% EDAB/0.5 wt% BN under constant blue irradiation and intermittent near UV light irradiation for 0.5 minute periods at a time

Irradiation conditions	**Average C=C conversion rate (M.s^{-1})**
Blue (470 nm, 100 mW/cm^2) (0 – 0.5 min)	0.0661±0.0008
Concurrent blue & near UV (365 nm, 30 mW/cm^2) (0.5 – 1.0 min)	0.0037±0.0001
Blue (1.0 – 1.5 min)	0.0186±0.0008
Concurrent blue & near UV (1.5 – 2.0 min)	0.0018±0.0001
Blue (2.0 – 2.5 min)	0.0072±0.0002
Concurrent blue & near UV (2.5 – 3.0 min)	0.0008±0.00002
Blue (3.0 – 3.5 min)	0.0042±0.0001

Having determined BN as an effective (meth)acrylate photoinhibitor, where the polymerization rates for resin formulations exposed exclusively to blue light is significantly higher than those formulations concurrently exposed to both blue and near UV light, we examined the potential for the photopolymerization of BN-formulated resins to be spatially confined using concurrent blue and near UV irradiation. This dual-wavelength photopatterning was initially implemented in a two-dimensional plane by subjecting a TMPTA-based resin formulation sandwiched between glass microscope slides to flood irradiation with blue light from below, while concurrently irradiating the sample with near UV light through a photomask from above (Figure 5.8). Consequently, the regions irradiated exclusively with blue light cured rapidly to afford cross-linked, insoluble polymer, while the polymerization in the regions exposed to both blue and near UV light proceeded sufficiently slowly such that, after irradiation cessation, they remained liquid and were readily washed away with solvent (Figure 5.8). Through this antiparallel, concurrent irradiation scheme, we were able to successfully inhibit photopolymerization such that the resin remained liquid through a thickness of up to 5 mm.

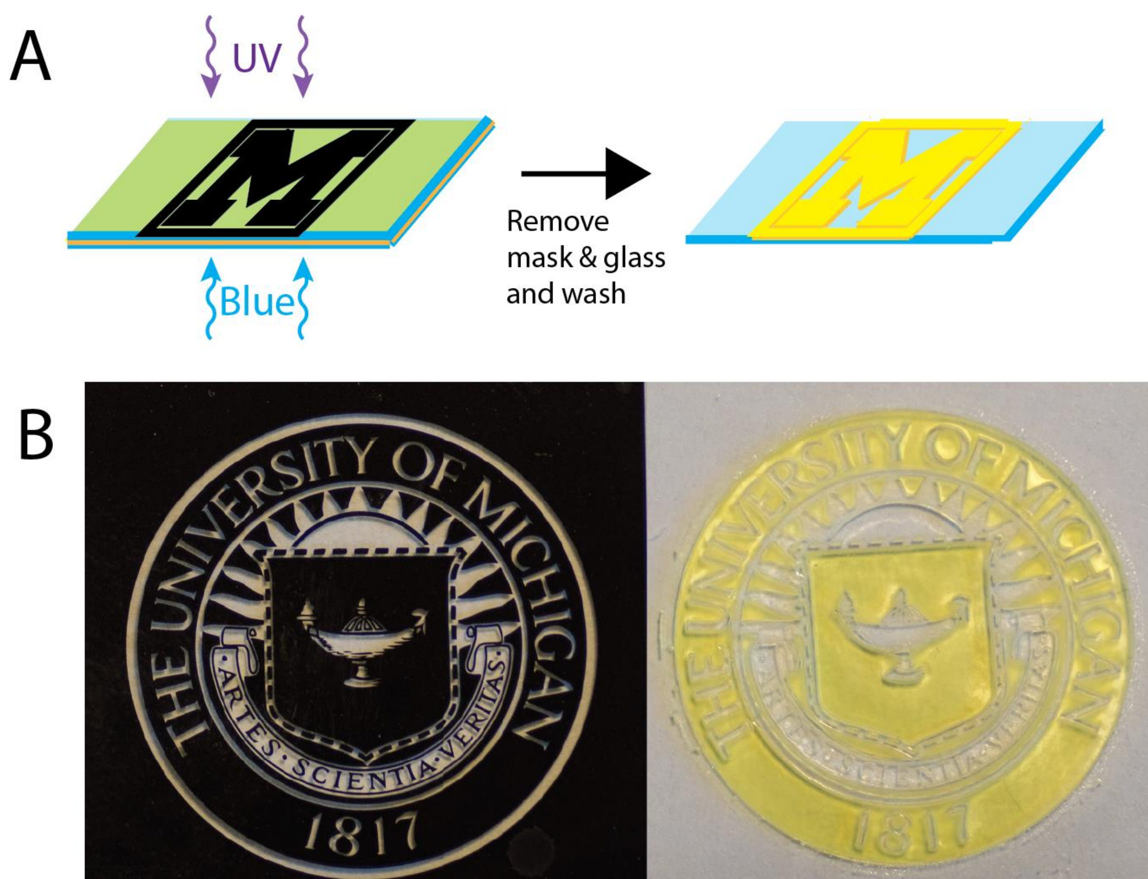

Figure 5.8 Polymerization confinement through dual-wavelength photopatterning in 2D. (A) Schematic diagram of formulated resin subject to flood blue light irradiation and concurrent, antiparallel irradiation with near UV light through a photomask. (B) A patterned sample of CQ/EDAB/BN-formulated TMPTA produced by using concurrent, antiparallel blue and near UV irradiation. The photomask used to pattern the near UV light is also shown.

Having demonstrated dual-wavelength photopatterning in two dimensions, we applied this concurrent photoinitiation and photoinhibition approach to confine in depth the photopolymerization of a formulated resin. Patterned irradiation of a photopolymer resin at a wavelength where the resin weakly absorbs typically yields prismatic polymerized regions. Reaction confinement in depth is often achieved through patterned irradiation at a wavelength where the resin strongly absorbs such that only a thin layer of resin closest to the irradiation source is solidified; nevertheless, the concurrent activation of BN as a photoinhibitor under near UV irradiation and CQ as a photoinitiator under

blue irradiation can also effect volumetric photopolymerization patterning. Thus, non-parallel, concurrent irradiation of formulated resin with both initiating and inhibiting wavelengths enables the fabrication of more complex, three-dimensional objects in a single exposure. We implemented this dual-wavelength approach to volumetric photopatterning with a quartz cuvette filled with a TMPTA-based resin formulation. Here, the resin was subject to concurrent, perpendicular, overlapping irradiation both with blue light through a triangular photomask and with near UV light a double circle photomask (see Figure 5.9). As a result, whereas the blue light irradiation resulted in the solidification of resin into a triangular prism, the near UV light prevented resin solidification in two circular regions through the prism thickness. Fabricating a similar part with a single light exposure is not attainable through contemporary photolithographic approaches; thus, this technique opens up a new, complementary direction for volumetric 3D printing.

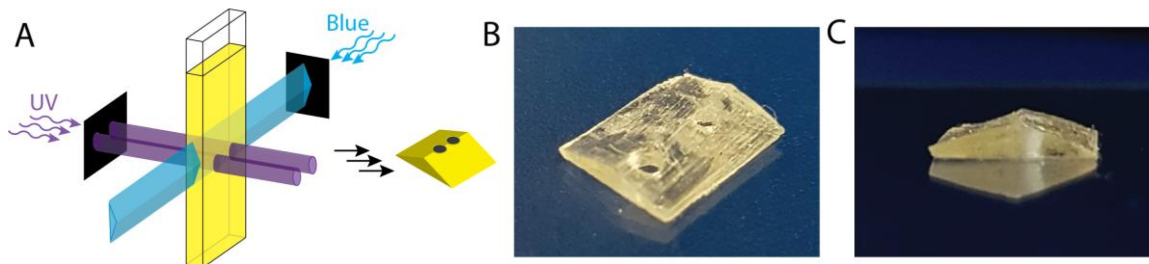

Figure 5.9 Polymerization confinement through dual-wavelength photopatterning in 3D (A) Schematic diagram of perpendicular blue and near UV irradiation to photopattern in depth the polymerization of a formulated resin. (B) and (C) Patterned sample of CQ/EDAB/BN-formulated TMPTA produced by using concurrent, perpendicular blue and near UV irradiation

5.5.1 Patterned free-radical and cationic photopolymerizations

Following the successful development of BN as a near-UV active photoinhibitor of free radical chain-growth photopolymerization a near-UV active coumarin-derived cationic photoinitiator[31, 32] (Sylanto 7-MS, Figure 5.10C) was introduced to the photoinitiating system. We hypothesized that this combination of photoinitiators and photoinhibitor could lead to cationic photopolymerization, while excluding free radical polymerization. The cationic initiation species is generated through a radical intermediate (See Scheme 5.2), but by itself it is not expected to interact with BN or its photolysis fragments, as these are neither basic nor anionic. In this approach, a combination of epoxide monomers and (meth)acrylate monomers would allow for exclusive cationic and radical polymerization respectively.

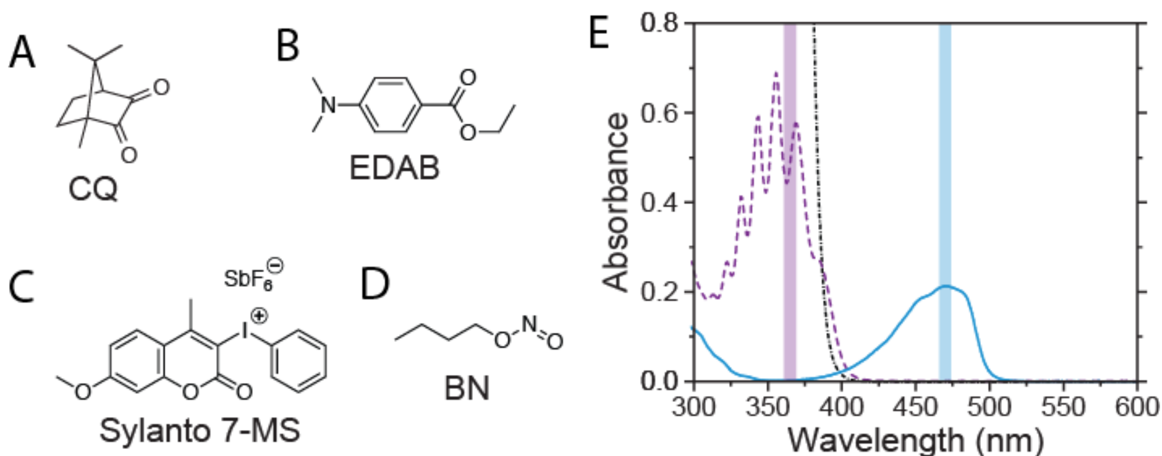

Figure 5.10 Structures of (a) free radical blue photoinitiator CQ, (b) free radical co-initiator EDAB, (c) near-UV cationic photoinitiator Sylanto 7-MS, free radical photoinhibitor BN. (e) UV-Vis spectra of CQ (solid blue line), Sylanto 7-MS (dash-dotted black line), and BN (dashed violet line) in THF

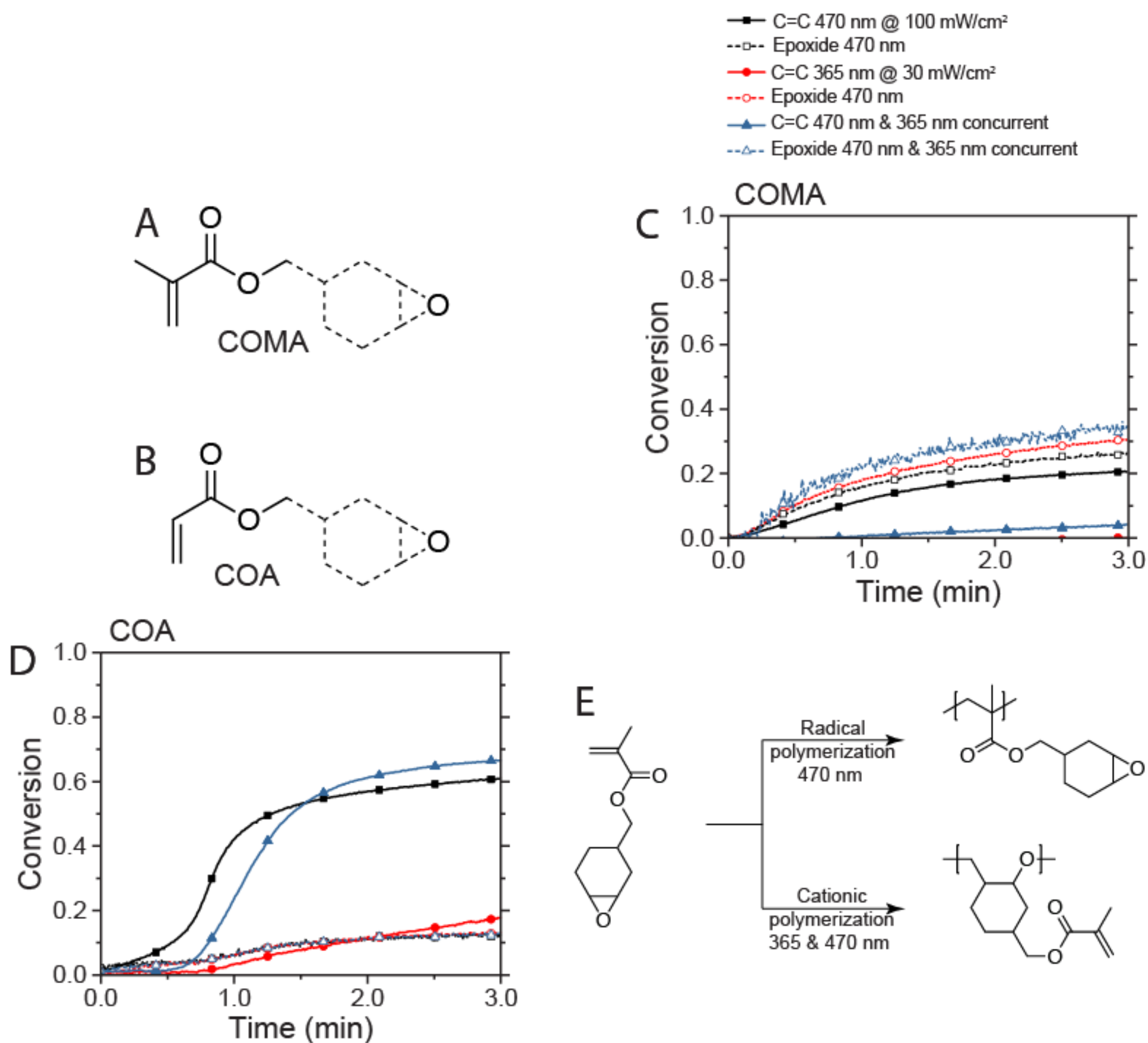

Figure 5.11 Structures of (a) COMA and (b) COA ((meth)acrylate solid and cyclohexene oxide dashed, conversion versus time for (c) cyclohexene oxide methacrylate and (d) cyclohexene oxide acrylate ((meth)acrylate and epoxide denoted by solid and dashed lines, respectively). Continuous irradiation with exclusively 470 nm @ 100 mW/cm² (black line, squares), and 365 nm @ 30 mW/cm² (red line, circles), and 470 nm @ 100 mW/cm² & 365 nm @ 30 mW/cm², (blue line, triangles). And (e) polymerization routes of monomer upon exposure to 365 nm and 470 nm light

The optical compatibility of Sylanto 7-MS with CQ is confirmed through UV-Vis spectroscopy (see

Figure 5.10E), allowing for independent activation of either photoinitiating species. The capacity of BN photolysis to allow for exclusive cationic and dual cationic/free radical photopolymerizations was explored by formulating a monomer employing 2-propenoic

acid-2-methyl-7oxabicyclo[4.1.0]hept-3-ylmethyl ester (cyclohexene oxide methacrylate, COMA, Figure 5.11A) with 1 wt% CQ, 1 wt% Sylanto 7-MS, 0.5 wt% EDAB, and 2 wt% BN. The conversion of the epoxide and methacrylate functional group was monitored in real-time by FTIR spectroscopy under irradiation with blue (470 nm) and near UV (365 nm) light.[21] The methacrylate moiety in COMA displayed conversion following exposure of the formulation to blue irradiation (see Figure 5.11B). Similarly, consumption of the epoxide moiety was observed under these conditions, in agreement with previously reported formulations of CQ with iodonium photoiniators.[33, 34] In contrast to this, negligible methacrylate conversion occurs under near-UV irradiation, whilst epoxide polymerization occurs at rates similar to blue irradiation (see Table 5.6). Under concurrent blue and near-UV irradiation, a significant induction period is observed for the methacrylate polymerization, following which conversion proceeds at significantly reduced rates relative to blue irradiation. Epoxide polymerization proceeded more rapidly under concurrent blue and near-UV than under either light source individually.

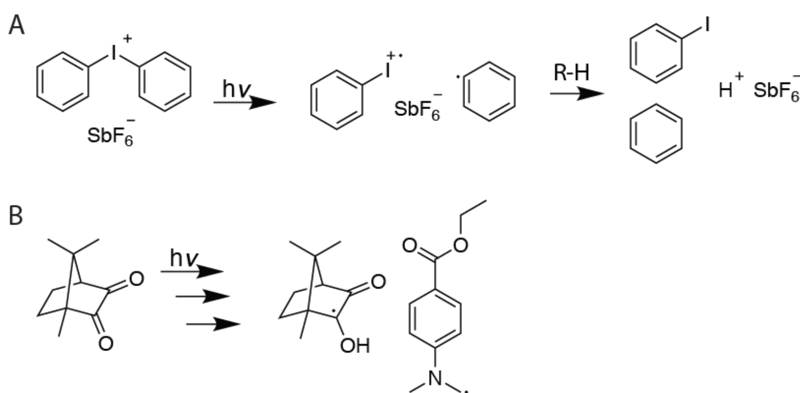

Scheme 5.2 Photochemical generation of initiation species of (a) diphenyliodonium salts and (b) CQ/EDAB

Table 5.6 Maximum C=C and epoxide conversion rates for the photopolymerizations of COMA formulated with 1 wt% CQ/0.5 wt% EDAB/1 wt% Sylanto 7-MS/2 wt% BN

Irradiation conditions	**C=C conversion rate (M.s^{-1})**	**Epoxide conversion rate (M.s^{-1})**
Blue (470 nm, 100 mW/cm^2)	0.0109±0.0001	0.0126±0.0002
Near UV (365 nm, 30 mW/cm^2)	0.0010±0.0009	0.0135±0.0004
Concurrent blue (470 nm, 100 mW/cm^2) & near UV (365 nm, 30 mW/cm^2)	0.0022±0.0003	0.0156±0.0010

To evaluate the broader utility of the butyl nitrite photoinhibition in a dual cure CQ/EDAB/Sylanto 7-MS free radical/cationic photoinitiation system glycidyl methacrylate and 2-propenoic acid-7oxabicyclo[4.1.0]hept-3-ylmethyl ester (cyclohexene acrylate ester, COA, Figure 5.11B) were similarly formulated with BN and the photoinitiating systems and their photopolymerization behavior studied under blue and near-UV irradiation. Glycidyl methacrylate showed poor conversion for both the methacrylate and epoxide moieties. Chain transfer and generally low rates of photopolymerization of monomethacrylates at room temperatures explain the poor methacrylate curing. The lack of epoxide polymerization can be explained by stabilization of the intermediate cationic species by the unpaired electrons of the nearby ester moiety. Similar rate retardation is observed in the room temperature photopolymerization of glycidyl ethers.[35] Cyclohexene oxide acrylate displayed significantly delayed photopolymerization under blue irradiation, while a significant induction period and slow polymerization were observed under near-UV exposure. While under concurrent irradiation appreciable induction of the acrylate occurred, extremely limited photopolymerization of the epoxide moiety occurred, possibly attributable to the

increased flexibility of the acrylate ester relative to the methacrylate, and thus stabilizing the intermediate cation.

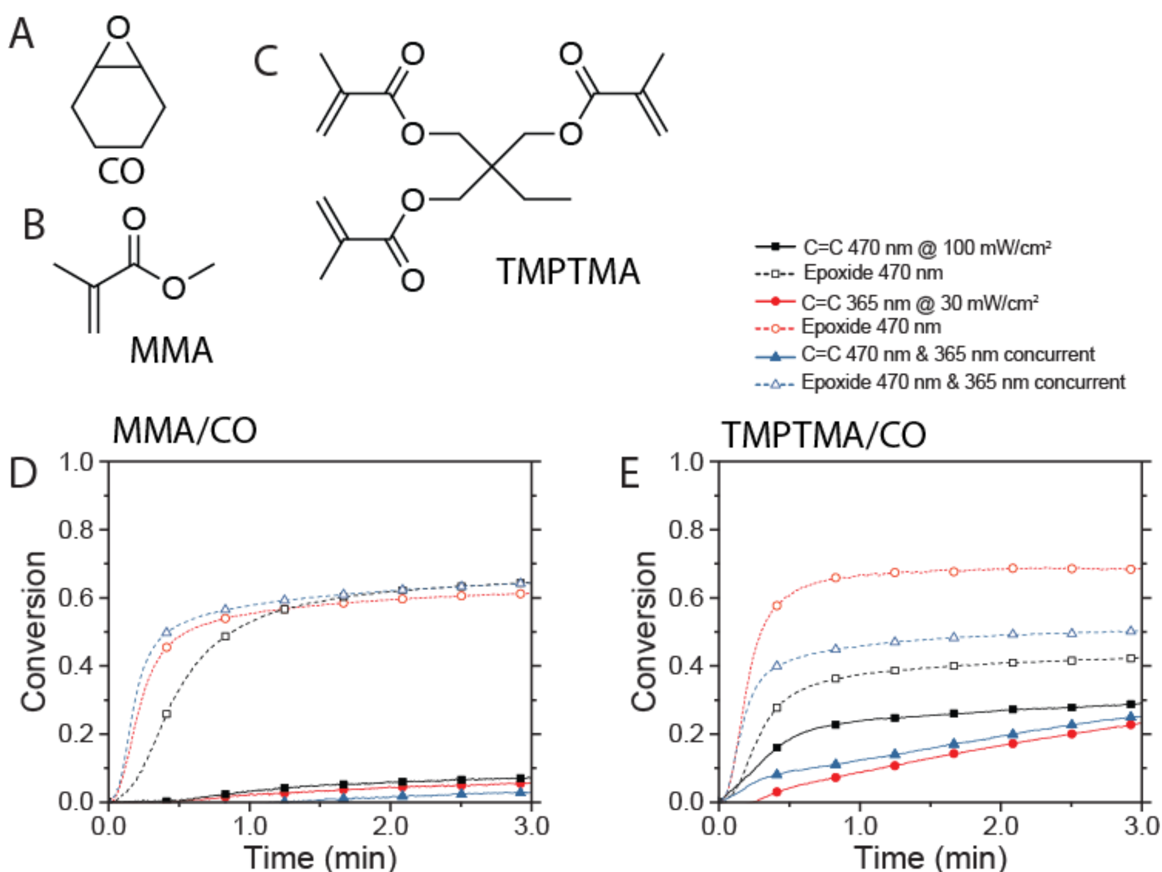

Figure 5.12 Structures of (a) CO, d (b) MMA, and (c) . conversion versus time for (d) 50:50 CO/MMA formulations and (d) 50:50 CO/TMPTMA (methacrylate and epoxide denoted by solid and dashed lines, respectively). Continuous irradiation with exclusively 470 nm @ 100 mW/cm^2 (black line, squares), and 365 nm @ 30 mW/cm^2 (red line, circles), and 470 nm @ 100 mW/cm^2 & 365 nm @ 30 mW/cm^2, (blue line, triangles). And (e) polymerization routes of monomer upon exposure to 365 nm and 470 nm light

Having determined methacrylate functional groups to be more readily inhibited in these formulations, the impact of this system was examined for methacrylate/epoxide monomer mixtures. As selective cationic photopolymerization has been demonstrated with COMA, cyclohexene oxide (CO, Figure 5.12A) was chosen as the cationically curing monomer. Poly(cyclohexene oxide) is particularly well-suited for this purpose, as

polymerization yields a tough, glassy polymer material.[36, 37] The polymer is expected to consist of near-exclusively linear chains, as crosslink formation through chain-transfer reactions is not a feasible reaction in cationic ring-opening polymerizations. Methyl methacrylate (MMA) and TMPTMA were respectively mixed with CO in a 50:50 ratio by weight, prior to formulating with photoinitiators and photoinhibitor. In both formulations, overall epoxide conversion and conversion rates are significantly increased relative to COMA. Epoxide conversions in the CO/MMA formulations (see Figure 5.12D) rapidly reached 60% under near-UV and concurrent irradiation, while a slight induction was observed under exclusive blue irradiation. Unfortunately, MMA showed very slow and extremely limited photopolymerization under all conditions, in stark contrast to the monomethacrylate COMA. TMPTMA on the other hand, proved to be readily curable in these formulations under blue irradiation, as observed previously (Figure 5.5). However, despite promising results in the photoinitiation/photoinhibition study of BN in TMPTMA, photopolymerization of TMPTMA in these cationic & radical curing formulations displayed a very weak contrast in methacrylate conversion under concurrent blue and near-UV irradiation relative to exclusive blue irradiation.

Table 5.7 Dissolution of polymer films containing cationic and radically curable moieties formulated with CQ/EDAB/Sylanto 7-MS/BN cured for 30-60 seconds in organic solvents

	Blue (470 nm, 100 mW/cm^2)	**Near UV (365 nm, 30 mW/cm^2)**	**Concurrent blue (470 nm, 100 mW/cm^2) & near UV (365 nm, 30 mW/cm^2)**
COMA	Insoluble	Soluble	Soluble
COA	Insoluble	N/A (liquid)	N/A (liquid)
MMA/CO	Soluble	Soluble	Soluble
TMPTMA/CO	Insoluble	Soluble	Insoluble

The dissolution testing results of polymeric films prepared through this approach are summarized in Table 5.7. All formulations resulted in soluble material upon exposure to exclusively near-UV irradiation, demonstrating that homopolymerization of the epoxide does not yield highly crosslinked material, even at high conversions. Exposure of the films to blue irradiation resulted in generally insoluble material, as methacrylate crosslinking through chain-transfer in COMA and COA occurs rapidly, while TMPTMA rapidly forms a crosslinked polymeric network. In these cationic/radial/inhibition formulations only COMA resulted in soluble polymeric material upon concurrent blue and near-UV irradiation. Rapid TMPMA crosslinking at low conversions prevents dissolution of the film, whilst COA displays too effective photoinhibition of the acrylate and low reactivity of the epoxide to form a glassy film. The only examined monomer demonstrating favorable polymerization characteristics is COMA, which results in insoluble polymer upon blue and concurrent exposure, while the polymer film obtained from near-UV exposure dissolved in organic solvent overnight. These results are encouraging and demonstrate the versatile potential of free radical photoinhibition chemistry in cationically curing formulations.

5.6 Conclusion

We have demonstrated the potential of butyl nitrite as a photoinhibitor of free-radical chain-growth photopolymerizations in a two-color irradiation setup. The effectiveness of BN as a photoinhibitor is strongly monomer dependent, and inclusion of BN can lead to reduced polymerization rates without BN activation. In contrast to previously-reported work, BN-derived inhibiting radicals are rapidly consumed in the absence of BN photolysis, affording prompt photopolymerization rate recovery after

cessation of near UV exposure. BN proved effective for 2D patterning of the inhibition through a photomask, the results of which translated effectively to a 3D irradiation setup. This allows for rapid, single-exposure fabrication of more complex, otherwise unattainable structures and provides a path for a new approach to “true” 3D printing. Additionally, BN was demonstrated in formulations containing both radical-mediated and cationically curing monomers to photoinhibit free radical photopolymerizations while selectively allowing for cationic photopolymerizations to proceed. This approach leads to formulation-dependent selective cationic photopolymerization and offers a route towards soluble supports for two-color stereolithography and new approaches to multimaterial printing.

5.7 References

1. Melchels, F. P. W.; Feijen, J.; Grijpma, D. W., A review on stereolithography and its applications in biomedical engineering. *Biomaterials* **2010,** *31* (24), 6121-6130.

2. Ligon, S. C.; Liska, R.; Stampfl, J.; Gurr, M.; Mulhaupt, R., Polymers for 3D Printing and Customized Additive Manufacturing. *Chemical Reviews* **2017,** *117* (15), 10212-10290.

3. Tumbleston, J. R.; Shirvanyants, D.; Ermoshkin, N.; Janusziewicz, R.; Johnson, A. R.; Kelly, D.; Chen, K.; Pinschmidt, R.; Rolland, J. P.; Ermoshkin, A.; Samulski, E. T.; DeSimone, J. M., Continuous liquid interface production of 3D objects. *Science* **2015,** *347* (6228), 1349-1352.

4. Janusziewicz, R.; Tumbleston, J. R.; Quintanilla, A. L.; Mecham, S. J.; DeSimone, J. M., Layerless fabrication with continuous liquid interface production. *Proceedings of the National Academy of Sciences of the United States of America* **2016,** *113* (42), 11703-11708.

5. Zhu, W.; Tringale, K. R.; Woller, S. A.; You, S. T.; Johnson, S.; Shen, H. X.; Schimelman, J.; Whitney, M.; Steinauer, J.; Xu, W. Z.; Yaksh, T. L.; Nguyen, Q. T.; Chen, S. C., Rapid continuous 3D printing of customizable peripheral nerve guidance conduits. *Materials Today* **2018,** *21* (9), 951-959.

6. De Beer, M. P.; Van der Laan, H. L.; Cole, M. A.; Whelan, R. J.; Burns, M. A.; Scott, T. F., Rapid, Continuous Additive Manufacturing by Volumetric Polymerization Inhibition Patterning. *Science Advances* **2019**, eaau8723.

7. Haske, W.; Chen, V. W.; Hales, J. M.; Dong, W. T.; Barlow, S.; Marder, S. R.; Perry, J. W., 65 nm feature sizes using visible wavelength 3-D multiphoton lithography. *Optics Express* **2007,** *15* (6), 3426-3436.

8. Maruo, S.; Fourkas, J. T., Recent progress in multiphoton microfabrication. *Laser & Photonics Reviews* **2008,** *2* (1-2), 100-111.

9. Scott, T. F.; Kloxin, C. J.; Forman, D. L.; McLeod, R. R.; Bowman, C. N., Principles of voxel refinement in optical direct write lithography. *Journal of Materials Chemistry* **2011,** *21* (37), 14150-14155.

10. Jang, J. H.; Ullal, C. K.; Maldovan, M.; Gorishnyy, T.; Kooi, S.; Koh, C. Y.; Thomas, E. L., 3D micro- and nanostructures via interference lithography. *Advanced Functional Materials* **2007,** *17* (16), 3027-3041.

11. Shusteff, M.; Browar, A. E. M.; Kelly, B. E.; Henriksson, J.; Weisgraber, T. H.; Panas, R. M.; Fang, N. X.; Spadaccini, C. M., One-step volumetric additive manufacturing of complex polymer structures. *Science Advances* **2017,** *3* (12), eaao5496.

12. Loterie, D.; Delrot, P.; Moser, C., Volumetric 3D printing of elastomers by tomographic back-projections. **2018**, DOI: 10.13140/RG.2.2.20027.46889, accessed June 10, 2019.

13. Kelly, B. E.; Bhattacharya, I.; Heidari, H.; Shusteff, M.; Spadaccini, C. M.; Taylor, H. K., Volumetric additive manufacturing via tomographic reconstruction. *Science* **2019,** *363* (6431), 1075-1079.

14. Junkers, T.; Wong, E. H. H.; Szablan, Z.; Davis, T. P.; Stenzel, M. H.; Barner-Kowollik, C., Laser induced marking of polymer chains with radical spin traps. *Macromolecular Rapid Communications* **2008,** *29* (6), 503-510.

15. Karatekin, E.; Landis, M.; Lem, G.; O'Shaughnessy, B.; Turro, N. J., Photocopying living chains. 1. Steady-state. *Macromolecules* **2001,** *34* (23), 8187-8201.

16. Karatekin, E.; Landis, M.; Lem, G.; O'Shaughnessy, B.; Turro, N. J., Photocopying living chains. 2. Time-dependent measurements. *Macromolecules* **2001,** *34* (23), 8202-8215.

17. Scott, T. F.; Kowalski, B. A.; Sullivan, A. C.; Bowman, C. N.; McLeod, R. R., Two-Color Single-Photon Photoinitiation and Photoinhibition for Subdiffraction Photolithography. *Science* **2009,** *324* (5929), 913-917.

18. Lovell, L. G.; Elliott, B. J.; Brown, J. R.; Bowman, C. N., The effect of wavelength on the polymerization of multi(meth)acrylates with disulfide/benzilketal combinations. *Polymer* **2001,** *42* (2), 421-429.

19. Cook, W. D., Photopolymerization kinetics of dimethacrylates using the camphorquinone amine initiator system. *Polymer* **1992,** *33* (3), 600-609.

20. Berdzinski, S.; Strehmel, N.; Lindauer, H.; Strehmel, V.; Strehmel, B., Extended mechanistic aspects on photoinitiated polymerization of 1,6-hexanediol diacrylate by hexaarylbisimidazoles and heterocyclic mercapto compounds. *Photochemical & Photobiological Sciences* **2014,** *13* (5), 789-798.

21. Ahn, D.; Sathe, S. S.; Clarkson, B. H.; Scott, T. F., Hexaarylbiimidazoles as visible light thiol–ene photoinitiators. *Dent. Mater.* **2015,** *31* (9), 1075-1089.

22. Kharasch, M. S.; Nudenberg, W.; Jensen, E. V.; Fischer, P. E.; Mayfield, D. L., Inhibition of Polymerization - Laboratory and Plant Control of Popcorn Polymer Growth. *Industrial and Engineering Chemistry* **1947,** *39* (7), 830-837.

23. Bortel, E.; Kochanowski, A.; Kudla, S.; Witek, E., Free radical polymerization in aqueous solution of acrylic acid mediated by nitroxides originated from NaNO2. *Journal of Macromolecular Science-Pure and Applied Chemistry* **1998,** *A35* (2), 401-409.

24. Lewis, E. E., Use of organic nitrites to inhibit polymerization of hydrocarbons during distillation. **January 10, 1956**, US Patent number 2,730,489.

25. Kabasakalian, P.; Townley, E. R.; Yudis, M. D., Photolysis of Nitrite Esters in Solution. III. Photochemistry of Primary, Secondary, and Tertiary Alkyl Nitrites. *Journal of the American Chemical Society* **1962,** *84* (14), 2718-2722.

26. Kabasakalian, P.; Townley, E. R., Photolysis of Nitrite Esters in Solution. I. Photochemistry of n-Octyl Nitrite. *Journal of the American Chemical Society* **1962,** *84* (14), 2711-2716.

27. Dolinski, N. D.; Page, Z. A.; Callaway, E. B.; Eisenreich, F.; Garcia, R. V.; Chavez, R.; Bothman, D. P.; Hecht, S.; Zok, F. W.; Hawker, C. J., Solution Mask Liquid Lithography (SMaLL) for One-Step, Multimaterial 3D Printing. *Advanced Materials* **2018,** *30* (31).

28. Schwartz, J. J.; Boydston, A. J., Multimaterial actinic spatial control 3D and 4D printing. *Nature Communications* **2019,** *10*, 791.

29. Sadykov, R. A.; Puzin, Y. I.; Shishlov, N. M.; Leplyanin, G. V., ESR study of the polymerization of methyl methacrylate photoinhibited by butyl nitrite. *Polymer Science USSR* **1988,** *30* (9), 2045-2049.

30. Asmusen, S.; Arenas, G.; Cook, W. D.; Vallo, C., Photobleaching of camphorquinone during polymerization of dimethacrylate-based resins. *Dent. Mater.* **2009,** *25* (12), 1603-1611.

31. Nowak, D.; Ortyl, J.; Kaminska-Borek, I.; Kukula, K.; Topa, M.; Popielarz, R., Photopolymerization of hybrid monomers Part I: Comparison of the performance of selected photoinitiators in cationic and free-radical polymerization of hybrid monomers. *Polymer Testing* **2017,** *64*, 313-320.

32. Nowak, D.; Ortyl, J.; Kaminska-Borek, I.; Kukula, K.; Topa, M.; Popielarz, R., Photopolymerization of hybrid monomers, Part II: Determination of relative quantum efficiency of selected photoinitiators in cationic and free-radical polymerization of hybrid monomers. *Polymer Testing* **2018,** *67*, 144-150.

33. Dolinski, N. D.; Page, Z. A.; Callaway, E. B.; Eisenreich, F.; Garcia, R. V.; Chavez, R.; Bothman, D. P.; Hecht, S.; Zok, F. W.; Hawker, C. J., Solution Mask Liquid Lithography (SMaLL) for One-Step, Multimaterial 3D Printing. *Advanced Materials* **2018,** *30* (31), 1800364.

34. Schwartz, J. J.; Boydston, A. J., Multimaterial actinic spatial control 3D and 4D printing. *Nature Communications* **2019,** *10*.

35. Crivello, J. V., Cationic photopolymerization of alkyl glycidyl ethers. *Journal of Polymer Science Part a-Polymer Chemistry* **2006,** *44* (9), 3036-3052.

36. Liu, B.; Li, H.; Ha, C.-S.; Kim, I.; Yan, W., Ring-opening polymerization of epsilon-caprolactone and cyclohexene oxide initiated by aluminum beta-ketoamino complexes: Steric and electronic effect of 3-position substituents of the ligands. *Macromolecular Research* **2008,** *16* (5), 441-445.

37. Plommer, H.; Reim, I.; Kerton, F. M., Ring-opening polymerization of cyclohexene oxide using aluminum amine-phenolate complexes. *Dalton Transactions* **2015,** *44* (27), 12098-12102.

Chapter 6

Summary and Future Work

6.1 Research Summary

In this dissertation we have demonstrated several thiol–ene formulations as excellent candidates for dental restorative resins. Through monomer design and pre-oligomerization, high T_g, low shrinkage stress thiol–ene polymers were obtained. Subsequently, these materials were improved upon by reducing shrinkage stress through addition-fragmentation chain-transfer chemistry, as well as demonstrating compatibility with acidic monomers to improve adhesion to mineralized tissues. In the second half of this dissertation, we study hexaarylbiimidazoles and alkyl nitrites as photoinhibitors of free radical chain-growth photopolymerizations. This resulted in development of a rapid continuous additive manufacturing approach, as well as volumetric photopolymerization confinement to 3D print complex structures.

In chapter 2, we designed and polymerized novel ester free, high T_g, low shrinkage stress pre-oligomerized thiol–ene resins. Typical dental restorative formulations consist primarily of dimethacrylate-based monomers. Despite their excellent thermomechanical and aesthetic properties, the free radical chain-growth polymerization of these dental composites exhibits significant volumetric shrinkage, which subsequently induces high polymerization-induced shrinkage stress. Thiol–ene polymers display a significantly lowered polymerization shrinkage and accompanied shrinkage stress, and

have often been suggested as materials to replace conventional dimethacrylate-based composites. The previously reported thiol–ene formulations typically contain hydrolysis-susceptible esters and exhibit thermomechanical properties significantly inferior to contemporary methacrylate materials. Attempts at high T_g thiol-based materials employ either methacrylates in thiol-methacrylate resins,[1] or demonstrate significantly reduced polymerization rates.[2] By improving monomer purification, and incorporating rigid norbornyl monomers through pre-oligomerization we were able to obtain rapidly curing, highly crosslinked vitrified thiol–ene polymers showing a 60% reduction in polymerization shrinkage stress relative to the thiol–ene reference material.

Chapter 3 entails further development of the thiol–ene resins developed in chapter 2, with the aim to further reduce shrinkage stress and expand toward acidic monomers to promote adhesion to mineralized tissues. Among the approaches to reduce polymerization-induced shrinkage stress in dental restorative formulations, addition-fragmentation chain-transfer chemistry has emerged as a mechanism to this end. In AFCT, network rearrangement of the crosslinking polymeric material is achieved through reversible addition and fragmentation of the chain-transfer moiety. While different AFCT chemistries have been explored,[3, 4] the allyl disulfide-based AFCT allows for excellent stress relaxation in thiol–ene formulations.[5] Whereas previously reported thiol–ene AFCT formulations resulted in elastomeric materials, in here we successfully demonstrate the application of allyl-sulfide AFCT additives in highly crosslinked vitrified thiol–ene polymers. Inclusion of these additives further reduced polymerization shrinkage stress, down to 19% of the thiol–ene reference. While pre-oligomerization lead to initial reduction in polymerization shrinkage stress, at increased concentrations of the AFCT

agent, no shrinkage stress difference was observed between the pre-oligomerized and regular formulations, while the pre-oligomerized resins still exhibited increased T_gs. To promote adhesion to mineralized tissue, several carboxylic acid and phosphoric acid-containing thiol–ene monomers have been successfully prepared. Incorporation of these monomers lead to reductions in polymerization rates, especially at high concentrations of phosphoric-acid containing formulations. These materials further resulted in a decrease in the crosslinking density and a subsequent reduction in T_g.

In Chapter 4 we describe the study of hexaarylbiimidazoles (HABIs) as photoinhibitors of free-radical chain-growth photopolymerizations. A significant limitation in contemporary stereolithographic additive manufacturing is found in the print rates as a result of the layer-by-layer process. This process necessitates time-consuming separation and recoating between layers, limiting print rates to centimeters per hour at best. Preventing adhesion to the curing window can significantly improve production rates, as demonstrated by the continuous liquid interface production (CLIP) technique.[6] Inspired by previously reported photoinhibition chemistries,[7] we demonstrated *o*-Cl-HABI to be an excellent photoinhibitor of acrylate-, methacrylate-, and maleimide/vinyl ether photopolymerizations. In contrast to previously reported photoinhibitors, *o*-Cl-HABI does not interfere with the photopolymerization through chain-transfer reactions, significantly improving photoinhibition contrast. Following a demonstration with 2D photopatterning, *o*-Cl-HABI was then successfully applied in rapid continuous additive manufacturing through two-color irradiation. The lifetime of the transient inhibiting species ultimately limits the print rates and print contrast of the continuous additive manufacturing process. Diffusion-limited covalently linked HABIs were subsequently

prepared and explored for their photoinhibitive properties. These HABIs were demonstrated to inhibit photopolymerization, it was found that too short a lifetime of the transient species drastically reduced the efficacy as a photoinhibitor.

Chapter 5 examines butyl nitrite as an alternative near-UV active photoinhibiting agent in the two-color photoinitiation/photoinhibition irradiation schemes. Despite the success of HABIs as seemingly universal photoinhibitors of free-radical chain-growth photopolymerizations,[8] the extended lifetime of the transient *o*-Cl-HABI-derived lophyl radical is ultimately limiting to the continuous additive manufacturing process. Butyl nitrite has previously been reported as a photoinhibitor of thermally initiated free-radical polymerizations of methyl methacrylate[9], and thus we hypothesized it could act as a near-UV activated photoinhibitor in two-color photoinitiation/photoinhibition irradiation schemes. We were able to confirm this hypothesis in acrylate and methacrylate monomer formulations through time-resolved FTIR spectroscopy, and 2D photopatterning. Through a perpendicular irradiation approach we were further able to 3D print complex glassy structures in a single exposure of light, allowing for unprecedented spatial control in 3D printing. The concept of 2-color photoinitiation/photoinhibition was then further expanded on through cationic photopolymerizations. Through selective free radical photoinhibition in a combined free radical/cationic photopolymerization system, we successfully demonstrated the ability for spatial control over linear and crosslinked photopolymerizations. This allows for dissolution of linear polymers in a stereolithographic system, potentially eliminating the need for mechanical removal of support structures in stereolithography in favor of linear methacrylate dissolution.

6.2 Future directions

The results outlined in Chapter 2 and Chapter 3 successfully demonstrate the development of low shrinkage stress, high T_g thiol–ene materials. The initial composite biocompatibility encourages further study into this area. The impact of filler material on the thiol–ene resins is an important aspect to evaluate. When considering composite materials, the nature of the filler material as well as the filler content in the composite will significantly impact the material. Shrinkage stress measurements, mechanical testing, and biological evaluation of the resins containing NAS would be prudent. Aspects not evaluated in the current studies, but of great importance for application in the dental clinic include depth of cure, composite shrinkage stress, thiol–ene resin stability. It is imperative to note that all thiol–ene resins evaluated in this work were cured at 405nm irradiation, whilst the dental practice employs blue light photoinitiators instead. Therefore, examining hexaarylbiimidazoles visible light thiol–ene photoinitiators is suggested, as the conventional CQ/EDAB system is a poor thiol–ene photoinitiator.[10]

A second aspect to consider for the dental practice is the aforementioned stability of thiol–ene formulations. Following mixing of the thiol and ene monomers, the thiol–ene reaction proceeds very slowly in the dark. Ideally a two-component system could be used for thiol–ene resins, but high viscosity of the oligomers and composite materials could impair rapid, complete mixing. A combination of radical inhibitors and acids of appropriate pK_a have been demonstrated to significantly increase the time to gelation of formulated thiol–ene resins[11] and would provide an excellent starting point.

A third facet of thiol–ene materials to focus on is adhesion to mineralized tissues. While Chapter 3 successfully demonstrates the compatibility of these thiol–ene

formulations with acidic monomers, unfortunately no adhesive examination of the prepared resins could be performed in time. Besides the impact of the self-etch acidic monomers on adhesion, the affinity of thiol–ene formulations in the "total etch" approach should also be considered. Although dimethacrylate-based HEMA-containing adhesives are expected to be compatible with thiol–ene formulations, a methacrylate-free thiol–ene adhesive would be preferred. To this end, examining thiol and vinyl/allyl monomers derived from HEMA could achieve similar penetration into demineralized dentin as HEMA. As the thiol–ene polymerization requires both a thiol and an ene, development of HEMA-inspired multifunctional thiol and ene monomers is likely required. Alternatively, thiol-methacrylate systems rich in HEMA could be examined as well.

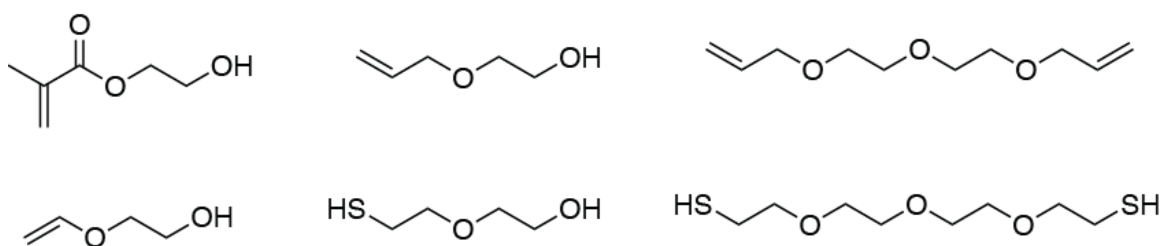

Figure 6.1 Structures of HEMA and potential adhesive thiol–ene monomers capable of penetration into demineralized dentin

The work in the latter half of Chapter 4 and that of Chapter 5 have been inspired by the necessity of shorter lifetime hexaarylbiimidazoles for this application. The long lifetime leads to a buildup of inhibiting species and results in hollow insides of the printed parts. While the use of covalently bound HABIs demonstrated some positive results, the synthetic accessibility of these materials is a significant limitation. While we hypothesize that a lophyl radical lifetime in the order of 10s-100s milliseconds is ideal for this type of continuous additive manufacturing, significant improvements to the printing process could be achieved through examining conventional functionalized

hexaarylbiimidazoles. In their studies of lophyl radicals, Cescon *et al*. thoroughly investigated the properties of several functionalized HABIs.[12] In particular, a 2,4-dichloro substituted lophyl radical displays significantly rapid dimerization in solvent at rates 1.8-4 times as fast as the *o*-chloro lophyl radical, despite the monosubstituted 4-chloro-HABI exhibiting exceedingly slow recombination.

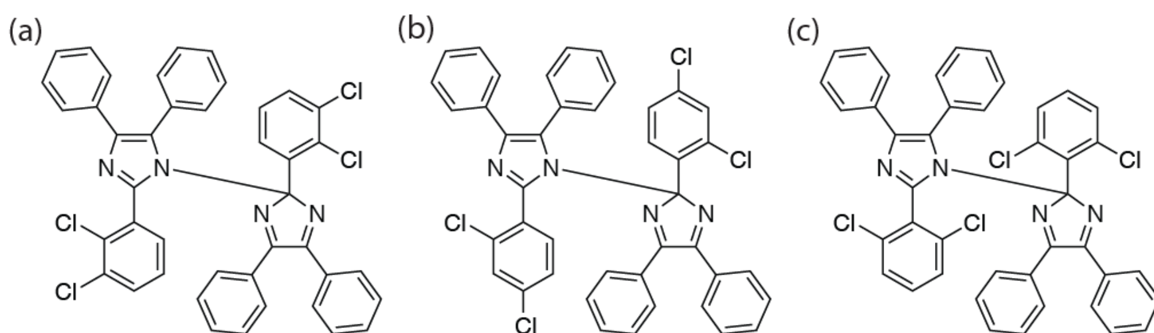

Figure 6.2 Structures of 2,3-dichloro, 2,4-dichloro, and 2,6-dichloro disubstituted hexaarylbiimidazoles

Following alternate substitution patterns, exchange of pendant groups for bromine atoms could also lead to more rapid recombination, as the *o*-bromo lophyl radical is suggested to recombine more rapidly as well, depending on the solvent. Examining these, and alternately functionalized hexaarylbiimidazoles could lead to valuable insights into the effects of aromatic group substitution on HABI photolysis and recombination behavior. While these HABIs are not available commercially, their starting materials are readily obtainable. The process of the Debus-Radziszewski reaction to yield functionalized lophines and oxidation to their respective HABIs with potassium ferricyanide is exceedingly high yielding and readily allows for large quantities to be prepared for additive manufacturing purposes.

Despite the challenges in oxygen sensitivity of the naphthalene-linked HABIs and the tedious synthetic procedure of cyclophane HABI, linked HABIs could still provide an avenue towards improving the continuous additive manufacturing process. As a balance between lophyl radical lifetime, diradical proximity and orientation seems to exist, linked HABIs connected through a flexible alkyl spacer could serve to produce oxygen-resistant, diffusion-limited HABIs. Similar approaches to coupling lophines to fluorescent dyes have been reported[13] before. This approach would allow for close control over the lophyl radical lifetime through the spacer length. Owing to the mild reaction conditions, further functionalization of the alkyl-linked HABIs through the benzil-derived phenyl rings is possible. This would allow for these materials to be included in cross-linked polymeric networks, and be dissociated without loss of crosslinking density, generating a visual cue for mechanochemical or photochemical processes affecting a material.

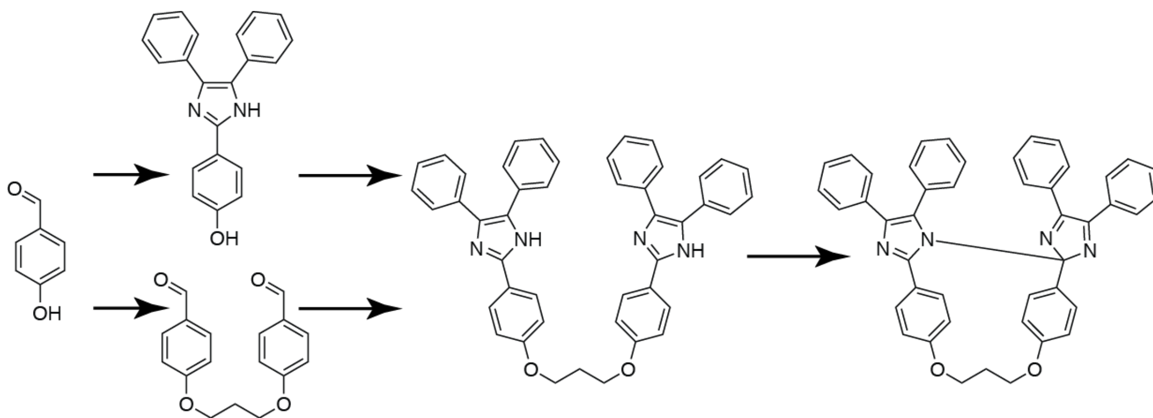

Scheme 6.1 Synthetic route towards alkyl linked HABIs

Despite the shortcomings in rapid continuous additive manufacturing, the two-color photoinitiation/photoinhibition chemistry grants unprecedented control over the location of polymer curing. An exciting recently developed approach towards additive manufacturing lies in tomography through backprojection[14] or iterative reconstruction.[15,

[16] In the published approaches light projection into the resin results in exceeding a gelation dose threshold in desired areas whilst other areas receive an insufficient dose. A significant limitation in these approaches is observed near the edges of the printed part, as light diffraction and light beam convergence result in a decrease in resolution. By introducing the photoinitiation/photoinhibition to this system, projection of near-UV light towards the edges of the printed part could result in a significant improvement of resolution, as well as easier handling of the printed part, now that higher conversions could be achieved without excessive undesired curing. While not a tomographic approach, the results from Chapter 5 are highly encouraging of such a system to be successful.

Alternatively, the two-color photoinitiation/photoinhibition irradiation approach could be used for the manufacturing of hydrogel materials. Demonstrated successfully with the CQ/TETD system[17], two-color irradiation approaches for the construction of hydrogels could be significantly expanded upon with the CQ/HABI system. Water soluble CQ[18] and HABIs[19] have been described before, and the system should be readily adaptable for this. Not only through continuous stereolithography, but through the tomographic projection methods as well.

The paradigm shift into employing two-color irradiation approaches need not be limited to free radical photopolymerizations. Any system that could be independently activated or deactivated through this type of irradiation could be used. Recently, spiropyran-derived materials have been employed in ring-opening and ring-closing of the spirothiopyran to induce thiol–Michael reactions to crosslink polymeric materials.[20-22]

Besides the thiol–Michael reaction, two-color irradiation schemes could prove themselves useful in cationic photopolymerizations. Introduction of recently described, independently activating photobases[23] could be used to control cationic polymerizations. Conversely, non spirothiopyran-based thiol-Michael photopolymerizations could conceivably be inhibited by cationic photoinitiators. Even the photoinitiated Cu(I) catalyzed Huisgens cycloaddition reactions[24] could be controlled through photo oxidation of Cu(I) to the catalytically inactive Cu(II).

6.3 References

1. Cramer, N. B.; Couch, C. L.; Schreck, K. M.; Boulden, J. E.; Wydra, R.; Stansbury, J. W.; Bowman, C. N., Properties of methacrylate-thiol–ene formulations as dental restorative materials. *Dental Materials* **2010,** *26* (8), 799-806.

2. Podgórski, M.; Becka, E.; Chatani, S.; Claudino, M.; Bowman, C. N., Ester-free thiol-X resins: new materials with enhanced mechanical behavior and solvent resistance. *Polym. Chem.* **2015,** *6* (12), 2234-2240.

3. Shah, P. K.; Stansbury, J. W.; Bowman, C. N., Application of an addition-fragmentation-chain transfer monomer in di(meth) acrylate network formation to reduce polymerization shrinkage stress. *Polymer Chemistry* **2017,** *8* (30), 4339-4351.

4. Gauss, P.; Ligon-Auer, S. C.; Griesser, M.; Gorsche, C.; Svajdlenkova, H.; Koch, T.; Moszner, N.; Liska, R., The Influence of Vinyl Activating Groups on beta-Allyl Sulfone-Based Chain Transfer Agents for Tough Methacrylate Networks. *Journal of Polymer Science Part a-Polymer Chemistry* **2016,** *54* (10), 1417-1427.

5. Kloxin, C. J.; Scott, T. F.; Bowman, C. N., Stress Relaxation via Addition-Fragmentation Chain Transfer in a Thiol–ene Photopolymerization. *Macromolecules* **2009,** *42* (7), 2551-2556.

6. Tumbleston, J. R.; Shirvanyants, D.; Ermoshkin, N.; Janusziewicz, R.; Johnson, A. R.; Kelly, D.; Chen, K.; Pinschmidt, R.; Rolland, J. P.; Ermoshkin, A.; Samulski, E. T.; DeSimone, J. M., Continuous liquid interface production of 3D objects. *Science* **2015,** *347* (6228), 1349-1352.

7. Scott, T. F.; Kowalski, B. A.; Sullivan, A. C.; Bowman, C. N.; McLeod, R. R., Two-Color Single-Photon Photoinitiation and Photoinhibition for Subdiffraction Photolithography. *Science* **2009,** *324* (5929), 913-917.

8. De Beer, M. P.; Van der Laan, H. L.; Cole, M. A.; Whelan, R. J.; Burns, M. A.; Scott, T. F., Rapid, Continuous Additive Manufacturing by Volumetric Polymerization Inhibition Patterning. *Science Advances* **2019,** *5* (1), eaau8723.

9. Sadykov, R. A.; Puzin, Y. I.; Shishlov, N. M.; Leplyanin, G. V., ESR study of the polymerization of methyl methacrylate photoinhibited by butyl nitrite. *Polymer Science USSR* **1988,** *30* (9), 2045-2049.

10. Ahn, D.; Sathe, S. S.; Clarkson, B. H.; Scott, T. F., Hexaarylbiimidazoles as visible light thiol–ene photoinitiators. *Dental Materials* **2015,** *31* (9), 1075-1089.

11. Esfandiari, P.; Ligon, S. C.; Lagref, J. J.; Frantz, R.; Cherkaoui, Z.; Liska, R., Efficient Stabilization of Thiol–ene Formulations in Radical Photopolymerization. *Journal of Polymer Science Part a-Polymer Chemistry* **2013,** *51* (20), 4261-4266.

12. Cescon, L. A.; Coraor, G. R.; Dessauer, R.; Silversm.Ef; Urban, E. J., Properties of Triarylimidazoyl Radicals and their Dimers. *Journal of Organic Chemistry* **1971,** *36* (16), 2262-2267.

13. Gong, W. L.; Zhang, G. F.; Li, C.; Aldred, M. P.; Zhu, M. Q., Design, synthesis and optical properties of a green fluorescent photoswitchable hexaarylbiimidazole (HABI) with non-conjugated design. *Rsc Advances* **2013,** *3* (24), 9167-9170.

14. Loterie, D.; Delrot, P.; Moser, C., Volumetric 3D printing of elastomers by tomographic back-projections. **2018**, DOI: 10.13140/RG.2.2.20027.46889, accessed June 10, 2019.

15. Shusteff, M.; Browar, A. E. M.; Kelly, B. E.; Henriksson, J.; Weisgraber, T. H.; Panas, R. M.; Fang, N. X.; Spadaccini, C. M., One-step volumetric additive manufacturing of complex polymer structures. *Science Advances* **2017,** *3* (12), eaao5496.

16. Kelly, B. E.; Bhattacharya, I.; Heidari, H.; Shusteff, M.; Spadaccini, C. M.; Taylor, H. K., Volumetric additive manufacturing via tomographic reconstruction. *Science* **2019,** *363* (6431), 1075-1079.

17. Hu, K.; An, J. N.; Yoon, Y. J., Two-Wavelength, Photo-Initiation and Photo-Inhibition Competing for Selective Photo-Patterning of Hydrogel Porous Microstructures. *International Journal of Precision Engineering and Manufacturing* **2018,** *19* (5), 729-735.

18. Kamoun, E. A.; Winkel, A.; Eisenburger, M.; Menzel, H., Carboxylated camphorquinone as visible-light photoinitiator for biomedical application: Synthesis, characterization, and application. *Arabian Journal of Chemistry* **2016,** *9* (5), 745-754.

19. Igarashi, H.; Igarashi, T.; Sagawa, M.; Mori, T.; Kotani, Y.; Muroya, Y.; Katsumura, Y.; Yamashita, T., Preparation and photoreactivity of a novel lophine dimer containing a hydrophilic group. *Journal of Photopolymer Science and Technology* **2007,** *20* (5), 757-762.

20. Vijayamohanan, H.; Palermo, E. F.; Ullal, C. K., Spirothiopyran-Based Reversibly Saturable Photoresist. *Chemistry of Materials* **2017,** *29* (11), 4754-4760.

21. Vijayamohanan, H.; Bhide, P.; Boyd, D.; Zhou, Z.; Palermo, E. F.; Ullal, C. K., Effect of Chemical Microenvironment in Spirothiopyran Monolayer Direct-Write Photoresists. *Langmuir* **2019,** *35* (11), 3871-3879.

22. Muller, P.; Muller, R.; Hammer, L.; Barner-Kowollik, C.; Wegener, M.; Blasco, E., STED-Inspired Laser Lithography Based on Photoswitchable Spirothiopyran Moieties. *Chemistry of Materials* **2019,** *31* (6), 1966-1972.

23. Zhang, X. P.; Xi, W. X.; Gao, G. Z.; Wang, X. C.; Stansbury, J. W.; Bowman, C. N., o-Nitrobenzyl-Based Photobase Generators: Efficient Photoinitiators for Visible -Light Induced Thiol-Michael Addition Photopolymerization. *Acs Macro Letters* **2018,** *7* (7), 852-857.

24. McBride, M. K.; Gong, T.; Nair, D. P.; Bowman, C. N., Photo-mediated copper(I)-catalyzed azide-alkyne cycloaddition (CuAAC) "click" reactions for forming polymer networks as shape memory materials. *Polymer* **2014,** *55* (23), 5880-5884.